

**Manufacture of and Environmental Effects on
Carbon Fiber-Reinforced PhenylEthyne-Terminated
Poly(EtherImide)**

Todd Aaron Bullions

Dissertation submitted to the Faculty of the
Virginia Polytechnic Institute and State University
in partial fulfillment of the requirements for the degree of

Doctor of Philosophy
in
Materials Engineering Science

Alfred C. Loos, Chair
Engineering Science and Mechanics

Donald G. Baird
Chemical Engineering

David Dillard
Engineering Science and Mechanics

Ron Kander
Materials Science and Engineering

James E. McGrath
Chemistry

September 13, 2000
Blacksburg, Virginia

Keywords: Composite, PhenylEthyne-Terminated Poly(EtherImide),
Cure Kinetics, Rheology, Dry Powder Prepregging, Moisture, Thermal-
Oxidative Aging

Copyright 2000, Todd Aaron Bullions

Manufacture of and Environmental Effects on Carbon Fiber-Reinforced Phenylethynyl-Terminated Poly(EtherImide)

Todd Aaron Bullions
Alfred C. Loos

Abstract:

The initial objective of this research project was to determine the feasibility of manufacturing carbon fiber-reinforced (CFR) composites with a matrix consisting of a phenylethynyl-terminated version of a thermoplastic poly(etherimide) termed PETU. Successful composite manufacture with 3,000 g/mol (3k) PETU led to a survey of CFR 3kPETU mechanical properties for comparison with other high-performance composites. Encouraging results led to a study of moisture sorption effects on CFR 3kPETU properties. The success of these initial studies spawned the large scale production of 2,500 g/mol (2.5k) PETU.

Thermal characterization of neat and CFR 2.5kPETU via differential scanning calorimetry, dynamic mechanical thermal analysis, and parallel plate rheometry resulted in an understanding of the influence of cure time and temperature on reaction progress via both reaction kinetics and monitoring of the glass transition temperature. From the rheological characterization, a two-stage, dual-Arrhenius model was developed to successfully model isothermal complex viscosity over the range of processing temperatures.

Neat 2.5kPETU and CFR 2.5kPETU specimens were exposed separately to elevated temperature environments of different moisture and different oxygen concentrations to evaluate the effects of moisture absorption, moisture desorption, and thermal oxidation on material properties. Moisture absorption took place in a 90 °C / 85% relative humidity environment followed by moisture desorption in a 90 °C / 10% relative humidity environment. Thermal-oxidative aging for up to 5000 hours took place at 204 °C in environments of four different oxygen partial pressures: 0.0 kPa, 2.84 kPa, 20.2 kPa, and 40.4 kPa. Following exposure to the different aging environments, the specimens were tested for retention of mechanical properties. In addition, moisture sorption properties were measured.

Results from the moisture sorption studies on CFR 3kPETU and CFR 2.5kPETU suggest that fully cured composites will withstand moisture absorption and desorption with

negligible effects on mechanical properties, whereas, lack of full cure allows moisture sorption to permanently damage the composites. Despite a lack of mass loss or visual evidence of degradation following thermal-oxidative aging, a decline in mechanical properties was observed with the reduction becoming greater with longer aging times and higher oxygen partial pressures.

Acknowledgments

I would first like to thank Dr. A. C. Loos for allowing me to work with him over the past five years. I greatly appreciate his patience, guidance, and insight.

I would like to acknowledge the National Science Foundation Science and Technology Center for High Performance Polymeric Adhesives and Composites for support under contract DMR 91-20004. In addition, the Department of Defense National Defense Science and Engineering Graduate Research Fellowship Program's support of this research is appreciated. Also, financial support by the Virginia Space Grant Consortium is appreciated.

I would also like to thank the faculty, staff, and students of the National Science Foundation Science and Technology Center for High Performance Polymeric Adhesives and Composites, the Materials Engineering Science Program, the Department of Engineering Science and Mechanics, the Department of Chemical Engineering, and the Center for Composite Materials and Structures at Virginia Tech for invaluable contributions and assistance with various aspects of the successful completion of this research.

Dedication

I would like to dedicate this work to my parents, Regina and Andrew Bullions; my fiancée, Melissa Hayworth; and our dogs, Hailey and Daphne.

I want to thank my parents for emphasizing education to me throughout my life and providing the means for me to earn my Bachelor of Science degree from North Carolina State University in Materials Science and Engineering. Their financial sacrifice allowed me to concentrate on school and build the academic foundation for my doctoral studies. I would not have been able to successfully complete my doctoral degree without hard work, perseverance, and a sense of responsibility. In recognition of my parents' efforts to instill these values in me through the course of my life, I dedicate this work to them.

I would also like to dedicate this work to the person I can not imagine living without, Melissa. She encouraged me when I struggled. She listened to the venting of my frustrations. She boosted my ego when it was needed with unwarranted praise of my intelligence and skills. She provided me with a sounding board for my ideas and speculations. And, of course, she was there to answer any chemistry-related questions I had throughout my research. In recognition of Melissa going through this experience with me, despite being 200 to 3000 miles away during the past five years, I dedicate this work to her.

My faithful companion Hailey has been living with me for the past 2 ¹/₂ years, and Daphne joined us a year ago. Though they sometimes pushed my patience beyond its limits, I have to thank them for forcing me to relax at times that I would not have done so myself. Hailey and Daphne got me out of the lab and office for games of Frisbee, fetch, and chase; swims at Pandapas Pond; romps through the snow; and just ordinary walks around the neighborhood during which I did my best thinking. For forcing me to relax and reflect at times when I needed it the most, I dedicate this work to Hailey and Daphne.

In conclusion, I dedicate this work to Mom, Dad, Melissa, Hailey, and Daphne who supported me in various ways, but all through their unconditional love.

Table of Contents

Chapter 1 - Introduction	1
1.1 General Background.....	1
1.2 PhenylEthyne-Terminated Ultem™ Background.....	1
1.3 Powder Prepregging.....	3
1.3.1 Powder Prepregging: Literature Review.....	3
1.3.2 Dry Powder Prepregging System Description.....	4
1.3.2.1 Tow Spreader.....	5
1.3.2.2 Electrostatic Fluidized Bed.....	5
1.3.2.3 Minimal Dry Powder Prepregging System.....	7
1.3.2.4 Polymer Binding.....	8
1.3.2.5 Towpreg Take-Up.....	9
1.4 Project Summary.....	9
1.5 References.....	11
Chapter 2 - 3kPETU Preliminary Research.....	14
2.1 Introduction.....	14
2.2 Importance of Mechanical Property Tests.....	14
2.2.1 Apparent Interlaminar Shear Strength.....	14
2.2.2 Flexural Properties.....	14
2.2.3 Open-Hole Compression Strength [4-8].....	15
2.2.4 Fracture Toughness.....	17
2.3 Thermal Analysis.....	18
2.3.1 Differential Scanning Calorimetry.....	18
2.3.2 Rheology.....	18
2.3.2.1 Experimental.....	18
2.3.2.2 Results and Discussion.....	19
2.4 Composite Manufacture and Physical Properties.....	19
2.4.1 Towpreg Production.....	19
2.4.2 Drum Winding.....	20
2.4.3 Composite Panel Consolidation.....	21
2.4.4 Consolidation Quality.....	21
2.4.5 Composite Fiber Volume Fraction.....	22
2.5 Mechanical Property Measurement.....	22
2.5.1 Apparent Interlaminar Shear Strength.....	22
2.5.1.1 Experimental.....	22
2.5.1.2 Results and Discussion.....	23
2.5.2 Flexural Properties.....	24
2.5.2.1 Experimental.....	24
2.5.2.2 Results and Discussion.....	24
2.5.2.2.1 Longitudinal Flexural Test.....	24
2.5.2.2.2 Transverse Flexural Test.....	26
2.5.3 Open-Hole Compression Strength.....	27
2.5.3.1 Experimental.....	27
2.5.3.2 Results and Discussion.....	28
2.5.4 Mode I Fracture Toughness.....	29
2.5.4.1 Experimental.....	29
2.5.4.2 Data Reduction and Calculations.....	32
2.5.4.3 Results and Discussion.....	34

2.5.5 Mode II Fracture Toughness.....	38
2.5.5.1 Experimental	38
2.5.5.2 Data Reduction and Calculations.....	40
2.5.5.3 Results and Discussion	41
2.6 Summary and Conclusion.....	42
2.7 References	44

Chapter 3 - Moisture Sorption Effects on CFR 3kPETU Composites48

3.1 Introduction.....	48
3.2 Experimental.....	49
3.2.1 Composite Manufacture	49
3.2.2 Specimen Preparation.....	50
3.2.2.1 Sectioning	50
3.2.2.2 As-Manufactured Dimensions.....	50
3.2.2.3 Drying.....	50
3.2.2.4 Sealant Application	51
3.2.3 Moisture Absorption	51
3.2.4 Moisture Desorption	52
3.2.5 Mechanical Testing.....	53
3.2.5.1 Controls.....	53
3.2.5.2 Wet.....	53
3.2.5.3 Wet/Dry.....	54
3.2.6 Density, Void Content, and Fiber Volume Fraction.....	54
3.3 Results and Discussion.....	55
3.3.1 Composite Consolidation and Physical Properties	55
3.3.2 Composite Moisture Absorption.....	55
3.3.3 Neat Resin Moisture Sorption	57
3.3.4 Composite Moisture Desorption.....	57
3.3.5 Discrepancies in Moisture Sorption Results.....	58
3.3.6 Moisture Induced Strain	60
3.3.7 Sealants.....	62
3.3.8 Mechanical Property Retention	63
3.3.9 Pre-Cut Versus Post-Cut.....	65
3.4 Conclusion.....	66
3.5 References	68

Chapter 4 - 2.5kPETU Cure Kinetics Model70

4.1 Introduction.....	70
4.2 PETU Cure Kinetics Review	70
4.3 Cure Kinetics Modeling Background.....	74
4.4 Cure Kinetics Experimental.....	76
4.5 Experimental Analysis and Results	77
4.6 Summary Discussion.....	101
4.7 References	103

Chapter 5 - Monitoring Reaction Progress via Glass Transition Temperature 105

5.1 Introduction.....105
5.2 Background.....105
 5.2.1 Glass Transition Temperature.....105
 5.2.2 Central Composite Design Experiment109
 5.2.3 Glass Transition Temperature Measurement Techniques.....109
5.3 Experimental.....110
 5.3.1 Preliminary Work110
 5.3.2 Composite Panels111
 5.3.2.1 Composite Manufacture.....111
 5.3.2.2 DMTA Testing112
 5.3.2.3 DSC Measurements112
 5.3.3 Neat Resin.....113
 5.3.4 Towpreg.....113
5.4 Results.....117
 5.4.1 Composite Panels117
 5.4.2 Neat Resin.....120
 5.4.3 Towpreg Resin121
5.5 Discussion126
5.6 Summary.....127
5.7 References128

Chapter 6 - Development of Two-Stage, Dual-Arrhenius Rheology Model for 2.5kPETU 131

6.1 Introduction.....131
6.2 Experimental.....133
6.3 Results.....136
6.4 Model Development.....136
 6.4.1 Model Development for DA1139
 6.4.2 Model Development for DA2147
 6.4.3 Completion of Model154
 6.4.4 Model Analysis156
6.5 Summary.....157
6.6 References158

Chapter 7 - Manufacture of 2.5kPETU Specimens for Moisture Exposure and Thermal-Oxidative Aging..... 160

7.1 Introduction.....160
7.2 Composite Panel Manufacture.....160
 7.2.1 Dry Powder Prepregging.....160
 7.2.2 Ply Production.....161
 7.2.3 Composite Panel Consolidation161
 7.2.4 Post Consolidation162
7.3 Neat Resin Plaques164
7.4 References164

Chapter 8 - Moisture Sorption Effects on CFR 2.5kPETU Composites 165

8.1 Introduction.....165
8.2 Mechanical Test Specimens - Experimental.....165
 8.2.1 Specimen Preparation.....165
 8.2.1.1 Specimen Distribution.....165
 8.2.1.2 Aluminum Specimens.....166
 8.2.1.3 As-Manufactured Dimensions and Masses166
 8.2.1.4 Drying.....166
 8.2.1.5 Sealant Application167
 8.2.2 Moisture Absorption and Preparation for Mechanical Testing167
 8.2.3 Moisture Desorption and Preparation for Mechanical Testing168
 8.2.4 Mechanical Testing.....169
 8.2.4.1 Transverse Flexural Strength.....169
 8.2.4.2 Open-Hole Compression Strength.....169
 8.2.4.3 Apparent Interlaminar Shear Strength.....169
8.3 Dependence of Specimen Moisture Content and Dimensions on Relative Humidity - Experimental170
 8.3.1 Moisture Content versus Relative Humidity170
 8.3.2 Moisture Induced Strain170
8.4 Results and Discussion - Moisture Sorption and Content.....171
 8.4.1 Through-the-Thickness Moisture Diffusion Coefficient.....171
 8.4.2 Equilibrium Moisture Contents178
 8.4.3 Moisture Induced Strain179
8.5 Results - Mechanical Property Tests.....180
8.6 Conclusion.....184
8.7 References185

Chapter 9 - Thermal-Oxidative Aging Effects on Composite Properties..... 186

9.1 Thermal-Oxidative Aging Background186
9.2 Anisotropic Degradation and Specimen Surface Area Effects190
9.3 Specimen Aging and Testing194
9.4 Experimental.....197
 9.4.1 Specimen Aging.....197
 9.4.1.1 Specimen Distribution.....197
 9.4.1.2 Details of Actual Aging History.....197
 9.4.1.3 Discussion of 177 °C Aging versus 204 °C Aging198
 9.4.2 Monitoring Mass Change.....200
 9.4.3 Mechanical Testing.....201
 9.4.3.1 Open-Hole Compression Testing.....201
 9.4.3.2 Apparent Interlaminar Shear Strength.....201
 9.4.3.3 Transverse Flexural Strength.....201
 9.4.4 Thermomechanical Analysis201
 9.4.5 Dynamic Mechanical Thermal Analysis.....202
 9.4.6 Microindentation of Neat Resin.....202
9.5 Results and Discussion.....202
 9.5.1 Monitoring Mass Change.....202
 9.5.2 TOA Effect on Softening Temperature Measured via TMA203
 9.5.3 TOA Effect on Glass Transition Temperature Measured via DMTA ...205
 9.5.4 Open-Hole Compression Strength205

9.5.5 Apparent Interlaminar Shear Strength.....207
9.5.6 Transverse Flexural Strength207
9.5.7 Optical Microscopy.....210
9.5.8 Vickers Hardness of Aged Neat Resin via Microindentation.....211
9.6 Summary Comments217
9.7 References218

**Chapter 10 - Conclusions and Recommendations for
Future Work 221**

10.1 Conclusions221
10.2 Recommendations for Future Work.....225

List of Figures

Chapter 1

Figure 1.1.	4-phenylethynylphthalic anhydride endcapped bisphenol-A dianhydride/ <i>meta</i> -phenylene diamine.....	2
Figure 1.2.	Electrostatic, Fluidized Bed, Dry Powder Prepregging System [14,15].....	5
Figure 1.3.	Dry Powder Prepregging System Components: (a) Pneumatic Tow Spreader (b) Electrostatic Fluidized Bed [14].....	6
Figure 1.4.	MDPPS: (a) Close-up (b) Location in Powder Coating Line.....	8

Chapter 2

Figure 2.1.	Kink Band [6].....	17
Figure 2.2.	10 °C/min Ramp of Virgin 3kPETU Powder in N ₂ Environment.....	19
Figure 2.3.	Rheological Behavior of 3kPETU During 3.1 °C/min Ramp	20
Figure 2.4.	Optical Micrograph of Composite Cross Section	22
Figure 2.5.	Apparent Interlaminar Shear Strength [14-16]	23
Figure 2.6.	Longitudinal Flexural Strength [14, 17-19].....	25
Figure 2.7.	Longitudinal Flexural Modulus [14, 17-19].....	25
Figure 2.8.	Longitudinal Flexural Tensile Fracture Surface (Gray Bar = 5 µm).....	26
Figure 2.9.	Transverse Flexural Strength [20-22].....	27
Figure 2.10.	Transverse Flexural Tensile Fracture Surface (Gray Bar = 10 µm).....	28
Figure 2.11.	OHCS Kink Band	29
Figure 2.12.	OHCS Fiber Buckling.....	29

Figure 2.13. Description of Typical DCB Test.....	30
Figure 2.14. DCB Loading Schematic	31
Figure 2.15. Compliance versus Crack Length.....	33
Figure 2.16. Delamination Resistance Curves.....	35
Figure 2.17.(a) Comparison of $G_{\text{initiation}}$ Values (Table 2.6).....	36
Figure 2.17.(b) Comparison of G_{critical} Values (Table 2.6)	37
Figure 2.18. Fracture Surface of Upper Arm of Panel A DCB Specimen (Gray Bar = 50 μm) Crack Growth Region; Crack Movement: Right to Left	38
Figure 2.19. ENF Loading Schematic.....	39
Figure 2.20. Fracture Surface of Upper Half of Panel A ENF Specimen (Bar = 100 μm).....	43

Chapter 3

Figure 3.1.(a) and (b) Composite Moisture Absorption	56
Figure 3.2.(a) Composite Moisture Desorption (b) Linear Fit of TFS Specimen Moisture Desorption.....	59
Figure 3.3. Optical Micrograph of Composite Cross Section - Varnish Sealed Surface	63
Figure 3.4. Optical Micrographs of Composite Cross Sections - Exposed Molded Surfaces: (a) Control (b) Wet (c) Wet/Dry.....	63
Figure 3.5. Summary of Mechanical Property Results.....	64
Figure 3.6. Pre-Cut Versus Post-Cut Mechanical Property Results	67

Chapter 4

Figure 4.1. Differential Scanning Calorimetry: 5 $^{\circ}\text{C}/\text{min}$ Ramp of 2.5kPETU.....	77
Figure 4.2.(a) Isothermal Exotherm - Cure of 2.5kPETU at 340 $^{\circ}\text{C}$	79

Figure 4.2.(b) Isothermal Exotherm - Cure of 2.5kPETU at 340 °C - Magnification of t_s region	79
Figure 4.3. Determination of Rate Constants	80
Figure 4.4. Determination of First-Order Reaction Activation Energy	82
Figure 4.5.(a) Comparison of Actual and Calculated Degree of Cure Versus Time, 330 °C	82
Figure 4.5.(b) Comparison of Actual and Calculated Degree of Cure Versus Time, 340 °C	83
Figure 4.5.(c) Comparison of Actual and Calculated Degree of Cure Versus Time, 350 °C	83
Figure 4.5.(d) Comparison of Actual and Calculated Degree of Cure Versus Time, 360 °C	84
Figure 4.6. Percent Error in Calculated Time to Reach Predicted Degree of Cure for First-Order Kinetics.....	84
Figure 4.7.(a) Representative $d\alpha/dt$ versus α_I Curves, Experimental and Calculated via First Order Reaction Kinetics, 345 °C	86
Figure 4.7.(b) Representative $d\alpha/dt$ versus α_I Curves, Experimental and Calculated via First Order Reaction Kinetics, 350 °C	86
Figure 4.8. Reaction Rate Versus Degree of Cure Plot Generated from Heat Flow Versus Time Data for 340 °C Isothermal Cure	87
Figure 4.9. Curve Fitting of $d\alpha/dt$ Versus α at 340 °C for k_1 , k_2 , m , and n	88
Figure 4.10. Arrhenius Plot of k_1 Data.....	89
Figure 4.11. Arrhenius Plot of k_2 Data.....	89
Figure 4.12. m Versus Temperature.....	90
Figure 4.13. n Versus Temperature.....	90
Figure 4.14.(a) 330 °C - $d\alpha/dt$ Versus α : Calculated Compared with Experimental	93
Figure 4.14.(b) 340 °C - $d\alpha/dt$ Versus α : Calculated Compared with Experimental	93

Figure 4.14.(c) 350 °C - $d\alpha/dt$ Versus α : Calculated Compared with Experimental	94
Figure 4.14.(d) 360 °C - $d\alpha/dt$ Versus α : Calculated Compared with Experimental	94
Figure 4.15.(a) 330 °C - $d\alpha/dt$ Versus α : Calculated Compared with Experimental - Individually Selected Values of n (Table 4.2).....	95
Figure 4.15.(b) 340 °C - $d\alpha/dt$ Versus α : Calculated Compared with Experimental - Individually Selected Values of n (Table 4.2).....	95
Figure 4.15.(c) 350 °C - $d\alpha/dt$ Versus α : Calculated Compared with Experimental - Individually Selected Values of n (Table 4.2).....	96
Figure 4.15.(d) 360 °C - $d\alpha/dt$ Versus α : Calculated Compared with Experimental - Individually Selected Values of n (Table 4.2).....	96
Figure 4.16.(a) α_I Versus Time (330 °C): Empirical Model Compared with Experimental Data.....	97
Figure 4.16.(b) α_I Versus Time (330 °C): Empirical Model Compared with Experimental Data for α_I Greater than 0.9	97
Figure 4.17.(a) α_I Versus Time (340 °C): Empirical Model Compared with Experimental Data.....	98
Figure 4.17.(b) α_I Versus Time (340 °C): Empirical Model Compared with Experimental Data for α_I Greater than 0.9	98
Figure 4.18.(a) α_I Versus Time (350 °C): Empirical Model Compared with Experimental Data.....	99
Figure 4.18.(b) α_I Versus Time (350 °C): Empirical Model Compared with Experimental Data for α_I Greater than 0.9	99
Figure 4.19.(a) α_I Versus Time (360 °C): Empirical Model Compared with Experimental Data.....	100
Figure 4.19.(b) α_I Versus Time (360 °C): Empirical Model Compared with Experimental Data for α_I Greater than 0.9	100
Figure 4.20. Percent Error in Calculated Time to Reach Predicted Degree of Cure for Combination Kinetics.....	101
Figure 4.21. Lack of Simple Reaction Order.....	102

Chapter 5

Figure 5.1.	Resultant Isothermal T_g Versus Isothermal Hold Temperature	107
Figure 5.2.	Influence of Cure Time on T_g for an Isothermal 350 °C Hold	108
Figure 5.3.	Second-Order Central Composite Design {From Myers and Montgomery [4], page 299}	110
Figure 5.4.	Cure Schedule CCD Scheme for Composites and First Set of Neat Resin Samples.....	111
Figure 5.5.	Cure Schedule CCD Scheme for Second Set of Neat Resin Samples.....	114
Figure 5.6.	Cure Schedule CCD Scheme for First Set of Towpreg Samples.....	116
Figure 5.7.	Cure Schedule CCD Scheme for Second Set of Towpreg Samples.....	116
Figure 5.8.	Sample Plot of Data Taken Using Polymer Laboratories DMTA - Composite Specimen: 360 °C / 40 minutes	117
Figure 5.9.	DMTA T_g Results for Composite Specimens.....	118
Figure 5.10.	Contour Plot of DMTA T_g (°C) Results for Composite Specimens.....	118
Figure 5.11.	DSC T_g Results for Composite Specimens (Each Point Shows TA Instruments T_g followed by Perkin-Elmer T_g).....	119
Figure 5.12.	Contour Plot of TA Instruments DSC T_g (°C) Results for Composite Specimens.....	120
Figure 5.13.	Contour Plot of Perkin-Elmer DSC T_g (°C) Results for Composite Specimens.....	120
Figure 5.14.	DSC T_g Results for Neat Resin Specimens Following Composite Cure Schedules.....	122
Figure 5.15.	Contour Plot of TA Instruments DSC T_g (°C) Results for Neat Resin Specimens Following Composite Cure Schedules.....	122

Figure 5.16. DSC T_g Results for Second Set of Neat Resin Specimens	123
Figure 5.17. Contour Plot of DSC T_g ($^{\circ}\text{C}$) Results for Second Set of Neat Resin Specimens.....	123
Figure 5.18. DSC T_g Results for First Set of Towpreg Resin Specimens.....	124
Figure 5.19. Contour Plot of DSC T_g ($^{\circ}\text{C}$) Results for First Set of Towpreg Resin Specimens.....	124
Figure 5.20. DSC T_g Results for Second Set of Towpreg Resin Specimens.....	125
Figure 5.21. Contour Plot of DSC T_g ($^{\circ}\text{C}$) Results for Second Set of Towpreg Resin Specimens	125

Chapter 6

Figure 6.1.(a) Rheology Results for a 3 $^{\circ}\text{C}/\text{min}$ Ramp Using a 25 mm Diameter Sample	131
Figure 6.1.(b) Rheology Results for a 3 $^{\circ}\text{C}/\text{min}$ Ramp Using a 40 mm Diameter Sample	132
Figure 6.2. Comparison of 2.5kPETU Complex Viscosity: 25 mm Diameter Sample versus 40 mm Diameter Sample.....	135
Figure 6.3. Results of Isothermal Rheology Measurements	136
Figure 6.4. Isothermal Viscosities versus Degree of Cure	137
Figure 6.5. Schematic DA Representation of DA Isothermal Viscosity Behavior	138
Figure 6.6. Isothermal Complex Viscosities versus Time to Gel Points.....	139
Figure 6.7.(a) Linear Fit of Lower Time Range of 325 $^{\circ}\text{C}$ Complex Viscosity	140
Figure 6.7.(b) Linear Fit of Lower Time Range of 330 $^{\circ}\text{C}$ Complex Viscosity	140
Figure 6.7.(c) Linear Fit of Lower Time Range of 340 $^{\circ}\text{C}$ Complex Viscosity	141

Figure 6.7.(d) Linear Fit of Lower Time Range of 350 °C Complex Viscosity	141
Figure 6.8. Arrhenius Fit of $\ln \eta_0$ versus $1/T$ for DA1.....	143
Figure 6.9. Arrhenius Fit of $\ln k$ versus $1/T$ for DA1.....	144
Figure 6.10.(a) DA1 Fit of $\ln \eta^*$ versus Time for 325 °C	145
Figure 6.10.(b) DA1 Fit of $\ln \eta^*$ versus Time for 330 °C	146
Figure 6.10.(c) DA1 Fit of $\ln \eta^*$ versus Time for 340 °C	146
Figure 6.10.(d) DA1 Fit of $\ln \eta^*$ versus Time for 350 °C	147
Figure 6.11.(a) Linear Fit of Upper Time Range of 325 °C Complex Viscosity	148
Figure 6.11.(b) Linear Fit of Upper Time Range of 330 °C Complex Viscosity	148
Figure 6.11.(c) Linear Fit of Upper Time Range of 340 °C Complex Viscosity	149
Figure 6.11.(d) Linear Fit of Upper Time Range of 350 °C Complex Viscosity	149
Figure 6.12. Arrhenius Fit of $\ln \eta_0$ versus $1/T$ for DA2.....	150
Figure 6.13. Arrhenius Fit of $\ln k$ versus $1/T$ for DA2.....	151
Figure 6.14.(a) DA1 and DA2 Fit of $\ln \eta^*$ versus Time for 325 °C	152
Figure 6.14.(b) DA1 and DA2 Fit of $\ln \eta^*$ versus Time for 330 °C	153
Figure 6.14.(c) DA1 and DA2 Fit of $\ln \eta^*$ versus Time for 340 °C	153
Figure 6.14.(d) DA1 and DA2 Fit of $\ln \eta^*$ versus Time for 350 °C	154
Figure 6.15. Arrhenius Plot of $\ln(\text{intersection time})$ versus $1/T$	155
Figure 6.16. Arrhenius Fit of $\ln(t_{gel})$ versus $1/T$	156

Chapter 7

Figure 7.1. Specimen Layout.....	163
----------------------------------	-----

Chapter 8

Figure 8.1.(a) Moisture Absorption by Wet TFS Specimens	172
Figure 8.1.(b) Linear Fit of Wet TFS Specimen Moisture Absorption.....	172
Figure 8.2.(a) Moisture Absorption by Wet/Dry TFS Specimens	173
Figure 8.2.(b) Linear Fit of Wet/Dry TFS Specimen Moisture Absorption.....	173
Figure 8.3.(a) Moisture Absorption by OHCS Specimens	174
Figure 8.3.(b) Linear Fit of OHCS Specimen Moisture Absorption.....	174
Figure 8.4.(a) Moisture Desorption by Wet/Dry TFS Specimens	175
Figure 8.4.(b) Linear Fit of Wet/Dry TFS Specimen Moisture Desorption.....	175
Figure 8.5.(a) Moisture Desorption by OHCS Specimens	176
Figure 8.5.(b) Linear Fit of OHCS Specimen Moisture Desorption.....	176
Figure 8.6. Moisture Equilibrium Content versus Relative Humidity.....	178
Figure 8.7. Moisture Induced Transverse Strain.....	180
Figure 8.8. Effect of Moisture Exposure on Transverse Flexural Strength	182
Figure 8.9.(a) Control TFS - Undamaged Exposed Surface.....	182
Figure 8.9.(b) Control TFS - Damaged Exposed Surface.....	182
Figure 8.10.(a) Wet TFS - Undamaged Exposed Surface.....	183
Figure 8.10.(b) Wet TFS - Damaged Exposed Surface: Crevices, Cracks, and Exposed Fibers.....	183
Figure 8.10.(c) Wet TFS - Fiber/Matrix Interface Cracks.....	183
Figure 8.11.(a) Wet/Dry TFS - Undamaged Exposed Surface	183

Figure 8.11.(b) Wet/Dry TFS - Damaged Exposed Surface: Crevices, Cracks, and Exposed Fibers	183
--	-----

Chapter 9

Figure 9.1. Description of Nelson's [9] AISS Specimen Selection	191
Figure 9.2. Softening Temperature Measured by TMA.....	204
Figure 9.3. Influence of Oxygen Partial Pressure on T_g after 5000 Hours.....	206
Figure 9.4. TFS Percent Retention Versus Time at 204 °C	208
Figure 9.5. [5000 hr / 40.4 kPa $p(O_2)$ / 204 °C] Aged Composite Surface	211
Figure 9.6. [5000 hr / 40.4 kPa $p(O_2)$ / 204 °C] Aged Composite TFS Specimen	211
Figure 9.7. Vickers Hardness Profile of Unaged Neat Resin	214
Figure 9.8. Vickers Hardness Profile of Neat Resin [5000 hr / 2.84 kPa $p(O_2)$ / 204 °C]	214
Figure 9.9. Vickers Hardness Profile of Neat Resin [5000 hr / 0.0 kPa $p(O_2)$ / 204 °C]	215
Figure 9.10. Vickers Hardness Profile of Neat Resin [720 hr / 2.84 kPa $p(O_2)$ / 177 °C // 5000 hr / 0.0 kPa $p(O_2)$ / 204 °C]	215
Figure 9.11. Vickers Hardness Profile of Neat Resin [5000 hr / 20.2 kPa $p(O_2)$ / 204 °C]	216
Figure 9.12. Vickers Hardness Profile of Neat Resin [5000 hr / 40.4 kPa $p(O_2)$ / 204 °C]	216

List of Tables

Chapter 2

Table 2.1. Apparent Interlaminar Shear Strength Test Information.....	23
Table 2.2. Flexural Test Information	24
Table 2.3. Fracture Toughness Panel Physical Properties	31
Table 2.4. Mode I SERR Values.....	34
Table 2.5. Apparent Crack Length Offset (ACLO) Values.....	35
Table 2.6. System Descriptions for Figure 2.17	36
Table 2.7. G_{IIC} Values	41
Table 2.8. System Comparison of G_{IIC}	42

Chapter 3

Table 3.1. Composite Physical Properties	54
Table 3.2. Moisture Sorption Property Comparisons	60
Table 3.3. Moisture Induced Strain - Variations of Increased Moisture Content.....	61
Table 3.4. 3kPETU Composite Moisture Expansion Coefficients (MEC).....	62
Table 3.5. Transverse Moisture Expansion Coefficients from Literature	62
Table 3.6. Mechanical Property Results.....	67

Chapter 4

Table 4.1. Determination of Rate Constants	81
Table 4.2. Curve Fitting Determination of Kinetic Parameters	88
Table 4.3. Calculated Values of Kinetic Parameters	91

Chapter 5

Table 5.1. Isothermal Cure Conditions and Isothermal Glass Transition Temperatures.....	106
Table 5.2. Ramp Rates Between 325 °C and Hold Temperatures for Composite Cures.....	112

Table 5.3. Ramp Rates Between 325 °C and Maximum Cure Temperatures for Neat Resin and Towpreg Resin DSC Cures	114
---	-----

Chapter 6

Table 6.1. Isothermal Complex Viscosities versus Time to Gel Points	139
Table 6.2. DA1 Values for Initial Viscosity and Rate Constant of Gelation	142
Table 6.3. DA2 Values for Initial Viscosity and Rate Constant of Gelation	147
Table 6.4. Time and Degree of Cure at DA1 to DA2 Transition.....	155

Chapter 8

Table 8.1. Comparison of D_z values for TFS, OHCS, Absorption, and Desorption	171
Table 8.2. Moisture Content versus Relative Humidity	179
Table 8.3. Coefficients a and b for Selected Composite Materials	179

Chapter 9

Table 9.1. Isothermal TGA Results of Epoxy Powders in Various Gases at 100 ml/min.....	187
Table 9.2. Pre-aging of 0.0 kPa p(O ₂) / 204 °C Specimens	198
Table 9.3. Percent Mass Losses for TOA Carbon Fiber-Reinforced Composites.....	203
Table 9.4. Open-Hole Compression Strength Results.....	207

Chapter 1 - Introduction

1.1 General Background

Fiber-reinforced polymeric composite (FRPC) materials have been heavily researched and advanced over the past forty years and offer the potential to meet the material demands of future products that will alter the way goods are manufactured, business is conducted, and people make use of their personal time. People, goods, and information are being transported around the world at an increasing rate. This acceleration is producing a demand for even faster movement as people, corporations, and governments search for a competitive edge. The demand for accelerated movement is accompanied by a requirement of efficiency. However, raising the rate of transport generally results in elevated operating temperatures. For example: 1) increasing the speed of the aerospace craft or the high-speed train results in an increase in friction-generated heat; and 2) increasing the circuit density of circuit boards results in more electrical resistance-generated heat. FRPCs allow for the construction of lighter, yet stronger, structures that may be tailored to meet the mechanical demands of service and operation, thus allowing for faster and more efficient transport of goods, people, and information. However, the relatively poor high-temperature properties of traditional polymer matrix materials (e.g., epoxies) generally limit the applications of FRPCs.

To take full advantage of the high-specific strength characteristics of FRPCs, processable polymers with high-temperature stability must be developed. Several polymer candidates have been synthesized and are currently in different stages of development and evaluation to determine their potential for high-performance FRPC applications. Included in this group of candidates are phenylethynyl-terminated polyimides, a type of crosslinkable thermoplastic. This research project focuses on the use of one of these crosslinkable thermoplastics, which is introduced below, as a matrix material for FRPCs.

1.2 PhenylEthynyl-Terminated Ultem™ Background

General Electric has developed a thermoplastic poly(etherimide) known as Ultem™-1000 that has a glass transition temperature, T_g , of about 215 °C [1]. This material is reported to have good melt-processability, high mechanical strength and ductility, good self-extinguishing characteristics, and outstanding electrical properties. However, Ultem™-1000 has relatively poor chemical and solvent resistance as it is only moderately resistant to salt solutions, dilute bases, gasoline, hydraulic fluid, methylethylketone, toluene, and possible de-icers, such as ethylene glycol [2,3].

Several groups [4 and references within] have reported that phenylethynyl-encapped imide oligomers can provide curable, solvent-resistant materials with good mechanical and adhesive properties. A phenylethynyl-terminated version of Ultem™ (PETU) has been synthesized by the research group of Dr. J.E. McGrath in the Chemistry Department at Virginia Polytechnic Institute and State University (VPI&SU) in conjunction with General Electric [1]. The phenylethynyl termination groups provide chain growth and crosslinking sites to improve the solvent resistance and increase the T_g of the Ultem™ material. This synthesis of an Ultem™-type, melt-processable poly(etherimide) with a 4-phenylethynylphthalic anhydride endcapping agent was successful in producing a melt-processable, high- T_g , sufficiently ductile network material with good thermal-oxidative stability and solvent resistance [1]. Of particular interest here is the *meta*-linked phenylethynylphthalic anhydride poly(etherimide) shown in Figure 1.1.

The first productions of PETU on a lab scale large enough to investigate composite manufacture were of oligomers having molecular weights of 2000 g/mol (2kPETU) and 3000 g/mol (3kPETU). Due to the superior neat resin mechanical properties of 3kPETU, the higher molecular weight version was chosen for initial composite study. Later, a 2500 g/mol (2.5kPETU) version was produced in a 50 gallon reactor by General Electric Research and Development. The oligomer molecular weight was reduced by 500 g/mol in hope of improving processability without significantly sacrificing mechanical properties. The PETU oligomers were synthesized in powder form.

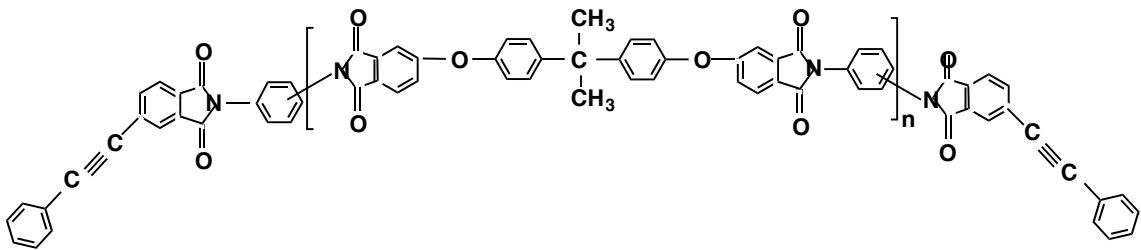


Figure 1.1. 4-phenylethynylphthalic anhydride endcapped bisphenol-A dianhydride/*meta*-phenylene diamine

Good fiber wet-out, or impregnation of the fiber tow, by the matrix resin is required to achieve uniform fiber/matrix distribution and good composite consolidation. Both of these qualities are necessary for the composite structure to have good mechanical integrity. Powder prepregging, which has been developed as a method for production of composite prepreg with high-melt viscosity thermoplastics, was utilized to produce towpreg (powder impregnated tow). Prepregs and towpregs are sheets and tapes, respectively, of fabric or

fiber impregnated with polymer that are later assembled to build composite structures. Various unsized carbon fiber tows manufactured by Toho Carbon Fibers, Inc., have been used in the towpreg production [5]. All of the composite material tested in this study was manufactured from towpreg produced via dry powder prepregging.

1.3 Powder Prepregging

Since all of the composite material tested in this study was manufactured via dry powder prepregging, it is important that the introduction include both a review of powder prepregging and a discussion of the operation of the dry powder prepregging system at VPI&SU.

The high-melt viscosity of thermoplastics and some high-performance thermosets (e.g., PEEK, PEKK, PPS, and PETU) inhibits the impregnation of fibrous structures by cost-effective methods such as resin transfer molding or resin film infusion, where the polymer must enter and flow throughout a whole fibrous structure to wet-out all the fibers. For large structures, the resin may be required to flow on the order of decimeters. The application of the pressures necessary to infuse high-performance resins at their processing temperatures into reinforcing structures generally results in high shear stresses at the resin/fiber interfaces that are damaging to the fiber. Attempting to reach an impregnable viscosity by further increases in resin temperature can result in resin degradation. Some resins can be dissolved in solvents to lower the viscosity to an impregnable level. However, dissolution is not possible with some of the high-performance resins that have been developed to have good solvent resistance. Furthermore, the use of solvents adds material and handling costs to the manufacturing process.

Powder prepregging avoids these flow problems by significantly reducing the distance that the matrix resin is required to flow to achieve complete fiber wet-out. Resin droplets are distributed throughout the fiber tow; fiber wet-out is achieved by each droplet flowing far enough to fuse with its nearest neighbors. Therefore, flow distances are reduced to the order of microns up to millimeters. These minimal flow distances avoid the problems associated with forcing high-melt viscosity resin to travel through all or most of a reinforcing fiber structure.

1.3.1 Powder Prepregging: Literature Review

Powder prepregging methods may be separated into two main categories: wet and dry. Within these categories, research groups have developed many different variations of the

powder prepregging technique. Wet powder prepregging techniques mostly depend on aqueous suspensions of the polymer powder through which the spread fiber tow is passed [6,7]. Aqueous foam is also being studied as a method of impregnating spread fiber tow with polymer powder [8].

A dry powder prepregging process of simply passing spread tow through a bed of a powdered thermoplastic was patented in 1973 [9]. Spread tow may also be dry impregnated by allowing the powder to rain down on the tow as it passes through a curtain of powder [10]; this technique was used in a portion of the present research and the specifics are described later. A patent has also been issued for a process in which spread tow is impregnated as it passes through a fluidized bed of polymer powder [11,12]. A variation on the fluidized bed technique has been patented in which the spread tow is electrically grounded and the powder particles in the fluidized bed are charged by the fluidizing air [13]. A similar system has been developed at VPI&SU and has successfully been utilized in the production of towpreg and subsequent composite materials (Figure 1.2) [14,15]. The fluidized particles impinge on the spread tow and embed themselves within the tow. This mechanical entrapment is the dominant contributor to the coating process; the electrostatic attractions provide minor assistance in the coating process and help to temporarily hold particles in the tow. The same concept is also applied by using an electrostatic spray gun, which sprays, or aspirates, particles onto grounded, spread tow [16,17]. Another patented technique relies on acoustic energy to fluidize polymer powder for deposition onto acoustically spread fiber tow [18]. In all of these techniques, the impregnated tow is subsequently heated in some manner to affix the powder to the tow.

1.3.2 Dry Powder Prepregging System Description

Discussion of the operation and purpose of each stage of the electrostatic, fluidized bed (EFB), dry powder prepregging system implemented at VPI&SU and modifications to the system begin here with the tow delivery system (Figure 1.2) [14,15]. The first step in a continuous prepregging operation involves unspooling the fiber tow and delivering it to the rest of the operation. Carbon fiber tows of 12,000 (12k) and 24,000 (24k) filaments were used in this research. The fiber spool is mounted on a large air bearing that provides necessary smooth delivery of the fiber to the rest of the system. An inconsistent tow speed and tension produces dramatic difficulties for subsequent prepregging operations, particularly tow spreading and polymer deposition.

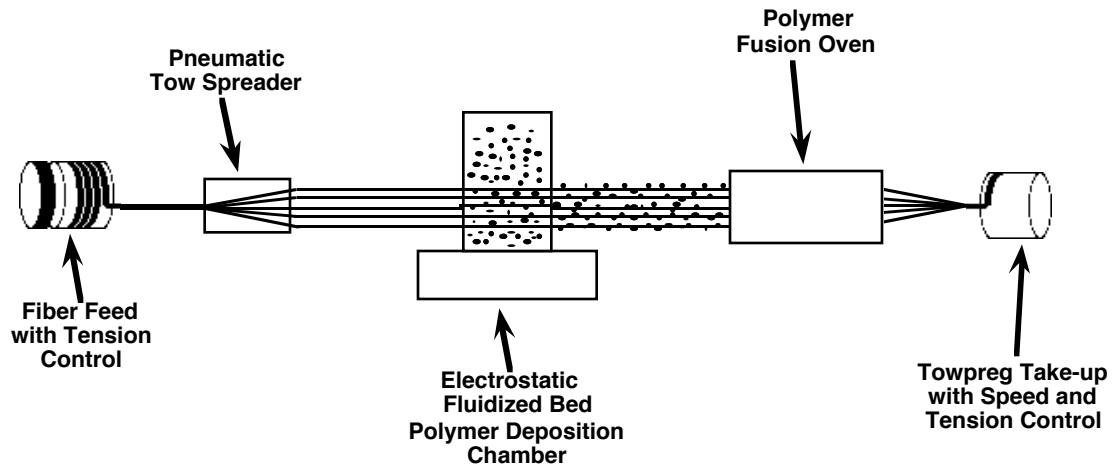


Figure 1.2. Electrostatic, Fluidized Bed, Dry Powder Prepregging System [14,15]

1.3.2.1 Tow Spreader

The tow spreader is the one piece of equipment which has the greatest impact on the quality of the resultant towpreg. Poor tow spread leads to inadequate distribution of the polymer throughout the tow, which often leads to poorly consolidated composites. Conversely, a high level of tow spreading exposes more of the fiber tow to the fluidized polymer cloud, producing a very even coating. Traditionally, fiber spreading has been achieved with a mechanical approach comprised of a series of rollers which gradually spread the tow. This approach results in a high degree of fiber damage, lowering the performance of the composite product.

In order to minimize fiber damage, a pneumatic system was constructed based on the Celanese developed air banding jet [19]. A schematic of the tow spreader is shown in Figure 1.3.(a). Compressed, filtered air introduced into the box as illustrated, escapes through the top of the box from 0.0254 cm wide slits cut in a double chevron pattern. This streaming air impacts the top plate and rushes sideways, carrying all or part of the tow with it. Key variables associated with degree of tow spread are the air pressure, tow tension, and the top plate's height and orientation in relation to the box. Micrometer adjusters located on each corner of the box allow precise control over both the top plate's height and orientation with respect to the box. A grounding wire is attached to the plate to electrically ground the fiber before it enters the EFB.

1.3.2.2 Electrostatic Fluidized Bed

A laboratory sized (152.4 mm by 152.4 mm) EFB unit, model C-30, produced by Electrostatic Technology Incorporated having controls for electrostatic voltage and

fluidization velocity accomplishes the powder deposition stage. A schematic of the system is given in Figure 1.3.(b). The EFB forces filtered, dry, compressed air over two electrostatic brushes to which the desired charge has been applied. The brushes impart a negative electrostatic charge to the compressed air, which then passes up through the chamber and a porous bed containing the polymer powder. The charged air fluidizes the polymer and transmits the negative charge to the individual particles producing a negatively charged cloud of polymer particles through which the grounded, spread tow travels. Deposition takes place as the result of random collisions as well as the electrostatic attraction between the charged particles and the grounded tow. In addition to providing a driving force for deposition, the electrostatic charging helps produce an even coating of the tow; charged particles are less attracted to powder coated portions of tow than bare sections.

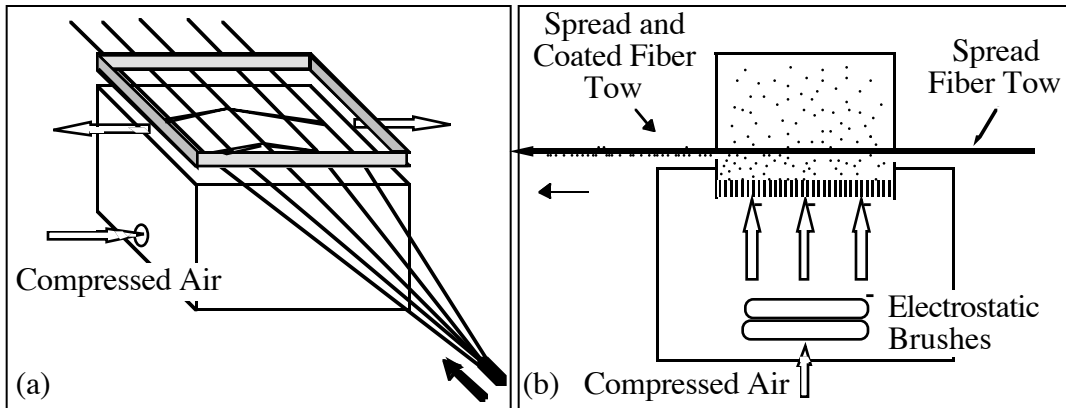


Figure 1.3. Dry Powder Prepregging System Components: (a) Pneumatic Tow Spreader, (b) Electrostatic Fluidized Bed [14]

Polymer is constantly being removed from the chamber either due to deposition on the fiber tow or suction into the vacuum unit connected to the chamber. The vacuum creates a "tight" polymer cloud in the chamber, eliminating polymer contamination of the working environment and polymer loss through the tow entrance and exit slots. To maintain constant processing conditions, the polymer level in the deposition chamber must not vary. Replenishing polymer to the chamber is accomplished through a port at the back of the chamber through which an Accurate Model 320 Screw Feeder enters. The screw feeder is set to deliver the appropriate amount of polymer per unit time to maintain a constant volume of polymer in the chamber throughout prepregging runs.

A key advantage of the EFB powder prepregging system is that the polymer particles come into contact with both sides of the spread tow. Contact from both sides produces a uniform distribution of polymer in the resultant towpreg and minimizes the need for large scale polymer flow during consolidation. Unfortunately, for proper operation the fluidized bed requires a minimum charge of approximately 500 grams of polymer. For commercially available polymers, a 500 gram supply is an insignificant drawback. However, for developmental polymers, the production of 500 grams, if feasible, represents a considerable investment of time and capital.

1.3.2.3 Minimal Dry Powder Prepregging System

Many investigators in the National Science Foundation Science and Technology Center for High Performance Polymeric Adhesives and Composites at VPI&SU are focusing on the synthesis and development of new polymer systems and the modification of existing systems for use in composite materials. With novel polymers in mind, a minimal dry powder prepregging system (MDPPS) was developed to produce prepreg from small quantities of polymer powder.

The MDPPS (Figure 1.4), which substitutes for the EFB, is composed of a thin wall, 86 mm diameter, metal cylinder attached to a Thermolyne Maxi-Mix III type 65800 orbitally-vibrated shaker table. The cylinder contains a stadium-shaped funnel at the bottom to direct the polymer to a nylon mesh screen covered rectangular slot (76 mm x 9.5 mm) aligned along the center line of the cylinder. The squares of the mesh are aligned parallel with the funnel slot. A typical mesh measures 1.0 mm along each edge and is bordered by 0.50 mm diameter nylon thread; mesh size is changed to adapt to different polymer powders.

Even though the polymer particles are much smaller than the mesh openings, clumping and attractive forces keep them from flowing freely through the openings. The agitation provided by the orbital table is required to induce flow. To further reduce the possibility of clogging, 4.5 mm diameter, steel spheres (i.e., Daisy® BBs) may be placed in the funnel to jar the nylon mesh and break up any newly formed agglomerates. Clogging results in a gradually diminishing rate of powder deposition, thus producing towpreg with a gradually increasing fiber volume fraction.

Coating is accomplished as the shaker table provides controlled agitation to the funnel depositing a curtain of powder on tow passing underneath. The length of the funnel slot runs normal to the direction of tow movement, thus providing a powder curtain with a

width at least as wide as the tow spread. Rather than holding the polymer powder electrostatically, the tow carries the polymer out of the powder deposition area as would a conveyor belt.

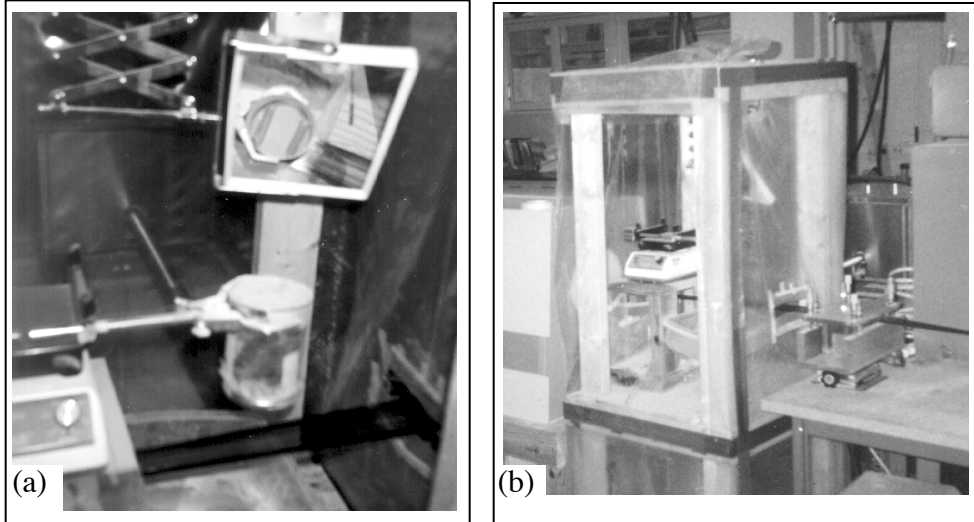


Figure 1.4. MDPPS: (a) Close-up (b) Location in Powder Coating Line

The differences in powder capture by the two deposition methods result in differences in the preferred tow spread for each method. The EFB method prefers extensive spread exposing as many individual filaments as possible. If the same spread were used with the MDPPS, the majority of the powder would fall through the tow and an insufficient amount would be captured. Therefore, the spread used with the MDPPS is dictated by the need to minimize significant gaps between individual fibers through which powder can fall, but at the same time maintaining a wide enough spread to catch sufficient polymer for the desired volume fraction.

1.3.2.4 *Polymer Binding*

Exiting the powder deposition region is a spread carbon fiber tow with polymer powder either embedded in or simply riding on the tow. Any perturbation of the system, such as air movement, sudden tension changes, or physical contact, will cause polymer to fall from the tow. Therefore, the coated tow is immediately run through a 0.914 m Lindberg Tube Furnace Model 55666. This furnace has three heating zones allowing for control of the temperature profile and is long enough to effectively melt and bind the polymer on the tow. Hence, the towpreg can be handled and processed with minimal loss of polymer.

1.3.2.5 Towpreg Take-Up

The final step of the prepregging process involves spooling of the towpreg for future use. A Deitz-Schell model DS 28 WS textile take-up winder has been modified so that all surfaces in contact with the towpreg spin or roll, reducing friction and thus damage to the delicate towpreg. The unit controls tow speed from five to thirty meters per minute and uses a dancer arm to control winding tension. The result of a prepregging run is a spool of towpreg helically wound in a manner similar to the original spool of bare fiber.

1.4 Project Summary

The initial objective of this research project was to determine the feasibility of manufacturing carbon fiber reinforced (CFR) PETU matrix composites. Following successful composite manufacture with 3kPETU, a survey of composite mechanical properties was undertaken to compare CFR 3kPETU composites with other high-performance composite materials. The success of these initial studies spawned the large scale production of 2.5kPETU.

This polymer is a candidate for high-performance applications, meaning the CFR 2.5kPETU composites will be exposed to harsh service conditions including environments that may be: at high-temperature, oxidative, and rapidly changing in moisture content. These three environmental factors may work individually or together to degrade the composite's physical and mechanical properties. Therefore, it is important to consider that thermal, oxidative, and hydrolytic degradation of reactive polymers is often accelerated by lack of complete cure. To minimize environmental damage, a cure schedule that minimizes unreacted oligomer in a composite part is desired. Thermal and rheological studies of 2.5kPETU were completed to produce a cure schedule that approaches full cure, while achieving fiber wet-out, in a reasonable manufacturing time.

Moisture is a critical environmental factor that can be damaging to composite properties. Composite components may be constantly absorbing or desorbing moisture due to fluctuations in service temperature and relative humidity. The absorption of moisture can reduce glass transition temperatures and mechanical properties by matrix plasticization, swelling, cracking, and fiber/matrix interface damage [20-22].

One objective of this study was to investigate the effects of moisture sorption on the mechanical properties of CFR PETU composites. In addition to mechanical properties, moisture absorption and desorption rates were measured to verify compliance by this

material with the Fickian diffusion model per the ASTM Test Method for Moisture Absorption Properties and Equilibrium Conditioning of Polymer Matrix Composite Materials (D 5229-92). Moisture absorption took place in an environment of 90 °C and 85% relative humidity; the relative humidity was decreased to approximately 2% and 10% for moisture desorption. These measurements also allowed for the determination of the through-the-thickness moisture diffusion coefficient and the maximum moisture equilibrium content. Following both moisture absorption and desorption, composite specimens were tested for retention of transverse flexural strength (TFS), apparent interlaminar shear strength (AISS), and open-hole compression strength (OHCS).

Studies of several polymer matrix composites aged at elevated temperatures below their glass transition temperatures indicate oxidation, not thermal effects, is the more critical degradation mechanism in the polymer matrixes [23-31]. Therefore, CFR 2.5kPETU composite panels were aged at 204 °C in environments of four different oxygen partial pressures: 13.8 kPa air, 100% nitrogen gas, 80 mol% nitrogen / 20 mol% oxygen gas mixture, and 60 mol% nitrogen / 40 mol% oxygen gas mixture. An air pressure of 13.8 kPa is representative of cruise conditions for high-performance aircraft [32]. The composite panels were removed from the aging environments following exposure times of 720, 1750, 3500, and 5000 hours. Upon removal from the aging environments, specimens were cut from the panels for testing of mechanical property retention. The combination of varying oxygen partial pressures and exposure times allowed for the prediction of TFS retention as a function of time and oxygen partial pressure. Other mechanical properties tested were AISS and OHCS.

In addition to measurements of mechanical property retention, microindentation measurements were done across the cross sections of neat resin specimens to profile changes in Vickers Hardness with increasing depth from the molded surfaces of the neat resin specimens. These measurements provided insight into other observations, including TFS retention, of changes in aged composite and neat resin specimens.

This study determined the processing conditions to manufacture well-consolidated CFR 2.5kPETU composite panels. The effects of oxidative environments of varying degrees of severity, moisture absorption, and moisture desorption on the physical and mechanical properties are investigated. The diffusion parameters for water vapor in 2.5kPETU matrix FRPCs were also determined from these environmental exposure experiments. These results allow for the assessment of using CFR 2.5kPETU composites in different high-

performance applications. In addition, this information may be used in designing future aging studies.

Prior to the final summary chapter, eight chapters detail different portions of this study. Chapter 2 covers the first two stages of the feasibility study on CFR 3kPETU. The successful manufacture of CFR 3kPETU composites and measurement of their basic mechanical properties are discussed. Evaluation of the effects of moisture absorption and desorption on the mechanical properties of CFR 3kPETU composites completes the feasibility study in Chapter 3. Chapter 4 commences the study of 2.5kPETU by developing a cure kinetics model for neat 2.5kPETU. Cure is studied further in Chapter 5 where the influence of cure time and temperature on the resultant glass transition temperature is evaluated for both neat resin and CFR 2.5kPETU. An isothermal chemorheological model for 2.5kPETU is developed in Chapter 6. Chapter 7 briefly details the manufacture of neat 2.5kPETU plaques and CFR 2.5kPETU composite panels for use in the moisture sorption and thermal oxidation studies. The moisture sorption study of neat resin and composite material is discussed in Chapter 8 followed by a discussion of the thermal-oxidative aging effects on neat resin and composite material in Chapter 9.

1.5 References

1. G.W. Meyer, B. Tan, and J.E. McGrath, "Solvent-resistant polyetherimide network systems via phenylethynylphthalic anhydride endcapping," *High Performance Polymers*, **6**, 423-435 (1994).
2. J.E. McGrath, B. Tan, V. Vasudevan, G.W. Meyer, A.C. Loos, and T. Bullions, "Synthesis and Characterization of High Performance Thermosetting Polyimides for Structural Adhesives and Composite Matrix Systems," *SAMPE International Technical Conference*, **28**, 29-38 (1996).
3. R.A. McCarthy, "Chemically Resistant Polymers," in Encyclopedia of Polymer Science and Engineering, 2nd Edn., Vol. 3, J.I. Kroschwitz, ed., Wiley Interscience, New York, 1985, pp. 421-430.
4. B. Tan, V. Vasudevan, Y.J. Lee, S. Gardner, R.M. Davis, T. Bullions, A.C. Loos, H. Parvatareddy, D.A. Dillard, J.E. McGrath, and J. Cella, "Design and Characterization of Thermosetting Polyimide Structural Adhesive and Composite Matrix Systems," *Journal of Polymer Science, Part A: Polymer Chemistry*, **35**, 2943-2954 (1997).
5. Toho Carbon Fibers, Inc., Palo Alto, CA, product brochure (1997).
6. A. Gonzalez-Ibarra, R.M. Davis, C.L. Heisey, J.P. Wightman, and J.J. Lesko, "The Effect of Polyamic Acid Binder Concentration on the Processability and Properties of LaRC TPI Composites Made by Suspension Prepregging," *Journal of Thermoplastic Composite Materials*, **10**, 85-105 (1997).

7. L. Tang, L. Li, X. Yi, and Z. Pan, "Aqueous Powder Slurry Manufacture of Continuous Fiber Reinforced Polyethylene Composite," *Polymer Composites*, **18**, (2), 223-231 (1997).
8. J.A. Dugger and D.E. Hirt, "PMR-15 / Carbon Fiber Composites Produced From Powder Coated Towpreg," *Polymer Composites*, **17**, (3), 492-496 (1996).
9. U.S. Patent 3,742,106 (1973) R.V. Price, "Production of Impregnated Rovings."
10. T.H. Hou, N.J. Johnston, E.S. Weiser, and J.M. Marchello, "IM7/LaRC™ -IAX Polyimide Composites," *Journal of Advanced Materials*, **27**, (4), 37-46 (1996).
11. J.W. Klett and D.D. Edie, "Flexible Towpreg for the Fabrication of High Thermal Conductivity Carbon / Carbon Composites," *Carbon*, **33**, (10), 1485-1503 (1995).
12. U.S. Patent 5,057,338 (1991) R.M. Baucom, J.J. Snoha, and J.M. Marchello, "Process For Application of Powder Particles to Filamentary Materials."
13. U.S. Patent 5,094,883 (1992) J.D. Muzzy and B. Varughese, "Flexible Multiply Towpreg and Method of Production Therefor."
14. R.A. Bucher and A.C. Loos, "High Performance Thermoplastic Matrix Composite Processing: Dry Powder Prepregging, Plasma Treatment, Consolidation / Crystallization Analysis," Report No. CCMS-95-02 and VPI-E-94-10, Center For Composite Materials and Structures (0257), Virginia Polytechnic Institute and State University, Blacksburg, VA 24061-0257 (1994).
15. R.A. Bucher and A.C. Loos, "Parametric Statistical Analysis of Electrostatic Powder Prepregging," *Journal of Advanced Materials*, **25**, (4), 44-50 (1994).
16. J.L. Throne and M.S. Sohn, "Electrostatic Dry Powder Prepregging of Carbon Fiber," *Proceedings of the 35th International SAMPE Symposium and Exhibition*, 2086-2101 (1990).
17. K. Ramani, D.E. Woolward, and M.S. Duvall, "An Electrostatic Spray Process for Manufacturing Thermoplastic Composites," *Polymer Composites*, **16**, (6), 459-469 (1995).
18. U.S. Patent 5,102,690 (1992) S. Iyer, L.T. Drzal, and K. Jayaraman, "Method Coating Fibers with Particles by Fluidization in a Gas."
19. L. Ying, NASA Contract #NASI-15749, Task Assignment No. 6, Progress Report (1982).
20. M.R. Van Landingham, R.F. Edulje, and J.W. Gillespie, Jr, "The Effects of Moisture on the Material Properties and Behavior of Thermoplastic Polyimide Composites," in High Temperature and Environmental Effects on Polymeric Composites, Vol. 2, ASTM STP 1302, T.S. Gates and A.H. Zureick, eds., American Society for Testing and Materials, Philadelphia, 1997, pp. 50-63.
21. D. Cornelia, "Hygrothermal Performance of Polyimides," *Proceedings of the 39th International SAMPE Symposium and Exhibition*, 917-929 (1994).

22. B.A. Pratt and W.L. Bradley, "Effect of Moisture on the Interfacial Shear Strength: A Study Using the Single Fiber Fragmentation Test," in High Temperature and Environmental Effects on Polymeric Composites, Vol. 2, ASTM STP 1302, T.S. Gates and A.H. Zureick, eds., American Society for Testing and Materials, Philadelphia, 1997, pp. 64-72.
23. J.R. Kerr and J.F. Haskins, "Effects of 50,000 h of Thermal Aging on Graphite/Epoxy and Graphite/Polyimide Composites," *AIAA Journal*, **22**, (1), 96-102 (1984).
24. T.K. Tsotsis, "Thermo-Oxidative Aging of Composite Materials," *Journal of Composite Materials*, **29**, (3), 410-422 (1995).
25. H. Parvatareddy, J.Z. Wang, D.A. Dillard, T.C. Ward, and M.E. Rogalski, "Environmental Aging of High-Performance Polymeric Composites: Effects on Durability," *Composites Science and Technology*, **53**, 99-409 (1995).
26. K.J. Bowles, D. Jayne, T.A. Leonhardt, "Isothermal Aging Effects on PMR-15 Resin," *SAMPE Quarterly*, **24**, (2), 2-9 (1993).
27. K.J. Bowles, "Transverse Flexural Tests as a Tool for Assessing Damage to PMR-15 Composites from Isothermal Aging in Air at Elevated Temperatures," *SAMPE Quarterly*, **24**, (2), 49-53 (1993).
28. K.J. Bowles and A. Meyers, "Specimen Geometry Effects on Graphite/PMR-15 Composites During Thermo-Oxidative Aging," *Proceedings of the 31st International SAMPE Symposium and Exhibition*, 1285-1299 (1986).
29. J.B. Nelson, "Thermal Aging of Graphite/Polyimide Composites," in Long-Term Behavior of Composites, ASTM STP 813, T.K. O'Brien, ed., American Society for Testing and Materials, Philadelphia, 1983, pp. 206-221.
30. S. Ciutacu, P. Budrugaec, and I. Niculae, "Accelerated Thermal Aging of Glass-Reinforced Epoxy Resin Under Oxygen Pressure," *Polymer Degradation and Stability*, **31**, (3), 365-372 (1991).
31. B. Crossland, G.J. Knight, and W.W. Wright, "Thermal Degradation of Some Polyimides," *British Polymer Journal*, **19**, 291-301 (1987).
32. M.D. Brunner and T. Cebeci, "Development of the California State University, Long Beach Composite Durability Laboratory," *Proceedings of the 39th International SAMPE Symposium and Exhibition*, 1554-1563 (1994).

Chapter 2 - 3kPETU Preliminary Research

2.1 Introduction

This chapter discusses the preliminary research done with 3kPETU to determine the feasibility of manufacturing CFR PETU matrix composites and to survey the mechanical properties of this composite material. Knowledge of the rheological behavior of the polymer was required to determine if the polymer's melt viscosity was low enough to allow for the infiltration of reinforcing structures. If the polymer's viscosity can be lowered to a workable level, this information allows for the selection of appropriate composite manufacturing techniques. Furthermore, knowledge of the polymer's rheology assists in the development of a consolidation schedule. Therefore, the study of 3kPETU commenced with rheological analysis. Additional thermal analysis included differential scanning calorimetry (DSC) to provide more information for the development of a cure and consolidation schedule. Upon completion of the preliminary thermal analysis study, dry powder prepregging followed by compression molding was selected for composite manufacture. Composite panels were consolidated for measurement of several mechanical properties: apparent interlaminar shear strength (AISS), longitudinal and transverse flexural properties, open-hole compression strength, (OHCS), and Mode I and Mode II fracture toughness. These tests were selected for their sensitivity to matrix and fiber/matrix interface properties. The importance of these tests will be described below, followed by further detail on each stage of the 3kPETU preliminary study. Additional information regarding the preliminary 3kPETU research may be found in references 1 and 2.

2.2 Importance of Mechanical Property Tests

2.2.1 Apparent Interlaminar Shear Strength

The comparative testing of the interply strength of the composite materials followed the ASTM Standard Test Method for Apparent Interlaminar Shear Strength of Parallel Fiber Composites by Short-Beam Method (D 2344-84). Poor bulk matrix or interface properties will result in low AISS. When the specimens produce the desired interlaminar shear failure, this test is a quick, simple technique for comparing matrix candidates and different fiber treatments.

2.2.2 Flexural Properties

Fiber properties dominate longitudinal flexural (LF) properties, however, the inclusion of voids and poor interfaces will hinder the matrix's ability to transfer load between fibers. Thus, poor consolidation may be detected by reduced LF properties. Longitudinal flexural

strength and modulus are mainly used for quality control purposes. Direct comparisons with other matrix materials in the literature are often difficult due to differing fiber volume fractions and use of various reinforcing fibers.

In contrast to the LF test, transverse flexural (TF) properties are a better indicator of the matrix and fiber/matrix interface properties. The TF test directly loads the matrix and interface in tension, shear, and compression in different locations of the composite specimen. However, failure will consistently occur in the tensile mode with no mixed mode failures due to the geometry of the test specimen and material properties. Furthermore, a poor interfacial bond between fiber and matrix will result in poor TF strength since this interface will likely fail well before the bulk matrix [3]. The TF test is good for analyzing the consolidation quality achieved with a new matrix material due to the test's sensitivity to: voids within the matrix, sites of poor interfacial bonding, or the lack of complete fiber wet out. These flaws act as stress concentrations and significantly reduce the measured TF strength.

Perhaps as important as the values measured during flexural tests is the information garnered from inspection of the fracture surfaces. Fracture surface analysis can show the dominant mode(s) of failure. For instance, TF failure will occur either in the bulk matrix (cohesive) or at the fiber/matrix interface. Observation of bare fiber and smooth grooves in the matrix at the fracture surface would be a result of interfacial failure; thus, the composite's TF strength would be limited by the interface. Cohesive failure would be indicated by the absence of bare fiber at the fracture surface. Cohesive failure suggests there is either a good fiber/matrix interface or the matrix is weak; the matrix may be weak due to included voids, which may be visible as pits in the fracture surface. Of course, both modes of failure can occur within the same composite. In addition, the ductility, or toughness, of the matrix may be qualitatively analyzed by the amount of plastic deformation visible in the matrix.

2.2.3 Open-Hole Compression Strength [4-8]

Despite the longitudinal testing of unidirectional OHCS specimens, compressive strength is a good measure of consolidation quality, matrix properties, and interface strength. Compression failure may occur in several modes ranging from buckling of the whole composite specimen to actual material compression at the microstructural level depending on material properties and loading scheme.

Due to Poisson's ratio differences between the matrix and fiber, longitudinal compressive loading produces transverse tensile stresses within the matrix. These transverse tensile stresses can result in longitudinal cracks developing parallel to the fibers within a weak matrix. In addition, a weak interface can also fail under these transverse tensile stresses. Voids within the matrix or at the interface will act as stress concentrations and increase the chance of longitudinal cracking. Upon further loading, these cracks will grow and result in transverse rupture of the composite. The longitudinal cracks also allow more freedom for fiber buckling, thus failure can also occur by buckling and bending fracture of fibers.

In many cases, the matrix and interface are strong enough to withstand the Poisson's ratio induced transverse tensile stresses. Thus, other failure modes become active. During longitudinal compressive loading, the fibers' desire to buckle is resisted by the surrounding matrix; either the matrix must deform and/or the interface fail to allow buckling. Failure in strong-fiber (glass, carbon, graphite) reinforced composites initiates by microbuckling of fibers that have the least lateral support due to free boundaries, voids, stress concentrations, or locally weak matrix. Microbuckling may progress into many different failure modes depending on the matrix and interface properties.

The matrix and interface may be strong enough to withstand the Poisson's ratio induced transverse tensile stresses, but as fiber microbuckling begins, shear stresses are created at the interface. The interfaces may begin to fail in shear and lead to ultimate composite failure.

In the case of a strong matrix and good fiber/matrix adhesion, the modulus of the matrix controls the fibers' ability to buckle. A low modulus matrix will allow the microbuckled fibers to buckle further and ultimately the fibers will fracture due to bending stresses. A more rigid matrix will inhibit further microbuckling and likely lead to fiber kinking and what is known as shear crippling failure (Figure 2.1). Microbuckled fibers carry shear stresses from the matrix along with the overall compressive load. These stresses combine to cause the fibers to rotate and break in two places resulting in the kink band, or shear crippling zone. Following formation of the shear crippling zone, the matrix within the kink band deforms plastically in shear under the applied compressive load. Final compression failure occurs as the matrix can not carry the compressive load by itself. High modulus matrix materials can result in pure compression failure of the reinforcing fibers, which are sheared at an angle of 45° to the load; no fiber microbuckling occurs.

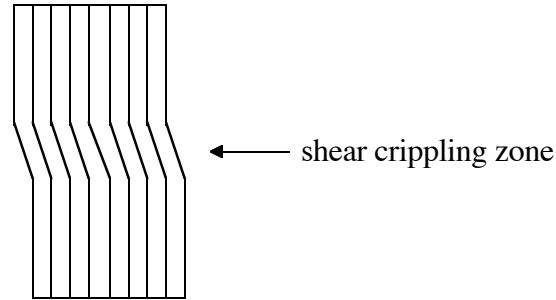


Figure 2.1. Kink Band [6]

2.2.4 Fracture Toughness

One of the major deficiencies of high performance laminated composite structures is their susceptibility to delamination [9]. The term delamination is often chosen to describe the propagation of an interlaminar crack, which can undermine the flexural stiffness of a composite laminate. A composite's ability to resist delamination is known as its toughness. A critical force or combination of forces, known as the critical crack-extension force, G_C , is needed to initiate crack growth. This value is also known as the fracture toughness of a material and has been given the name fracture energy since it gives the necessary energy for crack growth [10,11]. From here on, the term strain-energy release rate (SERR), which describes "the rate of transfer of energy from the elastic stress field of the crack structure to the inelastic process of crack extension" [10], and the symbol, G , will be used when discussing crack propagation. With the simple addition of a subscript, G may be used to describe the initial critical SERR to initiate crack growth, G_{init} ; the maximum SERR during propagation, G_{max} ; the SERR when crack growth halts, G_{arrest} ; and the critical SERR to re-initiate crack growth, G_C .

The response of a laminated composite to crack growth in any mode is essential knowledge during the product development processes of material selection and structural design [9]. Double cantilever beam (DCB) and end-notch flexure (ENF) tests were performed to determine the Mode I (G_I) and Mode II (G_{II}), respectively, crack opening SERRs of CFR 3kPETU composites.

A composite's fracture toughness is heavily influenced by its matrix and fiber/matrix interface properties. Interlaminar cracks can cause delamination by interfacial failure, cohesive failure, or a combination of both. A poor interface in a polymer matrix composite will result in low fracture toughness due to the ease with which an interlaminar crack could propagate along the interface. The fracture toughness of composites that have strong

interfaces and fail cohesively will mostly be dictated by the toughness of the matrix. Voids and other defects within the matrix and at interfaces can cause interlaminar cracks to jump between cohesive and interfacial pathways. As with the flexural tests, fracture surface inspection reveals significant information regarding composite properties. The interface strength can be judged qualitatively by the amount of bare fiber present in the fracture surface. Furthermore, the toughness of the matrix can be assessed by the amount of deformation seen along the crack's pathway through the matrix.

2.3 Thermal Analysis

Development of a process schedule for a reactive polymer requires information regarding the time and temperature dependence of degree of cure and viscosity. For this preliminary study, full resin characterization was not completed; rather, enough information was gathered to select a processing schedule that would produce well-consolidated and near fully, if not fully, cured composites.

2.3.1 Differential Scanning Calorimetry

The synthesizers of 3kPETU recommended curing for one hour at 350 °C [12]. Therefore, little DSC analysis was done. A few 10 °C/min temperature ramps were run to determine the cure onset and exotherm peak temperatures. This thermal analysis shows 3kPETU to be an amorphous system with an exothermic cure peak that onsets at about 350 °C to 365 °C and peaks near 400 °C (Figure 2.2).

2.3.2 Rheology

2.3.2.1 Experimental

The rheological behavior of 3kPETU was measured on a RMS-800 using parallel plate geometry. Discs were pressed from 3kPETU powder and trimmed to fit the 40 mm diameter of the parallel plates. Once loaded and heated to the initial temperature of 240 °C, the plates were closed to a gap of 1 mm and the excess material scraped from the sides of the plates. The storage modulus, loss modulus, and complex viscosity were measured during a 3.1 °C/min ramp from 240 °C to 394 °C in a nitrogen environment. The properties were measured in the dynamic mode with an oscillation frequency of 1 rad/s. The initial strain of 2.5% was maintained until the temperature reached 271 °C. At this temperature, the strain was gradually adjusted upward by 25% to maintain the torque above the transducer's minimum (e.g., a 25% increase in a strain of 2.5% resulted in a strain of 3.12%). The maximum test strain was 29%, which was held from 317 °C to 384 °C,

before the strain was adjusted downward. The linear viscoelastic limit for these conditions lay between 30 to 40% strain.

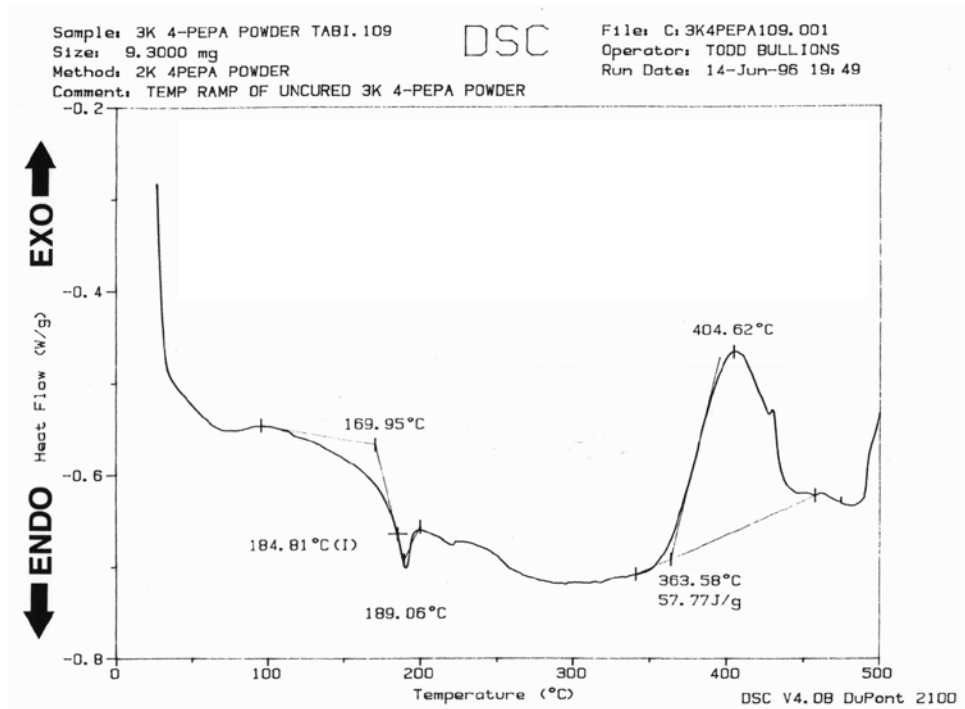


Figure 2.2. 10 °C/min Ramp of Virgin 3kPETU Powder in N₂ Environment

2.3.2.2 Results and Discussion

Cure onset of 3kPETU was again seen to occur in the 350 °C to 365 °C range evident by a significant increase in complex viscosity beginning around 350 °C (Figure 2.3). The viscosity remains below 10 Pa•s from 300 °C to 360 °C with the minimum viscosity, 5.5 Pa•s, occurring near 330 °C. With a viscosity of 6 Pa•s to 10 Pa•s, successfully manufacturing thick composite parts via resin film infusion, resin transfer molding, or similar cost effective fabrication methods is doubtful. In addition, the high temperatures required to reach 3kPETU's low viscosity range would require significant investment in high temperature tooling and equipment. Therefore, powder prepregging was selected for towpreg production.

2.4 Composite Manufacture and Physical Properties

2.4.1 Towpreg Production

The dry powder prepregging system implemented at VPI&SU is described in the Introduction Chapter. Due its developmental status, the supply and powder size

distribution of 3kPETU were not adequate to utilize the electrostatic fluidized bed. Therefore, the minimal dry powder prepregging system was used to coat 3kPETU powder onto unsized carbon fiber from Toho Carbon Fibers, Inc. [13]. Towpreg was manufactured using both a standard modulus (G30-500), 12k tow of 7 μm diameter filaments and an intermediate modulus (G40-800) 24k tow of 5 μm diameter filaments. All of the mechanical properties discussed in this chapter, except OHCS, were measured on composites manufactured using the G30-500 tow. The OHCS specimens were manufactured using the G40-800 tow. The towpreg production rate varied from 5 m/min to 10 m/min; tow speeds were varied to maintain the proper polymer mass fraction (0.33 to 0.38) on the tow. The powder was affixed to the tow by the 420 °C tube furnace.

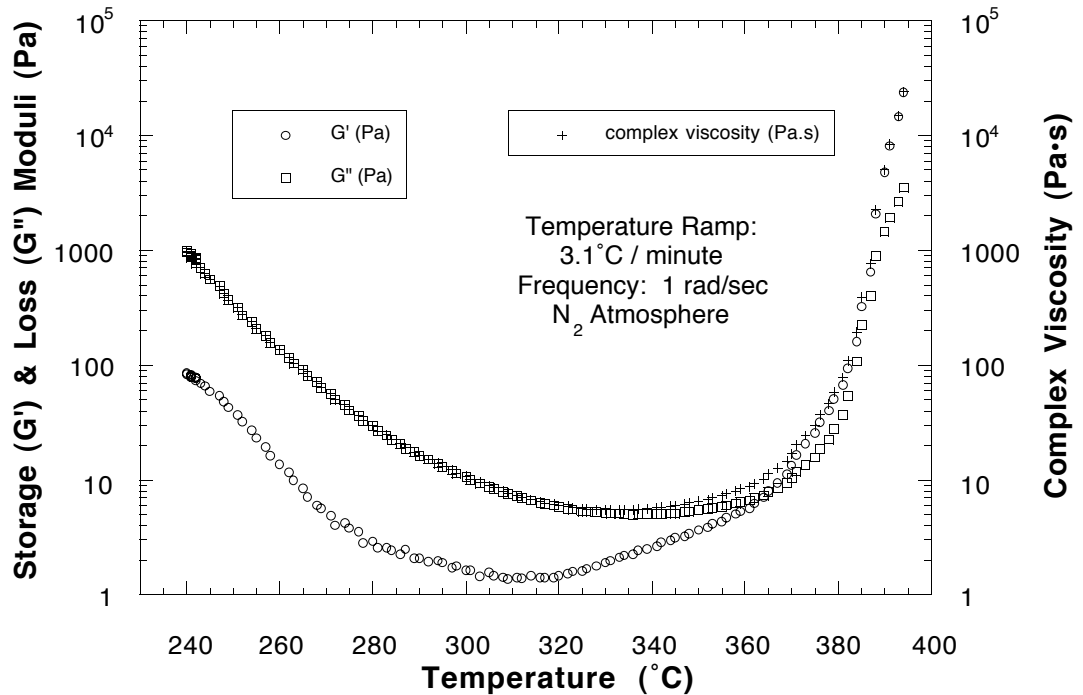


Figure 2.3. Rheological Behavior of 3kPETU During 3.1 °C/min Ramp

2.4.2 Drum Winding

Towpreg plies were assembled by drum winding. The towpreg was wound on a 0.610 m diameter drum, which simultaneously rotated and translated so that the towpreg could be placed next to its position from the previous revolution until a width of approximately 160

mm was obtained. The 160 mm wide wrap of towpreg was then sectioned into lengths of approximately 160 mm with 13 mm wide strips of masking tape. The wrap was cut crosswise along the centerline of one of these strips of tape and removed from the drum producing a rectangle with a length equal to the drum circumference. Each piece of tape was then mirrored with a second piece of tape on the opposite side of the wrap. The wrap was then cut crosswise along the centerline of each tape pair producing square plies with edges of approximately 160 mm.

2.4.3 Composite Panel Consolidation

The square plies were trimmed to fit a 152.4 mm square steel mold and stacked in the mold. The panel consolidated for TFS and AISS specimens contained 28 plies and the panel consolidated for LFS specimens contained 22 plies. Consolidation of the composite and curing of 3kPETU was done between the platens of a computer interfaced hotpress. The consolidation pressure, which fluctuated between 1.2 MPa to 1.4 MPa, was applied prior to the mold reaching 50 °C via the hot press platens. The mold temperature was ramped from room temperature to 250 °C at 5 °C/min followed by a ramp at 3 °C/min to 350 °C. This 100 °C temperature range contains 3kPETU's minimum viscosity region before crosslinking commences on a large scale. The mold was then held at 350 °C for 60 minutes before cooling to room temperature at -4 °C/min.

Lay up of the two fracture toughness panels included pieces of Kapton® film to act as starter cracks during testing. A 152.4 mm x 40 mm x 12.7 µm piece of DuPont Kapton® polyimide film was placed between the middle two plies of the panels after the film was coated on both sides with Dexter Frekote® 33 mold release; each panel contained a total of 20 plies. The 152.4 mm length of the films ran perpendicular to the unidirectional fiber direction, and the films were placed such that each film extended 40 mm from the edge into the panel in the fiber direction.

2.4.4 Consolidation Quality

Ultrasonic imaging through the thickness of the panels and optical microscopy of panel cross sections generally indicated good consolidation with some resin rich regions and very low void content (Figure 2.4). Locations of poor consolidation were avoided in selection of mechanical test specimens. In addition, as desired in the two fracture toughness panels, the regions in which the Kapton® film bonded to the composites are few.

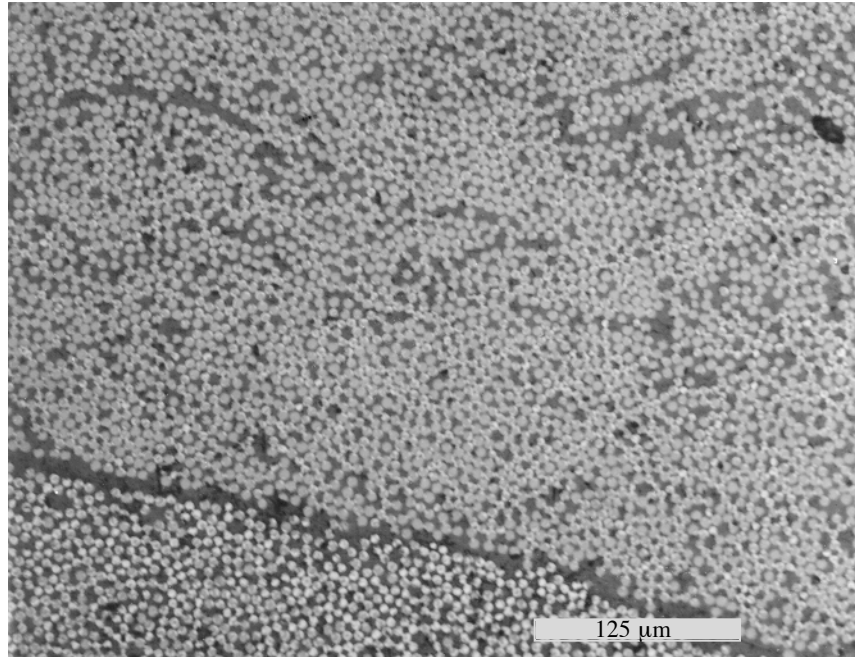


Figure 2.4. Optical Micrograph of Composite Cross Section

2.4.5 Composite Fiber Volume Fraction

Knowing the fiber, matrix, and composite densities, the fiber volume fraction can be calculated if a specific void content is selected. Composite and neat resin densities were measured following the ASTM Standard Test Method for Density and Specific Gravity (Relative Density) of Plastics by Displacement (D 792-91) using distilled water as the immersion fluid. From these densities, fiber volume fractions ranging from 0.60 to 0.65 were calculated [1,2].

2.5 Mechanical Property Measurement

2.5.1 Apparent Interlaminar Shear Strength

2.5.1.1 Experimental

The AISS tests were performed according to ASTM D 2344-84 for flat laminates; the loading and support noses had diameters of 6.35 mm. The twelve AISS specimens were cut from the TF test specimens following TF testing such that the 25.4 mm length of the AISS specimens ran parallel to the 25.4 mm width of the TF specimens. Additional test information is given in Table 2.1.

Table 2.1. Apparent Interlaminar Shear Strength Test Information

Test Parameter	Value
Specimen Depth (mm)	4.42
Specimen Width (mm)	6.36
Support Span (mm)	18
Support Span : Depth	4 : 1
Rate of Crosshead Motion (mm/min)	1.3

2.5.1.2 Results and Discussion

The results of the AISS tests are given in Figure 2.5; the 3kPETU/G30-500 composite compares well with the high-performance thermoset and thermoplastic composites shown. All but one of the specimens exhibited the expected horizontal shear crack propagation from the end inward. The vertical locations of the cracks were anywhere between the specimen midplane and about a quarter of the way up from the specimen bottom. All of these edge-initiated cracks propagated from the right end of the specimens and appeared to end near center span of the specimens. The lone specimen not exhibiting typical AISS crack propagation appeared to have some delaminations that initiated within the specimen.

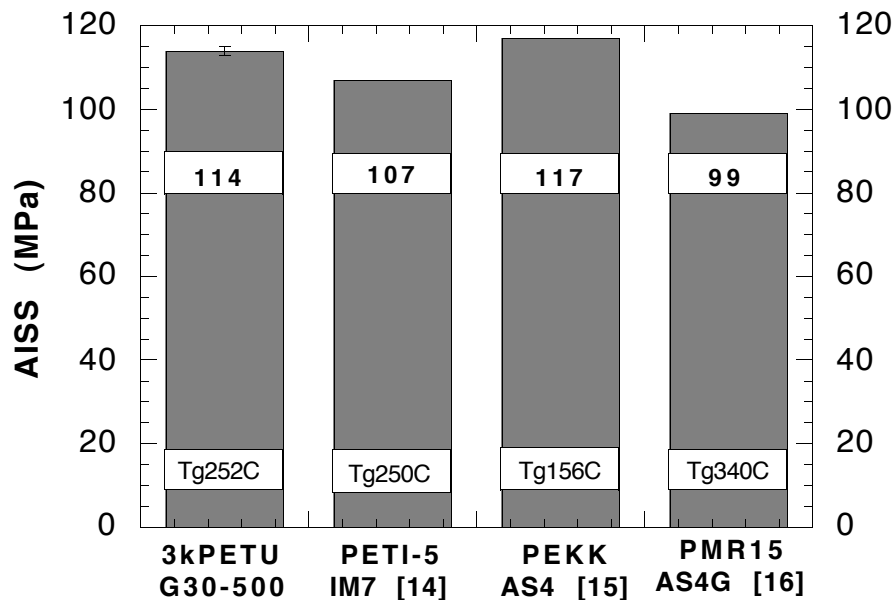


Figure 2.5. Apparent Interlaminar Shear Strength [14-16]

2.5.2 Flexural Properties

2.5.2.1 Experimental

The longitudinal and transverse flexural tests were performed according to the ASTM Standard Test Method for Flexural Properties of Unreinforced and Reinforced Plastics and Electrical Insulating Materials (D 790-92) following the four-point bend method with the load span equal to one-third of the support span (Test Method II - Procedure A); the loading and support noses had diameters of 12.70 mm. Each flexural test was performed on five specimens. Additional test information is given in Table 2.2.

Table 2.2. Flexural Test Information

Test Parameters	Longitudinal (0°)	Transverse (90°)
Specimen Depth (mm)	2.37	4.42
Specimen Width (mm)	25.4	25.4
Support Span (mm)	76	142
Support Span : Depth	32:1	32:1
Rate of Crosshead Motion (mm/min)	4.5	8.5

2.5.2.2 Results and Discussion

2.5.2.2.1 Longitudinal Flexural Test

The resultant values of this test are given in Figures 2.6 and 2.7. The LF strength and modulus of 3kPETU/G30-500 composites exceeds those of the other high-performance composites shown. Two of the five specimens catastrophically fractured into three pieces with the fractures occurring under the loading noses. These specimens appeared to have failed in compression since a much greater amount of damage is evident on the compression surface of the specimens. Two other specimens catastrophically fractured into two pieces with the fracture occurring under a loading nose and severe cracking located beneath the other loading nose. These specimens appeared to have failed in compression also. The crack at the unfractured location appeared to have propagated from the top (compression surface) down. In addition, at the fracture, the compression side of the specimen showed much greater deformation than the tension surface. The cracks in these specimens appeared to have propagated downward and inward toward center span. The fifth specimen remained in one piece despite significant cracking and delamination on the tension surface. The compression surface showed no visible signs of damage; this specimen appeared to fail in tension. The electron micrograph in Figure 2.8 shows a typical portion of the tensile region of the fracture surface of one of the two specimens that

fractured into three pieces. In this image, one can see an appreciable amount of deformation in the matrix and that the matrix remained well adhered to the fibers.

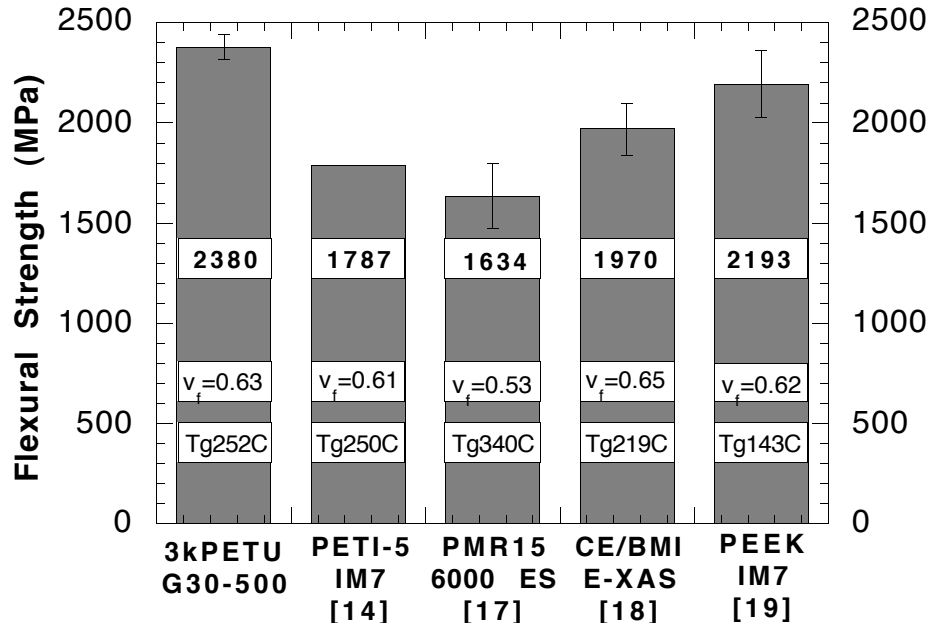


Figure 2.6. Longitudinal Flexural Strength [14,17-19]

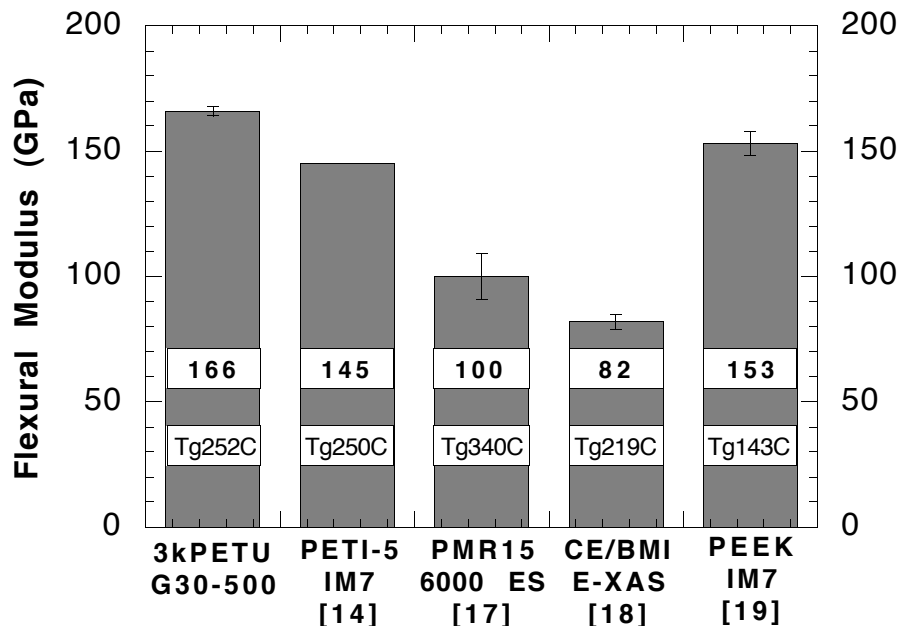


Figure 2.7. Longitudinal Flexural Modulus [14,17-19]

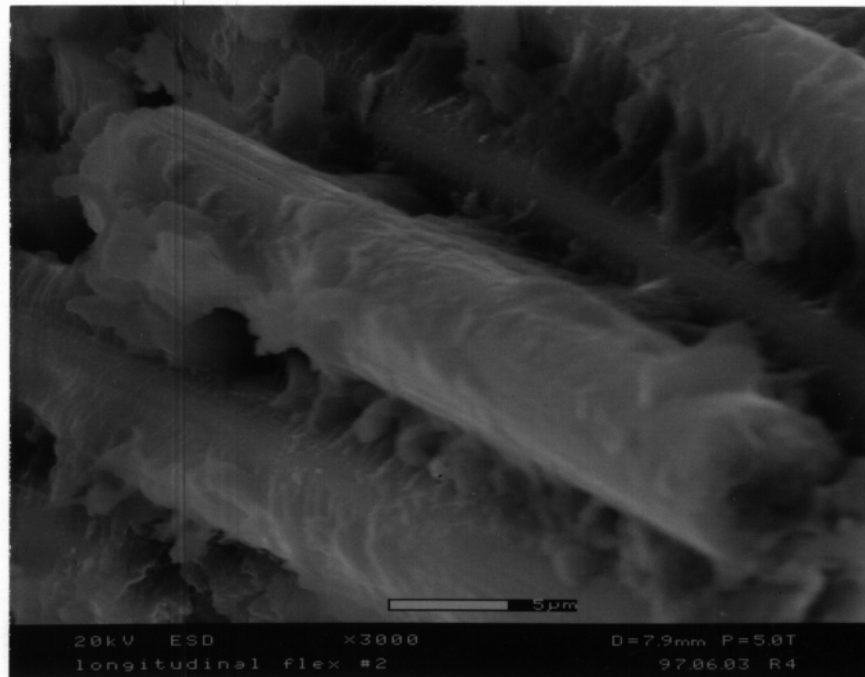


Figure 2.8. Longitudinal Flexural Tensile Fracture Surface (Gray Bar = 5 μm)

2.5.2.2.2 Transverse Flexural Test

The resultant values of this test are given in Figure 2.9; the 3kPETU/G30-500 composites have a slightly lower TF strength than the other high-performance composites referenced. All five specimens fractured catastrophically with three of them fracturing into three pieces and the fourth and fifth specimens into two pieces. The fractures mostly occurred either near a loading nose or between the two loading noses. The failed region of the fifth specimen was located between one loading nose and one support nose. Inspection of the C-scan of this panel indicated that failure occurred in a poorly consolidated region. Therefore, values for the fifth specimen were excluded in the average reported values.

The lack of damage on and near the fracture surfaces made it difficult to determine from visual inspection whether these specimens failed in compression or tension. Since polymers generally have lower tensile strengths than compression strengths, tensile failure is most likely. The fracture surfaces indicated crack growth straight down normal to the plane of the specimen.

The electron micrograph in Figure 2.10 shows a portion of the tensile region of the fracture surface of one of the three specimens that fractured into two pieces. Again, a significant amount of matrix deformation is visible with good matrix adhesion to the fiber, although a

spot of bare fiber is apparent. This bare spot could be due to either locally poor fiber/matrix adhesion or a void. Such bare spots were not typical in this fracture surface, but this region was selected to provide reference between bare fiber and well-coated fiber. Fragments of fractured matrix indicative of specimen fracture within the matrix can also be seen on this fracture surface.

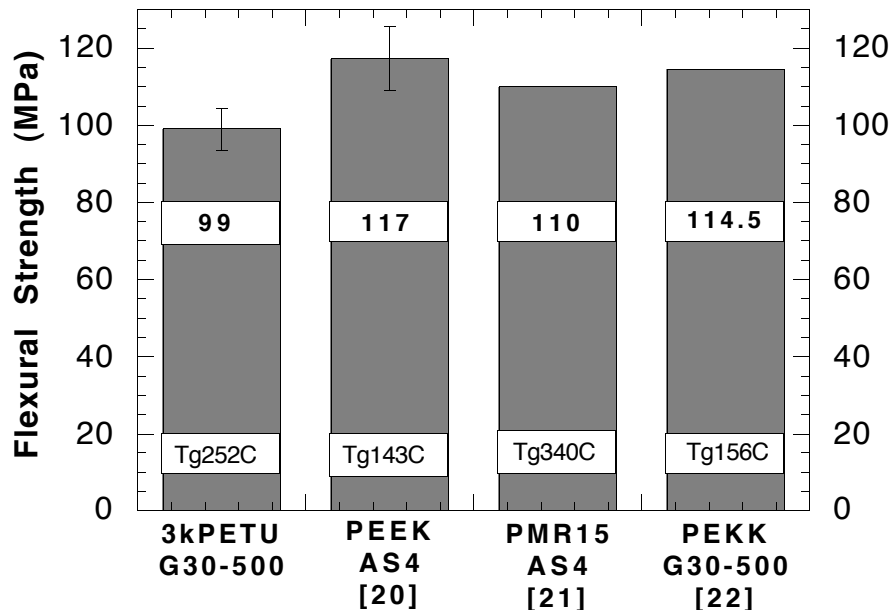


Figure 2.9. Transverse Flexural Strength [20-22]

2.5.3 Open-Hole Compression Strength

2.5.3.1 Experimental

Four OHCS specimens were tested following the Northrop Material Specification for Open-Hole Compression Test Method (NAI-1504C). These specimens were 76.2 mm long by 25.4 mm wide by 3.18 mm thick. A 6.35 mm diameter hole was located at the center of each specimen. The unidirectional fibers ran parallel to the specimens' long direction. The specimens were end-loaded by a crosshead moving at 1.27 mm/min. Testing was performed in a Northrop Open Hole Compression Test Fixture manufactured by Wyoming Test Fixtures.

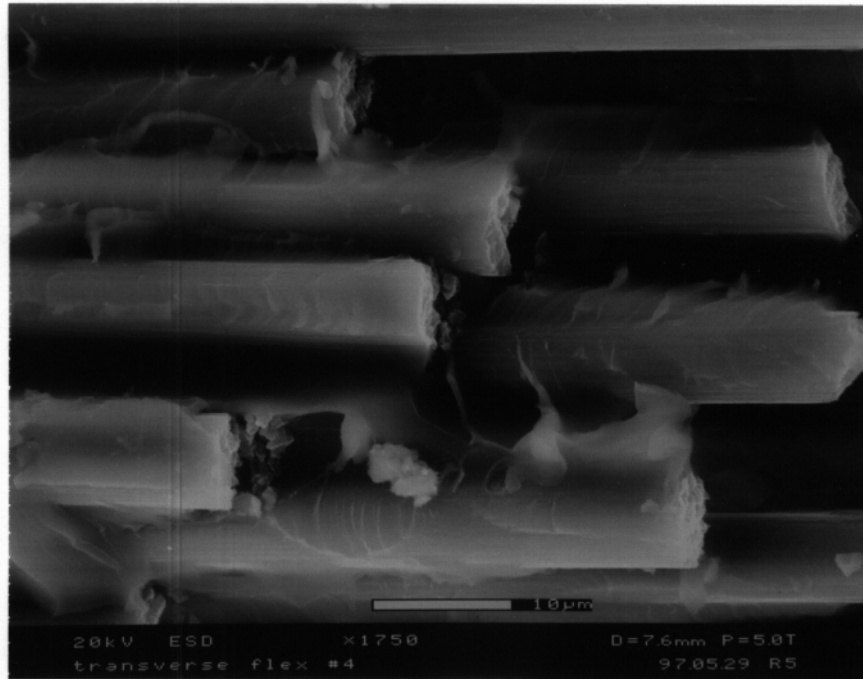


Figure 2.10. Transverse Flexural Tensile Fracture Surface (Gray Bar = 10 μm)

2.5.3.2 Results and Discussion

The average OHCS of the four specimens was 708 MPa with a standard deviation of 37 MPa. Two modes of failure were visible in the tested specimens. Longitudinal cracks ran tangent to both sides of the center hole. The second mode of failure was a transverse break which ran normal to the fiber direction. This transverse break connected one of the longitudinal cracks to the specimen edge. The transverse breaks' vertical location coincided with the end of the top gripping block. In three of the specimens, the transverse breaks consisted of two cracks on one specimen face that angled towards one another to form a single crack on the opposite face of the specimen. The two cracks on the one specimen face were parallel and separated by about 2 mm. The confluence of these two cracks created a wedge within the specimen; the wedge shape was clearly visible from the specimen edge. Inspection of the wedge-shaped failure from specimen edges via a microscope revealed fiber kinking at the dual crack surface (Figure 2.11) and extensive fiber buckling and breakage at the single crack surface (Figure 2.12). The lack of focus in some regions of the images is due to changes in depth of the specimen edge. The failure mode in the interior of the specimen was indistinguishable due to a lack of material between the surfaces of the crack. In addition, there was some delamination at the intersection of the transverse and longitudinal cracks.

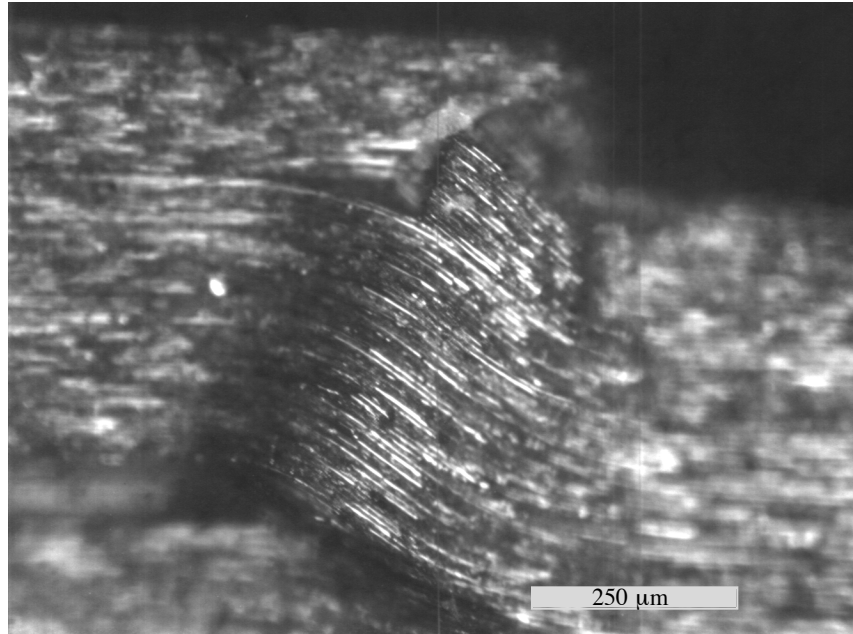


Figure 2.11. OHCS Kink Band

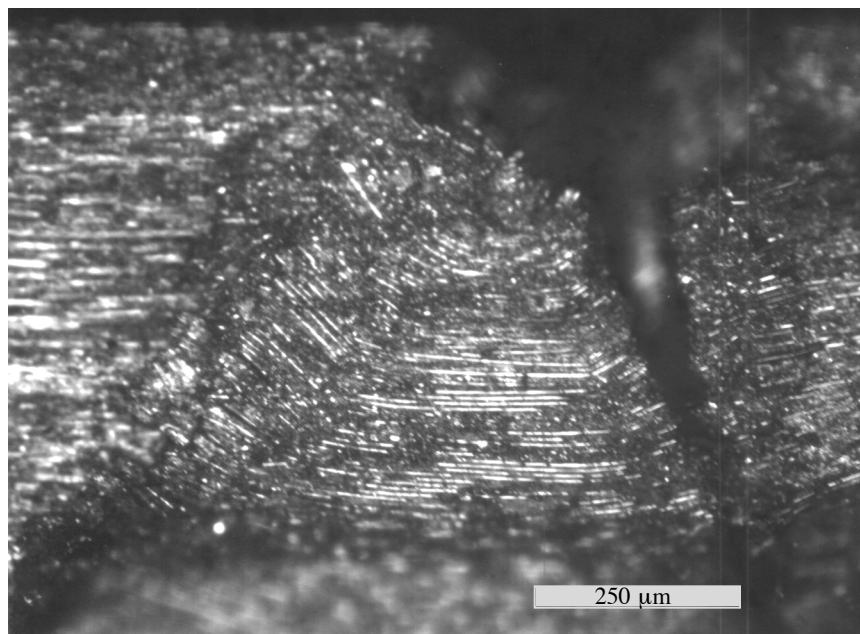


Figure 2.12. OHCS Fiber Buckling

2.5.4 Mode I Fracture Toughness

2.5.4.1 Experimental

G_{limit} is the SERR measured when the compliance, which is proportional to the ratio of crack opening displacement to load, first becomes nonlinear in relation to the crack opening

displacement (COD) (Figure 2.13). This is the point at which the crack first begins to propagate beyond the crack initiating Kapton® insert in each specimen. G_{init} is measured only once for each specimen. G_{Imax} is a measure of the maximum SERR of the material during crack propagation as the two crack faces are being separated at a constant COD rate. G_{Imax} is measured at a point of maximum load in the load versus COD plot (Figure 2.13). Several G_{Imax} measurements are taken for each specimen. Following the G_{Imax} measurement, the COD is fixed to allow crack propagation to cease and the load to stabilize. At this point, the SERR of a practically stationary crack, $G_{Iarrest}$, is measured. A fourth SERR, G_{Icrit} , is the critical SERR to initiate crack growth following crack arrest (i.e., it is similar to G_{Iinit} , only G_{Iinit} takes place on a virgin specimen prior to any cracking beyond the region near the end of the Kapton® film). G_{Icrit} would be measured during loading following crack arrest and specimen unloading. However, in these tests, the point at which compliance becomes nonlinear, G_{Icrit} , is very near $G_{Iarrest}$ (Figure 2.13), which is easier to measure. Therefore, only $G_{Iarrest}$ is reported with the understanding that this value may be taken as G_{Icrit} .

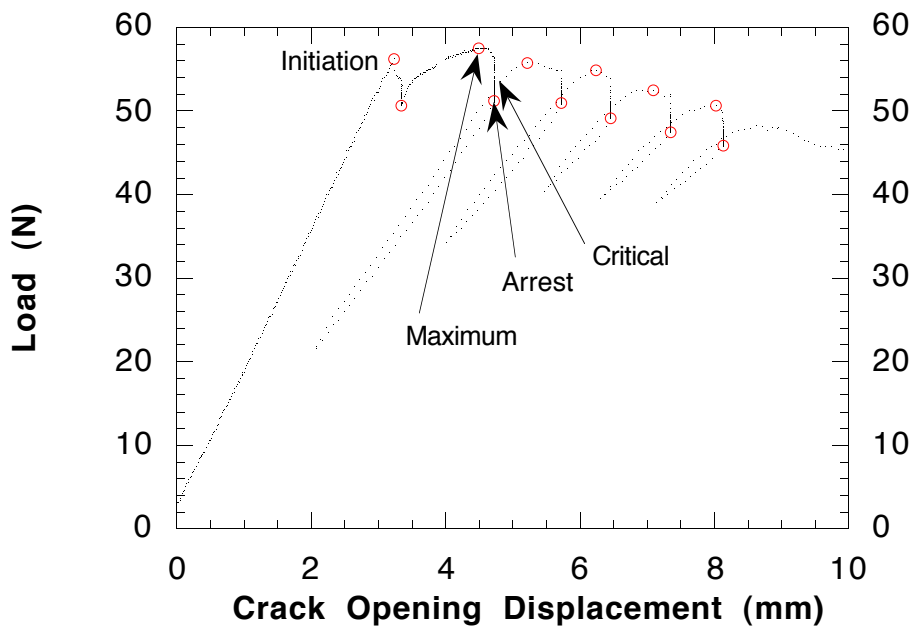


Figure 2.13. Description of Typical DCB Test

Three specimens were taken from each of the two fracture toughness panels (Panel A and Panel B): one from near each edge and one from near the center of each panel. These specimens were approximately 150 mm long and 12.7 mm wide with thicknesses

determined by their parent panels (Table 2.3). T-tabs, or loading blocks, were attached to each specimen with a high strength epoxy adhesive to facilitate loading of the specimens (Figure 2.14) [23]. The sides of the specimen were painted white to assist in monitoring crack propagation [23].

Table 2.3. Fracture Toughness Panel Physical Properties

Panel	Thickness (mm) ^a	Density (g/cm ³) ^b	Fiber Volume Fraction ($v_v=0\%$)	Fiber Volume Fraction ($v_v=1\%$)
Panel A	3.22	1.60 ± 0.01	0.609	0.658
Panel B	3.06	1.61 ± 0.01	0.639	0.664

a. Average of eight measurements: each corner and midway along each edge

b. Standard deviation given for fracture toughness panels

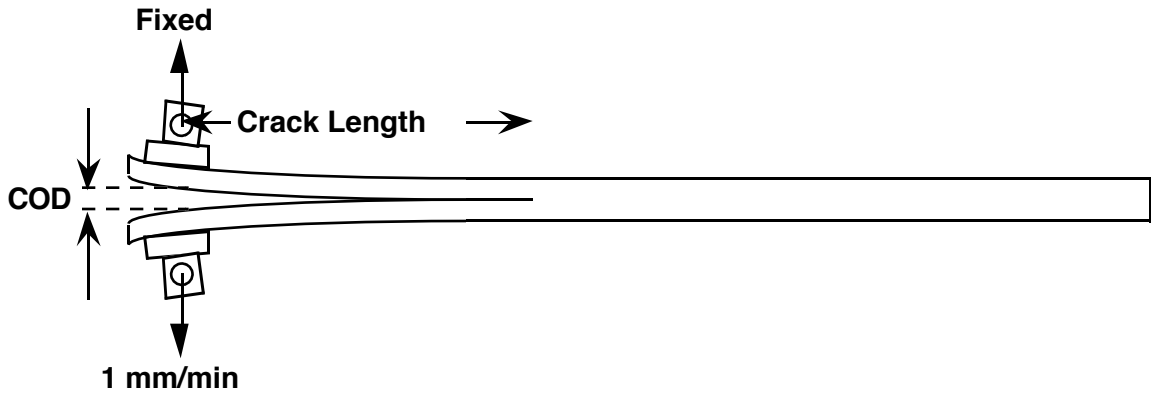


Figure 2.14. DCB Loading Schematic

The crack was initiated in the specimen along the Kapton[®] insert by loading the specimen at a constant COD rate of 1 mm/min. Loading continued as the crack propagated beyond the Kapton[®] insert. During loading, the load versus COD plot was monitored (Figure 2.13). As the load approached a local maximum, the crack length was measured using a lighted 10x magnifying glass and then saved in the data file with the corresponding load and COD. Crack length was measured from the tip of the crack to the load application point (center of T-tab) according to a scale attached to the bottom surface of the DCB specimen. Once the load began to decrease with increasing COD, the COD was held constant to allow the crack to arrest and the load to stabilize. At this point, the crack length was again measured and entered into the data file. The COD was then reduced to partially unload the specimen before the next test cycle. Each test cycle was begun by increasing the COD until a local maximum load was achieved and the corresponding crack length noted. Each test cycle

was completed by measuring the arrested crack length. This procedure was repeated until four or five maximum and arrest crack lengths were measured. The specimen was then unloaded and removed from the Instron.

The above procedure differs from that given in the ASTM Standard Test Method for Mode I Interlaminar Fracture Toughness of Unidirectional Fiber-Reinforced Polymer Matrix Composites (D 5528-94a), where a constant crack opening displacement rate is applied to the specimen throughout crack propagation; ASTM D 5528-94a does not call for the cycling described in the previous paragraph. Both techniques provide a measure of G_I required to initiate crack growth from the insert; this value is preferred over values measured from additional crack propagation due to the influence of fiber bridging on G_I values. Fiber bridging is not a factor for the delamination that grows from the insert [23].

The fracture surfaces of two specimens were selected for analysis by environmental scanning electron microscopy (ESEM). From the G_I test results that are discussed later, the specimen with highest toughness and the specimen with lowest toughness were selected to explore possible correlations between fracture surface characteristics and toughness. Their selection allowed for the comparison of specimens from the two panels and for the comparison of a specimen from the interior of a panel with a specimen from the exterior of a panel. The specimens were cut such that the inspected region ranged from the end of the Kapton® film (crack length of approximately 40 mm) to approximately 15 mm in the direction of crack propagation. This region was selected because it contained the majority of repeated crack propagation and arrest.

2.5.4.2 Data Reduction and Calculations

A hybrid compliance-beam theory (C-BT) analysis of the DCB specimen was used to determine the SERRs from the test data for each specimen. This C-BT analysis is outlined here. For a more thorough description see reference 11. This calculation method is also discussed as the Modified Beam Theory in ASTM D 5528-94a. First, a linear regression is performed on the experimental data (load, COD, and crack length) to determine the values of m and b in Equation 2.1 (Figure 2.15).

$$(C)^{1/3} = (\delta/P)^{1/3} = m \cdot a + b \quad (2.1)$$

where:

C = specimen compliance;

P = load applied to the specimen;

δ = crack opening displacement at point of load application;
 a = crack length (measured from point of load application to crack tip);
 m = slope of linear fit of experimental data; and
 b = y-intercept of the experimental data.

Next, the effective flexural rigidity, $(EI)_{eff}$, as defined by the experimental data, of the DCB specimen arms, is calculated using Equation 2.2.

$$(EI)_{eff} = 2 / (3 \cdot m^3) \quad (2.2)$$

Next, an apparent crack length offset (ACLO), Δ , is calculated using Equation 2.3.

$$\Delta = b / m \quad (2.3)$$

The ACLO accounts for crack tip rotations and deflections that produce a greater than expected COD for a given load and crack length. Thus the ACLO is added to the crack length to produce a longer crack length to satisfy beam theory.

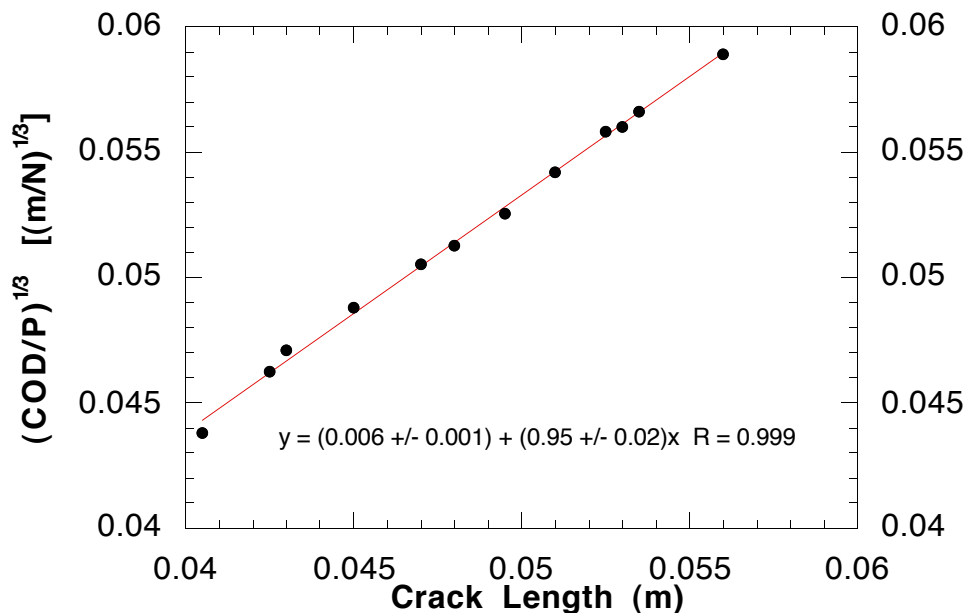


Figure 2.15. Compliance versus Crack Length

During the data collection process, crack lengths were entered near the points at which SERR values were desired as described in the DCB testing procedure. To obtain the crack

lengths at the desired points marked by open circles in Figure 2.13, predicted crack lengths must be calculated from the linear regression shown in Equation 2.1. The SERR at each point is now calculated using Equation 2.4.

$$G_I = \frac{9\delta^2 (EI)_{eff}}{4B(a_p + |\Delta|)^4} \quad (2.4)$$

where:

B = specimen width and

a_p = predicted crack length.

For the calculation of G_{limit} , the predicted crack lengths agreed well with the initial delamination lengths, defined by the Kapton® inserts [23]. Equation 2.4 becomes Equation 7 of ASTM D 5528-94a if the moment of inertia, I , for a rectangular cross section is substituted (Equation 2.5, where $h/2$ is the thickness of each specimen arm).

$$I = \frac{B\left(\frac{h}{2}\right)^3}{12} \quad (2.5)$$

2.5.4.3 Results and Discussion

The Mode I SERR values are given in Table 2.4. The ACLO values for the specimens are reported in Table 2.5. The delamination resistance, or R, curves for each specimen are given in Figure 2.16. Due to the cycling in the test procedure used here, the delamination resistance curves only display from crack initiation, which correlates with deviation from linearity, to the first G_{Imax} value for each specimen. The complete load versus COD plots for each specimen are given in the Appendix at the end of the chapter.

Table 2.4. Mode I SERR Values

Panel	G_{limit} (J/m ²)	G_{Imax} (J/m ²)	$G_{Iarrest}$ (J/m ²)
A	500 ± 60	830 ± 130	760 ± 110
B	440 ± 20	720 ± 80	680 ± 70
Both	470 ± 50	780 ± 120	720 ± 100

G_{Imax} and $G_{Iarrest}$ were observed to increase with increasing crack length in all samples. Russell [24] states that an increase in Mode I fracture toughness would be expected as a crack progresses. Russell suggests that this increase is due to fiber bridging, which occurs when delamination fracture occurs around a fiber leaving it as the only connection between

the fracture faces. As the crack moves forward, the crack faces move further apart and the strain on the bridging fiber is increased. This increase in the fiber strain diverts some of available strain energy away from the crack tip [24]. The increased fiber strain will ultimately result in fiber breakage.

Table 2.5. Apparent Crack Length Offset (ACLO) Values

Specimen	$ \Delta $ (mm)	Statistics
a2	6.3	
a6	8.0	mean: 8.0 mm
a10	10	
b2	4.5	standard deviation: 2.4 mm
b6	8.0	
b10	11	coefficient of variation: 0.30

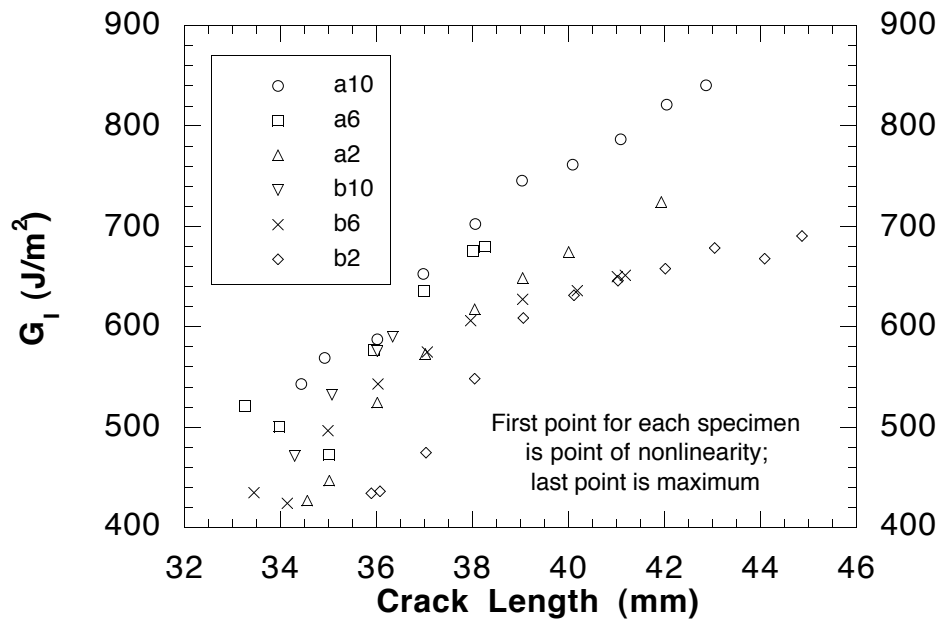


Figure 2.16. Delamination Resistance Curves

Russell [24] suggests several mechanisms for energy absorption by fiber breakage. First there is debonding as the fiber is pulled away from encompassing matrix. As the fiber is pulled away, matrix fracture may also occur. The third mechanism is the storage of elastic energy in the fiber, which is lost when it fractures.

The Mode I initiation and arrest values for this 3kPETU/G30-500 system are compared with Mode I initiation and critical SERR values for other systems in Figure 2.17, remembering that the arrest values reported here are similar to the respective critical value. Table 2.6 contains a key to the notation in Figure 2.17, along with a brief description and the source of the data.

Table 2.6. System Descriptions for Figure 2.17

System	Description	Reference
1	BP907 (tough epoxy matrix) / AS4 carbon fiber	25
2	3501-6 (brittle epoxy) / AS4	25
3	PEEK (tough thermoplastic) / AS4	25
4	PEKK (thermoplastic) / G30-500 carbon fiber	26
5	Dow Chemical XU71788 (crosslinkable thermoplastic) / sized AS4	27
6	Dow Chemical XD7342 (brittle epoxy) / unsized AS4	27
7	3501-6 (brittle epoxy) / unsized AS4	27
8	Novalac epoxy / sized AS4	27
9	Novalac epoxy (tougher version of #8) / sized AS4	27
10	PEEK (tough thermoplastic) / AS4 (APC-2)	28

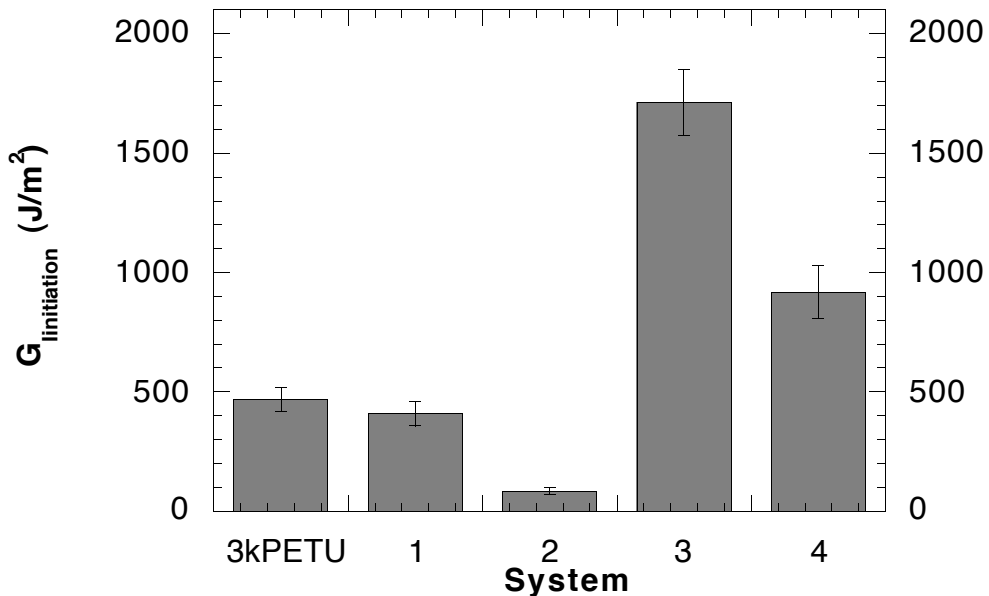


Figure 2.17.(a) Comparison of $G_{\text{initiation}}$ Values (Table 2.6)

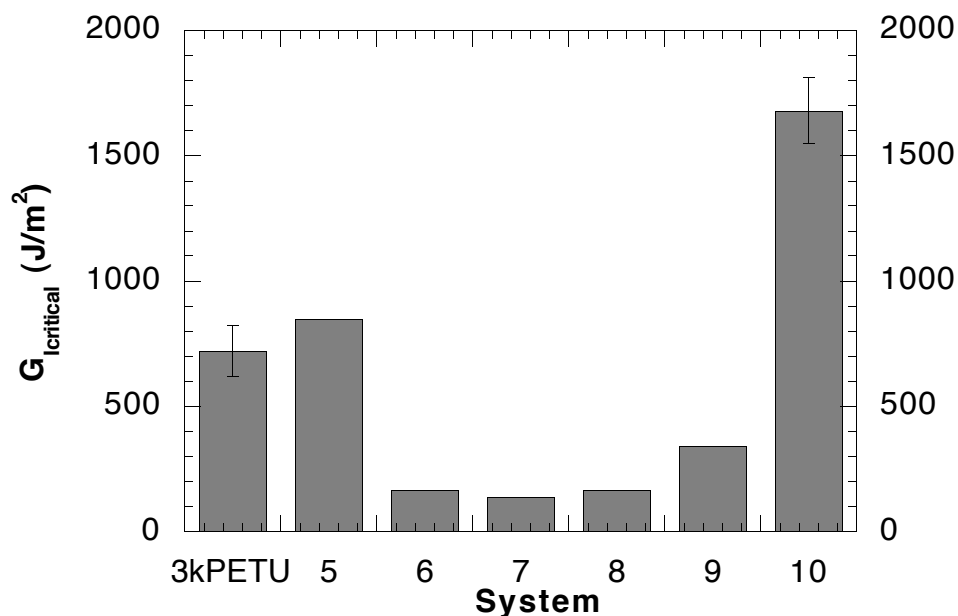


Figure 2.17.(b) Comparison of $G_{critical}$ Values (Table 2.6)

The toughness of the 3kPETU/G30-500 composite is comparable to that of another crosslinkable thermoplastic matrix (#5; XU71788) composite as would be expected since 3kPETU is a crosslinked thermoplastic itself. Also, as expected, the 3kPETU/G30-500 composite is significantly tougher than the epoxy matrix systems, but does not have the toughness of the thermoplastic matrix systems. One toughened epoxy matrix system (#1; BP907) has toughness comparable to the 3kPETU system.

The ESEM analysis resulted in an interesting observation. The fracture surfaces of the stationary upper arms were dominated by matrix, whereas, the fracture surfaces of the crosshead-driven lower arms were dominated by fiber. The upper and lower arms of one Panel B specimen and the upper arm of one Panel A specimen were inspected. The Kapton[®] strip remained adhered to the lower arm of the Panel A specimen and the upper arm of the Panel B specimen. This difference in Kapton[®] position indicates that the surface character is not due to the presence or absence of Kapton[®]. The fracture surface character appears to be influenced by the arm position (upper or lower). The ESEM analysis also shows that fracture occurred both within the matrix and along the fiber/matrix interface.

Some typical features of Mode I delamination fracture surfaces are evident in Figure 2.18. Debonding between the fiber and matrix will produce a corrugated surface consisting of smooth troughs and scalloped regions between the fiber debonds [29]. The scalloped fracture surface results from the coalescence of many microcracks around the crack tip [29]. Figure 2.18 also shows fiber breakage that usually results following debond. No apparent differences were observed in the fracture surfaces to account for the disparities in the measured fracture toughness of the two inspected specimens.

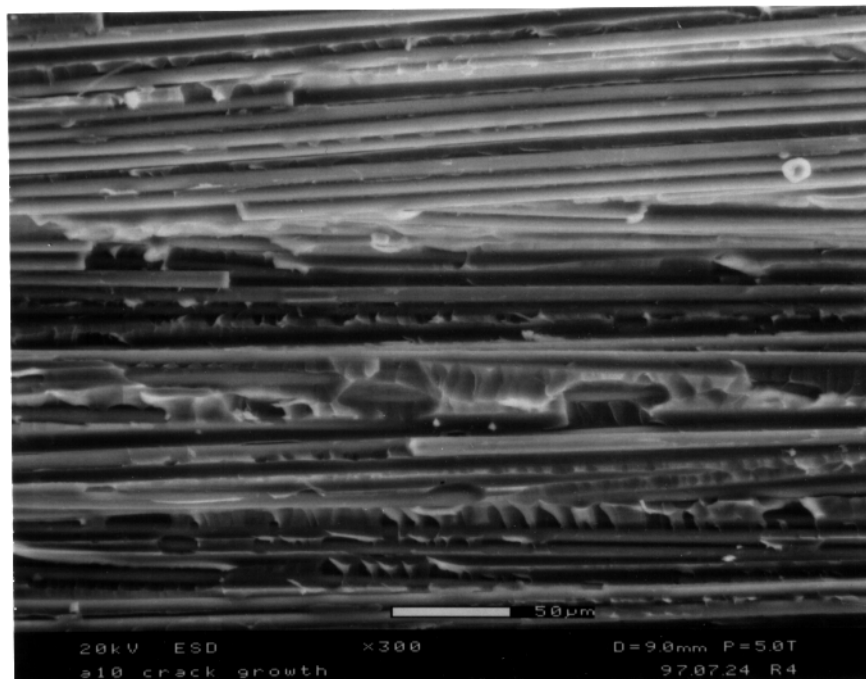


Figure 2.18. Fracture Surface of Upper Arm of Panel A DCB Specimen (Gray Bar = 50 μm) Crack Growth Region; Crack Movement: Right to Left

2.5.5 Mode II Fracture Toughness

2.5.5.1 Experimental

Ten specimens were tested: five each from Panels A and B. These are the same two panels from which the DCB specimens were taken. Each specimen was approximately 150 mm long and 12.7 mm wide with a thickness determined by their parent panels (Table 2.3).

The specimens were tested in a three-point bend fixture in a flexural test (ASTM D 790-92) manner (Figure 2.19). A support span to thickness ratio of 32 to 1 was used resulting in a support span ($2L$) of 100 mm. The central loading nose had a 6.3 mm diameter, and the

outer support noses had diameters of 9.5 mm. A crosshead speed of 5.3 mm/min per ASTM D 790-92 was used when applying load to the specimens.

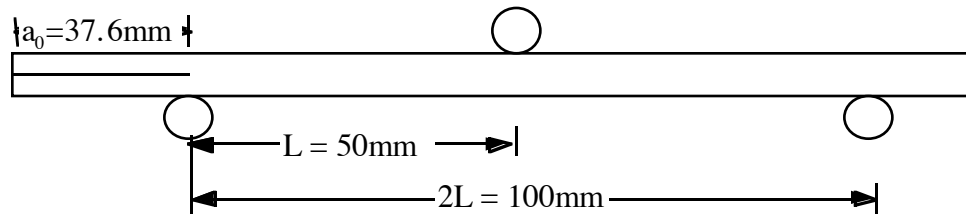


Figure 2.19. ENF Loading Schematic

The general test procedure will now be described. The specimen was initially placed in the fixture such that the Kapton[®] insert lay completely outside of the support span; an optical microscope with a magnification of 216x was used to find the end of the Kapton[®] insert. The specimen was then loaded within its elastic region (300 to 350 N) to determine its bending compliance. After the compliance loading, the specimen was moved to the right such that the interior end of the Kapton[®] insert was positioned half-way between the left support nose and the central loading nose. The specimen was then loaded until crack propagation beyond the interior end of the Kapton[®] insert took place. Propagation was indicated by a significant load drop. At this point, the crosshead was halted and held for two minutes before returning the crosshead to its original position.

The specimen was then reinstalled in the fixture with 20 mm of the new crack being located within the support span. The specimen was then loaded to 300 to 350 N for a compliance measurement. These compliance loadings were repeated with 30, 35, and 40 mm of the crack length within the support span. Finally, the specimen was positioned with 25 mm of the crack length within the support span. The specimen was then loaded to failure, which was indicated by a large drop in the increasing load being carried by the specimen. One specimen was loaded to failure with a crack length of 30 mm within the support span because the initial loading to propagation produced a crack length too long to set a 25 mm crack length and support the uncracked end of the specimen on the right support nose. The values obtained from this specimen agreed well with the other results.

The G_{II} test results are discussed later. From these results, the highest toughness and lowest toughness specimens were selected for fracture surface inspection by scanning electron microscopy (SEM). As with the DCB specimens, these two ENF specimens were

selected to compare fracture surface characteristics of specimens with significant toughness differences and specimens from different regions of different panels.

2.5.5.2 Data Reduction and Calculations

Whitney [30] develops an equation for G_{II} involving only specimen dimensions, load, deflection, and crack length:

$$G_{II} = \frac{9a^2 P \delta}{2w(2L^3 + 3a^3)} \quad (2.6)$$

where:

- a = crack length in the specimen;
- P = load;
- δ = deflection of specimen at load point;
- w = specimen width; and
- L = half the support span.

To correct for possible experimental error, the crack length, a , in Equation 2.6 is replaced with a modified crack length, a_{mod} . The value of a_{mod} for a specific crack length is dependent on the effective bending modulus, E_x^b , calculated from the zero crack length measurement and the value of the compliance for that specific crack length measurement. The use of a_{mod} corrects for errors in crack length measurement and more importantly, unseen crack growth during previous compliance measurements. The calculation of a_{mod} corrects for slight gradual crack growth assuming that away from the crack tip the specimen is behaving in a linear elastic manner. Equation 2.6 may therefore be replaced with Equation 2.7; the calculation of a_{mod} is given in Equation 2.8.

$$G_{II} = \frac{9a_{mod}^2 P \delta}{2w(2L^3 + 3a_{mod}^3)} \quad (2.7)$$

$$a_{mod} = \left(\frac{8E_x^b w h^3 C_a - 2L^3}{3} \right)^{1/3} \quad (2.8)$$

where:

- h = half the specimen thickness;
- E_x^b = the effective bending modulus in the axial direction of a beam of thickness $2h$;
- and
- C_a = specimen compliance.

The subscript, a , on the compliance indicates that the compliance measured for a specific experimental crack length is used when calculating the modified crack length that is replacing that specific experimental crack length.

The effective bending modulus is all that remains to be calculated. It is calculated from the specimen dimensions and the compliance measured during the zero crack length measurement.

$$E_x^b = \frac{2L^3}{8wh^3} \frac{1}{C_0} \quad (2.9)$$

2.5.5.3 Results and Discussion

The G_{IIC} values are given in Table 2.7. The results are listed for each panel as calculated using the experimental crack length and using the modified crack length. The average value for $G_{IIC}(a_{mod})$ is compared to other materials in Table 2.8. For this material, the load versus displacement was linear until crack propagation took place with a large load decrease. This result differs from some thermoplastic matrix composites where there is deviation from linearity prior to the maximum load at crack propagation from the insert [26].

Table 2.7. G_{IIC} Values

	G_{IIC} (J/m ²) ^a	$G_{IIC}(a_{mod})$ (J/m ²) ^a
Panel A	1400 ± 400	1700 ± 200
Panel B	1200 ± 100	1200 ± 100
All	1300 ± 400	1400 ± 300

a. Plus or minus standard deviation

Recalling from Table 2.3, Panel A has a lower fiber volume fraction than Panel B. This lower fiber volume fraction may translate into a greater interlaminar matrix thickness. The results given in Table 2.7 show that the greater interlaminar matrix thickness may be producing a greater value of G_{IIC} . Russell [24] found that G_{IIC} increased linearly with increases in matrix thickness while working with AS/3501-6 composite materials. Investigators have shown that shear stress in the interlaminar matrix is proportional to (matrix thickness)^{-1/2}. Therefore, an increase in the thickness of the interlaminar matrix layer will result in a decrease in the matrix strain. In turn, a greater strain energy release rate will be required to initiate fracture [24].

Table 2.8. System Comparison of G_{IIC}

System	Reference	G_{IIC} (J/m ²)
3kPETU / G30-500	--	1400 ± 300
PEKK / G30-500 G_{IIC} nonlinearity onset	26	1570 ± 130
PEKK / G30-500 G_{IIC} max	26	6270 ± 729
Hercules 3501-6 epoxy / AS4	27	1267
Novalac Epoxy / sized AS4	27	1532
Novalac Epoxy modified for increased toughness and adhesion / sized AS4	27	1724
Dow XU71788 (crosslinkable thermoplastic) / sized AS4	27	2836
PEEK / AS4 (APC-2)	26	2224
PES / AS4	31	1290 ± 30

During fracture, the major energy absorbing mechanisms are: matrix fracture, fiber/matrix debonding, and fiber breakage [24]; evidence of these mechanisms can be seen in Figure 2.20, where several smooth fibers are visible. Signs of debonding are also apparent where fiber shear-out grooves remain in the matrix. Extensive matrix deformation occurred near the stray fiber, and hackles, tooth-like structures, can be seen between the grooves. According to Russell [24], these hackles are due to tensile fracture of the matrix. The shear strain in the matrix can be resolved into a normal tensile strain and a normal compressive strain acting at an angle 45° to the interlaminar shear plane [24]. This 45° tensile strain is credited with producing the tooth-like appearance of the fractured matrix located between the shear-out grooves.

The existence of good fiber/matrix adhesion, debonding by fiber shear-out, fiber breakage, and matrix deformation (all evident in Figure 2.20) is indicative of synergistic energy dissipation by the fiber and matrix in the composite material. As with the DCB specimens, the fracture surfaces showed no apparent source for the difference in the measured fracture toughness values of the two inspected specimens.

2.6 Summary And Conclusion

The minimal dry powder prepregging system proved to be an excellent tool for the production of composite material consisting of *meta*-linked phenylethynylphthalic anhydride poly(etherimide) (PETU) reinforced with unidirectional G30-500 carbon fibers. Optical microscopy of the composite cross sections displayed good consolidation with

minimal void volume fraction. Because a practical technique for rapid processing of 3kPETU matrix composites exists, 3kPETU offers potential for production of high performance composites.

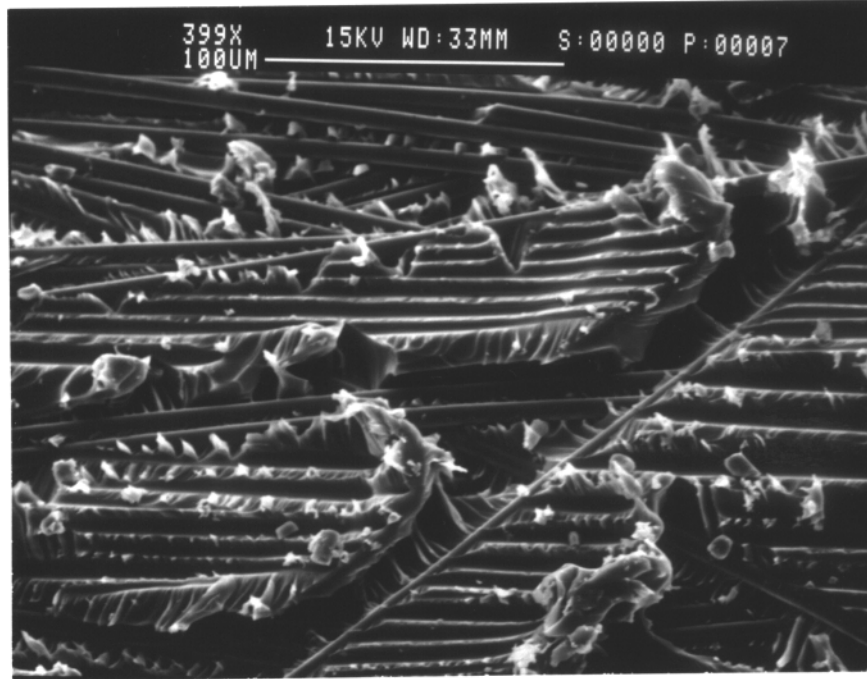


Figure 2.20. Fracture Surface of Upper Half of Panel A ENF Specimen
(Bar = 100 μm)

The strengths of carbon fiber-reinforced composites fabricated with a 3kPETU matrix compare well with other high-performance fiber reinforced polymer matrix composites. Furthermore, this 3kPETU matrix composite offers substantial increases in toughness over traditional epoxies and has toughness comparable to other toughened epoxies and crosslinkable thermoplastics. Thermoplastic matrixes offer much greater toughness than 3kPETU, but do not offer the high-temperature stability and solvent resistance of 3kPETU and have significantly higher melt viscosities than that of 3kPETU.

The evidence of matrix deformation and minimal bare fiber in the fracture surfaces of the 3kPETU/carbon fiber composites indicates good fiber/matrix adhesion. In general, a strong interface produces efficient load transfer and a polymer matrix composite with good mechanical properties.

The combination of the mechanical properties of 3kPETU/G30-500 composites presented here along with the excellent solvent resistance and thermo-oxidative stability of 3kPETU neat resin previously shown [32] results in a composite material possibly well suited for high-performance applications.

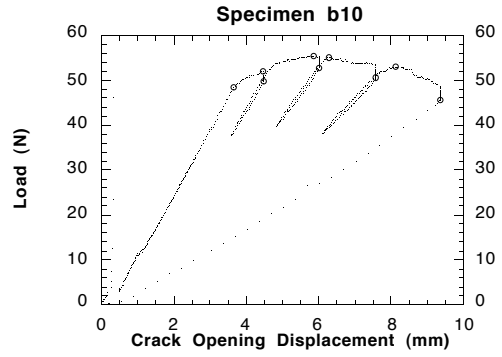
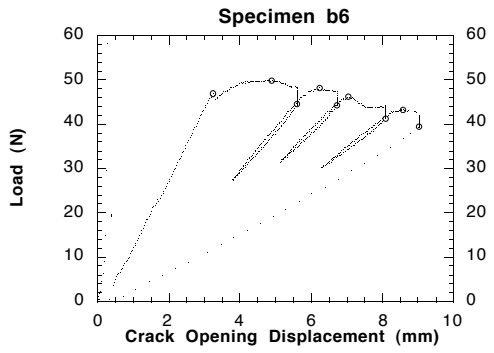
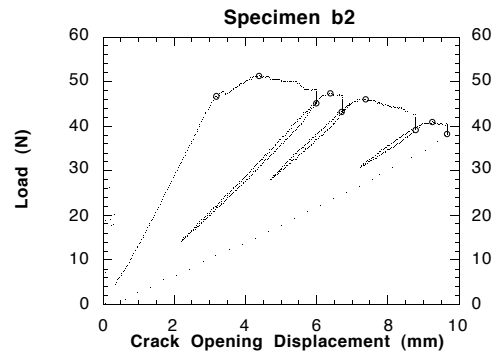
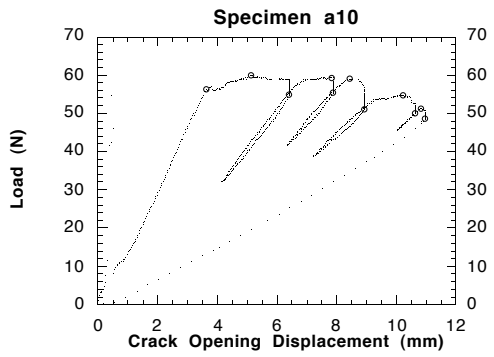
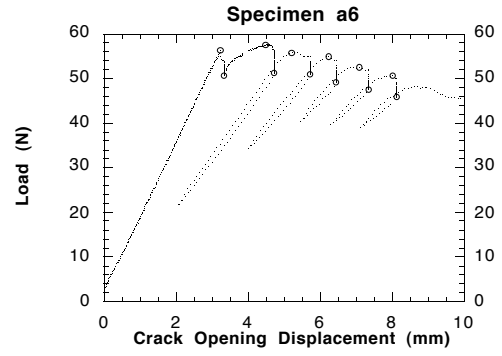
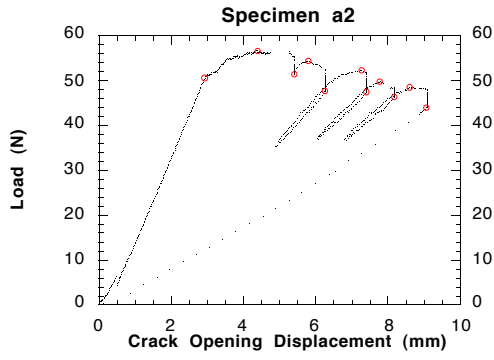
2.7 References

1. T.A. Bullions, R.H. Mehta, B. Tan, J.E. McGrath, and A.C. Loos, "Manufacture and Mechanical Properties of a High-Performance Thermosetting Poly(etherimide) / Continuous Carbon Fiber Composite," *29th International SAMPE Technical Conference*, Orlando, FL, October 28 - November 1, 1997, pp. 85-97.
2. T.A. Bullions, R.H. Mehta, B. Tan, J.E. McGrath, D. Kranbuehl, and A.C. Loos, "Mode I and Mode II Fracture Toughness of High-Performance 3000 g/mole Reactive Poly(EtherImide) / Carbon Fiber Composites," *Composites Part A: Applied Science and Manufacturing*, **30A**, (2), 153-162 (1999).
3. D.F. Adams, T.R. King, and D.M. Blacketter, "Evaluation of the Transverse Flexure Test Method for Composite Materials," *Composites Science and Technology*, **39**, 341-353 (1990).
4. E.T. Camponeschi, Jr., "Compression of Composite Materials: A Review," in Composite Materials: Fatigue and Fracture (Third Volume), ASTM STP 1110, T.K. O'Brien, ed., American Society for Testing and Materials, Philadelphia, 1991, pp. 550-578.
5. Y.M. Tarnopol'skii and T. Kincis, Static Test Methods for Composites, Van Nostrand Reinhold Company, Inc., New York, 1985, pp. 93-95.
6. H.T. Hahn and J.G. Williams, "Compression Failure Mechanisms in Unidirectional Composites," in Composite Materials: Testing and Design (Seventh Conference), ASTM STP 893, J.M. Whitney, ed., American Society for Testing and Materials, Philadelphia, 1986, pp. 115-139.
7. E.G. Guynn and W.L. Bradley, "A Detailed Investigation of the Micromechanisms of Compressive Failure in Open Hole Composite Laminates," *Journal of Composite Materials*, **23**, 479-504, (1989).
8. P. Berbinau, C. Soutis, and I.A. Guz, "Compressive Failure of 0° Unidirectional Carbon-Fibre-Reinforced Plastic (CFRP) Laminates by Fibre Microbuckling," *Composites Science and Technology*, **59**, 1451-1455, (1999).
9. Standard Test Method for Mode I Interlaminar Fracture Toughness of Unidirectional Fiber-Reinforced Polymer Matrix Composites. ASTM Standard D 5528-94, American Society for Testing and Materials, Philadelphia, PA, 1994.
10. G.E. Dieter, *Mechanical Metallurgy*, McGraw-Hill, Inc., New York, 1986, pp. 348-349.

11. M.D. Rakestraw, M. Vrana, T. Chang, D.A. Dillard, T.C. Ward, J.G. Dillard, *Evaluation of Adhesive Performance Using Static, Fatigue, and Environmental Fracture Testing; Report No. CASS / MESC / 94-2.*, 1994, Center For Adhesive And Sealant Science, Virginia Polytechnic Institute and State University, Blacksburg, VA 24061.
12. B. Tan and J.E. McGrath, personal discussion
13. Toho Carbon Fibers, Inc., Palo Alto, CA, product brochure, 1997.
14. J.G. Smith, Jr., J.W. Connell, and P.M. Hergenrother, "Imide Oligomers Containing Pendent and Terminal Phenylethynyl Groups," *Polymer*, **38**, (18), 4657-4665 (1997).
15. I.Y. Chang, "PEKK as a New Thermoplastic Matrix for High Performance Composites," *SAMPE Quarterly*, **19**, (4), 29-34 (1988).
16. K.J. Bowles, D. Jayne, T.A. Leonhardt, and D. Bors, "Thermal Stability Relationships Between PMR-15 Resin and Its Composites," *SAMPE Quarterly*, **26**, (1), 23-32 (1994).
17. D.E. Hirt, "Mechanical Properties of Interleaved PMR-15 Composites," *SAMPE Quarterly*, **26**, (2), 48-53 (1995).
18. J.M. Barton, I. Hamerton, J.R. Jones, and J.C. Stedman, "Mechanical Properties of Tough, High Temperature Carbon Fiber Composites From Novel Functionalized Aryl Cyanate Ester Polymers," *Polymer*, **37**, (20), 4519-4528 (1996).
19. E.M. Silverman, C.R. Wiacek, and R.A. Griese, "Characterization of IM7 Graphite / Thermoplastic Polyetheretherketone (PEEK) for Spacecraft Structural Applications," in Composite Materials: Testing and Design (Tenth Volume), ASTM STP 1120, G.C. Grimes, ed., American Society for Testing and Materials, Philadelphia, 1992, pp. 118-130.
20. T.A. Bullions, A.C. Loos, and J.E. McGrath, "Advanced Composites Manufactured Via Dry Powder Prepregging," *12th International Conference on Composite Materials*, Paris, July 5 - 9, 1999, pages unavailable.
21. J.A. Dugger and D.E. Hirt, "PMR-15 Carbon Fiber Composites Produced From Powder-Coated Towpreg," *Polymer Composites*, **17**, (30), 492-496 (1996).
22. R.A. Bucher and J.A. Hinkley, "Fiber/Matrix Adhesion in Graphite/PEKK Composites," *Journal of Thermoplastic Composite Materials*, **5**, 2-13 (1992).
23. Standard Test Method for Mode I Interlaminar Fracture Toughness of Unidirectional Fiber-Reinforced Polymer Matrix Composites. ASTM Standard D 5528-94, American Society for Testing and Materials, Philadelphia, PA, 1994.
24. A.J. Russell, "Micromechanisms of Interlaminar Fracture and Fatigue," *Polymer Composites*, **8**, (5), 342-351 (1997).
25. T.K. O'Brien and R.H. Martin, "Round Robin Testing for Mode I Interlaminar Fracture Toughness of Composite Materials," *Journal of Composites Technology and Research*, **15**, (4), 269-281, (1993).

26. K. Davis and A.C. Loos, *The Effects of Cooling Rate on Toughness and Crystallinity in Poly(Ether Ketone Ketone) (PEKK) / G30-500 Composites; Report No. CCMS-97-02 and VPI-E-97-01*, 1997, Center For Composite Materials and Structures, Virginia Polytechnic Institute and State University, Blacksburg, VA 24061.
27. M.F. Hibbs, M.K. Tse, and W.L. Bradley, "Interlaminar Fracture Toughness and Real-Time Fracture Mechanism of some Toughened Graphite / Epoxy Composites," in Toughened Composites, ASTM STP 937, N.J. Johnston, ed., American Society for Testing and Materials, Philadelphia, PA, 1987, pp. 115-130.
28. M.F. Talbott, G.S. Springer, and L.A. Berglund, "The Effects of Crystallinity on the Mechanical Properties of PEEK Polymer and Graphite Fiber Reinforced PEEK," *Journal of Composite Materials*, **21**, 1056-1081 (1987).
29. W.L. Bradley and R.N. Cohen, "Matrix Deformation and Fracture in Graphite-Reinforced Epoxies," in Delamination and Debonding of Materials, ASTM STP 876, W.S. Johnson, ed., American Society for Testing and Materials, Philadelphia, PA, 1985, pp. 389-410.
30. J.M. Whitney, "Experimental Characterization of Delamination Fracture", in Interlaminar Response of Composite Materials, N.J. Pagano, ed., Elsevier Science Publishers, Tarrytown, NY, 1989, pp. 162, 180-184, 213.
31. S. Hashemi, A.J. Kinloch, and J.G. Williams, "The Analysis of Interlaminar Fracture in Uniaxial Fibre-Polymer Composites," *Proceedings of the Royal Society of London*, **A 427**, 173-199 (1990).
32. B. Tan, V. Vasudevan, Y.J. Lee, S. Gardner, R.M. Davis, T. Bullions, A.C. Loos, H. Parvatareddy, D.A. Dillard, J.E. McGrath, and J. Cella, "Design and Characterization of Thermosetting Polyimide Structural Adhesive and Composite Matrix Systems," *Journal of Polymer Science: Part A: Polymer Chemistry*, **35**, 2943-2954 (1997).

Appendix



Chapter 3 - Moisture Sorption Effects on CFR 3kPETU Composites

John M. Jungk must be given a major acknowledgement for this chapter. He did a great deal of the work presented here as a participant in the Summer Undergraduate Research Program sponsored by the National Science Foundation Science and Technology Center for High Performance Polymeric Adhesives and Composites at Virginia Polytechnic Institute and State University.

3.1 Introduction

The previous chapter discussed preliminary research investigating the use of 3kPETU as a composite matrix material. This chapter extends the preliminary research to studying moisture sorption effects on CFR 3kPETU composite properties. To properly design structural aerospace components, not only do the basic mechanical properties of the components' material constituents need to be known, the effects of the service environment on these mechanical properties need to be understood. Moisture is a critical environmental factor that can be damaging to composite properties. Composite components can be constantly absorbing or desorbing moisture due to fluctuations in service temperature and relative humidity. The absorption of moisture can reduce glass transition temperatures and mechanical properties by matrix plasticization, swelling, cracking, and fiber/matrix interface damage [1-5].

The objective of this study was to investigate the effects of moisture sorption on the mechanical properties of 3kPETU/G40-800 carbon fiber composites. In addition to mechanical properties, moisture sorption rates were measured to verify behavior consistent with the Fickian diffusion model per ASTM Test Method for Moisture Absorption Properties and Equilibrium Conditioning of Polymer Matrix Composite Materials (D 5229-92). These measurements also allowed for the determination of the through-the-thickness moisture diffusion coefficient, D_z , and the maximum moisture equilibrium content, M_m . Following both moisture absorption and desorption, composite specimens were tested for retention of transverse flexural strength (TFS) and apparent interlaminar shear strength (AISS).

In addition to measuring material properties, two aspects of the moisture exposure experimental process that may play a role in the observed results are investigated. One aspect is the point at which mechanical test specimens are cut from a consolidated panel:

before or after moisture exposure. The second aspect is the quality of the sealant used on specimen edges to ensure one-dimensional diffusion.

If the specimens are machined prior to moisture exposure, they may fail to meet the 5 g minimum mass specified by ASTM D 5229-92, thus reducing the accuracy of moisture mass measurements. Also, poor edge seals on the specimens may produce error in the determination of the one-dimensional diffusion properties. However, if the specimens are machined before environmental exposure, then no post-conditioning machining is necessary. Elimination of post-conditioning machining allows immediate mechanical testing upon completion of environmental exposure.

The advantages of leaving the panels “as-manufactured” prior to environmental exposure are: easily meeting the minimum specimen mass (D 5229-92) and more accurate representation of a one-dimensional moisture diffusion model even with possible areas of poor sealant (D 5229-92). The major drawback to leaving the panels “as-manufactured” is that the environment can not be controlled while specimens are machined from the panels. Machining creates new surface area for moisture sorption due to exposure to aqueous coolants and an uncontrolled relative humidity during machining.

3.2 Experimental

3.2.1 Composite Manufacture

Carbon fiber tow (G40-800 from Toho Carbon Fibers, Inc.) coated with 3kPETU powder (towpreg) was manufactured utilizing a powder shaking system [6,7]. Square plies were assembled from the towpreg, trimmed, and stacked unidirectionally into a 152.4 mm square mold. Using a hot press, the plies were consolidated into two panels following a consolidation schedule that commenced with a 5 °C/min ramp to 250 °C, followed by a 3 °C/min ramp to 350 °C. The panels then cured for 90 minutes at 350 °C. The consolidation schedule was completed with a -4 °C/min ramp to room temperature. During consolidation, the panels were subjected to a maximum pressure of approximately 1.4 MPa (200 psi). The pressure was applied gradually such that the maximum pressure was reached when the mold temperature was between 150 °C to 200 °C. The resultant panels had thicknesses of 3.25 ± 0.05 mm. In addition to the composite panels, a neat resin plaque was cured. Four specimens were cut from this plaque for neat resin M_m measurements.

3.2.2 Specimen Preparation

3.2.2.1 Sectioning

The two square panels, referred to as Wet and Wet/Dry, were manufactured with edge lengths of 152.4 mm. The title of “Wet” is applied to any specimens that are mechanically tested following moisture absorption. The title of “Wet/Dry” is applied to any specimens that are mechanically tested following both moisture absorption and moisture desorption. Both panels were cut in half with the cut running parallel to the fiber direction producing two rectangular Wet and two rectangular Wet/Dry panels with widths of approximately 75 mm transverse to the fiber direction. One rectangular Wet panel and one rectangular Wet/Dry panel were retained “as-manufactured”, hereafter referred to as Wet(am) and Wet/Dry(am). The rectangular Wet(am) panel had dimensions of: 160 mm x 75.3 mm. The rectangular Wet/Dry(am) panel had dimensions of: 132 mm x 75.3 mm. After isolating the regions of the panels that had the greatest absence of defects determined from ultrasonic inspection, the second pair of rectangular panels were machined into AISS and TFS specimens following specimen dimensions calculated from the ASTM Test Method for Apparent Interlaminar Shear Strength of Parallel Fiber Composites by Short-Beam Method (D 2344-82) and the ASTM Test Method for Flexural Properties of Unreinforced and Reinforced Plastics and Electrical Insulating Materials (D 790-92). Specified dimensions were 19.8 mm x 6.35 mm and 76.2 mm x 12.7 mm for AISS and TFS, respectively. Fourteen AISS and seven TFS specimens were cut from the rectangular Wet panel, and sixteen AISS and seven TFS specimens were cut from the rectangular Wet/Dry panel.

3.2.2.2 As-Manufactured Dimensions

Prior to any environmental conditioning, the dimensions and masses of the machined specimens and the remaining rectangular as-manufactured panels were recorded. All thicknesses were measured with an anvil-faced micrometer and widths and lengths were measured with a caliper. The thicknesses of the Wet(am) and the Wet/Dry(am) panels were measured at fourteen points along their edges. The widths and thicknesses of the TFS specimens were measured at five locations along the length of the specimens. The widths and thicknesses of the AISS specimens were measured at both ends of the specimens.

3.2.2.3 Drying

Prior to sealing, all specimens were placed in a vacuum oven at 90 °C under a vacuum of approximately 95 kPa to bring the specimens to an equilibrium baseline moisture content.

After Wet(am) and Wet/Dry(am) reached a stable mass (163 hours), all specimens were removed from the vacuum oven and weighed.

3.2.2.4 Sealant Application

To achieve one-dimensional, through-the-thickness diffusion, a sealant was needed to block moisture diffusion into specimen edges. Two different sealants were chosen for this purpose. A GC Electronics insulating varnish was applied to half the specimens, and a stainless steel foil tape was used on the remaining specimens. The edges of the Wet(am) panel were sealed with the varnish, while the edges of the Wet/Dry(am) panel were sealed with the foil tape. The specimens to be mechanically tested as controls (no moisture exposure) were not sealed; four TFS and ten AISS specimens were reserved for control measurements. Once the insulating varnish had dried, all sealed specimens were weighed to determine the mass of applied sealant.

Sealant control specimens were also prepared. The purpose of these specimens was to monitor fractional mass gain or loss by the sealants such that appropriate corrections could be made to mass measurements of the sealed composite specimens. The set of sealant controls consisted of eight aluminum sheets with dimensions of 63 mm x 45 mm x 280 μm . Three sheets were coated on one side with the insulating varnish over an area of 50 mm x 32 mm. The same area was covered on three more sheets with the foil tape. The remaining two sheets were left untreated. As with the composite specimens, the coated sheets were weighed for the mass of applied sealant.

3.2.3 Moisture Absorption

After the composite specimens were machined, dried, and sealed, they, along with unsealed neat resin specimens, were placed into a temperature/humidity (T/H) chamber (Blue M Model FRS-13C) at 85% relative humidity (RH) and 90 °C. This temperature was chosen to increase the moisture uptake rate and decrease the time required to reach M_m while avoiding a steam environment. The relative humidity was chosen per ASTM D 5229-92: “a worst case aircraft service water vapor environment is generally considered to be 85% relative humidity.” To record moisture uptake, the panels and specimens were periodically removed from the T/H chamber; allowed to cool in a sealed, humid environment; weighed; and then quickly returned to the T/H chamber. The panels were determined to have reached M_m when the percent moisture uptake changed less than 0.01% by mass in 168 hours (7 days).

Upon reaching M_m , the specimens were removed from the T/H chamber to begin the next stages of the experiment. Five TFS and ten AISS non-control specimens cut from the Wet panel prior to vacuum drying were mechanically tested immediately following removal from the T/H chamber, weighing, and dimension measurements; these specimens are referred to as the Pre-Cut Wet specimens. Upon removal from the T/H chamber, the Wet(am) panel was weighed and measured for thickness. This rectangular panel was then machined into AISS and TFS specimens with specified dimensions identical to the control specimens; these specimens are referred to as the Post-Cut Wet specimens. Except during machining, the Wet(am) panel and the resultant Post-Cut Wet specimens were kept in an airtight, damp bag prior to mechanical testing to maintain the moisture content in the composite. Machining involved cutting the specimens from the panel with a water cooled saw and then grinding under a water/coolant mixture. The specimens were rinsed with tap water and returned to the damp, airtight bags when machining was complete. Mechanical testing was completed within ninety-six hours of removing the Wet (am) panel from the T/H chamber.

The Wet/Dry(am) panel and the remaining non-control specimens cut from the Wet/Dry panel prior to vacuum drying (Pre-Cut Wet/Dry specimens) were weighed and measured for thickness; the presence of sealants precluded the measurement of width and length. These composite samples were then placed in a 90 °C convection oven along with the neat resin samples and the sealant controls, which were weighed prior to the transfer.

3.2.4 Moisture Desorption

Moisture desorption took place in a Blue M Inert Gas Furnace convection oven (model IGF-6680G-MP) at 90 °C and ambient relative humidity. The relative humidity in the laboratory was not consistently monitored, but random measurements placed the relative humidity at about 50% at 23.5 °C. These conditions translate to a relative humidity of approximately 2% at 90 °C. The temperature of 90 °C was chosen to maintain consistency such that the absorption and desorption rates could be compared. Moisture desorption was monitored by periodically removing the Wet/Dry(am) panel and the specimens from the oven; allowing them to cool in a sealed, dry environment; weighing; and then quickly returning them to the oven. Specimens were determined to have reached effective moisture equilibrium when the percent moisture content changed less than 0.01% by mass in 168 hours (7 days). Upon removal from the convection oven, the masses and dimensions of the Wet/Dry Pre-Cut specimens were measured along with the mass of the Wet/Dry(am) panel.

Machining of the Post-Cut Wet/Dry specimens exposed the material to the same elements as described in machining of the Post-Cut Wet specimens. The Wet/Dry(am) panel and Pre-Cut Wet/Dry specimens were stored in an airtight bag along with desiccant (Drierite) for sixty-three days awaiting machining and mechanical testing of the AISS and TFS specimens, which were cut with specified dimensions identical to the control specimens; these specimens are referred to as the Post-Cut Wet/Dry specimens. No discoloration of the desiccant took place during the sixty-three days between removal from the oven and mechanical testing, indicating the specimens were kept in a moisture-free environment except for specimen machining.

3.2.5 Mechanical Testing

3.2.5.1 Controls

While the Pre-Cut Wet, Pre-Cut Wet/Dry specimens, and as-manufactured panels were undergoing moisture exposure, the ten AISS (four from the Wet panel and six from the Wet/Dry panel) and four TFS (two from each panel) control specimens were tested. These control specimens remained in the 90 °C vacuum oven until testing, which occurred less than ninety hours after the other specimens had been transferred to the T/H chamber. Since the specimen masses had reached equilibrium, the additional ninety hours should have no significant effect on the results.

The AISS specimens were tested according to ASTM D 2344-84 for flat laminates using an Instron™ with a 50 kN load cell. Specimens were loaded via a three-point bend fixture with a support span of 13.2 mm. The span-to-thickness ratio was approximately 4:1, the loading nose diameter was 6.35 mm, and the crosshead speed was 1.3 mm/min. The TFS specimens were tested according to ASTM D 790-92 following the four-point bend method with the load span equal to one-third of the support span (Test Method II - Procedure A). Using the same Instron™ and 50 kN load cell, a four-point bend fixture was used with a load span of 17.8 mm and a support span of 53.4 mm. The span-to-thickness ratio was 16:1, the loading nose diameter was 12.7 mm, and the crosshead speed was 1.6 mm/min.

3.2.5.2 Wet

Mechanical testing of the Pre-Cut Wet and Post-Cut Wet specimens at maximum moisture equilibrium content followed the same conditions as those used with the control specimens, except the AISS specimens were tested using a 5 kN load cell rather than the 50 kN load cell to improve measurement resolution. Upon removal from the T/H chamber, the varnish

on the varnish-sealed Pre-Cut Wet specimens was removed with acetone, and the foil tape was peeled off the tape-sealed Pre-Cut Wet specimens; residual tape adhesive was removed with acetone. The Pre-Cut Wet specimens were then immediately tested such that testing was completed within three hours of removal from the T/H chamber. Testing of the Post-Cut Wet specimens was delayed by the need to machine the specimens from the Wet(am) panel. The specimens were cut from the Wet(am) panel within twenty-four hours of removal from the T/H chamber. Mechanical testing was completed within ninety-six hours of removal from the T/H chamber.

3.2.5.3 Wet/Dry

Mechanical testing of the Pre-Cut Wet/Dry and Post-Cut Wet/Dry specimens at effective moisture equilibrium content followed slightly different testing conditions than the controls and Wet specimens due to the Wet/Dry panel being slightly thicker than the Wet panel (Table 3.1). The AISS specimens were tested using a 5 kN load cell and a support span of 12.7 mm giving a span-to-thickness ratio of approximately 4:1. A crosshead speed of 1.3 mm/min was used (D 2344-84). Transverse flexural testing was done with a load span of 17.1 mm and a support span of 53.4 mm giving a span-to-thickness ratio of 16:1. The crosshead speed was 1.52 mm/min (D 790-92).

Table 3.1. Composite Physical Properties

Panel	Thickness (mm) ^(a)	Density (g/cm ³) ^(b)	v_f (%)
Wet	3.25 ± 0.05	1.56 ± 0.01	61.3 ± 0.5
Wet/Dry	3.25 ± 0.05	1.57 ± 0.01	62.1 ± 0.6

a. measured along edges of 152.4 mm square panel

b. ± standard deviation

3.2.6 Density, Void Content, and Fiber Volume Fraction

The densities of composite specimens were determined via the ASTM Test Method for Density and Specific Gravity (Relative Density) of Plastics by Displacement (D 792-91) using 23.5 °C distilled water as the immersion fluid. Three or four density specimens were taken from each TFS control specimen to determine the average composite density. Knowing the composite, fiber [8], and resin [6] densities, the volume fractions of fiber, resin, and void were calculated given two assumptions. The first assumption was that the mass of fiber in the composite was known (i.e., there is no fiber loss during manufacture). The second assumption is that the gas in any voids has the density of air, 1.29 x 10⁻³ g/cm³.

3.3 Results And Discussion

3.3.1 Composite Consolidation And Physical Properties

Ultrasonic imaging revealed that both panels had two opposing corners in which there was poor consolidation. Specimens were cut from the panels such that the presence of these poorly consolidated regions in the load bearing area of specimens was minimized. The poor consolidation was verified with optical microscopy. Outside of these regions, good consolidation was achieved; optical microscopy revealed low void content and some resin rich regions. Calculation of the void volume fractions in the composites utilized Equation 3.1:

$$\rho_c = \rho_r v_r + \rho_f v_f + \rho_a v_a \quad (3.1)$$

where:

ρ = density;

v = volume fraction;

r = resin;

f = fiber; and

a = void.

The composite and resin densities were determined experimentally (D 792-91) and composite densities are reported for both Wet and Wet/Dry panels in Table 3.1; the density of 3kPETU is 1.28 g/cm³ [6]. Using the assumption that the gas filling the voids has the density of air leaves the volume fractions as the only unknowns. The assumption of no fiber loss during manufacture provides the fiber mass and volume; combining this information with an experimentally determined composite volume allows for the estimation of v_f . Knowing that the three volume fractions must sum to one, along with Equation 3.1, provides two equations for the two unknown volume fractions. Thus v_a and v_r may be estimated. Following this procedure, the void volume percent in both panels was estimated to be less than 1.8%.

3.3.2 Composite Moisture Absorption

The average composite moisture uptake data for the two as-manufactured rectangular panels and the TFS specimens are shown in Figure 3.1. Due to a misjudgement of the initial moisture uptake rate, no measurements were taken in what appears to have been the linear region of moisture absorption. Thus, only M_m may be evaluated for this data and no conclusion regarding Fickian behavior may be made. The M_m values in Figure 3.1 are averages of all measurements taken at times greater than 400 hours (20 hours^{1/2}). The

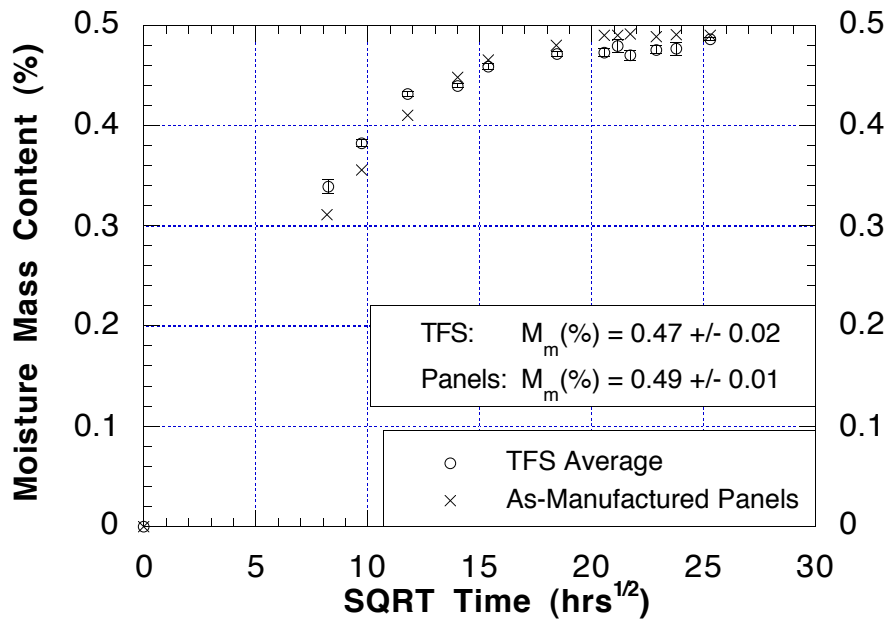


Figure 3.1.(a) Composite Moisture Absorption

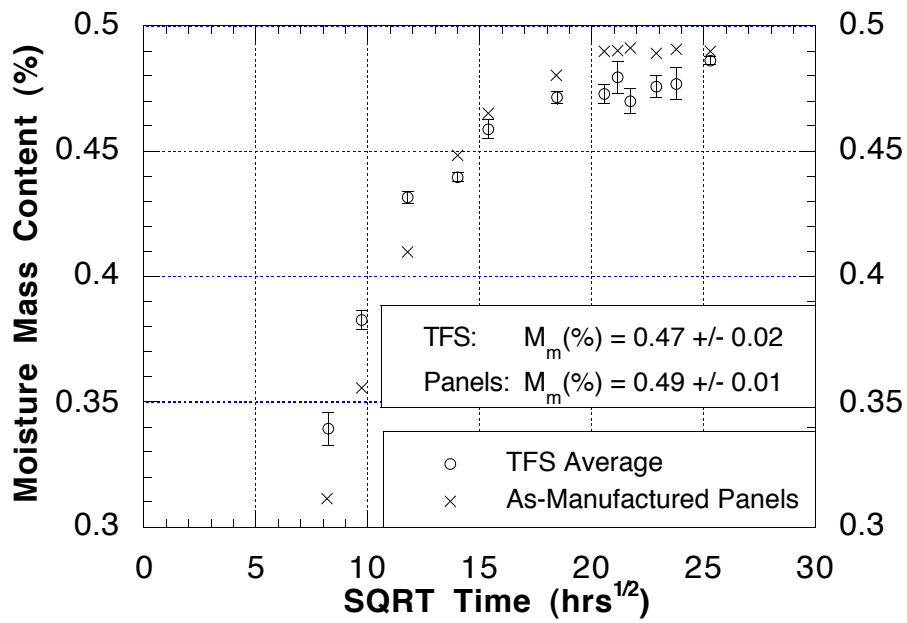


Figure 3.1.(b) Composite Moisture Absorption

slightly higher M_m for the panels may be due to the better overall consolidation of the TFS specimens versus the panels; the TFS specimens were cut from well-consolidated regions, whereas, the panels include edge areas that are not as well consolidated and contain more void volume for moisture to occupy.

3.3.3 Neat Resin Moisture Sorption

The M_m value for 3kPETU neat resin was measured to be $1.44 \pm 0.02\%$. This average value was calculated from all measurements on four specimens over the same time range that composite M_m measurements were taken. Utilizing the average resin mass fraction (0.29) of the as-manufactured composite panels, a M_m value of approximately 0.42% is estimated for the composite panels; slightly less than that actually measured (Figure 3.1). The average resin mass fraction was determined from the known mass of carbon fiber placed into the molds prior to consolidation and the composite panel masses measured following consolidation. The additional moisture uptake by the composites could easily reside in voids or surface porosity.

Following 960 hours at 90 °C and 2% RH in the convection oven, the neat resin moisture content was reduced to $0.051 \pm 0.010\%$. Again, using the resin mass fraction of the as-manufactured composite panels, a composite moisture content of approximately 0.015% is estimated for 90 °C and 2% RH.

3.3.4 Composite Moisture Desorption

Figure 3.2.(a) shows the moisture desorption data for the Wet/Dry(am) panel and the average data for the five Wet/Dry TFS specimens. The value of D_z may be calculated from the desorption data since data was obtained in the linear region; moisture desorption demonstrated behavior consistent with Fickian diffusion. Using the slope of the linear region and M_m (at 90 °C and 85% RH), D_z was determined for the composite specimens utilizing Equation 3.2. The second term in brackets is equivalent to the slope of the linear region.

The value of D_z (3.8×10^{-6} mm²/s) for the Wet/Dry(am) panel was calculated from the linear fit shown in Figure 3.2.(a). The linear fit of the TFS specimen average demonstrates the range of data fitted in Figure 3.2.(b). The data for each TFS specimen was fit individually, from which a value of D_z was calculated for each specimen. These five values

of D_z were used to calculate the average D_z for the TFS specimens: $5.9 \times 10^{-6} \pm 0.6 \times 10^{-6}$ mm²/sec.

$$D_z = \pi \left(\frac{h}{4M_m} \right)^2 \left(\frac{M_2 - M_1}{\sqrt{t_2} - \sqrt{t_1}} \right)^2 \quad (3.2)$$

where:

h = panel thickness (mm);

M_m = maximum moisture equilibrium content (%);

$M_{1,2}$ = moisture content at time, t (%); and

$t_{1,2}$ = time sample points (s).

The value of D_z for the TFS specimens was about 35% greater than D_z measured for the Wet/Dry(am) panel. Though D_z could not be calculated for moisture uptake, it is evident in Figure 3.1 that the moisture sorption rate was higher in the TFS specimens than the as-manufactured panels prior to 196 hours (14 hours^{1/2}). This observation is in agreement with Figure 3.2.(a). Therefore, the difference in size between mechanical test specimens and larger panels does appear relevant in selecting specimens for moisture sorption studies. However this size difference does not appear to influence the ultimate values of equilibrium moisture content as seen in Figures 3.1.(b) and 3.2.(a). The composite values for equilibrium moisture content at 2% RH are listed in Figure 3.2.(a); the actual composite values are slightly less than those predicted by the neat resin results.

3.3.5 Discrepancies in Moisture Sorption Results

Unexpectedly, the composite specimens took on more moisture than predicted by neat resin specimens at 85% RH and lost more moisture than predicted by neat resin specimens at 2% RH. Additional moisture uptake by the composites can easily be rationalized by additional moisture residing in surface porosity, voids, or even between overlapping edges of the stainless steel foil tape. However, the negative composite moisture content at 2% RH can not be explained away so easily. Any loss of sealant in the 90 °C / 2% RH conditions should have been seen in the sealant controls. However, there is the possibility the insulating varnish and foil tape adhesive bonded better with the aluminum controls than with the cut composite surfaces, and thus more control sealant than composite sealant survived the harsh 90 °C / 2% RH conditions. The lack of damage, which will be discussed later, to the composites suggests that this extra mass loss is not a result of degradation products.

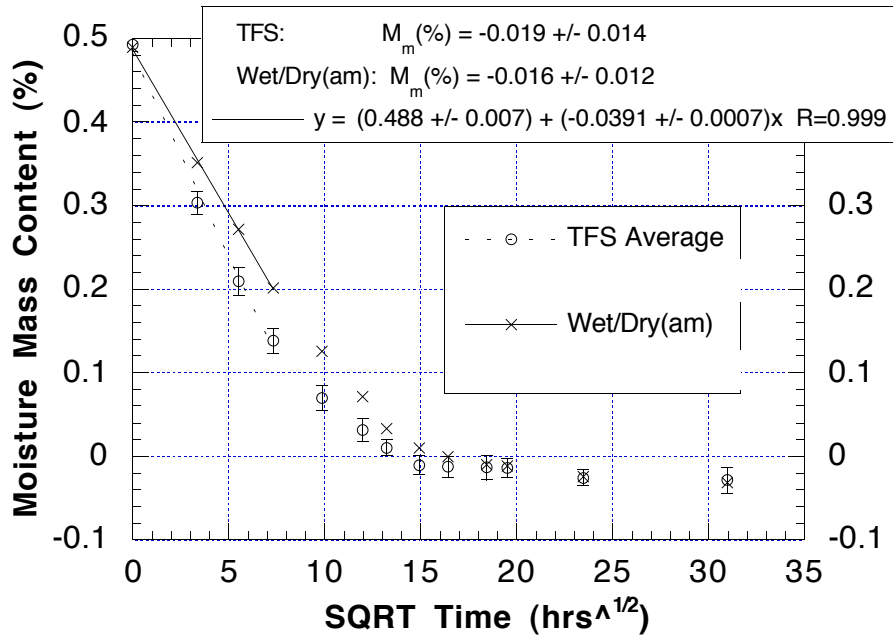


Figure 3.2.(a) Composite Moisture Desorption

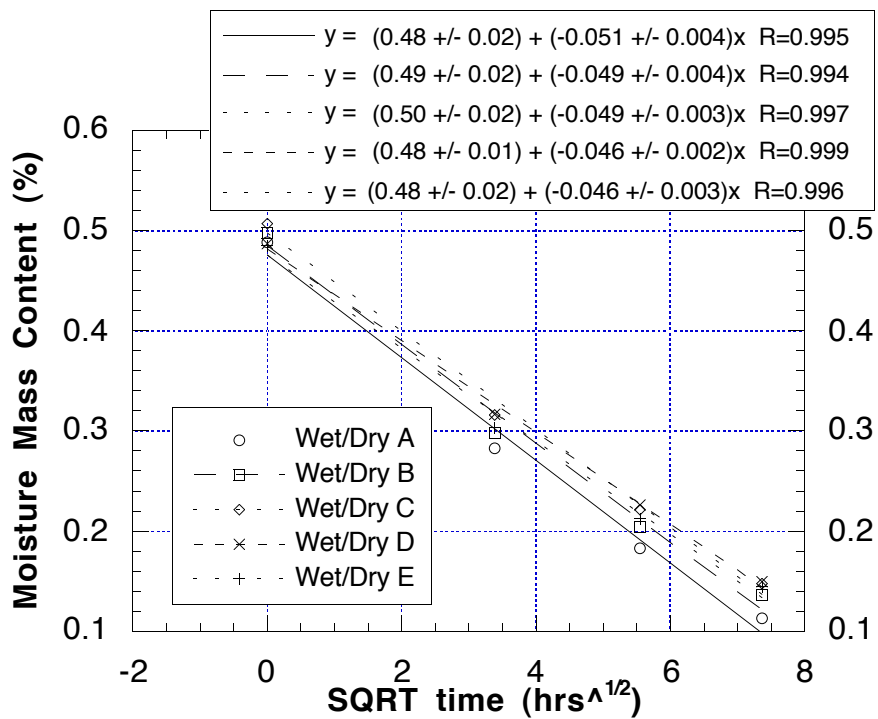


Figure 3.2.(b) Linear Fit of TFS Specimen Moisture Desorption

Another discrepancy in moisture sorption measurements was that moisture absorbed into and desorbed out of the TFS specimens faster than with the rectangular panels. Because the specimens and panels had the same thickness, their surface area-to-volume ratios were the same, thus this ratio would not be a factor. The most likely explanation appears to be that the sealants did not completely block moisture diffusion into and out of the composite edges; the sealants will be addressed again later. Moisture diffusion at the edges would have a much greater impact on TFS specimens than on the panels due to the difference in the exposed surface area-to-sealed surface area ratios.

Despite these discrepancies in measurements, 3kPETU/G40-800 was found to have a moisture diffusion coefficient and maximum moisture equilibrium content comparable with other fiber-reinforced polymer matrix composite materials (Table 3.2).

Table 3.2. Moisture Sorption Property Comparisons

Material	v_f (%)	D_z (mm ² /s) ^(a)	M_m (%) ^(b)	Reference
3kPETU G40-800	61	$5.0 \times 10^{-6} \pm 1.0 \times 10^{-6}$	0.48 ± 0.02 ^(c)	---
BMI5292 IM7	NR	6.06×10^{-6} (30 °C)	1.25 (90% R.H.)	9
Avimid K3B IM7	62	2.08×10^{-6}	0.42	3
3501-5 AS	65	9.29×10^{-7}	1.62	10

a. at 90 °C unless specified

b. at 85 % R.H. unless specified

c. for all TFS specimens and as-manufactured panels

3.3.6 Moisture Induced Strain

Moisture induced strain, ϵ_M , calculations are based on thickness measurements since the use of edge sealants prohibited accurate measurements of width and length during the course of environmental conditioning. Unfortunately, thickness measurements were not taken immediately following vacuum drying. Therefore, strain calculations based on the thicknesses of the vacuum dried specimens were not possible. Thickness measurements were done on various specimens following different stages of environmental conditioning as discussed in the experimental section. These thickness measurements were used to calculate the ϵ_M results presented in Table 3.3. Three variations are reported: 85% RH vs. as-manufactured, 85% RH vs. 2% RH, and as-manufactured vs. 2% RH. The first variation compares the thicknesses following 85% RH and prior to any environmental conditioning. The second variation compares the thicknesses following 85% RH and

following 2% RH. The third variation compares the thicknesses prior to any environmental exposure and following 2% RH. There are a few cases where increased moisture content apparently reduced the specimen thickness; it is expected there was error or inconsistency in these measurements.

Table 3.3. Moisture Induced Strain - Variations of Increased Moisture Content

Specimen Group	85% RH vs. as-manufactured	85% RH vs. 2% RH	as-manufactured vs. 2% RH
Wet TFS	$4.3 \times 10^{-4} \pm 0.5 \times 10^{-4}$	Not Available	Not Available
Wet/Dry TFS	$7.7 \times 10^{-4} \pm 0.8 \times 10^{-4}$	$9.9 \times 10^{-4} \pm 0.7 \times 10^{-4}$	$2.2 \times 10^{-4} \pm 0.5 \times 10^{-4}$
All TFS	$6.0 \times 10^{-4} \pm 0.7 \times 10^{-4}$	Not Available	Not Available
Wet(am)	$-6.7 \times 10^{-4} \pm 1.0 \times 10^{-4}$	Not Available	Not Available
Wet/Dry(am)	$4.5 \times 10^{-4} \pm 0.5 \times 10^{-4}$	Not Available	Not Available
Wet(am) & Wet/Dry(am)	$-1.1 \times 10^{-4} \pm 1.0 \times 10^{-4}$	Not Available	Not Available
Wet AISS	$7.4 \times 10^{-4} \pm 0.8 \times 10^{-4}$	Not Available	Not Available
Wet/Dry AISS	Not Available	Not Available	$-2.3 \times 10^{-4} \pm 1.0 \times 10^{-4}$

The moisture expansion coefficients (MEC) for these specimens may be calculated using the ϵ_M values in Table 3.3 and the equilibrium moisture contents following exposure to the different environments. The MEC is calculated by dividing ϵ_M by the change in the percent moisture content. Moisture expansion coefficients were calculated for those specimen groups that displayed positive moisture induced strains (Table 3.4). The average MEC was calculated to be: 0.0017 ± 0.0005 (1 / % moisture). Table 3.5 contains moisture expansion coefficients reported in the literature for other fiber-reinforced polymeric composites. The moisture expansion coefficients of the 3kPETU composites lie in the lower range of those values listed in Table 3.5. It is expected that the MEC for 3kPETU composites would be even lower if the resin rich molded surfaces were taken into account.

Table 3.4. 3kPETU Composite Moisture Expansion Coefficients (MEC)

Specimen Group	Environment Change	MEC (1 / % moisture)
Wet TFS	as-manufactured to 85% RH	0.0014
Wet/Dry TFS	as-manufactured to 85% RH	0.0023
Wet/Dry TFS	2% RH to 85% RH	0.0019
Wet/Dry(am)	as-manufactured to 85% RH	0.0013

Table 3.5. Transverse Moisture Expansion Coefficients from Literature

Material	MEC (1 / % moisture)	Reference
Boron / Epoxy	0.00168	11
Boron / Polyimide	0.00168	11
Thornel 300 / Epoxy	0.00129	11
Kevlar 49 / Epoxy	0.00151	11
Graphite AS / Epoxy	0.00129	11
Carbon / Epoxy	0.003	12
AS4 / Epoxy 3501-6	0.0022	13
Carbon PMR15	0.00104 ^(a)	14

a. average of six measurements over $M_m = 0.17$ to $M_m = 0.49$

3.3.7 Sealants

On the sealant control specimens, the insulating varnish lost approximately 17% mass over the duration of the 85% RH moisture exposure; an additional 2.5% was lost during 2% RH desorption conditions. The mass of the stainless steel foil tape remained more constant. The tape lost about 0.6% mass during 85% RH moisture exposure followed by an equivalent loss during 2% RH desorption conditions.

Inspection of sealed edges revealed no observable damage, such as microcracks in the matrix or along the fiber/matrix interface (Figure 3.3). Foil and varnish sealed specimens were inspected, as were mechanical property control specimens. The lack of a visual difference between control specimens and exposed specimens is inconclusive evidence to determine whether the sealants were adequate. Moisture may have still passed through and/or around the sealants and diffused through the matrix without causing any observable damage as seen in Figure 3.4, where no visual damage is evident at exposed surfaces. The possibility of moisture passing through or bypassing the edge sealants was previously discussed amongst the discrepancies seen in the moisture sorption results.

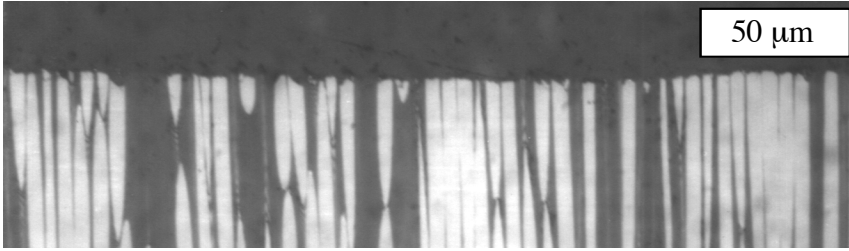


Figure 3.3. Optical Micrograph of Composite Cross Section - Varnish Sealed Surface

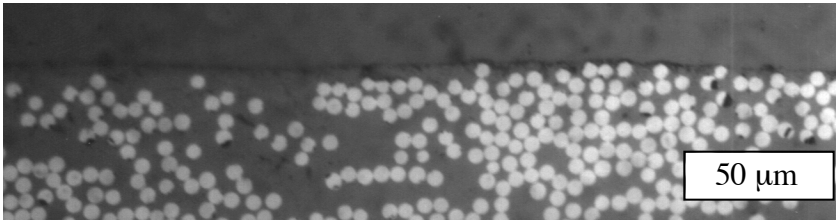


Figure 3.4.(a) Control

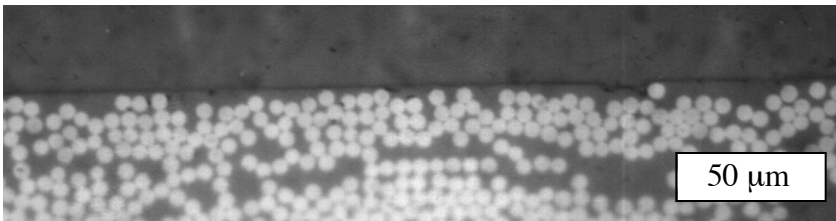


Figure 3.4.(b) Wet

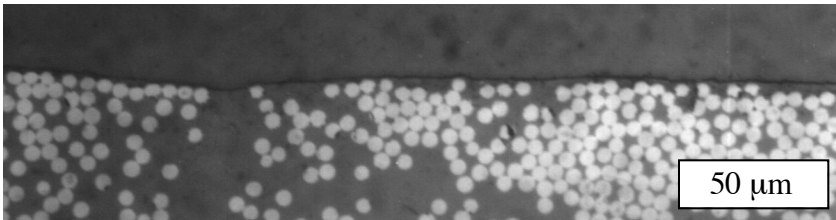


Figure 3.4.(c) Wet/Dry

Figure 3.4. Optical Micrographs of Composite Cross Sections - Exposed Molded Surfaces

3.3.8 Mechanical Property Retention

The effects of moisture absorption and desorption on the mechanical properties of carbon fiber-reinforced 3kPETU were measured via transverse flexural properties and AISS. The results of these tests following exposure are given in Figure 3.5. The absorption of 0.47% by mass of moisture appears to reduce the AISS of the composite, but does not have a

statistically significant effect on the TFS and TF modulus. The TF modulus was calculated using the equation given in ASTM D 790-92 for tangent modulus of elasticity.

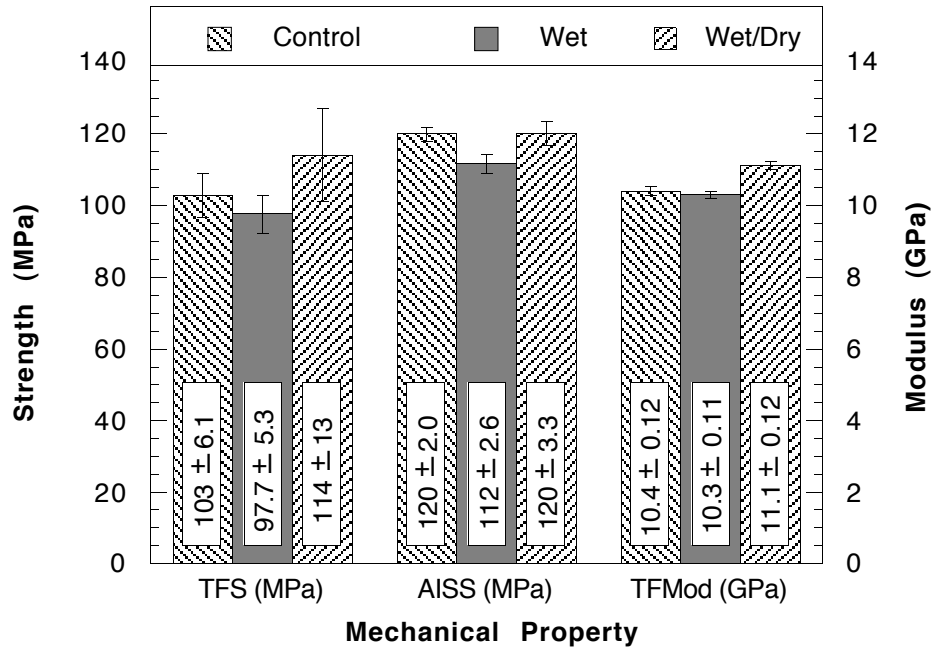


Figure 3.5. Summary of Mechanical Property Results

Two likely causes of this reduction in AISS are matrix plasticization and microcracking. As shown in Figure 3.4, optical microscopy did not reveal cracks within the matrix. Furthermore, cracking during moisture absorption often results in a second moisture saturation level [3]. Figure 3.1 shows that a relatively constant moisture content is seen for 215 hours after reaching M_m ; no indication of an increase in moisture saturation level is seen. Mechanical property tests following desorption further dispute the presence of microcracking, therefore, the reduction in AISS is attributed to plasticization of the matrix. As moisture is absorbed into the matrix, van der Waals bonds between neighboring polymer chains are disrupted [4]. The disruption of bonds between chains allows them to more easily pass by one another, thus diminishing their ability to distribute load throughout the matrix and to the fibers; ultimately, composite properties such as modulus and yield stress are reduced [3,15].

The results of the mechanical property retention tests following desorption reinforce plasticization as the source of property changes. Again, large standard deviation in the TFS

results prohibit statistical conclusions. The AISS results show a recovery to the control value, and the TF modulus results show an increase following moisture desorption.

The recovery of pre-exposure properties indicates that the loss of moisture has allowed van der Waals bonds to be reestablished, thus returning the matrix to its pre-exposure mechanical properties. Furthermore, recovery of pre-exposure properties disputes the presence of permanent, unrecoverable damage, such as microcracking [3].

The increase seen in the TF modulus may be attributable to physical aging. Moisture desorption took place over 40 days at 90 °C. This elevated temperature may have increased the rate of physical aging enough to significantly effect the mechanical properties of the matrix during the 66 total days of moisture exposure (26 days of moisture absorption plus 40 days of moisture desorption). The elevated temperature increases chain mobility, thus increasing the rate at which molecules can move to their equilibrium positions. However, 90 °C may not be close enough to the glass transition temperature (approximately 250 °C) to result in physical aging. Though, the elevated moisture content within the material during a portion of the moisture exposure improves chain mobility via plasticization. Together, the elevated temperature and moisture content may have resulted in physical aging that ultimately reduced chain mobility, which would increase modulus and yield strength. Additional cure of the matrix is also a possible contributor to the modulus increase. The lack of an increase in modulus and yield stress following moisture absorption can be explained by the presence of plasticizing moisture that predominates over any physical aging or additional cure .

3.3.9 Pre-Cut Versus Post-Cut

Cutting specimens prior to, or after moisture exposure has no apparent effect on measured mechanical properties (Table 3.6 and Figure 3.6). Apparently, the time the Post-Cut specimens spent in the uncontrolled machine shop environment was not critical to the material properties.

Furthermore, despite the fact that the TFS specimens were slightly less than 5 g (4.89 g on average), M_m ($0.47 \pm 0.02\%$) for the TFS specimens agreed well with that of the larger rectangular panels ($0.49 \pm 0.01\%$). However, a higher value of D_z was measured with the TFS specimens ($5.9 \times 10^{-6} \pm 0.6 \times 10^{-6} \text{ mm}^2/\text{s}$) than for the Wet/Dry(am) panel ($3.8 \times 10^{-6} \text{ mm}^2/\text{s}$). Therefore, it may be satisfactory to pre-cut mechanical test specimens, but D_z measurements should be based on larger traveler coupons. The error in D_z may be a result

of the fact that mass changes in the sealants play a larger role in the overall specimen mass. Even though sealant controls were used, differences in the sealant controls and actual sealants would be more pronounced in the smaller, lighter, TFS specimens. The error may also be due to moisture entering along the specimen edges; edge diffusion would artificially increase D_c . As the exposed surface area is reduced (e.g., from rectangular panels to TF specimens), edge diffusion would introduce greater error.

3.4 Conclusion

Mechanical property retention for this material appears to be independent of the moisture exposure procedure; no statistical difference in percent strength retention of the Pre-Cut and Post-Cut specimens was observed. In addition, the investigation and comparison of the insulating varnish and stainless steel foil tape as edge sealants were inconclusive in determining if the sealants provided an adequate barrier to moisture diffusion. For future experiments, the stainless steel foil tape is recommended over the insulating varnish for three reasons. First, the mass change in the foil tape during moisture sorption was dramatically smaller than that for the insulating varnish. The much smaller change in sealant mass provides less chance for error in sealant corrections. Second, the foil tape is easier to apply and remove. Third, the insulating varnish can easily be scratched or otherwise damaged such that an unknown sealant mass is lost, and the barrier to moisture diffusion is compromised.

The 3kPETU/G40-800 composite displayed good mechanical property retention following moisture absorption to its maximum moisture equilibrium content ($0.48 \pm 0.02\%$). Furthermore, upon moisture desorption to the 2% RH effective moisture equilibrium content, the mechanical properties either recovered to or actually exceeded their original values. The full recovery of mechanical properties suggests the reduction in mechanical properties at maximum moisture equilibrium content was due to plasticization by absorbed moisture.

In summary, moisture sorption in the 3kPETU/G40-800 composite followed Fickian behavior, and the composite displayed moisture sorption properties similar to other fiber-reinforced polymer matrix composites. The composite demonstrated good mechanical property retention following moisture absorption with recoverable matrix plasticization being the source of mechanical property reductions.

Table 3.6. Mechanical Property Results

Condition	Transverse Flexural Strength (MPa) ^(a) [% Retention] ^(b)	Transverse Flexural Modulus (GPa) ^(a) [% Retention] ^(b)	Apparent Interlaminar Shear Strength (MPa) ^(a) [% Retention] ^(b)
Control	103 ± 6	10.4 ± 0.1	120 ± 2
Wet Pre-Cut	99.0 ± 4.0 [96.1 ± 3.8]	10.3 ± 0.1 [99.1 ± 0.4]	112 ± 3 [93.7 ± 2.8]
Wet Post-Cut	96.7 ± 6.3 [93.9 ± 6.1]	10.3 ± 0.2 [99.0 ± 1.4]	111 ± 2 [92.8 ± 1.3]
Wet All	97.7 ± 5.3 [94.9 ± 5.1]	10.3 ± 0.1 [99.0 ± 1.1]	112 ± 3 [93.2 ± 2.2]
Dry Pre-Cut	109 ± 11 [106 ± 11]	11.1 ± 0.1 [107 ± 1]	120 ± 4 [100 ± 4]
Dry Post-Cut	119 ± 14 [116 ± 13]	11.1 ± 0.1 [107 ± 1]	121 ± 2 [100 ± 1]
Dry All	114 ± 13 [111 ± 13]	11.1 ± 0.1 [107 ± 1]	120 ± 3 [100 ± 3]

a. ± standard deviation

b. % retention based on mean values

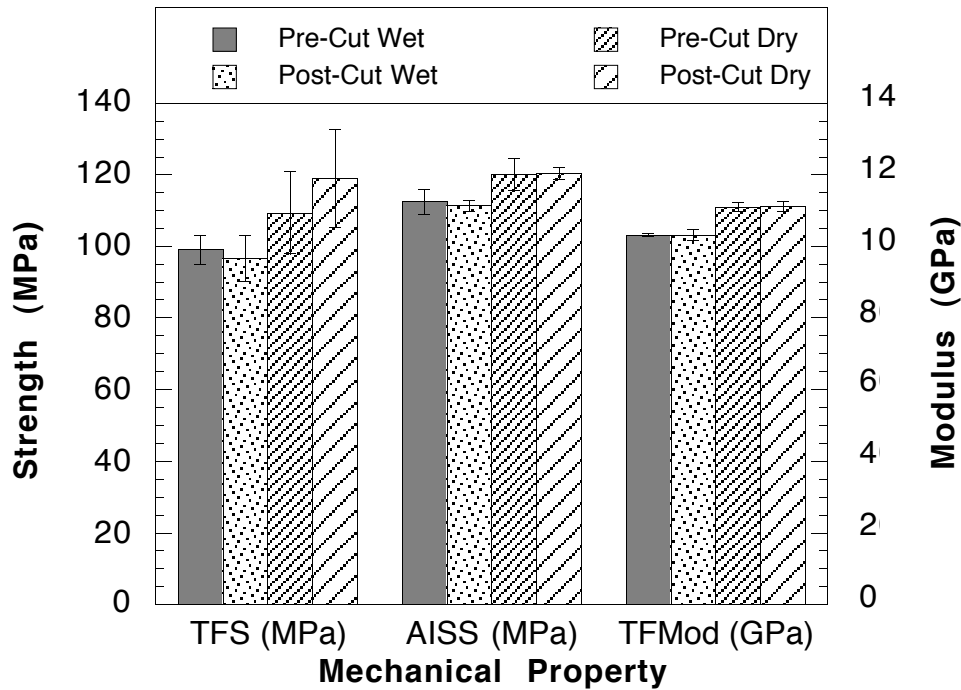


Figure 3.6. Pre-Cut Versus Post-Cut Mechanical Property Results

3.5 References

1. R.B. Pipes, J.R. Vinson, and T.W. Chou, "On the Hygrothermal Response of Laminated Composite Systems," *Journal of Composite Materials*, **10**, 129-148 (1976).
2. C.H. Shen and G.S. Springer, "Moisture Absorption and Desorption of Composite Materials," *Journal of Composite Materials*, **10**, 2-20 (1976).
3. M.R. Van Landingham, R.F. Edulje, and J.W. Gillespie, Jr., "The Effects of Moisture on the Material Properties and Behavior of Thermoplastic Polyimide Composites," in High Temperature and Environmental Effects on Polymeric Composites, Vol. 2, ASTM STP 1302, T.S. Gates and A.H. Zureick, eds., American Society for Testing and Materials, Philadelphia, 1997, pp. 50-63.
4. D. Cornelia, "Hygrothermal Performance of Polyimides," *Proceedings of the 39th International SAMPE Symposium and Exhibition*, 917-929 (1994).
5. B.A. Pratt and W.L. Bradley, "Effect of Moisture on the Interfacial Shear Strength: A Study Using the Single Fiber Fragmentation Test," in High Temperature and Environmental Effects on Polymeric Composites, Vol. 2, ASTM STP 1302, T.S. Gates and A.H. Zureick, eds., American Society for Testing and Materials, Philadelphia, 1997, pp. 64-72.
6. T.A. Bullions, R. Mehta, B. Tan, J.E. McGrath, and A.C. Loos, "Manufacture and Mechanical Properties of a High-Performance Thermosetting Poly(etherimide) / Continuous Carbon Fiber Composite," *Proceedings of the 29th International SAMPE Technical Conference*, 85-97 (1997).
7. R.A. Bucher and A.C. Loos, "High Performance Thermoplastic Matrix Composite Processing: Dry Powder Prepregging, Plasma Treatment, Consolidation / Crystallization Analysis," Report No. CCMS-95-02 and VPI-E-94-10, Center For Composite Materials and Structures (0257), Virginia Polytechnic Institute and State University, Blacksburg, VA 24061 (1994).
8. Toho Carbon Fibers, Inc., *Material Brochure*, 444 High Street, Suite 200, Palo Alto, CA 94301.
9. E.E. Shin, R.J. Morgan, M. Wilenski, J. Zhou, J. Lincoln, and L.T. Drzal, "The Structure Property Relations of Bismaleimide Composite Matrices and Durability of High Temperature Polymer Matrix Composites," *Proceedings of the 28th International SAMPE Technical Conference*, 225-235 (1996).
10. A.C. Loos and G.S. Springer, "Moisture Absorption of Graphite-Epoxy Composition Immersed in Liquids and Humid Air," in Environmental Effects on Composite Materials, G.S. Springer, ed., Technomic Publishing, Inc., Westport, CT, 1981, pp. 34-50.
11. C.C. Chamis and J.H. Sinclair, "Prediction of Composite Hygral Behavior Made Simple," *SAMPE Quarterly*, **14**, (1), 30-39 (1982).
12. T.A. Collings and D.E.W. Stone, "Hygrothermal Effects in CFRP Laminates: Strains Induced by Temperature and Moisture," *Composites*, **16**, (4), 307-316 (1985).

13. S.J. Hooper, R. Subramanian, R.F. Toubia, "Effects of Moisture Absorption on Edge Delamination, Part II: An Experimental Study of Jet Fuel Absorption on Graphite Epoxy," in Composite Materials: Fatigue and Fracture, Vol. 3, ASTM STP 1110, T.K. O'Brien, ed., American Society for Testing and Materials, Philadelphia, 1991, pp. 107-125.
14. P.M. Jacobs, M. Simpson, F.R. Jones, "Generation of Thermal Strains in Carbon Fiber-Reinforced Bismaleimide (PMR-15) Composites," *Composites*, **22**, (2), 99-103 (1991).
15. R.J. Young and P.A. Lovell, Introduction to Polymers, 2nd Edn., Chapman and Hall, New York, 1991, p. 372.

Chapter 4 - 2.5kPETU Cure Kinetics Model

4.1 Introduction

Due to the promising results obtained with 3kPETU, a larger supply of 2.5kPETU was produced by General Electric Research and Development. The oligomer molecular weight was reduced by 500 g/mol in hope of improving processability without significantly sacrificing mechanical properties. Prior to analyzing environmental effects on composite properties, thermal and rheological analyses were necessary to develop appropriate cure schedules for 2.5kPETU.

Thermal, oxidative, and hydrolytic degradation of thermosetting polymers often are accelerated by lack of complete cure; unreacted monomers may react with oxygen or moisture to weaken the matrix. The presence of unreacted monomers also may reduce the density of the matrix and thus accelerate diffusion of oxygen and moisture into the matrix. A consolidation and cure schedule that minimizes remaining unreacted monomer in a composite part is desired. Therefore, a model must be developed that accurately predicts degree of cure as a function of time and temperature.

4.2 PET Cure Kinetics Review

There is a consensus amongst researchers that the cure kinetics, mechanisms, and resultant cured structure of phenylethynyl-terminated (PET) monomers/oligomers (Figure 1.1) are not well understood [1-10]. An understanding of the cure mechanism and cured structure is necessary for theoretical predictions regarding the time and temperature effects on cure, long term properties, and durability. However, the scope of this research is limited to developing an appropriate cure schedule for 2.5kPETU, which may be satisfied with empirical models of cure kinetics. Therefore, this review is intended to gather available information concerning the reaction of PET mers to provide a background for critiquing results of thermal analysis of 2.5kPETU. The information summarized here is from results of differential scanning calorimetry (DSC) and Fourier transform infrared spectroscopy (FTIR). Both techniques are able to provide insight into the reaction kinetics of PET cure. In addition, the differences in the mechanisms by which each technique monitors reaction progress also provides information about reaction kinetics.

All possible reaction paths for PET mers consume the acetylene groups [1]. Therefore reaction progress can be observed via FTIR by monitoring the intensity of the infrared absorption at approximately 2212 cm^{-1} , which is a measure of the presence of acetylene, or

carbon-carbon triple bonds [1]. Several other studies [2-6] confirm that the carbon-carbon triple bonds are consumed with reaction progress and have monitored extent of reaction by using FTIR to measure changes in the intensity of the absorption at the acetylene wave number, approximately 2212 cm^{-1} .

Tan [2] investigated the cure of 2kPETU and 3kPETU at temperatures ranging from 300 to 345 °C and reports that the disappearance of the triple bond appeared to follow first-order reaction kinetics for the initial 80 minutes of cure. After 80 minutes, the triple bonds reportedly were consumed faster than dictated by first-order reaction kinetics. No clarification was given as to whether the change in reaction kinetics at 80 minutes was specific to a molecular weight and/or a temperature, or if the time at which the reaction kinetics changed was independent of molecular weight and temperature. If a change in reaction kinetics is occurring, one would expect this change to be influenced by the extent of reaction, which would be influenced by molecular weight and temperature. From these FTIR results, activation energies (E_a) of $114 \pm 10\text{ kJ/mol}$ and $75 \pm 10\text{ kJ/mol}$ were calculated for 3kPETU and 2kPETU, respectively.

The FTIR results were supplemented by dynamic DSC measurements to utilize the Ozawa method [11] to determine E_a s for 3kPETU and 2kPETU. Using the Ozawa method, Tan [2] calculated E_a s for both 2kPETU and 3kPETU using heating rates of 5, 10, 20, and 30 °C/min. The results were significantly higher than those obtained from FTIR; the E_a s calculated for 3kPETU and 2kPETU were 139 and 124 kJ/mol, respectively. The E_a s determined for several other similar PET oligomers demonstrated that E_a increased with increasing molar mass, suggesting diffusion plays an important role in the curing process. Molar mass increases produce more difficult molecular diffusion, thus more energy is required to drive the reaction.

Wood, et al. [4], studied a model PET compound containing a single ethynyl bond: 4-phenoxy-4'-phenylethynylbenzophenone (4-PPEB) having a molecular weight of 374 amu. The carbon-carbon triple bond FTIR peak was greatly diminished following a 15 minute hold at 375 °C indicating reaction was near completion and/or the remaining concentration of triple bonds was below the instrument's detection limit.

Johnston, et al. [6], studied film samples of PET imide oligomers having molecular weights of 7000 g/mol. The films were initially heated for 30 minutes at 370, 400, and 420 °C. The films were then analyzed with FTIR; in all three cases a significant ethynyl

peak remained. Following an additional 60 minutes of heating at these temperatures the ethynyl peak was no longer detectable in any of the films. Despite the absence of an ethynyl peak in all three films, the glass transition temperatures (measured via DSC) of the films increased with cure temperature: the 370 °C hold produced a T_g of 327 °C, the 400 °C hold produced a T_g of 339 °C, and the 420 °C hold produced a T_g of 360 °C. Furthermore, a 45 hour hold at 370 °C was required to reach a T_g of 360 °C, which was obtained in 90 minutes at 420 °C. These results indicate that despite disappearance of the ethynyl peak, cure, indicated by T_g advancement, appears to be continuing.

A promising PET imide with a molecular weight of 5,000 g/mol has been developed at the NASA Langley Research Center and is appropriately named LaRC PETI-5 [7]. A DSC study utilizing the isoconversional plot technique of Flynn, Wall, and Ozawa reports that all stages of the cure reaction of PETI-5 can apparently be described with an average E_a of 139.0 ± 3.3 kJ/mol [7]. In contrast to some of the other studies mentioned here, which report first-order reaction kinetics for at least part of the cure of PET oligomers, Hinkley [7] reports that the reaction can not be described by a simple order even though the temperature dependence of the reaction can reportedly be described with a single activation energy.

A second study of PETI-5 [5] reports FTIR results similar to those reported by Johnston, et al. [6]. Following a 30 minute hold at 350 °C a significant ethynyl peak is still evident and after 60 minutes at 350 °C, the ethynyl peak is barely evident. After 60 minutes at 350 °C the T_g is 269 °C, which is 4 °C less than the maximum T_g measured via DSC for PETI-5 following a 60 minute hold at 375 °C. An additional 60 minutes at 350 °C produces a T_g of 271 °C, still 2 °C short of the ultimate T_g . Therefore, T_g advancement appears to be occurring in PETI-5, as it did in the 7000 g/mol PETI, well after the ethynyl peak in the FTIR spectrum is gone. Admittedly, the discrepancy in PETI-5 glass transition temperatures achieved by 60 minute holds at 350 °C and 375 °C is 4 °C contrasting with the 33 °C difference in T_g of the 7000 g/mol PETI achieved by 60 minute holds at 370 °C and 420 °C. But, the difference in cure temperatures is 50 °C for the 7000 g/mol PETI, whereas, it is only 25 °C for the PETI-5. Holding PETI-5 for 60 minutes at 325 °C reportedly results in a DSC measured T_g that is 24 °C less than the 273 °C obtained by 60 minutes at 375 °C. This difference is more in the range seen with the 7000 g/mol PETI; unfortunately, FTIR data were not reported at 325 °C. An additional hour at 325 °C is required to raise the PETI-5 DSC measured T_g to 260 °C, indicating that possibly several hours of T_g advancement remain. This comparison of hold times, hold temperatures, and

resultant glass transition temperatures is rather tedious; the point to take away from it is that cure, indicated by T_g advancement, appears to be continuing well after the ethynyl peaks become undetectable by FTIR.

Sastri, et al. [1], studied the cure of a PET monomer by synthesizing 1,2,4-tris(phenylethynyl-benzene) with a molar mass of 384 g/mol. The monomer was cured at temperatures ranging from 240 to 300 °C at 20 °C increments. Even after nearly 1200 minutes, only the 300 °C hold displayed complete elimination of the FTIR acetylenic peak. These FTIR results indicate first-order reaction kinetics with an E_a of 135 kJ/mol. Isothermal and dynamic DSC were also utilized to monitor reaction advancement. In general, the degree of cure determined from residual exotherms measured following isothermal holds did not correlate well with the degree of cure calculated from intensities of the acetylenic FTIR peaks following identical isothermal holds. For example, after 180 minutes at 240 °C, a dynamic DSC scan revealed no residual exotherm, but FTIR indicated only about 50% conversion. In contrast, the E_a (137 kJ/mol) determined via the Ozawa method, did agree well with the FTIR determined E_a . However, the Ozawa method is not adversely affected by the diffusion control that apparently takes over the reaction at later stages. Evidence of diffusion control is apparent in the FTIR results which display an initial steep rise in conversion versus time followed by a transition to a gradual increase in conversion. The lack of correlation between DSC residual exotherms and remaining FTIR peak intensity is further evidence of diffusion control taking over the reaction. When the reaction becomes diffusion controlled, FTIR is much better suited than DSC to measure the fraction of unreacted material. For DSC to measure a residual exotherm, the remaining unreacted material must react. If the reaction has progressed to the point that the diffusion necessary for further reaction is severely restricted, a residual reaction can not occur and thus a residual exotherm is not detected. However, FTIR does not require reaction, and consequently diffusion, to measure the concentration of unreacted material. Therefore, FTIR is able to detect unreacted material that is undetectable via DSC.

Takekoshi and Terry [8] synthesized two model PET compounds: 1) N-(3-phenylethynyl)phthalimide (N3) and 2) N-phenyl[4-(phenylethynyl)phthalimide] (N4); each containing a single acetylenic group. Reaction progress was monitored by curing samples of the compounds at different temperatures, dissolving the cured samples in acetonitrile, and then analyzing the solutions with high performance liquid chromatography. The N3 compound displayed second-order reaction kinetics with an E_a of 132 kJ/mol. The N4 compound displayed first-order reaction kinetics with an E_a of 153 kJ/mol.

The purpose of this review is not to make a definitive statement on the cure process of PET imide oligomers and other PET monomers, but to present a brief summary of the literature in this area to provide the reader with a sense of the PET activation energies and the lack of consensus on reaction order of PET mers. Furthermore, the cure times and temperatures required by these materials and their resultant glass transition temperatures have been presented. Finally, it has been shown by tracking the resultant glass transition temperatures that cure continues well after DSC and FTIR detect reaction completion.

4.3 Cure Kinetics Modeling Background

Despite literary evidence that cure of PET imides may not be monitored to completion by FTIR or DSC, the cure of 2.5kPETU was analyzed via DSC in order to develop an empirical kinetics model to assist in the selection of a cure schedule for 2.5kPETU. In addition, there was a desire to compare the kinetics of 2.5kPETU with those of other PET imides. Reaction kinetics studies begin with a basic rate equation that correlates the reaction rate, $d\alpha/dt$, to the concentration of remaining reactants, $f(1-\alpha)$, through a rate constant, k (Equation 4.1) [12]. In the case of PETU, the remaining reactants are the phenylethynyl groups with one or two available reactive sites, and the concentration of the remaining reactants may be determined from the degree of cure, α .

$$\frac{d\alpha}{dt} = k(T) f(1 - \alpha) \quad (4.1)$$

Two general categories describe most thermoset cures: n th-order and autocatalytic. Kinetics of n th-order assume that once a reactant has reacted, it will not contribute to further reaction. As a result, the reaction rate is proportional to the concentration of unreacted material [12]. Therefore, only the unreacted material has to be considered in determining the reaction rate, as shown in Equation 4.2, where n is the reaction order.

$$f(\alpha) = (1 - \alpha)^n \quad (4.2)$$

During isothermal cure of an autocatalytic material, the reaction rate accelerates until a maximum is reached at 20% to 40% of full cure. The acceleration is a result of reaction products aiding further reaction. The reaction scheme for PET mers is unknown and there are several proposed schemes [4], but in short, the breaking of an ethynyl bond and creation of a new bond may aid additional reaction at that site or a nearby site. The dependence of reaction rate on degree of cure for an autocatalytic reaction is shown in Equation 4.3, where the superscripts m and n are reaction orders.

$$f(\alpha) = \alpha^m(1 - \alpha)^n \quad (4.3)$$

In both autocatalytic and n th-order reactions, the rate constant, k , carries the temperature dependence of the reaction through an Arrhenius relationship given in Equation 4.4. The Z parameter is the Arrhenius frequency factor in reciprocal seconds, E_a is the activation energy with units of J/mol, R is the gas constant equal to 8.314 J/mol•K, and T is the absolute temperature in Kelvin. Utilizing Equations 4.1 through 4.4, the complete equation for an n th-order reaction is given in Equation 4.5 and for an autocatalytic reaction in Equation 4.6.

$$k(T) = Z \exp\left[\frac{-E_a}{RT}\right] \quad (4.4)$$

$$\frac{d\alpha}{dt} = Z \exp\left[\frac{-E_a}{RT}\right] (1 - \alpha)^n \quad (4.5)$$

$$\frac{d\alpha}{dt} = Z \exp\left[\frac{-E_a}{RT}\right] \alpha^m (1 - \alpha)^n \quad (4.6)$$

Most thermoset reactions can be sufficiently represented by one of these chemically based models (Equations 4.5 and 4.6), which implies chemical reactions control the cure rate. Two notable exceptions exist. One exception is the case of diffusion control which often replaces chemical reaction control as a material vitrifies and becomes glassy. Considerations of diffusion control will be addressed later. The other exception occurs when more than one type of chemical reaction is occurring. In this situation, one reaction may be n th-order and the other autocatalytic. This combination of reactions may be represented by a sum of Equations 4.5 and 4.6 as shown in Equation 4.7. This combination reaction may be shown in a simpler way following rearrangement and the substitution of Equation 4.4 (Equation 4.8).

$$\frac{d\alpha}{dt} = Z_1 \exp\left[\frac{-E_{a1}}{RT}\right] (1 - \alpha)^n + Z_2 \exp\left[\frac{-E_{a2}}{RT}\right] \alpha^m (1 - \alpha)^n \quad (4.7)$$

$$\frac{d\alpha}{dt} = (k_1 + k_2 \alpha^m)(1 - \alpha)^n \quad (4.8)$$

This model corrects for reactions that appear autocatalytic in nature, yet do not have an initial reaction rate of zero as dictated by Equation 4.3. Therefore, this combination model

has been used in many cases where the reaction rate peaks after the beginning of the reaction, but the initial reaction rate is nonzero [13 and references within]. The combination reaction kinetics model given in Equations 4.7 and 4.8 worked well in the modeling of isothermal cure of 2.5kPETU, as will be described later.

4.4 Cure Kinetics Experimental

A DSC technique based mostly on isothermal measurements will be used to determine the kinetic parameters to describe the cure of 2.5kPETU. Prior to beginning thermal analysis, 2.5kPETU powder was degassed under vacuum at 165 °C for 4.5 days to remove residual o-dichlorobenzene remaining from synthesis. At ambient pressure, the boiling point of o-dichlorobenzene is 179 °C. However, heating the powder above 170 °C results in partial fusion of the powder. Under vacuum, 165 °C is adequate to evaporate the o-dichlorobenzene. DSC specimens were prepared by sealing 5-6 mg of degassed powder in hermetic aluminum pans. DSC experiments were done in a TA Instruments DSC 2920 with a 35 ml/min nitrogen purge. The DSC experiments commenced with three 5 °C/min ramps from 50 °C to 425 °C; degradation appeared to occur if ramps exceeded 425 °C. These ramps displayed a consistent exotherm onset temperature of 325 °C, peak temperatures ranging from 368 °C to 372 °C, and a total heat of reaction, ΔH_T , of 112.5 J/g. One of these ramps is displayed in Figure 4.1.

Isothermal measurements were run at 5 °C increments ranging from 315 °C to 390 °C. However, the shapes of da/dt versus α curves displayed three distinct temperature regions in which the cure kinetics appeared to differ: $T < 325$ °C, 325 °C $< T < 360$ °C, and $T > 360$ °C. Because previously recommended cure schedules for PETU materials utilized holds at 350 °C, the isothermal measurements from 325 °C to 360 °C were selected for the production of the isothermal data necessary for the development of a cure kinetics model. In addition, this temperature range covers the central portion of the frontside of the exotherm peak, where the reaction rate is increasing the most rapidly with temperature increase.

Isothermal measurements were performed by: preheating the closed DSC cell to the desired temperature, opening the cell and quickly placing the specimen in the nitrogen purged cell, allowing the cell temperature to recover to within 4 °C of the set temperature, and then beginning data collection [14].

After each specimen went through an isothermal measurement, it was removed from the DSC cell and allowed to cool. The specimen was then returned to the DSC cell for a 5 °C/min ramp from 150 °C to 425 °C to measure residual cure and the T_g resulting from each isothermal measurement.

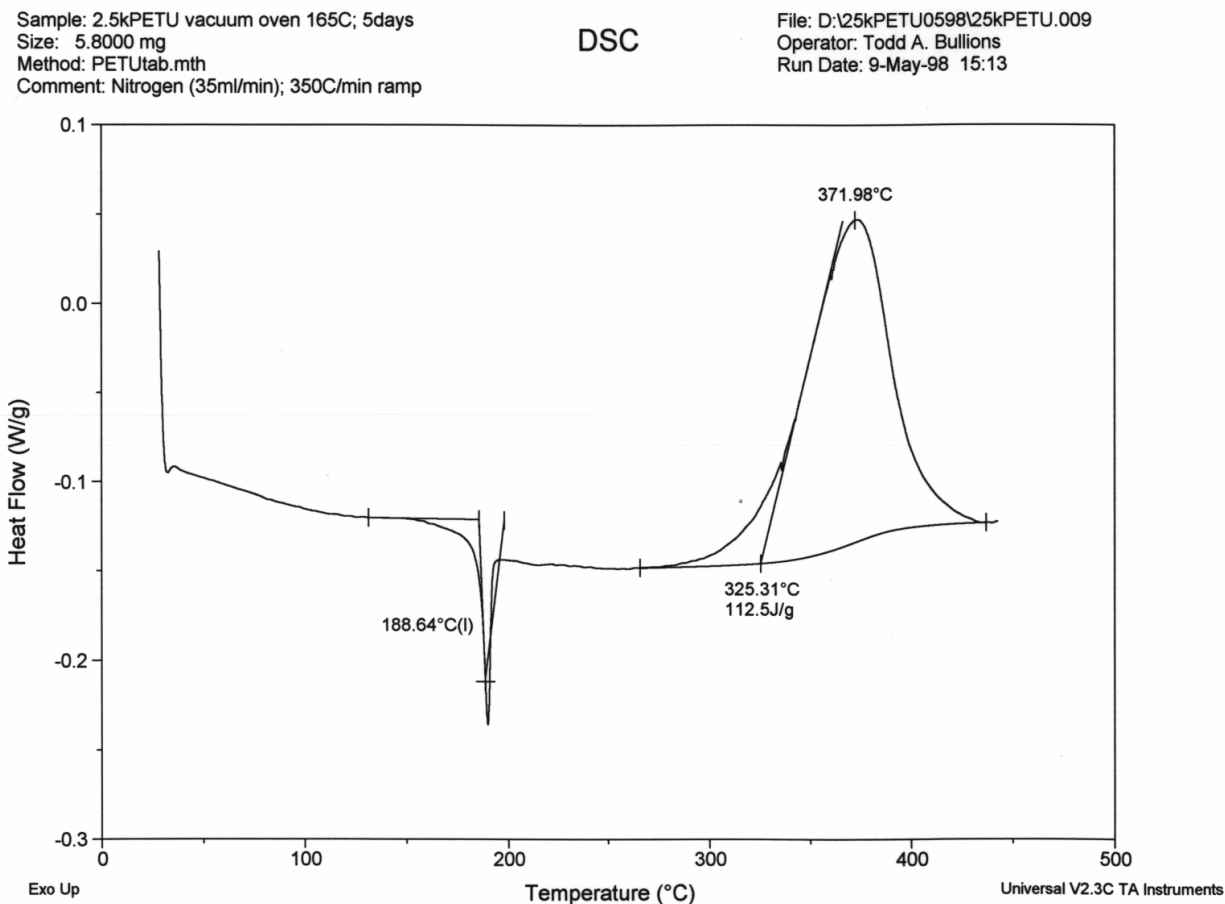


Figure 4.1. Differential Scanning Calorimetry: 5 °C/min Ramp of 2.5kPETU

4.5 Experimental Analysis and Results

As with the temperature ramp shown in Figure 4.1, the isothermal holds produce a measurement of heat flow that monitors reaction progress. However, the isothermal measurements monitor heat flow versus time rather than temperature as shown in Figure 4.2.(a). The area under the heat flow curve represents the total heat of reaction for the isothermal hold, ΔH_f . Thus, the selection of boundaries for this area is important. A time must be selected as the start of cure, t_s , and a time must be selected as the finish of detectable cure, t_f . The traditional method for selecting t_s and t_f begins by placing t_f at the first local minimum along the heat flow plateau (Figure 4.2.(a)). A baseline is then

constructed with the baseline heat flow equal to the reaction heat flow at t_f (Figure 4.2.(a)). The location of t_s is then moved until the sum of ΔH_I and ΔH_R , the residual heat of reaction measured via a temperature ramp after the isothermal measurement, is equivalent to ΔH_T , the total heat of reaction, from the temperature ramp on virgin material. However, the majority of the residual ramps in this study displayed negligible or no ΔH_R despite different values of ΔH_T . Sastri, et al. [1], saw the same lack of residual exotherms. The lack of a residual exotherm suggests the reaction has progressed into the diffusion control region as discussed previously. Thus a different method for selecting t_s was necessary.

The majority of the isothermal measurements demonstrated a small, local minimum within the overall heat flow maximum at the beginning of the hold as seen in Figure 4.2.(b). This local minimum is believed to be near the transition from DSC cell equilibration to energy output from the actual exothermic reaction. Thus, this point was selected as t_s for all isothermal measurements. Most likely, the reaction begins prior to t_s , but the local minimum is the most consistent landmark for choosing t_s from measurement to measurement. Some error is likely incurred from inconsistent amounts of reaction occurring prior to t_s and being omitted from the data collection.

Following the selection of t_s , ΔH_I was calculated for each isothermal measurement. Knowing ΔH_T , the isothermal degree of cure, α_t , could be calculated at any intermediate time, t_i , between t_s and t_f . Calculation of α_t required knowing $\Delta H_I(t)$, the heat evolved between t_s and t_i as shown in Figure 4.2.(b). The value of α_t was then simply $\Delta H_I(t)/\Delta H_T$. Thus at any time, the experimental value of α_t could be calculated.

Several sources [1,2,8] reported first-order reaction kinetics for PET monomers/oligomers. Having the ability to determine the experimental value of α_t at any time allows for the investigation of whether first-order reaction kinetics may be applicable to 2.5kPETU. To make this determination, a relationship between α_t and time must be derived to determine the kinetic parameters in Equation 4.5. Substituting Equation 4.4 into Equation 4.5 and assuming a reaction order of one produces Equation 4.9. Rearrangement and integration results in Equation 4.10.

$$\frac{d\alpha}{dt} = k(T)(1 - \alpha) \quad (4.9)$$

$$\ln(1 - \alpha) = -k(T) t \quad (4.10)$$

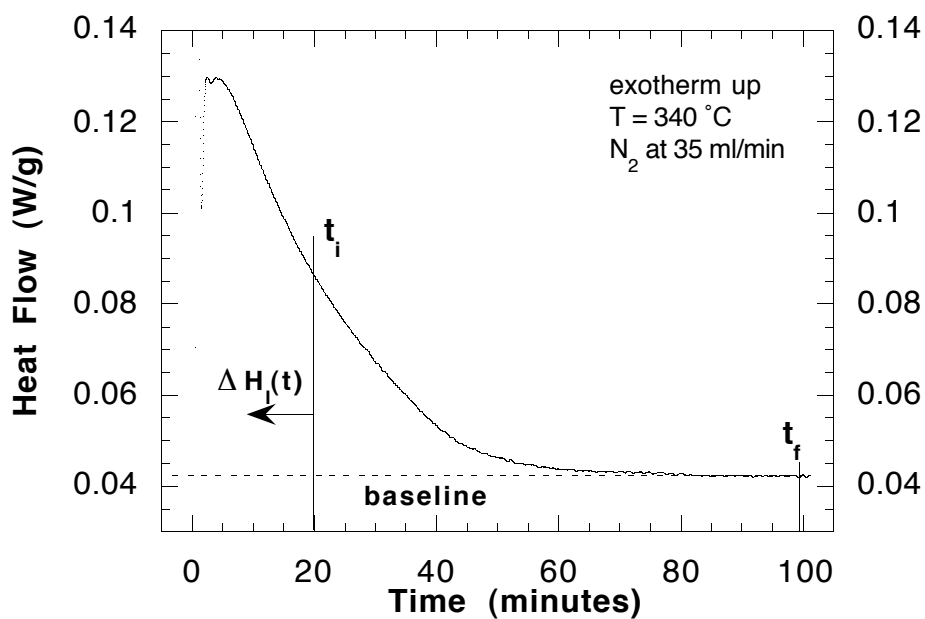


Figure 4.2.(a) Isothermal Exotherm - Cure of 2.5kPETU at 340 °C

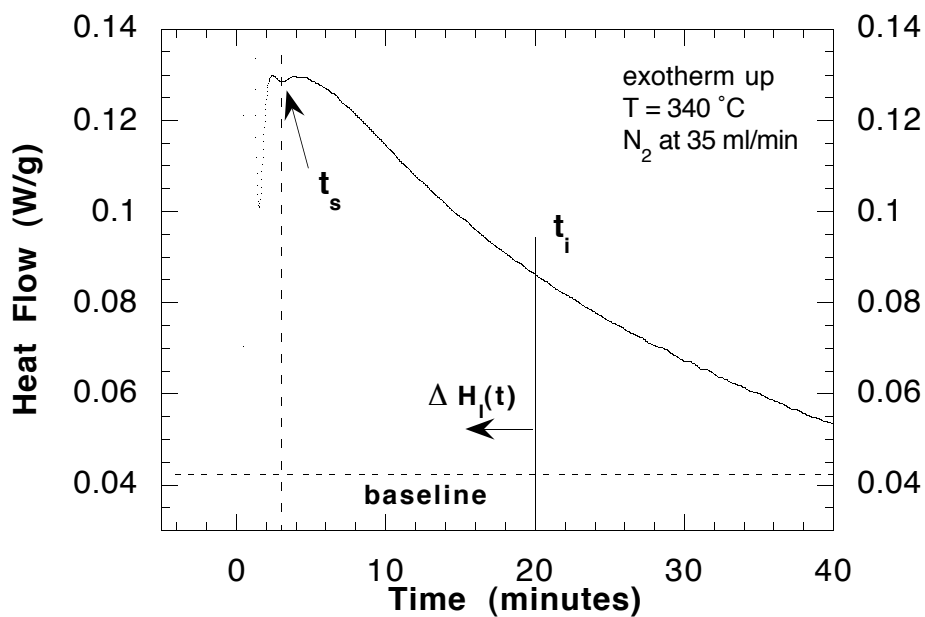


Figure 4.2.(b) Isothermal Exotherm - Cure of 2.5kPETU at 340 °C - Magnification of t_s Region

Subsequently, $\ln(1-\alpha)$ may be plotted versus time for each isothermal cure temperature with the slope of a linear fit providing the negative of the rate constant for each temperature. Such a plot is shown in Figure 4.3 for temperatures ranging from 325 °C to 360 °C. The plot of each temperature was fit linearly up to the point that the slope transitioned to an almost vertical relationship between $(1-\alpha)$ and time, or in the case of 355 °C, the slope leveled (fits are not shown). Details regarding the fits are given in Table 4.1. All fits except 355 °C were beyond $\alpha_f = 0.99$.

The high correlation coefficients indicate first-order kinetics may apply to the reaction of 2.5kPETU oligomers. Recalling from Equation 4.4 that the rate constant, k , is a function of temperature and depends on the activation energy, E_a , Equation 4.4 may be utilized to determine a single activation energy for 2.5kPETU. Taking the natural logarithm of Equation 4.4 results in an equation having the form of a straight line (Equation 4.11).

$$\ln[k(T)] = \ln Z + \left(\frac{-E_a}{R} \right) \frac{1}{T} \quad (4.11)$$

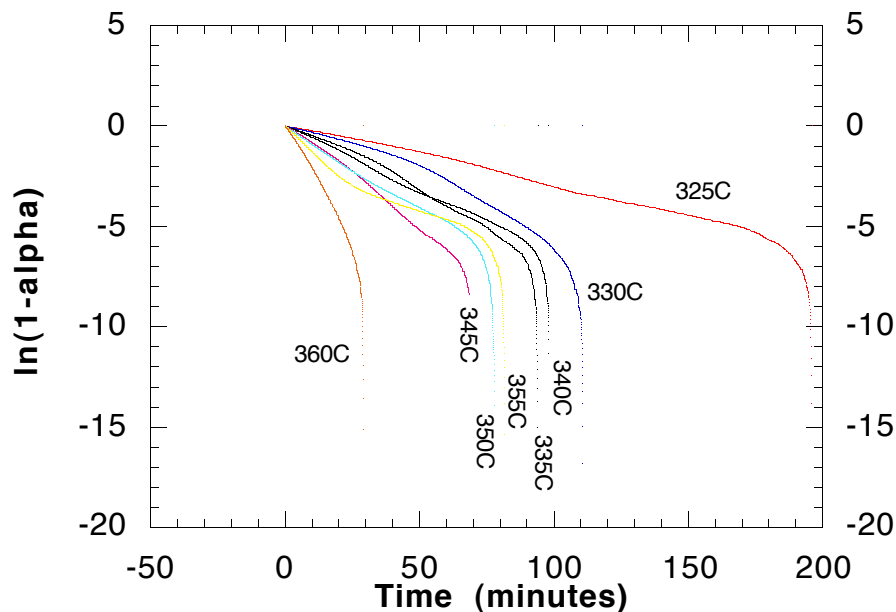


Figure 4.3. Determination of Rate Constants

Table 4.1. Determination of Rate Constants

Temperature (°C)	End Time of Fit (min)	Corresponding α_1	Correlation Coefficient (R)	k (1/sec)
325	175.5	0.995	0.999	$5.15 \times 10^{-4} \pm 0.30 \times 10^{-4}$
330	100.0	0.998	0.984	$1.00 \times 10^{-3} \pm 0.19 \times 10^{-3}$
335	90.0	0.999	0.995	$1.23 \times 10^{-3} \pm 0.13 \times 10^{-3}$
340	87.3	0.996	0.998	$1.06 \times 10^{-3} \pm 0.07 \times 10^{-3}$
345	64.0	0.999	0.999	$1.79 \times 10^{-3} \pm 0.12 \times 10^{-3}$
350	68.8	0.996	0.998	$1.30 \times 10^{-3} \pm 0.10 \times 10^{-3}$
355	24.5	0.946	0.999	$2.06 \times 10^{-3} \pm 0.20 \times 10^{-3}$
360	25.5	0.999	0.997	$4.12 \times 10^{-3} \pm 0.12 \times 10^{-3}$

Subsequently, the values for k in Table 4.1 were plotted versus $1/T$ (where temperature is in Kelvin) as shown in Figure 4.4. An E_a of 141 kJ/mol was calculated via an application of a linear fit to this plot. This activation energy agrees well with those reported for similar materials by Sastri, et al. [1], Tan [2], Hinkley [7], and Takeshoshi and Terry [8].

In addition to the E_a , the Arrhenius frequency factor, Z , may be determined from Equation 4.11 and the fit in Figure 4.4; Z was determined to be $1.30 \times 10^9 \text{ sec}^{-1}$. Knowing E_a and Z for 2.5kPETU allows for the calculation of α_t at any time during an isothermal hold. This calculation utilizes Equation 4.12, which is obtained upon manipulation of Equation 4.10 and subsequent substitution of Equation 4.4.

$$\alpha = 1 - \exp\left[-Z t \exp\left(\frac{-E_a}{RT}\right)\right] \quad (4.12)$$

Figure 4.5 demonstrates the level of accuracy of the prediction of α_t utilizing Equation 4.12 and the calculated values for E_a and Z at 330, 340, 350, and 360 °C. Figure 4.6 shows the percent error in predicting the time to reach selected values of α_t using first-order kinetics for temperatures ranging from 325 °C to 360 °C. The results represented in Figure 4.5 and

Figure 4.6 demonstrate that first-order kinetics do not accurately predict α_t for isothermal cures in the temperature range of 325 °C to 360 °C.

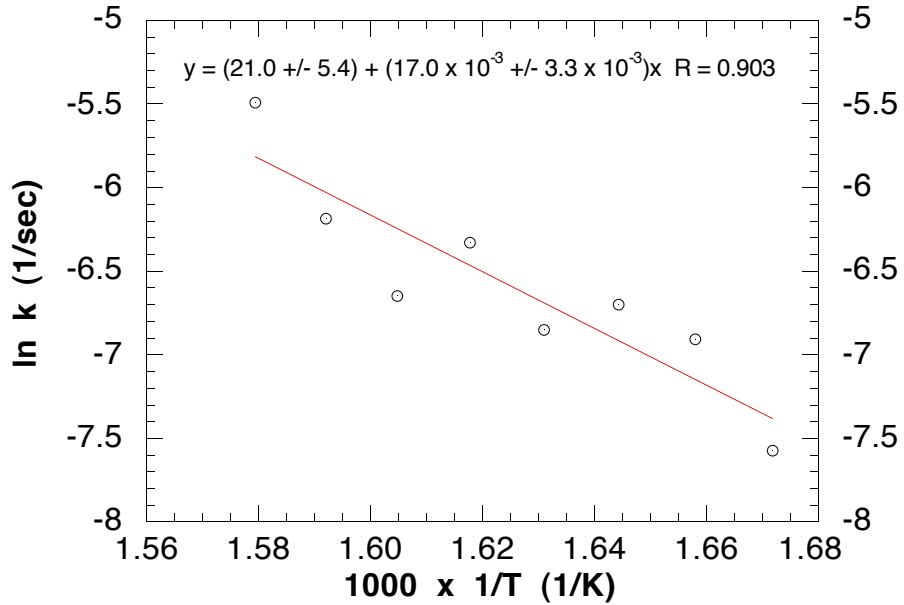


Figure 4.4. Determination of First-Order Reaction Activation Energy

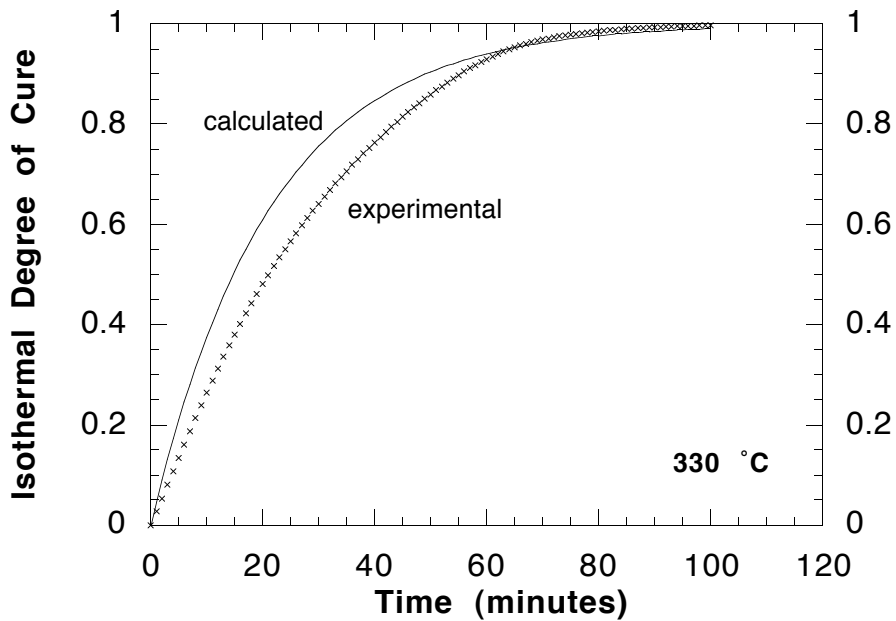


Figure 4.5.(a) Comparison of Actual and Calculated Degree of Cure Versus Time, 330 °C

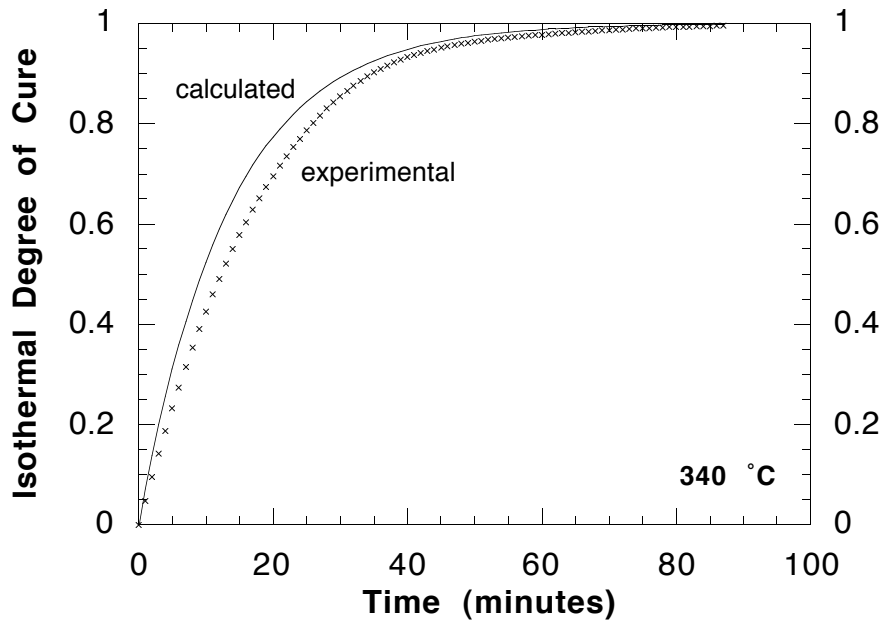


Figure 4.5.(b) Comparison of Actual and Calculated Degree of Cure Versus Time, 340 °C

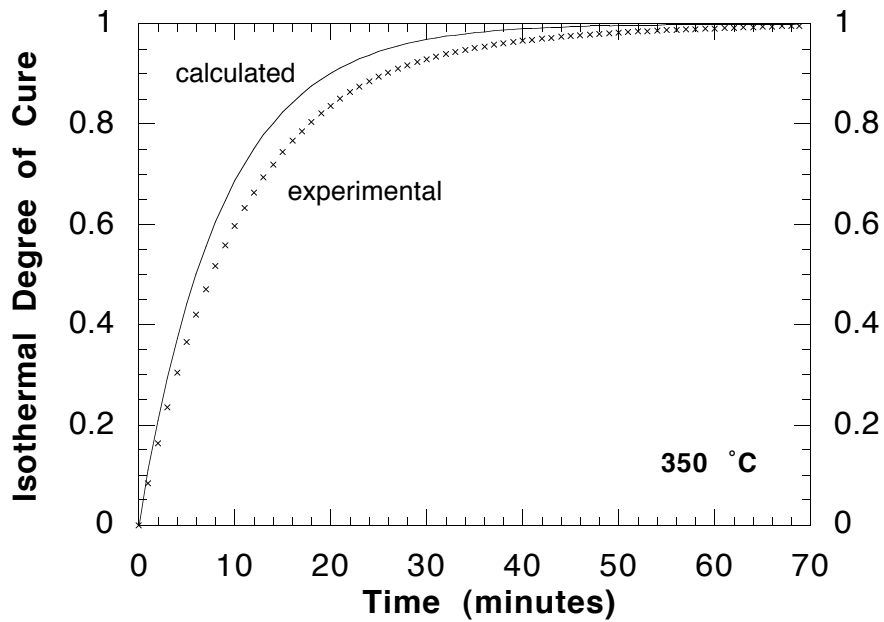


Figure 4.5.(c) Comparison of Actual and Calculated Degree of Cure Versus Time, 350 °C

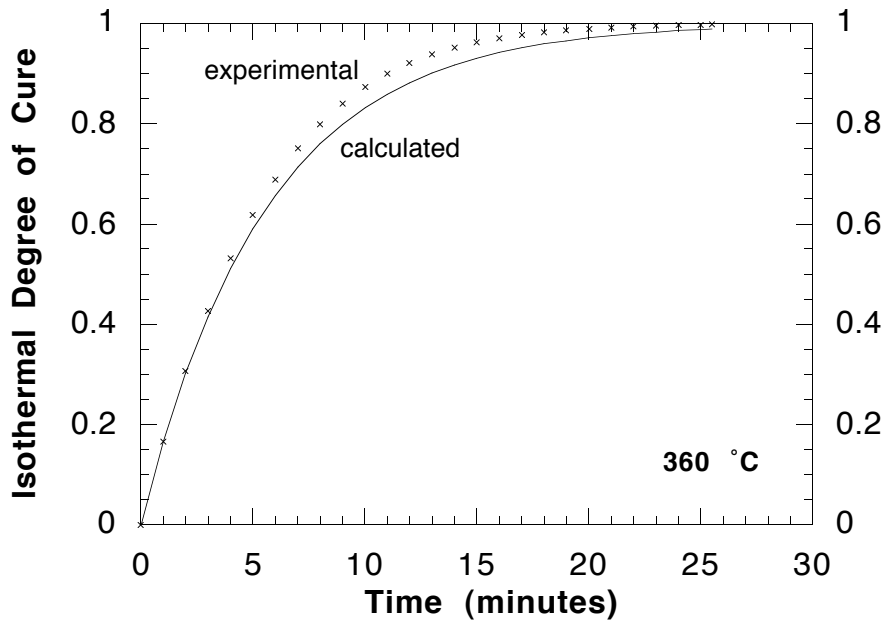


Figure 4.5.(d) Comparison of Actual and Calculated Degree of Cure Versus Time, 360 °C

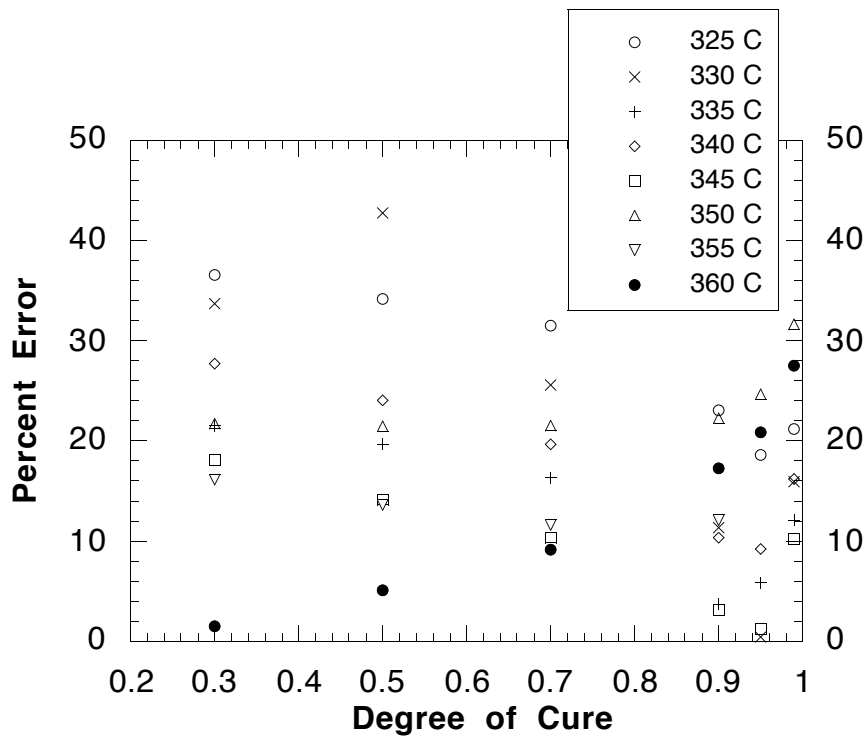


Figure 4.6. Percent Error in Calculated Time to Reach Predicted Degree of Cure For First-Order Kinetics

Further investigation of first-order reaction kinetics includes analysis of the relationship between $d\alpha_i/dt$ and α_i . Equation 4.5 may be used to calculate $d\alpha_i/dt$ for any given α_i using first-order reaction kinetics. The experimental value for the isothermal reaction rate at any time, $d\alpha_i/dt$ is $(d\Delta H_i(t)/dt)/\Delta H_p$, where $d\Delta H_i(t)/dt$ is the difference between the reaction heat flow and the baseline heat flow. Figures 4.7.(a) and (b) demonstrate the minimal correlation between the actual experimental $d\alpha_i/dt$ versus α_i curve and the calculated $d\alpha_i/dt$ versus α_i curve obtained with first-order reaction kinetics. The shape of the experimental $d\alpha_i/dt$ versus α_i curve appears to match better the combination cure kinetics represented by Equations 4.7 and 4.8 than first-order kinetics represented by Equation 4.5. These results along with the poor prediction ability shown in Figures 4.5 and 4.6 calls for an attempt to determine the necessary kinetic parameters to model the cure of 2.5kPETU via Equation 4.7.

Determination of the kinetic parameters in Equation 4.7 will be done by directly fitting Equation 4.7 to plots of isothermal reaction rate versus isothermal degree of cure. Close inspection of these plots reveals a change in slope between $\alpha_i = 0.85$ and $\alpha_i = 0.90$. This slope change appears in most of the isothermal measurements near the same range of α_i and demonstrates an increase in the rate at which the reaction rate is declining. It is thought that this slope change indicates diffusion control is replacing chemical control as the rate controlling portion of the reaction; the transition is demonstrated in Figure 4.8 for 340 °C. Since the cure kinetics models introduced earlier are only suited for modeling chemically controlled reactions and not diffusion controlled reactions, the combination cure kinetics model will be developed based on experimental data for: $0 < \alpha_i < 0.90$.

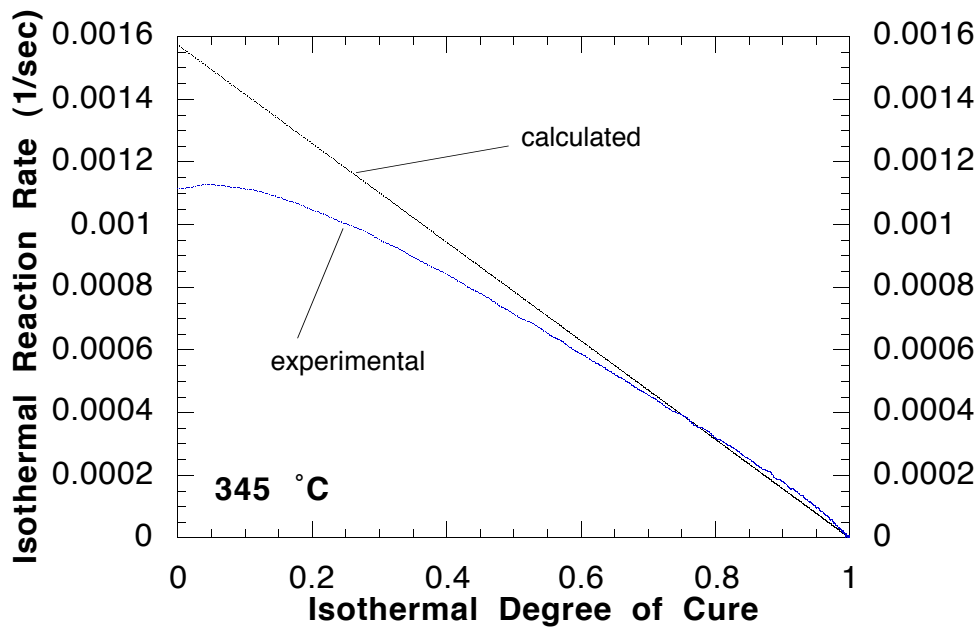


Figure 4.7.(a) Representative da_1/dt versus α_1 Curves, Experimental and Calculated via First-Order Reaction Kinetics, 345 °C

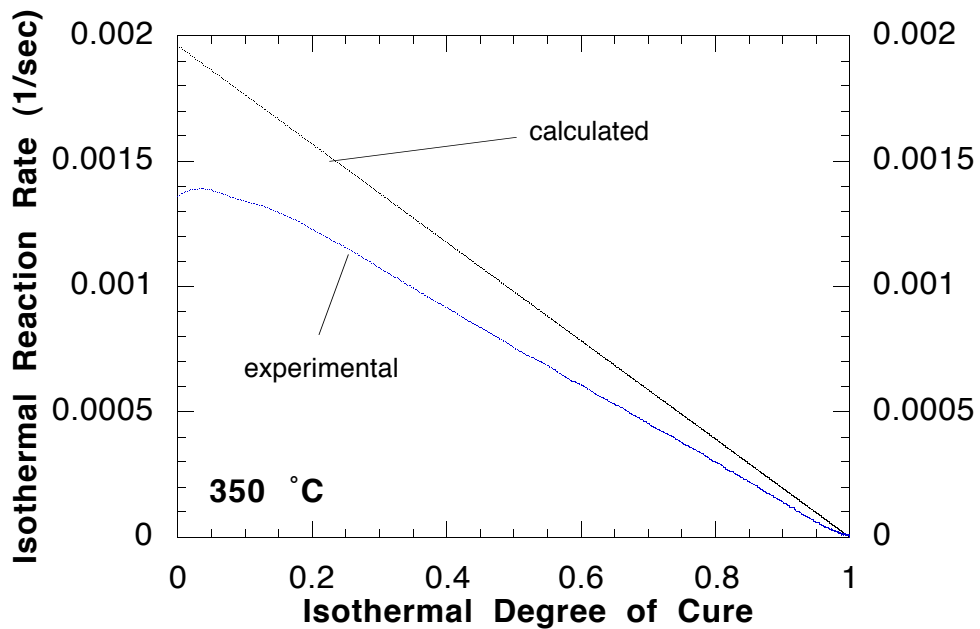


Figure 4.7.(b) Representative da_1/dt versus α_1 Curves, Experimental and Calculated via First-Order Reaction Kinetics, 350 °C

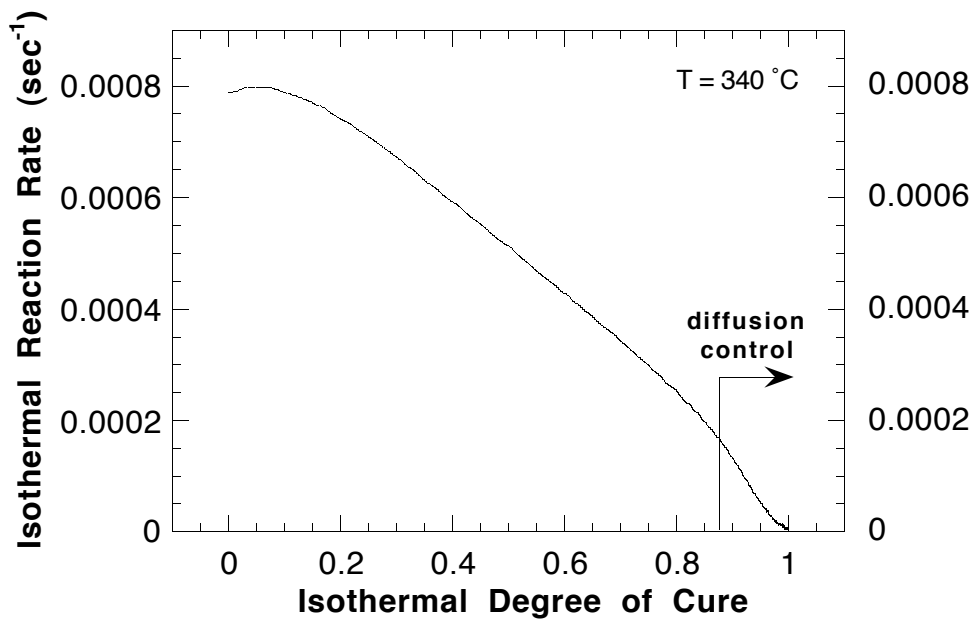
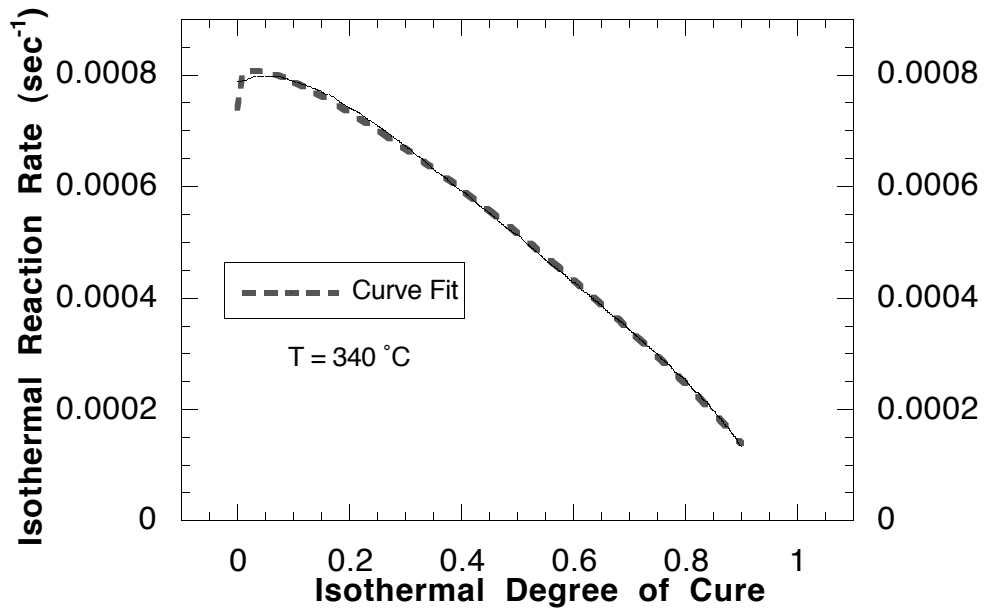


Figure 4.8. Reaction Rate Versus Degree of Cure Plot Generated from Heat Flow Versus Time Data for 340 °C Isothermal Cure

Curve fitting software utilizing the Levenburg-Marquardt algorithm determined the best values of k_1 , k_2 , m , and n for each isothermal temperature as shown in Figure 4.9 for 340 °C. The values determined from the curve fits are given in Table 4.2.

With values of k_1 and k_2 for each temperature, the Arrhenius frequency factors (Z_1 and Z_2) and activation energies (E_{a1} and E_{a2}) of Equation 4.7 may be determined as E_a and Z were determined previously for first-order kinetics. These parameters were determined by looking at k_1 and k_2 separately via Equation 4.11 as shown in Figures 4.10 and 4.11. Knowing the values of Z_1 , E_{a1} , Z_2 , and E_{a2} allows k_1 and k_2 to be calculated for any temperature within the experimental temperature range. The parameters k_1 and k_2 were calculated for each experimental temperature (Table 4.3). The values of m and n were plotted versus temperature (Figures 4.12 and 4.13) to determine the temperature dependence of m and n . For each experimental temperature, the values of m and n were calculated based on the temperature dependencies determined in Figures 4.12 and 4.13 (Table 4.3).



$$\frac{d\alpha}{dt} = (k_1 + k_2\alpha^m)(1 - \alpha)^n$$

Parameter	Value	Error
k_1 (1/sec)	7.42×10^{-4}	0.04×10^{-4}
k_2 (1/sec)	2.16×10^{-4}	0.03×10^{-4}
m	0.258	0.01
n	0.836	0.001
Chi Squared	3.18×10^{-8}	NA
Correlation Coefficient	0.999	NA

Figure 4.9. Curve Fitting of $d\alpha/dt$ Versus α at 340 °C for k_1 , k_2 , m and n

Table 4.2. Curve Fitting Determination of Kinetic Parameters

Temperature (°C)	$k_1 \times 10^{-4}$ (sec ⁻¹)	$k_2 \times 10^{-4}$ (sec ⁻¹)	m	n
325	3.12	0.886	0.154	0.835
330	3.90	1.30	0.140	0.722
335	6.63	0.491	0.0603	0.775
340	7.42	2.16	0.258	0.836
345	10.6	4.03	0.361	0.928
350	13.1	3.57	0.276	1.07
355	18.2	7.43	0.610	1.09
360	27.5	4.26	0.317	0.895

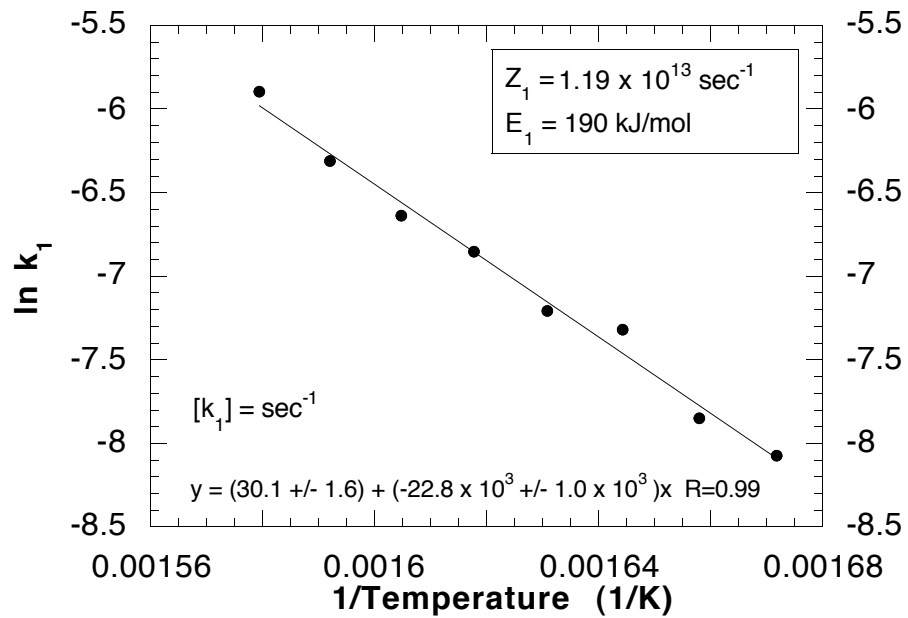


Figure 4.10. Arrhenius Plot of k_1 Data

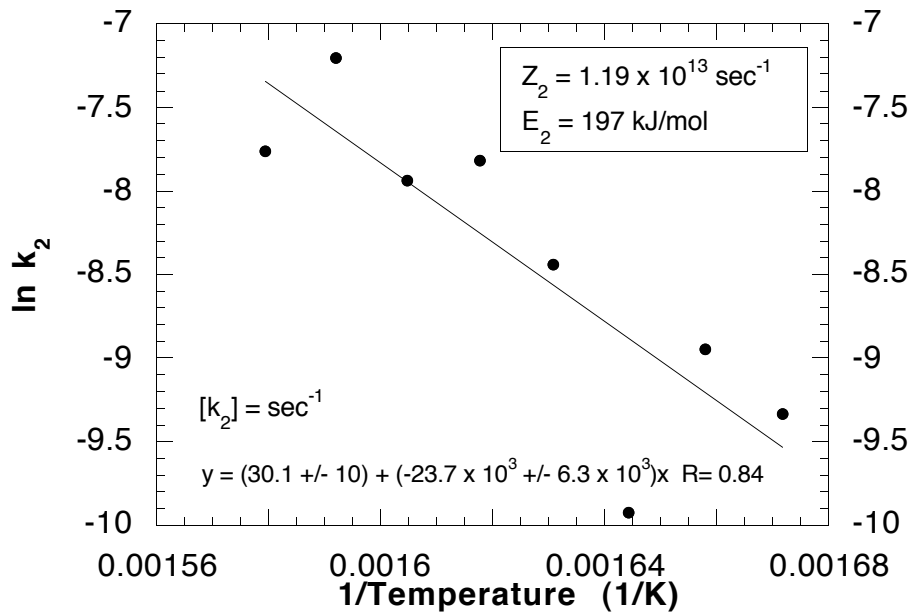


Figure 4.11. Arrhenius Plot of k_2 Data

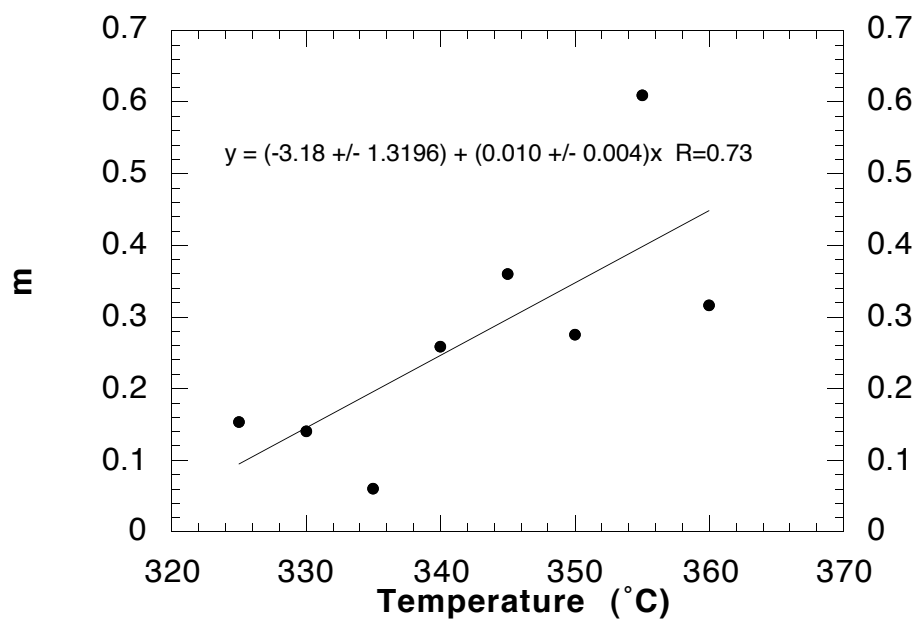


Figure 4.12. m Versus Temperature

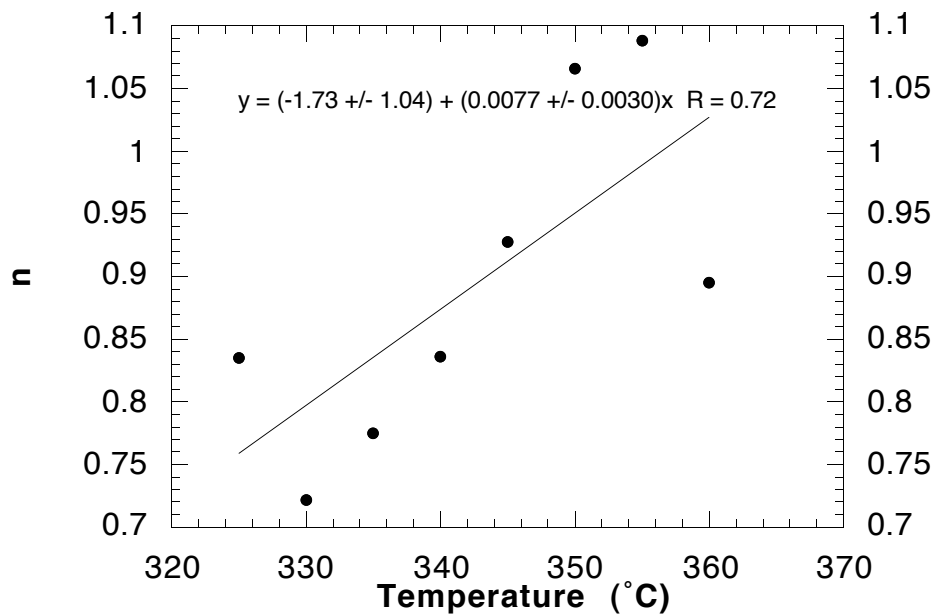


Figure 4.13. n Versus Temperature

Table 4.3. Calculated Values of Kinetic Parameters

Temperature (°C)	$k_1 \times 10^{-4}$ (sec ⁻¹)	$k_2 \times 10^{-4}$ (sec ⁻¹)	m	n
325	3.07	0.724	0.096	0.76
330	4.21	1.01	0.15	0.80
335	5.75	1.39	0.20	0.84
340	7.81	1.91	0.25	0.87
345	10.6	2.61	0.30	0.91
350	14.2	3.55	0.35	0.95
355	19.0	4.81	0.40	0.99
360	25.3	6.48	0.45	1.03

Enough information is known that at any temperature, $d\alpha/dt$ can be correlated with α via Equation 4.7 using the temperature dependencies determined in Figures 4.10 - 4.13. Therefore, calculated $d\alpha/dt$ versus α plots were compared with the actual experimental $d\alpha/dt$ versus α plots (Figures 4.14.(a), (b), (c), and (d)). The difference between the calculated plots and the experimental plots was unsatisfactory. Through trial and error, n was found to have more of an influence than m on the quality of agreement between the calculated plot and the experimental plot, which would be expected from analysis of Equation 4.7. Thus the calculated $d\alpha/dt$ versus α plots were repeated using the temperature dependence of k_1 (Figure 4.10 and Table 4.3), k_2 (Figure 4.11 and Table 4.3), and m (Figure 4.12 and Table 4.3) to determine these kinetic parameters. However, the values of n were taken from Table 4.2 rather than from Figure 4.13. The improvement in the agreement between the calculated $d\alpha/dt$ versus α_i and the experimental $d\alpha/dt$ versus α_i relations is visible in Figures 4.15.(a), (b), (c), and (d).

The information garnered up to this point allows for realization of the objective of this kinetics modeling experiment; α_i versus time and temperature predictions were made by inserting the appropriate kinetic parameters used in Figure 4.15 in Equation 4.7 for each temperature. Equation 4.7 was then rearranged and numerically integrated repeatedly to calculate the time to reach set values of α_i . The comparisons of experimental and predicted α_i versus time relationships are shown in Figures 4.16 - 4.19. Figure 4.20 shows the percent error in predicting the time to reach selected values of α_i using combination kinetics for temperatures ranging from 330 °C to 360 °C. The results represented in Figures 4.16 - 4.20 demonstrate that combination kinetics can be used to accurately predict α_i for isothermal cures in the temperature range of 330 °C to 360 °C.

Though the determination of kinetic parameters was based on $\alpha_1 < 0.9$, the fits are displayed up through $\alpha_1 = 0.99$ for the sake of comparing the abilities of first-order reaction kinetics and combination reaction kinetics to predict α_1 versus time.

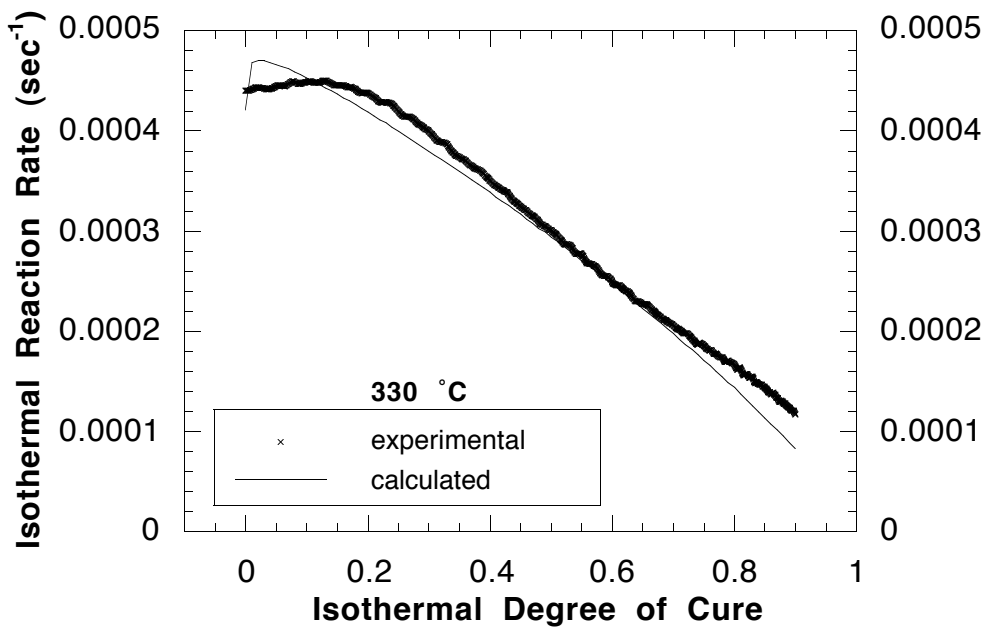


Figure 4.14.(a) 330 °C - $d\alpha/dt$ Versus α : Calculated Compared with Experimental

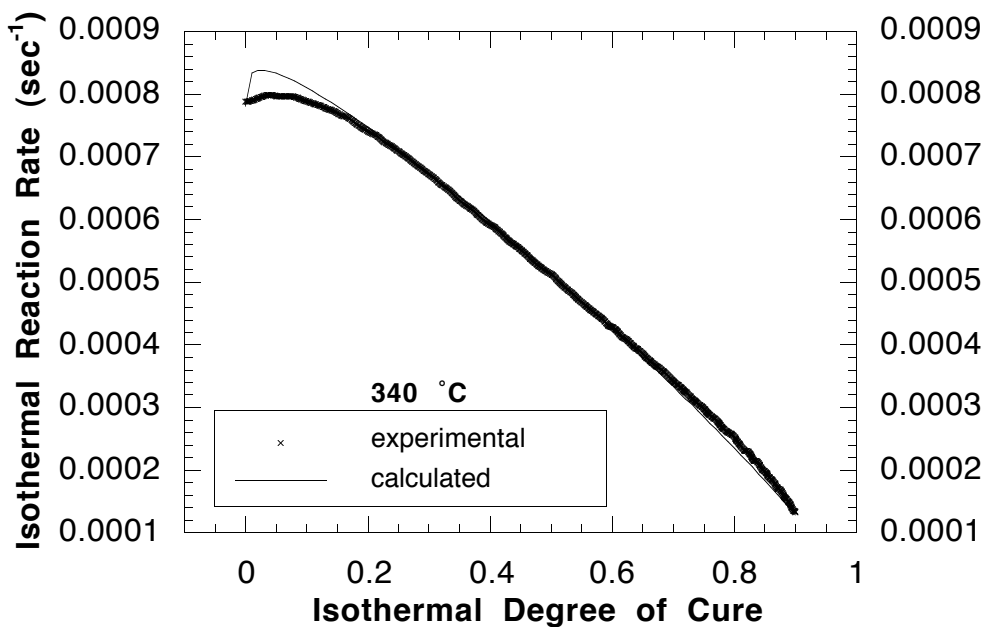


Figure 4.14.(b) 340 °C - $d\alpha/dt$ Versus α : Calculated Compared with Experimental

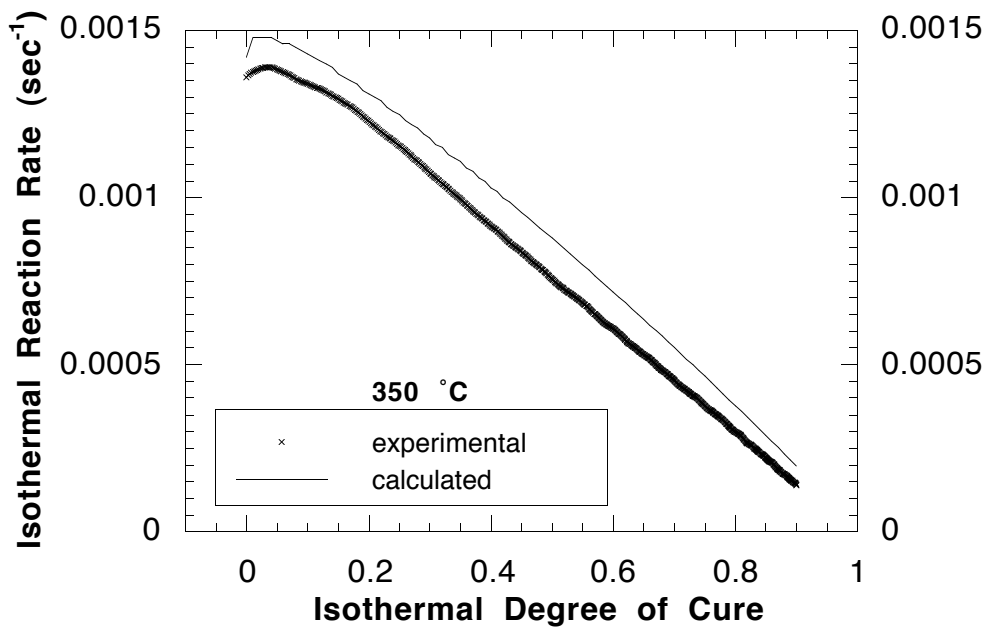


Figure 4.14.(c) 350 °C - $d\alpha/dt$ Versus α : Calculated Compared with Experimental

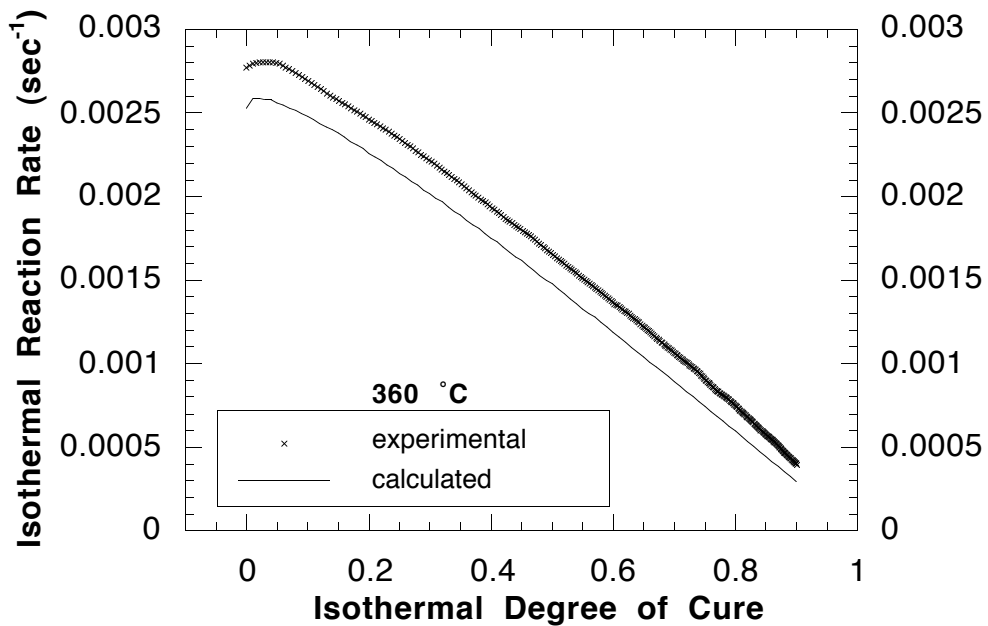


Figure 4.14.(d) 360 °C - $d\alpha/dt$ Versus α : Calculated Compared with Experimental

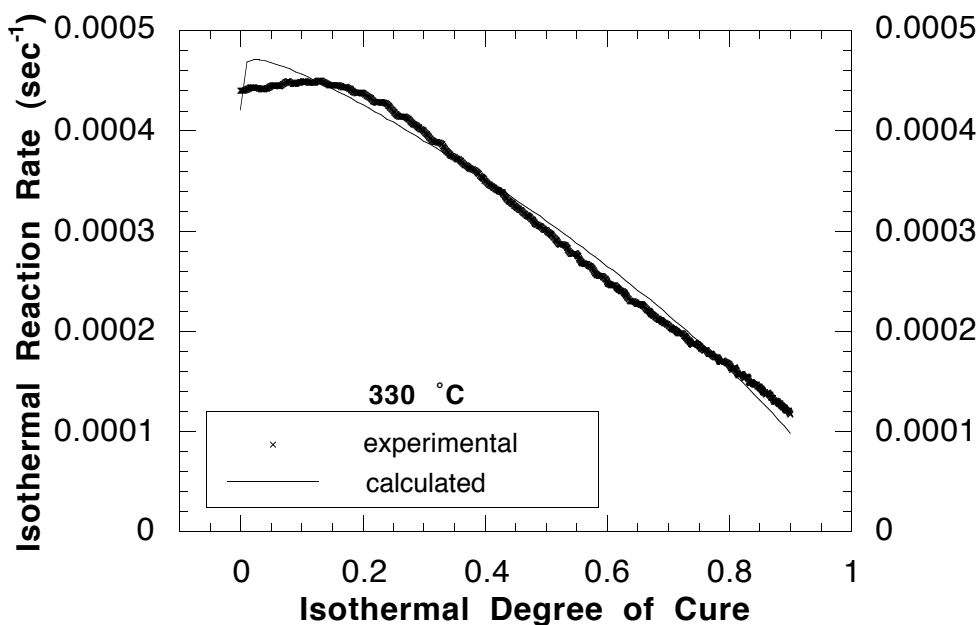


Figure 4.15.(a) 330 °C - da/dt Versus α : Calculated Compared with Experimental - Individually Selected Values of n (Table 4.2)

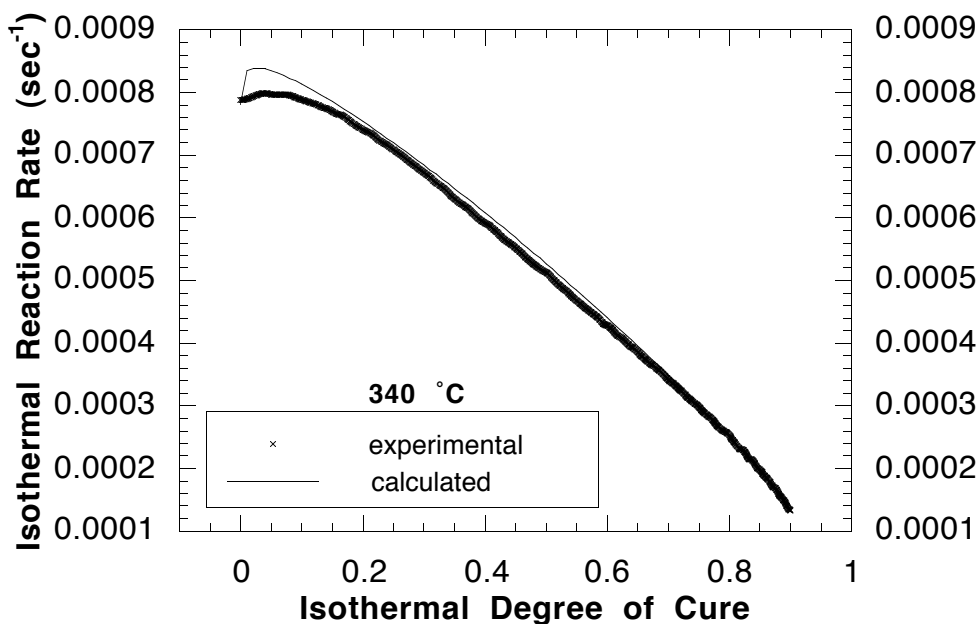


Figure 4.15.(b) 340 °C - da/dt Versus α : Calculated Compared with Experimental - Individually Selected Values of n (Table 4.2)

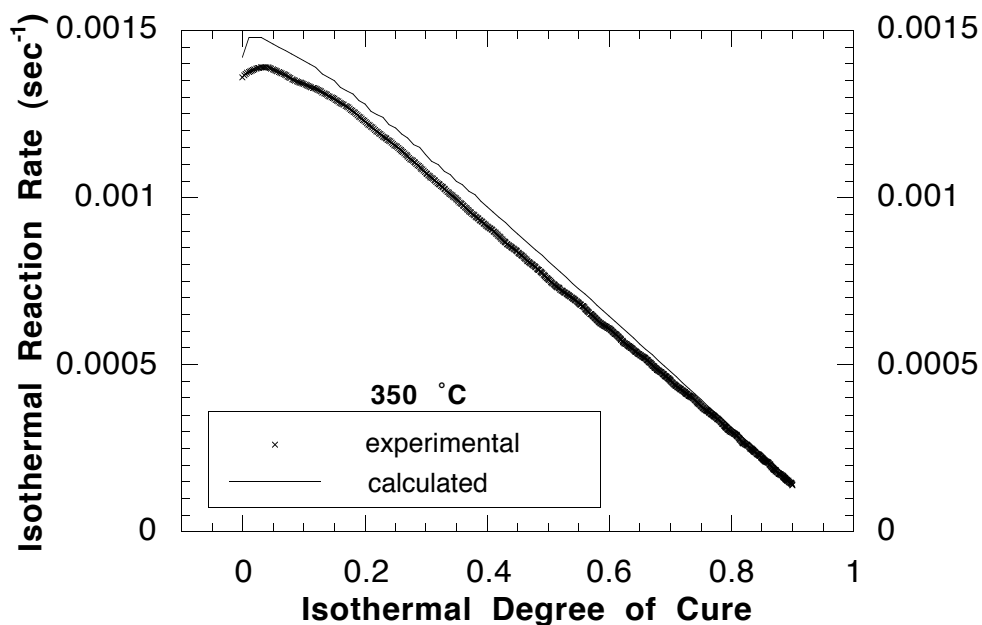


Figure 4.15.(c) 350 °C - $d\alpha/dt$ Versus α : Calculated Compared with Experimental - Individually Selected Values of n (Table 4.2)

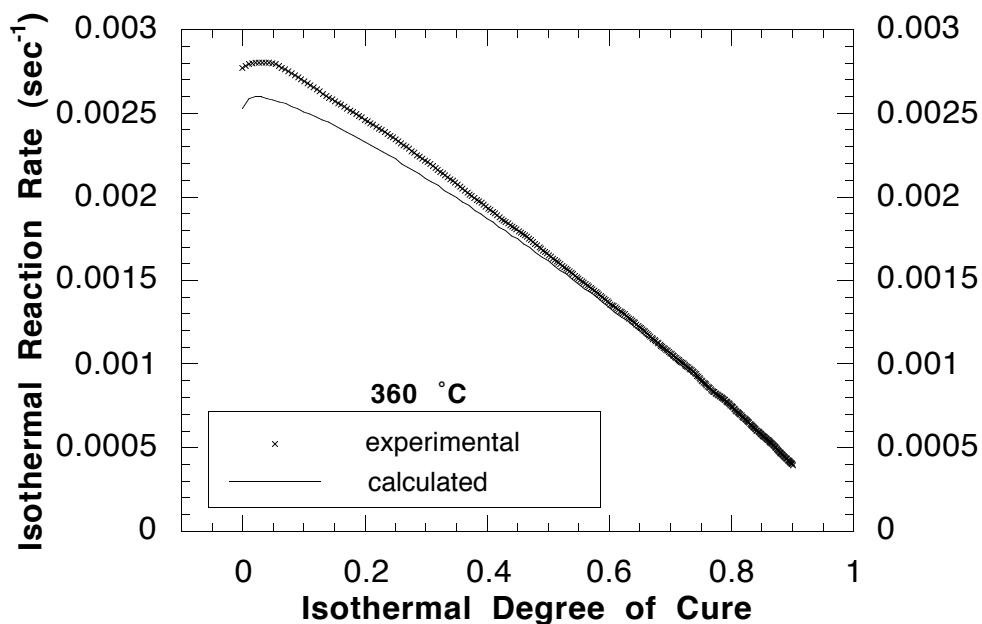


Figure 4.15.(d) 360 °C - $d\alpha/dt$ Versus α : Calculated Compared with Experimental - Individually Selected Values of n (Table 4.2)

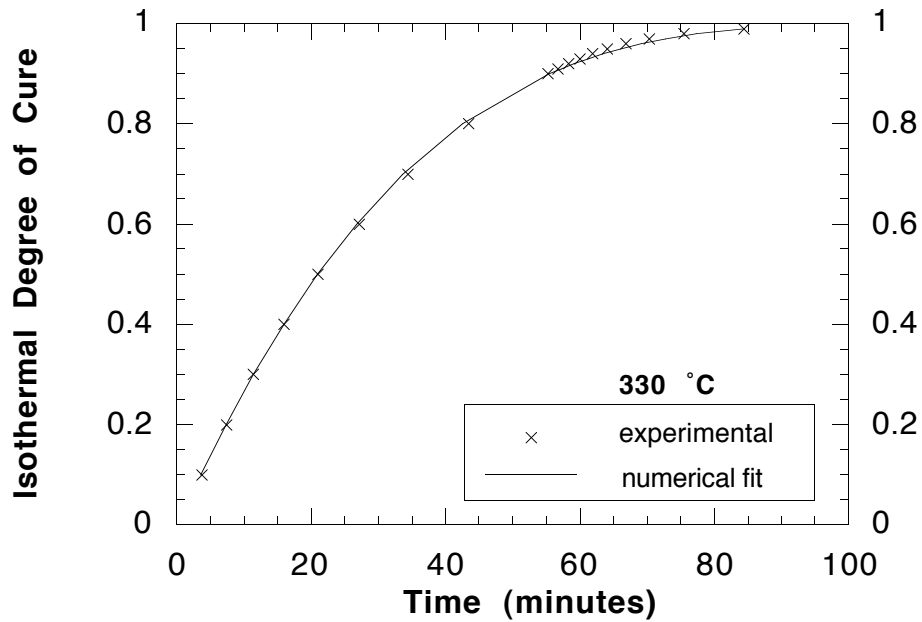


Figure 4.16.(a) α_I Versus Time (330 °C): Empirical Model Compared with Experimental Data

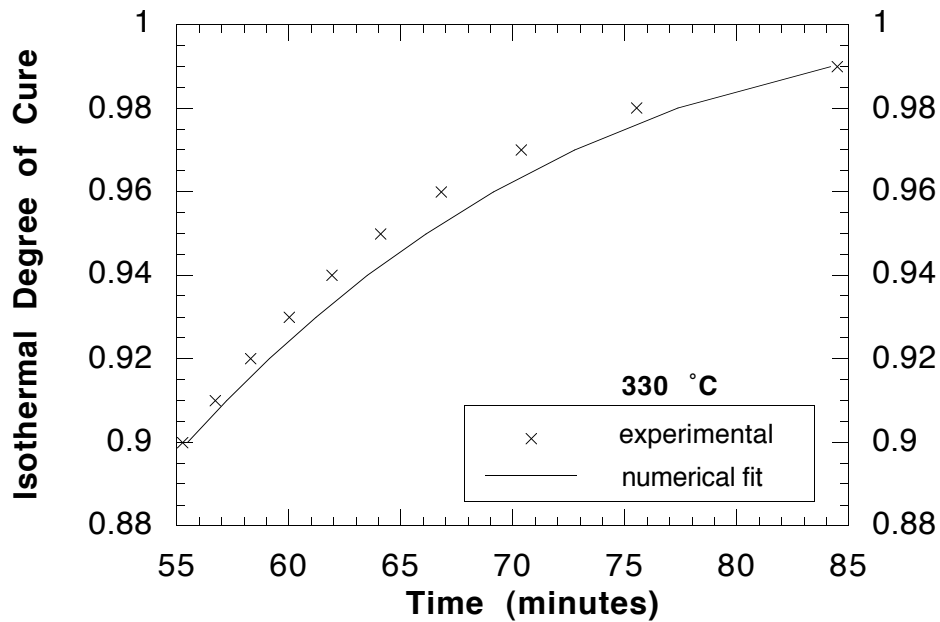


Figure 4.16.(b) α_I Versus Time (330 °C): Empirical Model Compared with Experimental Data for α_I Greater than 0.9

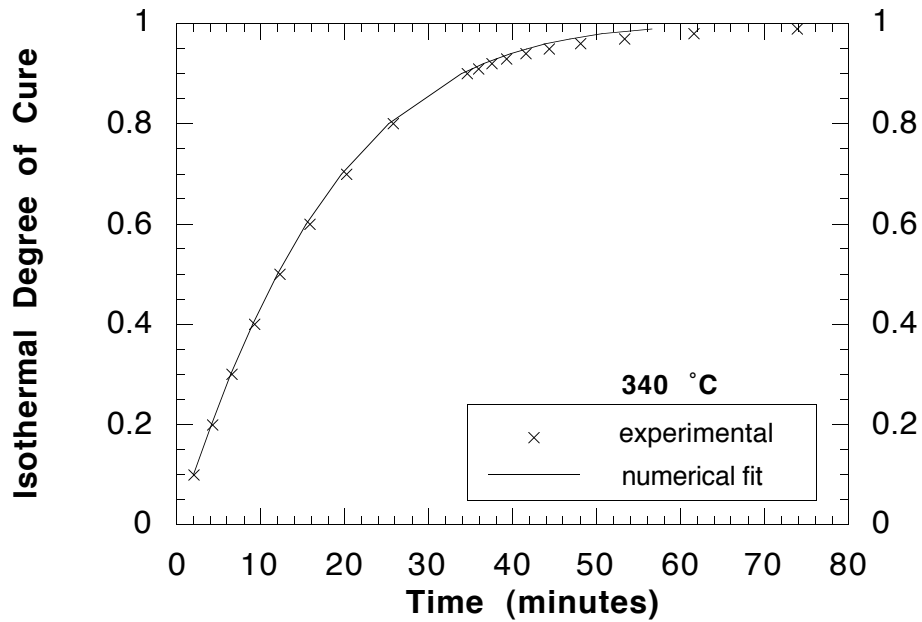


Figure 4.17.(a) α_I Versus Time (340 °C): Empirical Model Compared with Experimental Data

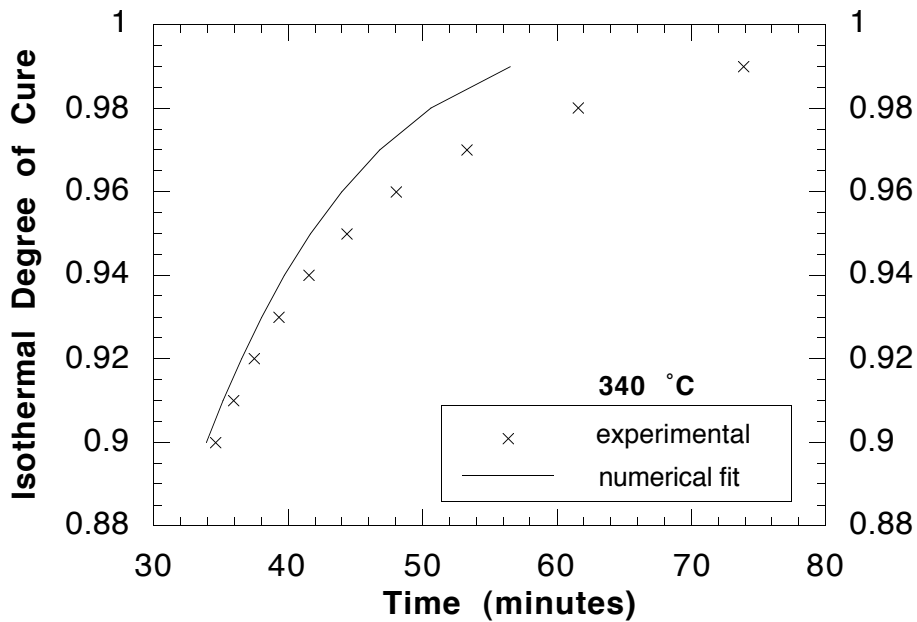


Figure 4.17.(b) α_I Versus Time (340 °C): Empirical Model Compared with Experimental Data for α_I Greater than 0.9

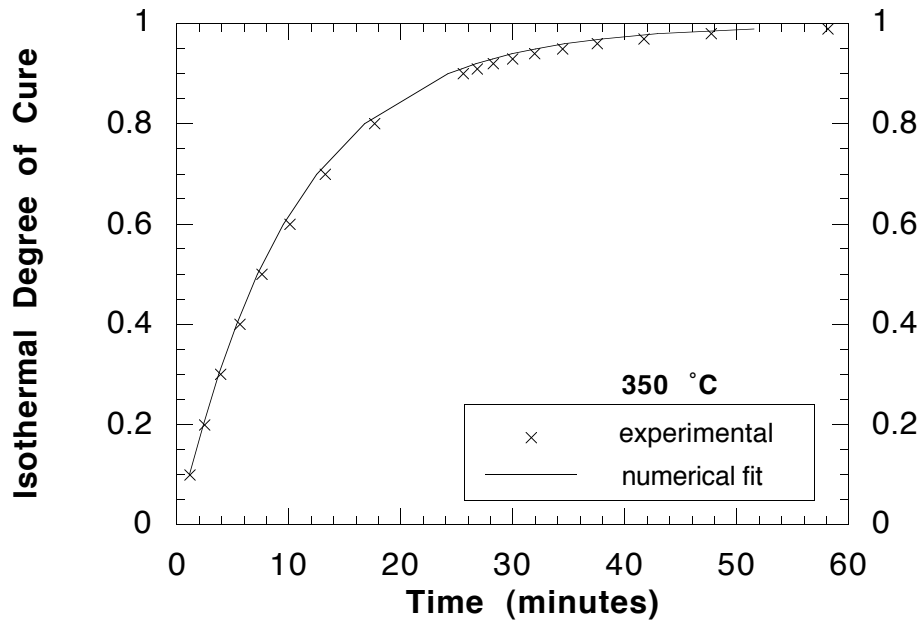


Figure 4.18.(a) α_l Versus Time (350 °C): Empirical Model Compared with Experimental Data

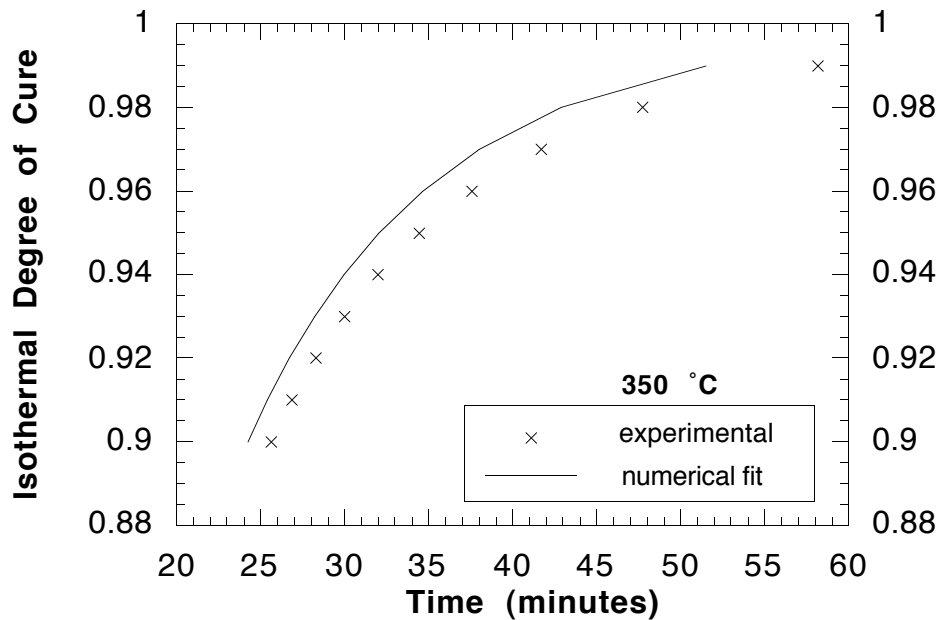


Figure 4.18.(b) α_l Versus Time (350 °C): Empirical Model Compared with Experimental Data for α_l Greater than 0.9

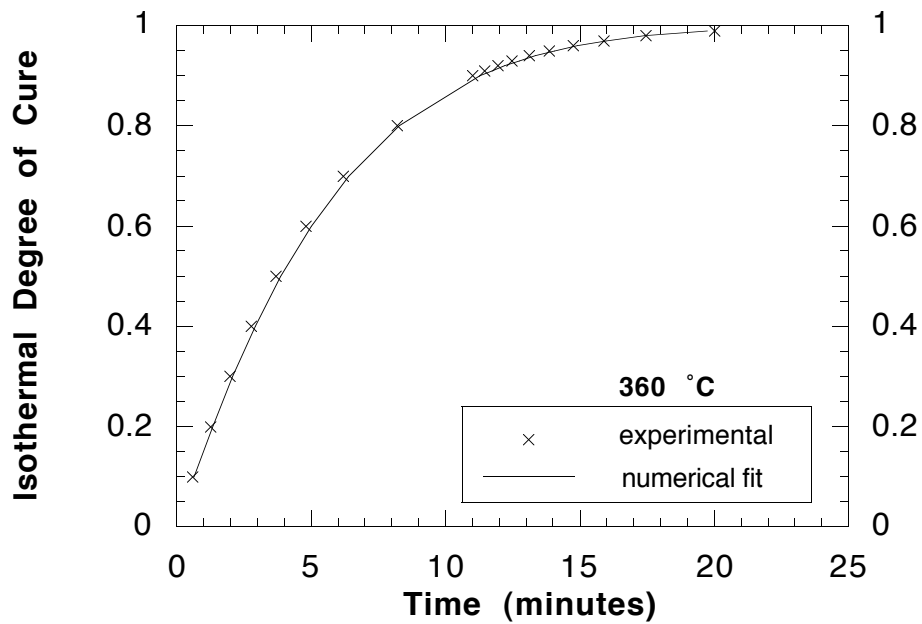


Figure 4.19.(a) α_l Versus Time (360 °C): Empirical Model Compared with Experimental Data

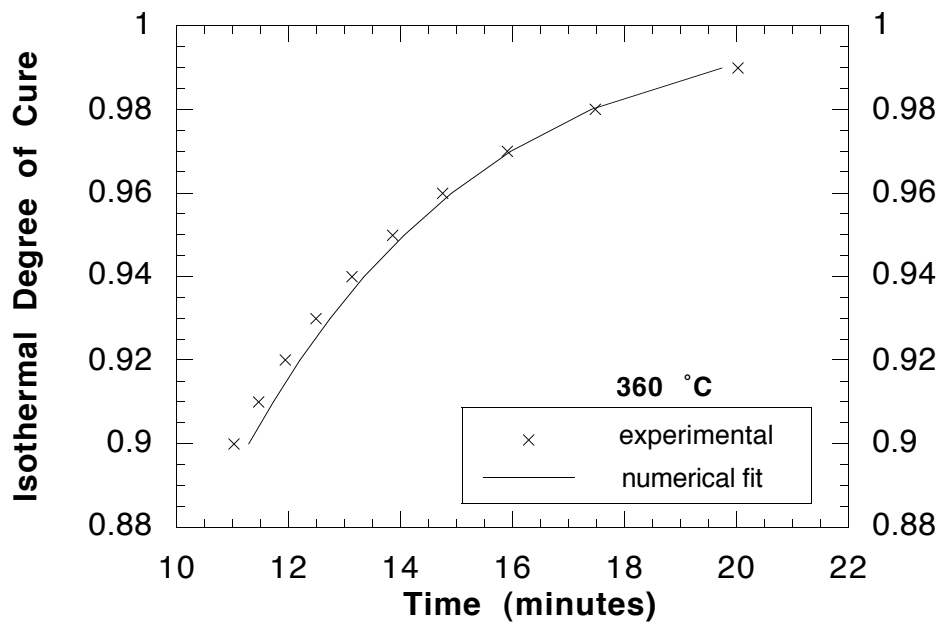


Figure 4.19.(b) α_l Versus Time (360 °C): Empirical Model Compared with Experimental Data for α_l Greater than 0.9

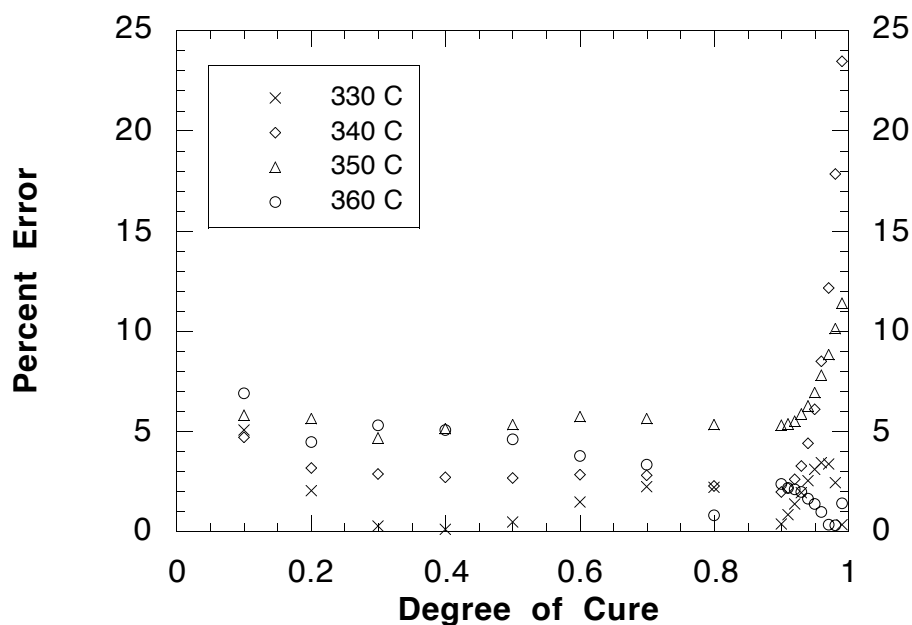


Figure 4.20. Percent Error in Calculated Time to Reach Predicted Degree of Cure For Combination Kinetics

4.6 Summary Discussion

Cure kinetics models were developed utilizing both first-order reaction kinetics and combination reaction kinetics. The combination reaction kinetics model is significantly more accurate than the first-order reaction kinetics model (Figures 4.6 and 4.20). Deviations between the models and experimental results at $\alpha_t > 0.9$ can be attributed to what appears to be a transition from a chemically controlled reaction to a diffusion controlled reaction (Figure 4.8).

The empirical model that was developed based on combination kinetics is temperature specific in that n is not given a fixed value or temperature dependence. Rather, n is individually selected for each temperature (Table 4.2). This selection of n significantly increases the agreement between predictions and experimental results. The combination reaction kinetics model works well for detailed prediction of degree of cure and reaction rate at any time throughout the whole range of cure for a selected temperature. If the model is made more general by giving n a fixed value or temperature dependence (Figure 4.14), accuracy is sacrificed. The first-order reaction kinetics model works better for quick estimation of degree of cure versus time for any temperature between 330 °C to 360 °C.

The calculations can be done by hand and do not require numerical integration to calculate α_t at any given time. Furthermore, the first-order reaction kinetics model is not temperature specific.

In the literature, there is a lack of consensus on the reaction order of PET mers. Some researchers [1,2,8] suggest that these reactions can be described by a simple order. Whereas, Hinkley [7] states that the reaction can not be described by a simple order. The results presented here show that whether the reaction order can be represented by a simple order depends on the level of analysis. If one simply looks to determine E_a and Z and predict α_t , it appears as though the reaction may follow first-order kinetics. However, upon attempting to verify that the reaction fits the shape of a $d\alpha/dt$ versus α curve for a n th-order reaction, one will find that the reaction does not appear to be n th-order (Figure 4.7). Analysis via combination reaction kinetics produces two reaction orders, m and n , for each temperature. Figures 4.12 and 4.13 demonstrate that neither m nor n has a set value or clear temperature dependence. The same can be said for their sum, which would be the reaction order for this combination reaction kinetics model, as shown in Figure 4.21.

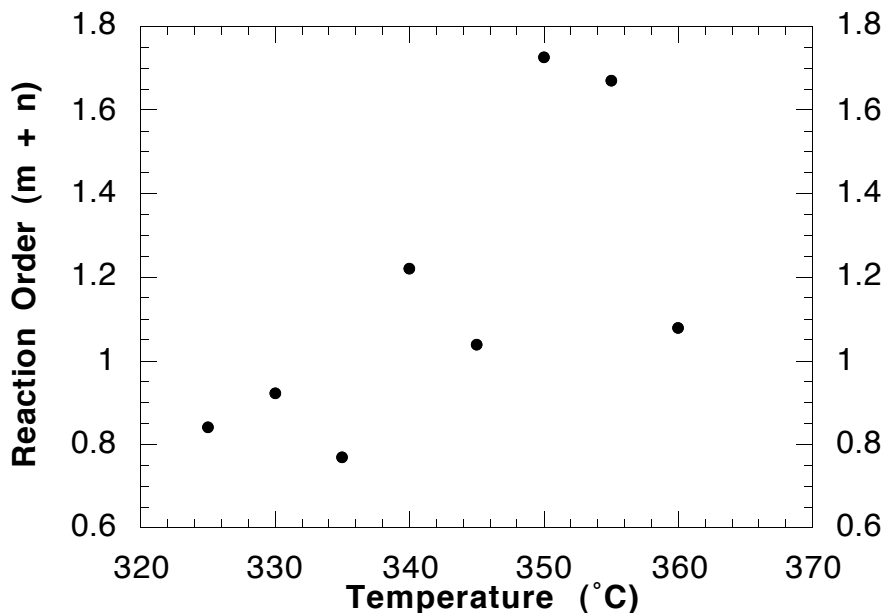


Figure 4.21. Lack of Simple Reaction Order

The cure kinetics models developed are based on isothermal DSC measurements. The chemically controlled portion of the reaction can be modeled well. However, it is apparent

that diffusion control overtakes chemical control. Thus, the end of the isothermal cures measured by DSC are not fit well by the developed models. Furthermore, other studies [5,6] have shown that cure of PET imide oligomers appears to continue despite being undetectable by DSC and FTIR. Therefore, additional information regarding cure was sought via other experimental techniques and methods. Discussion of these investigations follows in Chapter 5.

4.7 References

1. S.B. Sastri, J.P. Armistead, and T.M. Keller, "Cure Kinetics of a Multisubstituted Acetylenic Monomer," *Polymer*, **36**, (7), 1449-1454 (1995).
2. B. Tan, "Synthesis and Characterization of Phenylethynyl Endcapped Polyetherimide Oligomers," Ph.D. Dissertation, Virginia Tech, Blacksburg, VA, 1997.
3. T.V. Holland, T.E. Glass, and J.E. McGrath, "Investigation of the Thermal Curing Chemistry of the Phenylethynyl Group Using a Model Aryl Ether Imide," *Polymer*, **41**, (13), 4965-4990 (2000).
4. K.H. Wood, R.A. Orwoll, B.J. Jensen, P.R. Young, and H.M. McNair, "Cure Chemistry of Phenylethynyl Terminated Oligomers," *Proceedings of the 42nd International SAMPE Symposium and Exhibition*, 1271-1282 (1997).
5. K.A. Harrington, R.A. Orwoll, B.J. Jensen, and P.R. Young, "Characterization of Cure Chemistry of Selected Phenylethynyl-Terminated Polyimides and Model Compounds," *Proceedings of the 41st International SAMPE Symposium and Exhibition*, Anaheim, CA, 135-148 (1996).
6. J.A. Johnston, F.M. Li, F.W. Harris, and T. Takekoshi, "Synthesis and Characterization of Imide Oligomers End-capped with 4-(Phenylethynyl)Phthalic Anhydrides," *Polymer*, **35**, (22), 4865-4873 (1994).
7. J.A. Hinkley, "DSC Study of the Cure of a Phenylethynyl-Terminated Imide Oligomer," *Journal of Advanced Materials*, **27**, (3), 55-60 (1996).
8. T. Takekoshi and J.M. Terry, "High-Temperature Thermoset Polyimides Containing Disubstituted Acetylene End Groups," *Polymer*, **35**, (22), 4874-4880 (1994).
9. A. Ayambem, S. Mecham, Y. Sun, and J.E. McGrath, "Synthesis, Characterization, and Cure Studies of Phenylethynyl-Terminated Poly(arylene ether sulfones)," *Polymer Preprints*, **38**, (2), 373-374 (1997).
10. R.J. Cano and B.J. Jensen, "Effect of Molecular Weight on Processing and Adhesive Properties of the Phenylethynyl-Terminated Polyimide LaRC™-PETI-5," *Journal of Adhesion*, **60**, 113-123 (1997).
11. T. Ozawa, "Kinetic Analysis of Derivative Curves in Thermal Analysis," *Journal of Thermal Analysis*, **2**, pp. 301-324 (1970).

12. R.B. Prime in Thermal Characterization of Polymeric Materials, 2nd Edition, E.A. Turi, ed., American Press, New York, 1997, pp. 1600, 1601, 1608, 1641.
13. J.D. Nam and J.C. Seferis, "Application of the Kinetic Composite Methodology to Autocatalytic-Type Thermoset Prepreg Cures," *Journal of Applied Polymer Science*, **50**, 1555-1564 (1993).
14. TA Instruments, Inc., "A Review of DSC Kinetics Methods," TA Instruments, Inc., New Castle, DE, USA.

Chapter 5 - Monitoring Reaction Progress via Glass Transition Temperature

Mark P. Stoykovich must be given a major acknowledgement for this chapter. He did a great deal of the work presented here as a participant in the Summer Undergraduate Research Program sponsored by the National Science Foundation Science and Technology Center for High Performance Polymeric Adhesives and Composites at Virginia Polytechnic Institute and State University.

5.1 Introduction

The previous chapter presented an investigation of the cure kinetics of 2.5kPETU. The study found that the latter stages of cure displayed behavior indicative of diffusion control. It is likely diffusion would play a major role as network structures formed increasing the difficulty of moving long molecular chains through the growing networks. The previous chapter presented research [1,2] in which reaction progress had ceased according to monitoring via differential scanning calorimetry (DSC) and Fourier transform infrared spectroscopy (FTIR), but the glass transition temperature, T_g , continued to increase. DSC monitors reaction progress by detecting heat given off by the exothermic chain growth and crosslinking reaction. Due to diffusion control, the reaction rate may drop to such a low level that an undetectable amount of heat is given off by further cure. FTIR monitors reaction progress of phenylethynyl-terminated (PET) mers by tracking the presence of ethynyl groups. FTIR may see reaction as complete due the absence of these carbon-carbon triple bonds. However, further reaction may occur between compounds no longer containing triple bonds, thus explaining T_g increases beyond the disappearance of the ethynyl FTIR peak. Due to the limitations of monitoring cure of 2.5kPETU with DSC and FTIR, an attempt will be made to monitor reaction progress through T_g measurements following different cure schedules. Johnston, et al. [1], and Harrington, et al. [2], utilized DSC T_g measurements to monitor reaction progress of PET imide oligomers beyond the points at which DSC and FTIR could no longer detect additional cure.

5.2 Background

5.2.1 Glass Transition Temperature

In the development of the cure kinetics models for 2.5kPETU, isothermal DSC scans ranging in temperature from 315 °C to 390 °C were followed by temperature ramps at 5 °C/min from 150 °C to 425 °C to measure residual cure and the T_g resulting from the

isothermal cure (isothermal T_g). Most specimens showed very little, if any, residual cure. The isothermal T_g values did show an interesting trend. Isothermal hold temperatures of 345 °C and greater resulted in isothermal T_g values up to 17 °C below that of the maximum isothermal T_g , 258.97 °C, measured following a 259 minute hold at 325 °C. Isothermal hold conditions and the isothermal glass transition temperatures measured during the residual ramps are given in Table 5.1 and Figure 5.1. The resultant isothermal glass transition temperatures indicate isothermal hold time may need to be limited at temperatures of 345 °C and greater; the T_g of 2.5kPETU appears to degrade when held too long at these temperatures. Isothermal hold time does not appear to be a problem with lower temperatures since most of the lower temperatures (below 340 °C) were held for as long as, or much longer, than the higher temperatures (Table 5.1).

Table 5.1. Isothermal Cure Conditions and Isothermal Glass Transition Temperatures

Isothermal Hold Temperature (°C)	Isothermal T_g (°C)	Isothermal Hold Time (min)
315	254	418
320	251	413
325	259	259
330	259	122
335	257	110
340	258	101
345	244	104
350	242	90
350	253	113
355	243	120
360	244	121
370	247	69
380	244	95
390	246	67

Thermogravimetric analysis (TGA) of a simulated cure schedule produced no significant mass loss. If degradation is occurring, the resultant products are not volatilizing. A sample of 2.5kPETU was ramped from room temperature to 250 °C at 5 °C/min, then ramped from 250 °C to 350 °C at 3 °C/min, and finally held at 350 °C for approximately two hours. There was a mass loss of approximately 3.75% during the ramps up to 350 °C; based on previous degassing of PETU, this mass is suspected to be residual solvent

remaining from synthesis. During the first 20 minutes of the 350 °C hold, there was a mass loss of 0.06%. No additional mass loss was detected.

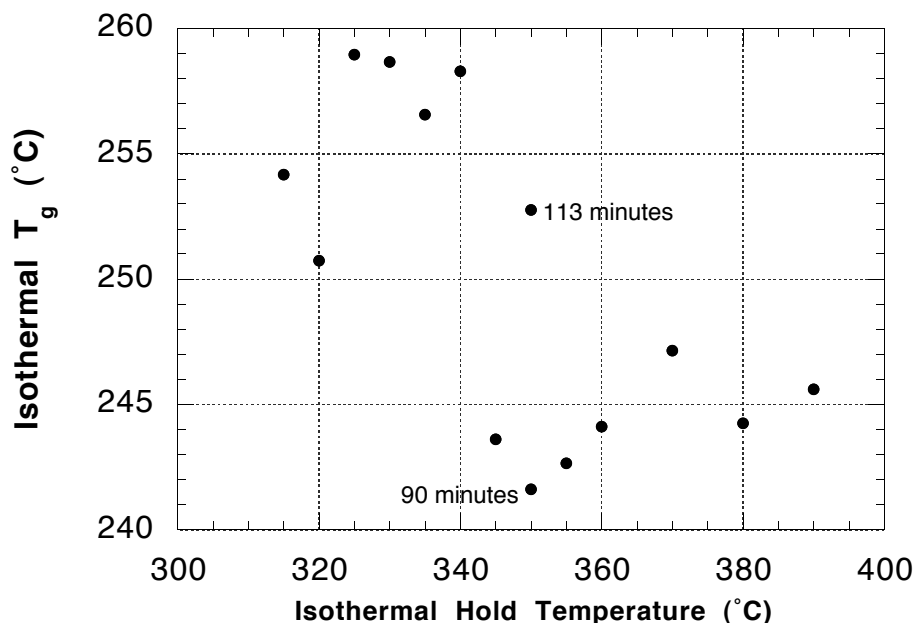


Figure 5.1. Resultant Isothermal T_g Versus Isothermal Hold Temperature

The temperature of 350 °C was selected to study the influence of varying isothermal cure time on the isothermal T_g. This temperature is near the transition region in Figure 5.1 and shows differing results for two isothermal holds similar in length (90 and 113 minutes). In addition, 350 °C was the suggested cure temperature of the synthesizers of PETU [3]. Isothermal 350 °C cures were run for: 40, 50, 60, 70, 75 and 80 minutes. These, along with the 90 and 113 minute, isothermal runs were followed by temperature ramps at 5 °C/min from 150 °C to 425 °C to measure T_g. The results of these T_g measurements are given in Figure 5.2. An increase in T_g is seen with increasing hold time up to 70 minutes. Beyond 70 minutes, the T_g is significantly reduced.

This reduction in T_g distinctly contrasts the conclusions drawn for the 5000 g/mol PETI-5 material studied by NASA [2]. These phenylethynyl-terminated imides have similar endcaps, structure, and properties to PETU. Harrington, et al. [2], report that the PETI-5 T_g measured via DSC following isothermal holds approaches a maximum value and plateaus with increasing time; one hour of curing at 375 °C produced the maximum T_g of 273 °C and this T_g was maintained for an additional hour of curing. Johnston, et al. [1],

studied a 7,000 g/mol PET imide using isothermal cures of 370 °C, 400 °C, and 420 °C. A 45 hour hold at 370 °C produced a T_g of 360 °C, which was achieved in one hour at 420 °C. These two PET imides do not display T_g reduction at cure temperatures that do reduce the T_g of 2.5kPETU. Their higher molecular weights may be responsible for their avoidance of T_g reduction during the reported cure schedules.

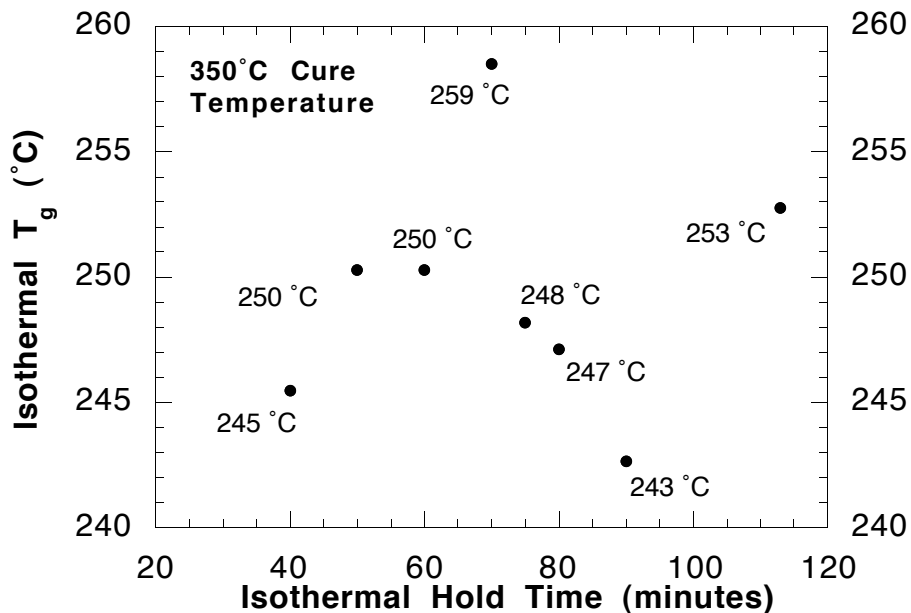


Figure 5.2. Influence of Cure Time on T_g for an Isothermal 350 °C Hold

Higher molecular weights translate into longer polymer chains that require more energy for diffusion and likely have a lower crosslink density. The greater energy needed for diffusion is seen in the 45 hours that are required for the 7,000 g/mol PET imide to reach its maximum T_g when cured at 370 °C. Additionally, the lower crosslink densities would allow chains to have more freedom for movement between crosslinks. These increases in energy absorption capability would reduce the amount of energy available for the degradative action of bond breaking. The point being that these two similar PET imides may display the same T_g reduction behavior seen in 2.5kPETU if their oligomer molecular weights were reduced to a similar value.

The preliminary research demonstrates the influence of cure time and temperature on the T_g of 2.5kPETU. In light of diffusion control of the latter stages of cure hindering reaction

monitoring by DSC and FTIR, cure schedule development will focus on optimizing T_g as a function of cure time and temperature.

5.2.2. Central Composite Design Experiment

A modified central composite design (CCD) experimental method was utilized to determine the optimal cure schedule to maximize the T_g of 2.5kPETU. CCD is a method of relating two experimental variables to a third response variable. Results from several experiments allow the prediction of the response variable upon fixing the values of the two independent variables [4]. Thus, cure time and temperature were selected as the independent variables, and T_g was chosen as the response variable.

Typically in a second-order CCD experiment, nine test conditions are selected based on the organization of the CCD and previous screening experiments (e.g., T_g versus cure time and temperature in Figures 5.1 and 5.2). The test scheme for a second-order CCD experiment is shown in Figure 5.3. However, the exact positions in the CCD do not have to be followed rigidly. The central point is chosen to be at or near the expected optimal conditions. From previous experiments, the designer should have an idea of the ranges of independent variables to test. The ranges determine the outer points of the CCD; the values in Figure 5.3 are the ratios of the distances of the outer points from the central point. The results of the experiments performed following the test conditions at each matrix point are analyzed to calculate a quadratic response surface fit and subsequently produce a contour plot describing the influence of the two independent variables on the response variable.

5.2.3 Glass Transition Temperature Measurement Techniques

Several analytical techniques can be used to measure T_g , and there has been considerable discussion in the literature as to which techniques provide the most consistent and accurate T_g results [5-10]. Three important analysis tools for determining T_g are the static techniques of thermomechanical analysis (TMA) and DSC, and the dynamic technique of dynamic mechanical thermal analysis (DMTA). Each of these techniques is influenced by distinct instrumental, material, and test characteristics (e.g., heating rate, test frequency, etc.). Moreover, for each technique, T_g can be defined in several different ways depending upon the methods of extrapolating baselines, taking derivatives, analyzing transition regions, and assigning onset criteria [5]. DSC measured glass transition temperatures are commonly reported by finding the half-height, inflection point, or onset of the transition in heat capacity or heat flow. The T_g of DMTA data can be reported as the $\tan \delta$ peak, loss

modulus peak, or onset of the storage modulus decrease. This study will define T_g by both DSC and DMTA using the inflection point and peak $\tan \delta$, respectively.

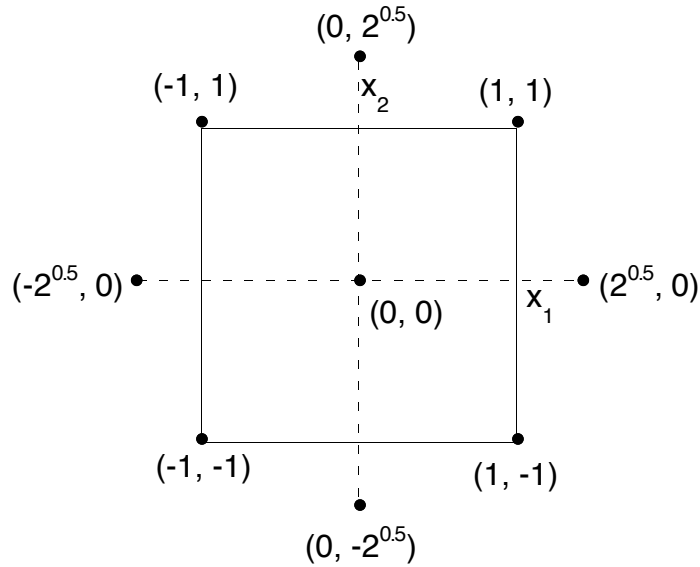


Figure 5.3. Second-Order Central Composite Design
{From Myers and Montgomery [4], page 299}

5.3 Experimental

5.3.1 Preliminary Work

The preliminary research of T_g dependence on cure time and temperature used solely isothermal runs. To develop an optimal cure schedule, the heating and cooling ramps involved in a real process must be considered. Therefore, this study utilized cure schedules involving these temperature ramps. The time required for these ramps was considered in the design of the CCD schemes. As seen in Figure 4.1, 2.5kPETU cure onsets at about 325 °C. Therefore, it was assumed that any time spent above 325 °C was time that cure may be taking place. Rather than designing the experiments such that each maximum cure temperature was held for a certain time upon reaching that temperature, the time was reported as the time the cure temperature was at or above 325 °C. For example, holds at 340 °C and 350 °C could have the same reported cure time, but would be at the maximum temperature for different lengths of time due to the longer time it would take to ramp up from 325 °C to 350 °C and back down to 325 °C than to complete the same ramps with a maximum temperature of 340 °C.

The T_g of 2.5kPETU was measured in three different material forms: neat resin, towpreg resin, and composite matrix. To measure the T_g of 2.5kPETU in composite matrix form, nine composite panels were consolidated in a hot press following different cure schedules. Specimens were then cut from these panels for T_g measurement via DSC and DMTA. Neat resin and towpreg resin DSC specimens were cured in the DSC cell following cure schedules modeled after the composite panel cure schedules. Following DSC curing, the specimens' glass transition temperatures were measured via DSC.

5.3.2 Composite Panels

5.3.2.1 Composite Manufacture

The carbon fiber-reinforced (CFR) 2.5kPETU composite panels were manufactured from powder coated towpreg utilizing an intermediate modulus (G40-800) 24k tow of 5 μm diameter filaments from Toho Carbon Fibers, Inc. The unidirectional panels were consolidated in a 76.2 mm square mold under maximum consolidation pressures that ranged from 650 to 1100 kPa. The cure times and temperatures for these nine panels are given in Figure 5.4. The lack of symmetry in the CCD scheme was a result of material limitations. The two panels consolidated at 350 $^{\circ}\text{C}$ were manufactured prior to the beginning of this study and enough material remained for the manufacture of only seven more panels.

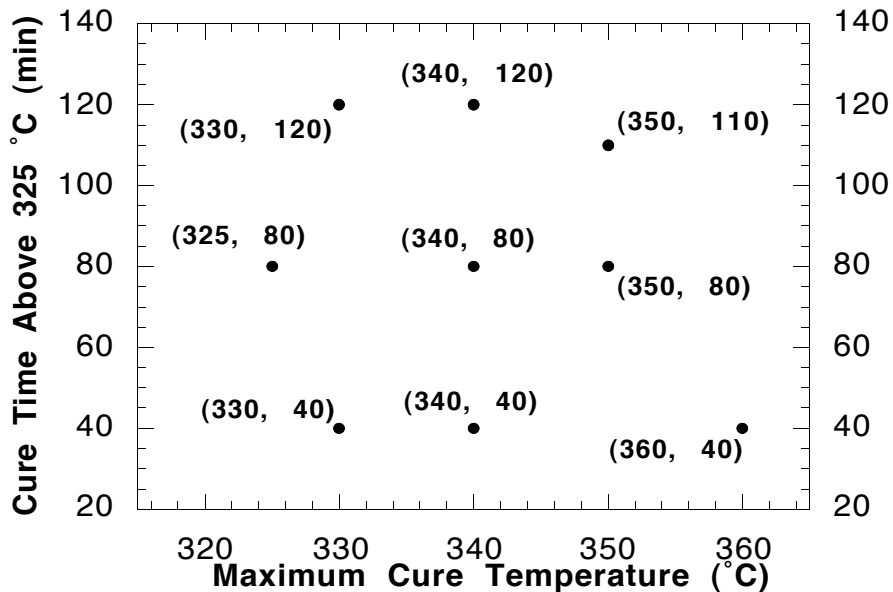


Figure 5.4. Cure Schedule CCD Scheme for Composites and First Set of Neat Resin Samples

The cure schedules commenced with a ramp at 5 °C/min from room temperature to 250 °C. The ramp rate was then reduced to 3 °C/min until the temperature reached 325 °C. The ramp rate from 325 °C to the hold temperature was programmed to be 3 °C/min, and the ramp rate from the hold temperature back down to 325 °C was programmed to be 4 °C/min, as was the ramp rate from 325 °C back to room temperature. However, the actual mold temperature did not exactly follow these ramp rates between the hold temperature and 325 °C. The actual average ramp rates are documented in Table 5.2. These deviations from the programmed ramp rate were taken into consideration in the design of DSC cure schedules of neat resin and towpreg.

Table 5.2. Ramp Rates Between 325 °C and Hold Temperatures for Composite Cures

Cure Conditions [°C] / [min]	Ramp Rate: 325 °C to Hold (°C/min)	Ramp Rate: Hold to 325 °C (°C/min)
325 / 80	NA	NA
330 / 40	1.94	2.30
330 / 120	1.75	2.27
340 / 40	2.34	2.99
340 / 80	2.29	2.64
340 / 120	1.91	2.62
350 / 80	2.33	2.64
350 / 110	2.33	2.64
360 / 40	3.05	3.15

5.3.2.2 DMTA Testing

Ultrasonic inspection was utilized to select the well-consolidated portions of the panels for cutting of DMTA specimens. Two 12.7 mm x 50.8 mm specimens were machined from the well-consolidated regions of each panel with the long edges parallel to the fiber direction. The specimens were approximately 1.6 mm thick. Using a Polymer Laboratories DMTA system, the specimens were tested in single cantilever mode at a frequency of 1 Hz, while the temperature was ramped at 2 °C/min from approximately 180 °C to approximately 10 °C beyond the tan δ peak.

5.3.2.3 DSC Measurements

Two DSC specimens were prepared from the composite panels by cutting small pieces of each panel and sealing them in aluminum hermetic pans. The composite masses ranged from 12.8 to 24.8 mg; these masses provided matrix resin masses of 3.7 to 6.7 mg. One

set of specimens was tested in a TA Instruments 2920 DSC; the second set was tested in a Perkin-Elmer Pyris 1 DSC. All DSC scans commenced with cell equilibration at 100 °C followed by a 20 °C/min ramp to approximately 300 °C. The DSC cell was purged with a nitrogen atmosphere.

5.3.3 Neat Resin

Following composite consolidation, nine DSC specimens were prepared by placing 5 to 6 mg of degassed, virgin 2.5kPETU powder in aluminum hermetic pans. Each one of these nine specimens was paired with one of the composite panel cure conditions shown in Figure 5.4. Each specimen was then cured in the nitrogen purged TA Instruments DSC cell following a cure schedule to duplicate that of the composite panel it was paired with in Figure 5.4. The cure schedule of the DSC neat resin specimens followed the same ramp rates as those given in Table 5.2 for the composites. The DSC cures were followed by DSC T_g measurements consisting of a 20 °C/min ramp from 100 °C to 300 °C in a nitrogen purged cell.

Based on the results of the T_g measurements on the samples cured following the cure schedules of Figure 5.4 and Table 5.2, a second cure schedule CCD scheme was developed with a narrower temperature range (Figure 5.5). Continuing with the theme of trying to simulate composite cure, the ramp rates between 325 °C and the hold temperature were based on those measured during composite cure (Table 5.2); the ramp rates for the CCD scheme shown in Figure 5.5 are given in Table 5.3. As before, the DSC cures were followed by DSC T_g measurements consisting of a 20 °C/min ramp from 100 °C to 300 °C in a nitrogen purged cell.

5.3.4 Towpreg

Due to significant discrepancies between the measured influences of time and temperature on the T_g of 2.5kPETU in composite matrix and neat resin forms, the possibility of a fiber influence was considered. Not enough towpreg remained to consolidate additional composite panels. Therefore, the possibility of a fiber influence on the resultant T_g of 2.5kPETU was investigated by running DSC measurements on towpreg samples. The towpreg DSC specimens contained approximately 2 to 5 mg of resin; exact quantities were not available due to the inconsistent fiber volume fraction of the towpreg on such a small scale. However, specimen mass is not critical to T_g measurement. The use of towpreg DSC specimens not only overcomes the inability to manufacture additional composite

panels for DMTA specimens, curing towpreg within the DSC cell eliminates any discrepancies that may exist between curing the composite panels in a hot press versus curing neat resin in the small, precisely controlled DSC cell.

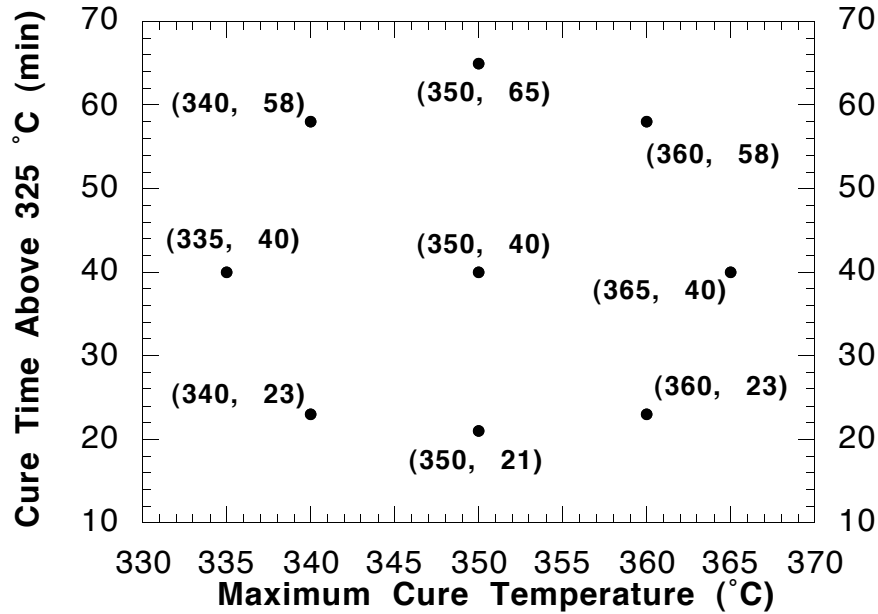


Figure 5.5. Cure Schedule CCD Scheme for Second Set of Neat Resin Samples

Table 5.3. Ramp Rates Between 325 °C and Maximum Cure Temperatures for Neat Resin and Towpreg Resin DSC Cures

Maximum Cure Temperature (°C)	Ramp Rate Up From 325 °C (°C/min)	Ramp Rate Down From 325 °C (°C/min)
335	2.1	2.6
340	2.3	2.7
350	2.3	2.7
355	2.65	2.95
360	3.0	3.2
365	3.0	3.2
372.5	3.0	3.2
385	3.0	3.2
395	3.0	3.2

A cure schedule CCD matrix (Figure 5.6) was designed for the towpreg measurements to include the optimal neat resin conditions, yet be broad enough to detect a different trend, if present. As with the neat resin DSC cures, the ramps between 325 °C and the hold

temperatures were based on the measured composite cure conditions and are given in Table 5.3. The resultant glass transition temperatures were measured via 20 °C/min ramps from 100 °C to 300 °C in a nitrogen purged cell.

The first towpreg cure schedule CCD scheme did not contain the optimal cure condition. Therefore a second towpreg CCD scheme was designed (Figure 5.7) that included higher cure temperatures. Three of the cure conditions from Figure 5.6 were used in the second towpreg CCD scheme; thus only six additional measurements were required. Ramp rates between 325 °C and hold temperatures are given in Table 5.3. The T_g measurements were done in the same manner as all previous DSC T_g measurements.

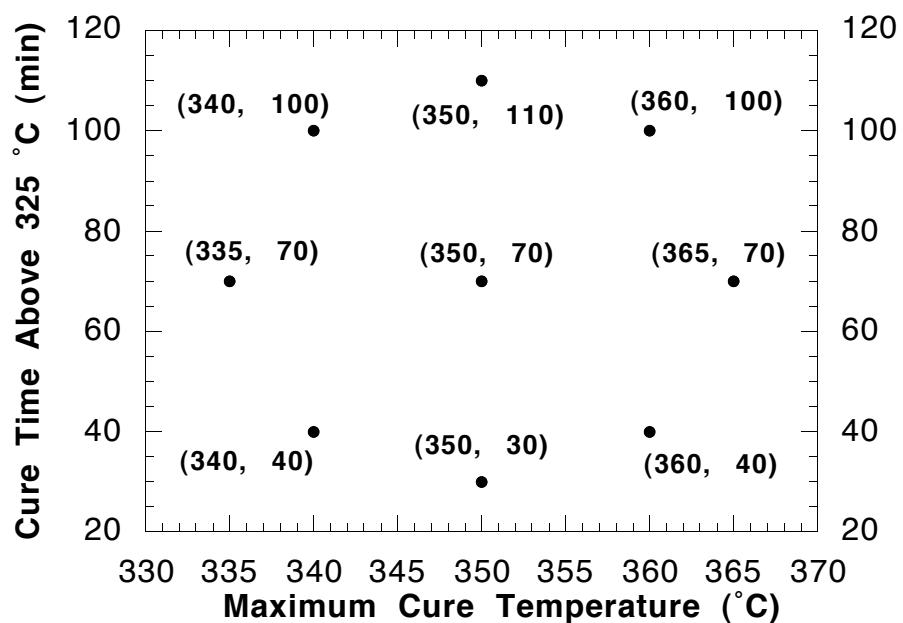


Figure 5.6. Cure Schedule CCD Scheme for First Set of Towpreg Samples

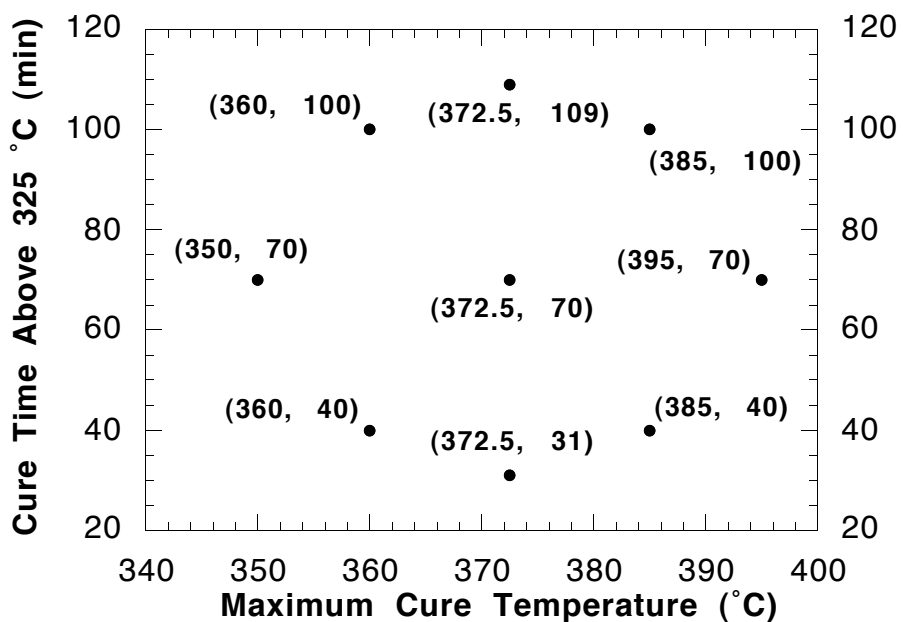


Figure 5.7. Cure Schedule CCD Scheme for Second Set of Towpreg Samples

5.4 Results

The results for this study will be presented by first giving the resultant glass transition temperatures for each test condition in each CCD scheme. Following each CCD scheme, the resultant contour plot of T_g versus cure time and temperature will be presented.

5.4.1 Composite Panels

The 2.5kPETU composite matrix T_g was measured via DMTA and DSC. A typical DMTA plot is shown in Figure 5.8; these results are for the 360/40 (360 °C for 40 minutes above 325 °C) composite specimen. The composite CCD scheme is shown in Figure 5.9 with the resultant T_g values for each condition. Minitab [11] statistics software used these conditions and results to calculate a quadratic response surface fit. The resulting best fit equation is given by Equation 5.1, where t is the cure time above 325 °C and T is the maximum cure temperature. Minitab was subsequently used to generate the contour plot of Figure 5.10.

$$T_g (\text{°C}) = -1.61 \times 10^3 - 0.0252t + 9.73T - 0.00184t^2 - 0.0129T^2 + 0.00213tT \quad (5.1)$$

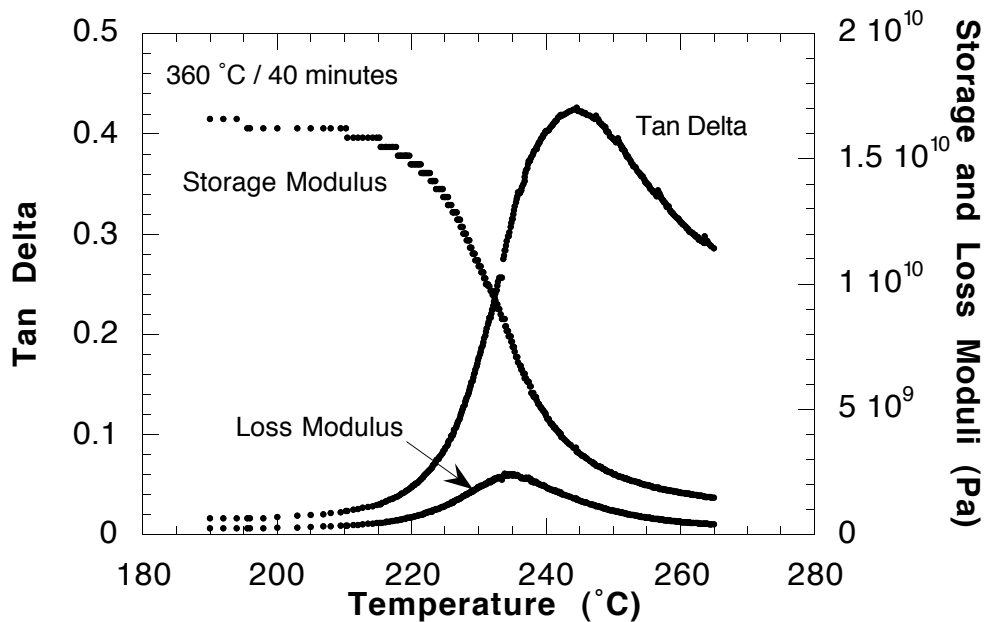


Figure 5.8. Sample Plot of Data Taken Using Polymer Laboratories DMTA
Composite Specimen: 360 °C / 40 minutes

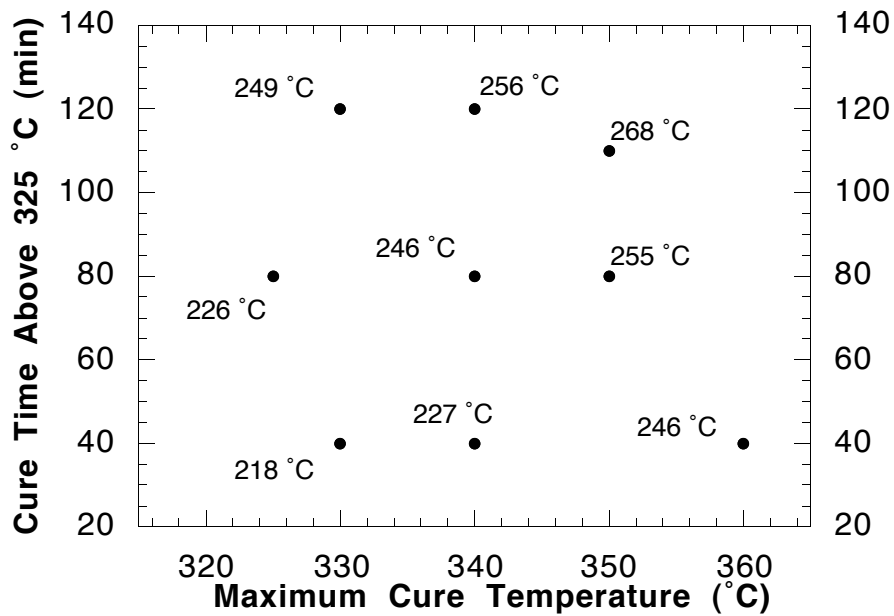


Figure 5.9. DMTA T_g Results for Composite Specimens

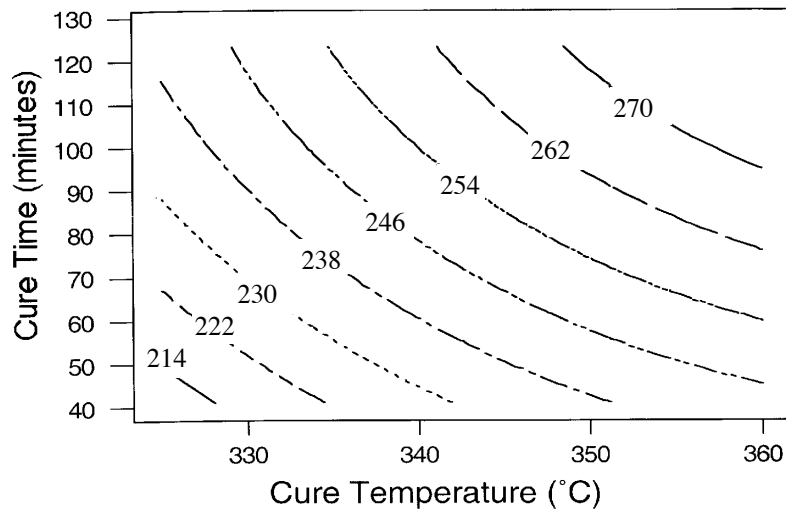


Figure 5.10. Contour Plot of DMTA T_g (°C) Results for Composite Specimens

The TA Instruments DSC measurements of the composite matrix glass transition temperatures are given in Figure 5.11. Though a difference is expected in the T_g values measured by DMTA and DSC, a difference as large as that seen in comparing Figures 5.9 and 5.11 was not expected. Due to the large discrepancy seen between the DMTA results and the TA Instruments DSC results, the DSC T_g measurements were repeated using a

Perkin-Elmer DSC. The composite matrix glass transition temperatures measured by the Perkin-Elmer DSC are also given in Figure 5.11. The calculated quadratic response surface fits for the TA Instruments and Perkin-Elmer DSC results are given in Equations 5.2 and 5.3, respectively. The contour plots generated from these fits are given in Figures 5.12 and 5.13.

$$T_g (\text{°C}) = -2.64 \times 10^3 + 0.641t + 15.6T - 0.00425t^2 - 0.0215T^2 + 0.000880tT \quad (5.2)$$

$$T_g (\text{°C}) = -3.48 \times 10^3 + 1.04t + 20.4T - 0.00289t^2 - 0.0284T^2 - 0.000917tT \quad (5.3)$$

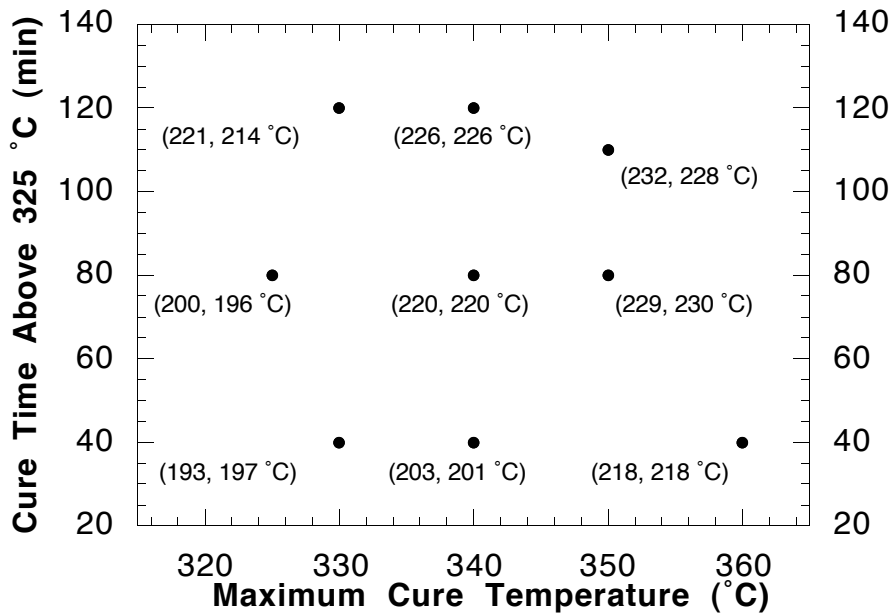


Figure 5.11. DSC T_g Results for Composite Specimens (Each Point Shows TA Instruments T_g followed by Perkin-Elmer T_g)

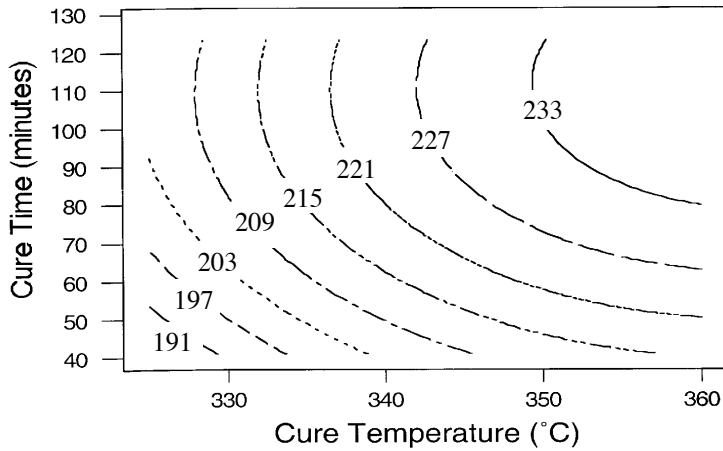


Figure 5.12. Contour Plot of TA Instruments DSC T_g ($^{\circ}\text{C}$) Results for Composite Specimens

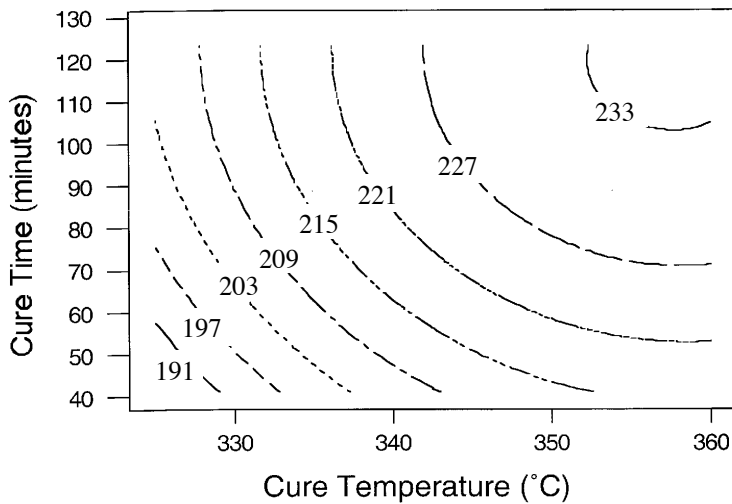


Figure 5.13. Contour Plot of Perkin-Elmer DSC T_g ($^{\circ}\text{C}$) Results for Composite Specimens

5.4.2 Neat Resin

The remaining T_g measurements for both neat resin and towpreg resin specimens were done in the TA Instruments DSC cell. The resultant glass transition temperatures for the neat resin specimens that were cured following the same cure schedules as the composite panels are given in Figure 5.14. The quadratic response surface fit calculated by Minitab for this data is given in Equation 5.4. The contour plot generated from this fit is shown in Figure 5.15. The measured glass transition temperatures for the second set (narrower temperature range) of neat resin specimens are shown in Figure 5.16. The quadratic

response surface fit is given in Equation 5.5, and the resultant contour plot is presented in Figure 5.17.

$$T_g (\text{°C}) = -1.04 \times 10^4 + 10.8t + 60.0T - 0.00319t^2 - 0.0840T^2 - 0.0304tT \quad (5.4)$$

$$T_g (\text{°C}) = -5.99 \times 10^3 + 5.57t + 34.4T - 0.0322t^2 - 0.0479T^2 - 0.00646tT \quad (5.5)$$

5.4.3 Towpreg Resin

Two cure schedule CCD schemes were run with towpreg DSC specimens. The cure conditions for the first scheme did not produce an optimal cure condition, thus the second CCD scheme implemented higher temperatures. The measured glass transition temperatures for the two towpreg CCD schemes are given in Figures 5.18 and 5.20. Equation 5.6 is the quadratic response surface fit for the first set of towpreg measurements (Figure 5.18), and Equation 5.7 is the fit for the second set (Figure 5.20). The contour plots demonstrating the effect of cure temperature and time on towpreg resin T_g are shown in Figures 5.19 and 5.21 for the first and second sets, respectively, of measurements.

$$T_g (\text{°C}) = 73.8 + 1.48t - 0.414T - 0.00389t^2 + 0.00213T^2 - 0.00148tT \quad (5.6)$$

$$T_g (\text{°C}) = -2.44 \times 10^3 + 3.71t + 13.3T - 0.00802t^2 - 0.0167T^2 - 0.00597tT \quad (5.7)$$

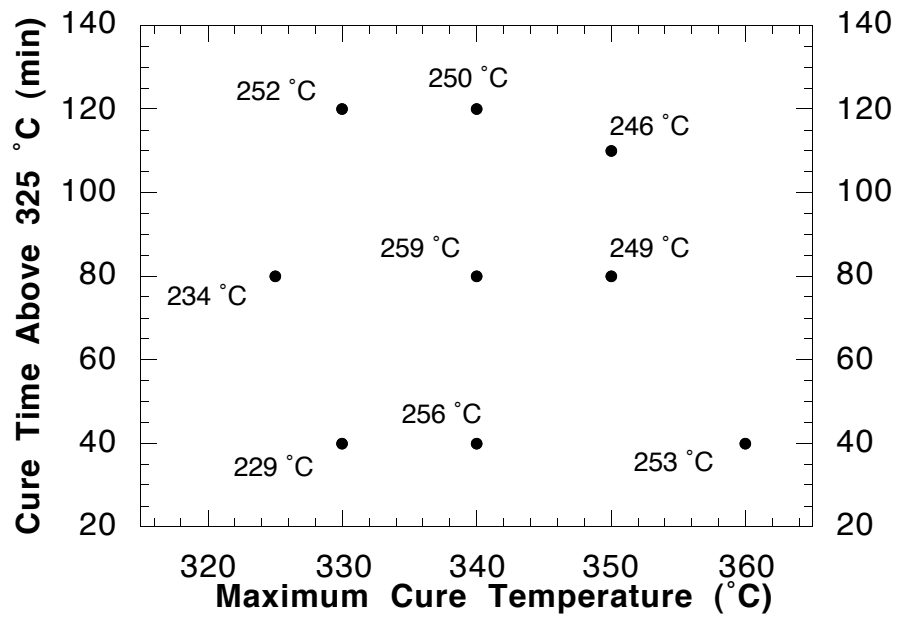


Figure 5.14. DSC T_g Results for Neat Resin Specimens Following Composite Cure Schedules

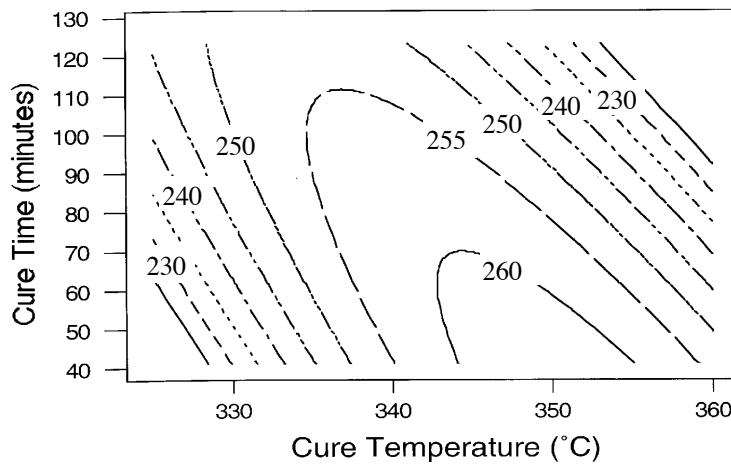


Figure 5.15. Contour Plot of TA Instruments DSC T_g (°C) Results for Neat Resin Specimens Following Composite Cure Schedules

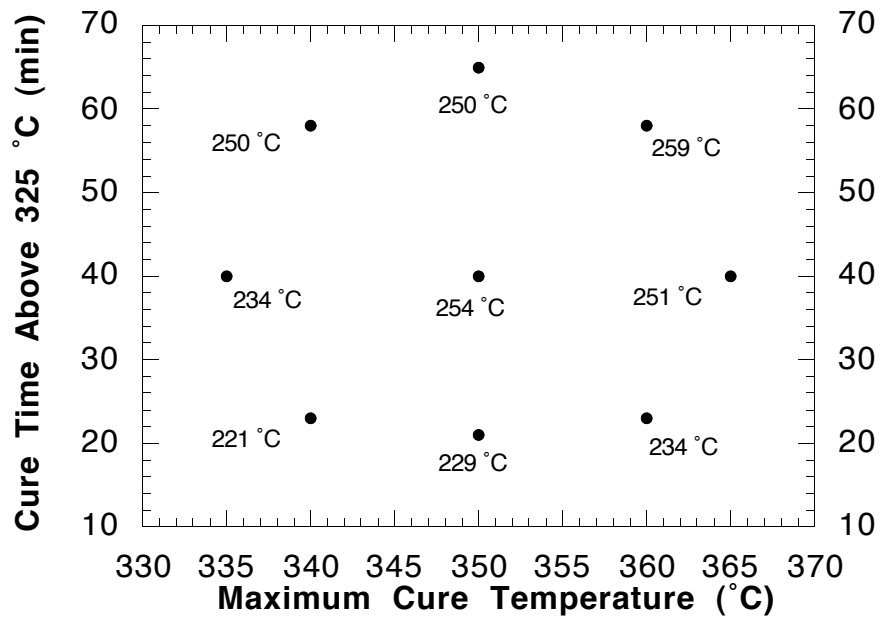


Figure 5.16. DSC T_g Results for Second Set of Neat Resin Specimens

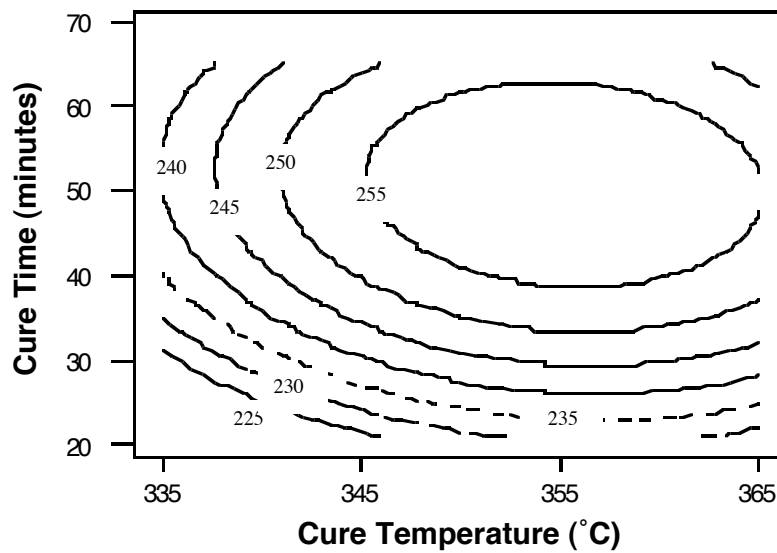


Figure 5.17. Contour Plot of DSC T_g (°C) Results for Second Set of Neat Resin Specimens

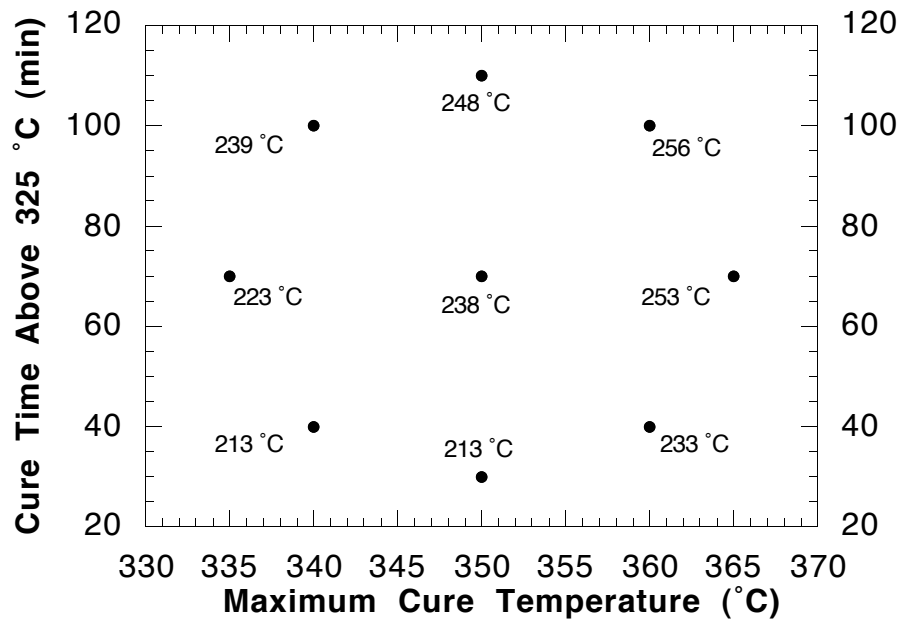


Figure 5.18. DSC T_g Results for First Set of Towpreg Resin Specimens

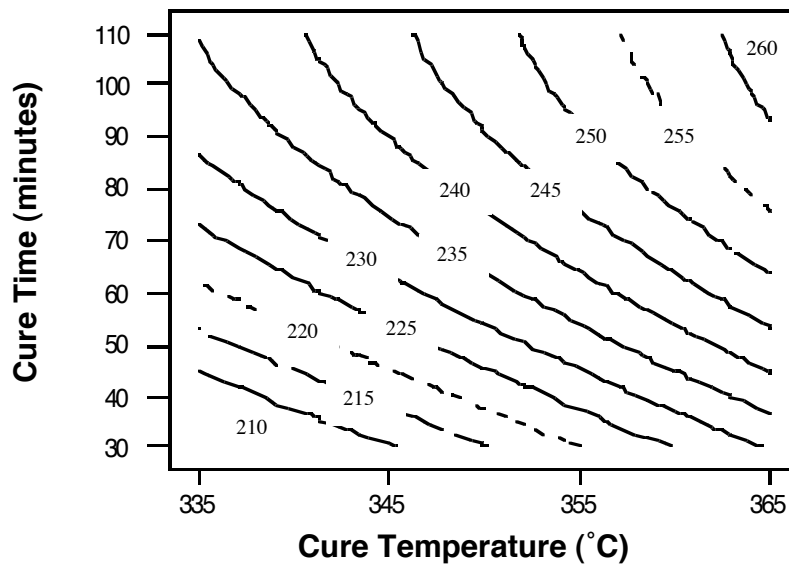


Figure 5.19. Contour Plot of DSC T_g (°C) Results for First Set of Towpreg Resin Specimens

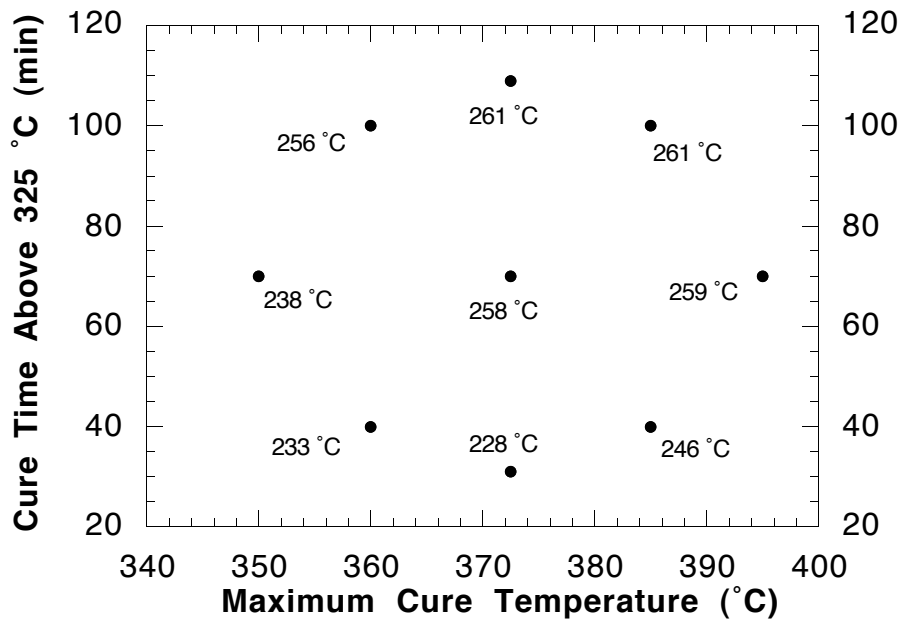


Figure 5.20. DSC T_g Results for Second Set of Towpreg Resin Specimens

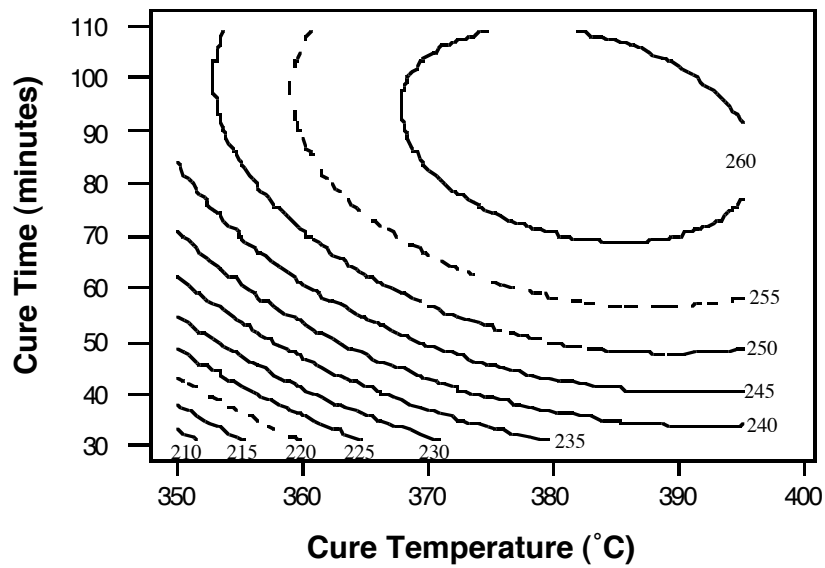


Figure 5.21. Contour Plot of DSC T_g (°C) Results for Second Set of Towpreg Resin Specimens

5.5 Discussion

Despite the large difference in the magnitudes of the composite matrix glass transition temperatures measured by DMTA (Figure 5.9) and DSC (Figure 5.11), the contour plots (Figures 5.10, 5.12, and 5.13) generated from these measured glass transition temperatures show the same trend in composite matrix T_g . These contour plots show the composite matrix T_g increasing with increasing cure time and temperature across cure time and temperature ranges that resulted in neat resin T_g reduction (Figures 5.1 and 5.2 and Table 5.1). The composite cure schedules selected in Figure 5.4 did not include combinations of cure time and temperature high enough to result in T_g reduction of composite matrix. However, repetition of the composite cure schedules with neat resin DSC specimens did demonstrate T_g reduction for the higher cure temperatures and times (Figure 5.14). Thus, the contour plot (Figure 5.15) generated from these neat resin glass transition temperatures demonstrated a different trend in T_g versus cure time and temperature than that shown by the composite matrix glass transition temperatures (Figures 5.10, 5.12, and 5.13). Rather than T_g increasing with increasing cure time and temperature, the neat resin specimens cured following the composite cure schedule predicted an optimal T_g for cure conditions near 350 °C and 40 minutes.

The second set of neat resin specimens also demonstrated T_g reduction and predicted an optimal cure condition near 355 °C and 50 minutes. The quadratic response surface fit (Equation 5.5) calculated from the results of the second set of neat resin specimens predicted a T_g of 259.7 °C for cure conditions of 355 °C and 50 minutes. An actual DSC cure of the neat resin at these conditions resulted in a DSC measured T_g of 259.0 °C. Thus, the apparent optimal cure conditions for neat 2.5kPETU consist of a ramp up to a maximum cure temperature ranging from 345 °C to 355 °C with a hold time selected to provide 45 to 55 minutes of temperature greater than 325 °C. These cure conditions agree well with those determined from the cure kinetics study on neat 2.5kPETU in Chapter 4 (Figure 4.18).

The optimal cure conditions determined for neat 2.5kPETU do not agree well with the optimal cure conditions determined for CFR 2.5kPETU. Towpreg samples demonstrated optimal cure conditions of approximately 380 °C for 90 minutes (Figure 5.21). Furthermore, inspection of Figure 5.20 shows the towpreg T_g plateauing with no T_g reduction. Though, these cure conditions may not be severe enough to initiate T_g reduction of the CFR 2.5kPETU. The difference seen in the T_g response to changing cure conditions for neat and CFR 2.5kPETU can be attributed to a fiber influence on cure kinetics.

One likely path for initiation and propagation of polymerization of PETU oligomers includes addition reactions involving the formation of unstable radicals. These addition reactions likely take place between ethynyl groups at the end of each oligomer. The important aspect of the reaction path is the presence of radicals. Investigations of glass-reinforced polyesters and vinyl esters have demonstrated that oxidized glass fiber surfaces influence the reaction rate of these systems that polymerize by free radical propagation [12-15]. Ishida and Koenig [12] state that polymerization of unsaturated polyesters is inhibited due to a charge transfer between free radicals and the inorganic oxide surfaces that eliminates free radicals. Thus, there are less free radicals to propagate reaction, and subsequently the reaction rate is reduced. It is possible a similar interaction is occurring in CFR PETU.

Although carbon fiber does not form inorganic oxides as a glass fiber does, several oxidized forms of carbon may exist: 1) C-O-R; 2) C=O; and 3) HO-C=O [16]. Several X-ray photoelectron spectroscopy (XPS) studies [16-19] of untreated, unsized carbon fiber have revealed oxidation of carbon fiber surfaces. The oxidized forms of carbon listed above result in positively polarized carbons and negatively polarized oxygens. Garton, et al. [20,21], report that oxidized carbon fibers influence the cure of epoxy resins due to hydrogen bonding of amines and hydroxyl groups with the oxidized carbon surfaces. It is likely similar interactions occur between oxidized carbon surfaces and radical PETU mers throughout different stages of PETU polymerization. Interaction of PETU mers with fibers rather than with other mers would slow reaction and explain the increased cure time and cure temperature needed by CFR 2.5kPETU to reach full cure versus the cure time and cure temperature needed by neat 2.5kPETU to reach full cure.

As an additional note, interaction between oxidized portions of the fiber surface and 2.5kPETU mers may be partially responsible for the good fiber/matrix adhesion seen in the fracture surfaces in Chapter 2. Such reasoning is based on results seen in studies of plasma treated carbon fibers [22-25]. These investigators demonstrated that increasing the oxygen content of carbon fiber surfaces improves mechanical properties that are heavily influenced by fiber/matrix interface quality.

5.6 Summary

Reaction of PETU continues beyond points at which DSC and FTIR can detect reaction. Additional reaction is demonstrated by increases in T_g . Therefore, optimization of 2.5kPETU cure was undertaken by monitoring the influence of cure time and temperature

on T_g . The inclusion of unsized, untreated carbon fiber was found to retard reaction progress. It is thought that oxidation of the carbon fiber resulted in PETU/fiber interactions that slowed reaction and possibly contributed to good fiber/matrix adhesion.

5.7 References

1. J.A. Johnston, F.M. Li, F.W. Harris, and T. Takekoshi, "Synthesis and Characterization of Imide Oligomers End-capped with 4-(Phenylethynyl)Phthalic Anhydrides," *Polymer*, **35**, (22), 4865-4873 (1994).
2. K.A. Harrington, R.A. Orwoll, B.J. Jensen, and P.R. Young, "Characterization of Cure Chemistry of Selected Phenylethynyl-Terminated Polyimides and Model Compounds," *Proceedings of the 41st International SAMPE Symposium and Exhibition*, 135-148 (1996).
3. B. Tan and J.E. McGrath, personal communication
4. R.H. Myers and D.C. Montgomery, Response Surface Methodology: Process and Product Optimization Using Designed Experiments, John Wiley and Sons, Inc., New York, 1995, pp. 16-67, 297-299.
5. B. Cassel and B. Twombly, "Glass Transition Determination by Thermomechanical Analysis, a Dynamic Mechanical Analyzer, and a Differential Scanning Calorimeter," in Materials Characterization by Thermomechanical Analysis, ASTM STP 1136, A.T. Riga and C.M. Neag, eds., American Society for Testing and Materials, Philadelphia, 1991, pp. 108-119.
6. H.R. O'Neal, S. Welch, J. Rogers, S. Guilford, G. Curan, and K.P. Menard, "Comparison of T_g Values for a Graphite Epoxy Composite by Differential Scanning Calorimetry (DSC), Thermomechanical Analysis (TMA), and Dynamic Mechanical Analysis (DMA)," *Journal of Advanced Materials*, **26**, (3), 49-54 (1995).
7. D. Wong, J. Jankowsky, M. DiBerardino, and R. Cochran, "Determining Upper Use Temperatures of Polymer Composites," *Proceedings of the 38th International SAMPE Symposium and Exhibition*, 1552-1565 (1993).
8. R.B. Prime, "Thermosets," in Thermal Characterization of Polymeric Materials, 2nd Edition, E.A. Turi, ed., Academic Press, New York, 1997, pp. 1400-1405.
9. R.P. Chartoff, P.T. Weissman, and A. Sircar, "The Application of Dynamic Mechanical Methods to T_g Determination in Polymers: An Overview," in Assignment of the Glass Transition, ASTM STP 1249, R.J. Seyler, ed., American Society for Testing and Materials, Philadelphia, 1994, pp. 88-107.
10. R.P. Chartoff, "Thermoplastic Polymers, in Thermal Characterization of Polymeric Materials, 2nd Edition, E.A. Turi, ed., Academic Press, New York, 1997, pp. 526-531.
11. Minitab, Minitab, Inc., State College, PA, 1995.

12. H. Ishida and J.L. Koenig, "An Investigation of the Coupling Agent/Matrix Interface of Fiberglass Reinforced Plastics by Fourier Transform Infrared Spectroscopy," *Journal of Polymer Science, Polymer Physics*, **17**, 615-626 (1979).
13. D.S. Lee and C.D. Han, "Effect of Particulates and Fiber Reinforcements on the Curing Behavior of Unsaturated Polyester Resin," *Journal of Applied Polymer Science*, **33**, 419-429 (1987).
14. G.R. Palmese, O.A. Andersen, V.M. Karbhari, "Effect of Glass Fiber Sizing on the Cure Kinetics of Vinyl-Ester Resins," *Composites: Part A*, **30**, 11-18 (1999).
15. A. Yousefi and P.G. Lafleur, "The Effects of Cobalt Promoter and Glass Fiber on the Curing Behavior of Unsaturated Polyester Resin," *SPE ANTEC*, 3030-3034 (1995).
16. Y. Xie and P.M.A. Sherwood, "X-ray Photoelectron-Spectroscopic Studies of Carbon Fiber Surfaces. Part IX: The Effect of Microwave Plasma Treatment on Carbon Fiber Surfaces," *Applied Spectroscopy*, **43**, (7), 1153-1158 (1989).
17. R.E. Allred and L.A. Harrah, "Effect of Plasma Treatment on Carbon/Bismaleimide Interfacial Adhesion," *Proceedings of the 34th International SAMPE Symposium and Exhibition*, 2559-2568 (1989).
18. X.S. Bian, L. Ambrosio, J.M. Kenny, L. Nicolais, E. Occhiello, M. Morra, F. Garbassi, and A.T. Dibenedetto, "The Effects of Surface Treatments of Fibers on the Interfacial Properties in Single-Fiber Composites. Part I. Single Carbon Fiber/Epoxy Resin Composite System," *Journal of Adhesion Science and Technology*, **5**, (5), 377-388 (1991).
19. M. Morra, E. Occhiello, F. Garbassi, and L. Nicolais, "Surface Studies on Untreated and Plasma-Treated Carbon Fibers," *Composites Science and Technology*, **42**, 361-372 (1991).
20. A. Garton, W.T.K. Stevenson, and S. Wang, "Interfacial Reactions in Carbon-Epoxy Composites," *British Polymer Journal*, **19**, 459-467 (1987).
21. A. Garton, W.T.K. Stevenson, and S.P. Wang, "The Crosslinking of Epoxy Resins at Interfaces. V. Amine-Cured Resins at Carbon and Graphite Surfaces," *Journal of Polymer Science: Part A: Polymer Chemistry*, **26**, 1377-1391 (1988).
22. R.A. Bucher and A.C. Loos, "High Performance Thermoplastic Matrix Composite Processing: Dry Powder Prepregging, Plasma Treatment, Consolidation / Crystallization Analysis," Report No. CCMS-95-02 and VPI-E-94-10, Center For Composite Materials and Structures (0257), Virginia Polytechnic Institute and State University, Blacksburg, VA 24061-0257 (1994).
23. L.Y. Yuan, S.S. Shyu, and J.Y. Lai, "Plasma Surface Treatments on Carbon Fibers. II. Mechanical Property and Interfacial Shear Strength," *Journal of Applied Polymer Science*, **42**, 2525-2534 (1991).
24. T.C. Chang and B.Z. Jang, "The Effects of Fiber Surface Treatments by a Cold Plasma in Carbon Fiber / Bismaleimide Composites," in Materials Research Society Symposium Proceedings: Interfaces in Composites, Vol. 170, C.G. Pantano and E.J.H. Chen, eds., Materials Research Society, Pittsburgh, 1989, pp. 321-326.

25. P.W. Yip and S.S. Lin, "Effect of Surface Oxygen on Adhesion of Carbon Fiber Reinforced Composites," in Materials Research Society Symposium Proceedings: Interfaces in Composites, Vol. 170, C.G. Pantano and E.J.H. Chen, eds., Materials Research Society, Pittsburgh, 1989, pp. 339-344.

Chapter 6 - Development of Two-Stage, Dual-Arrhenius Rheology Model for 2.5kPETU

6.1 Introduction

The rheological behavior of 2.5kPETU is well-suited for dry powder prepegging. The minimum viscosity of 5 Pa•s at 315 °C (Figure 6.1) is too high for melt-infusion composite manufacture techniques. However, for typical temperature ramp rates, the viscosity is low enough for a time span that easily allows for complete fiber wet-out by the matrix resin during hotpress consolidation of powder-coated tow. Thus, a rheological model is not as critical to developing a process schedule as is the ability to monitor cure. However, a chemoviscosity (chemical reaction dependent viscosity [1]) model is useful for both the definition of the range of this wide processing window and the generation of processing schedules for other composite manufacturing techniques such as online consolidation of powder-coated tow.

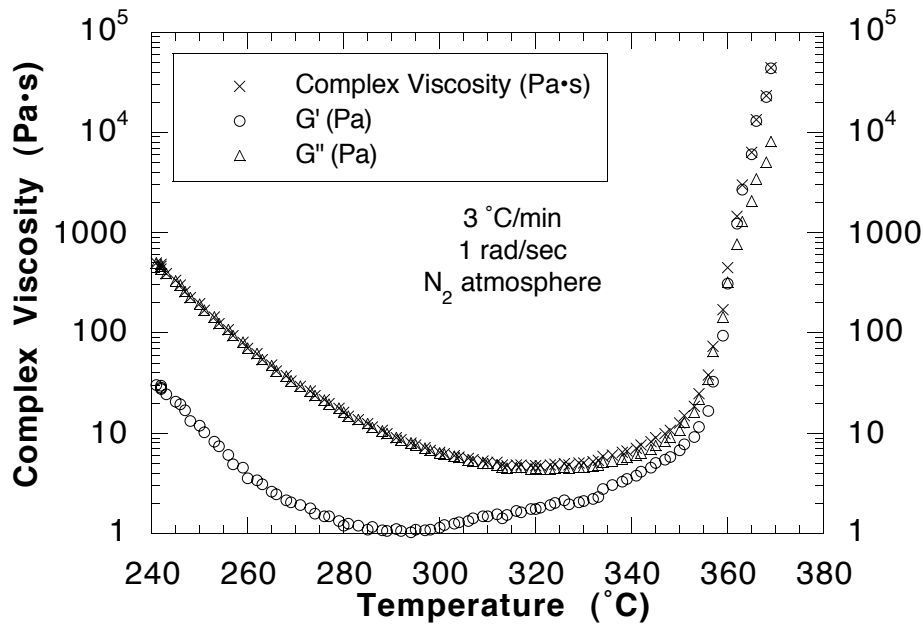


Figure 6.1.(a) Rheology Results for a 3 °C/min Ramp Using a 25 mm Diameter Sample

During a temperature ramp, the viscosity of a thermoset material initially decreases as the supplied heat provides energy for molecular chain movement. However, when a specific temperature range is reached, enough energy is available to initiate the thermoset cure reaction. As chains grow and crosslink, the viscosity gradually increases until the gel point

is reached. At the gel point, the viscosity increases dramatically, and the material no longer behaves as a liquid, but as a rubber-like solid. Following this transition, the material will no longer flow, thus severely limiting processing. In this particular case, flow of 2.5kPETU between fibers will cease upon, or immediately after, reaching the gel point. Therefore, if complete fiber wet-out is not obtained prior to the gel point, the resultant composite structure will contain an unnecessarily high void content. Understanding the time and temperature dependence of the 2.5kPETU chemoviscosity is necessary to develop a successful cure and consolidation schedule.

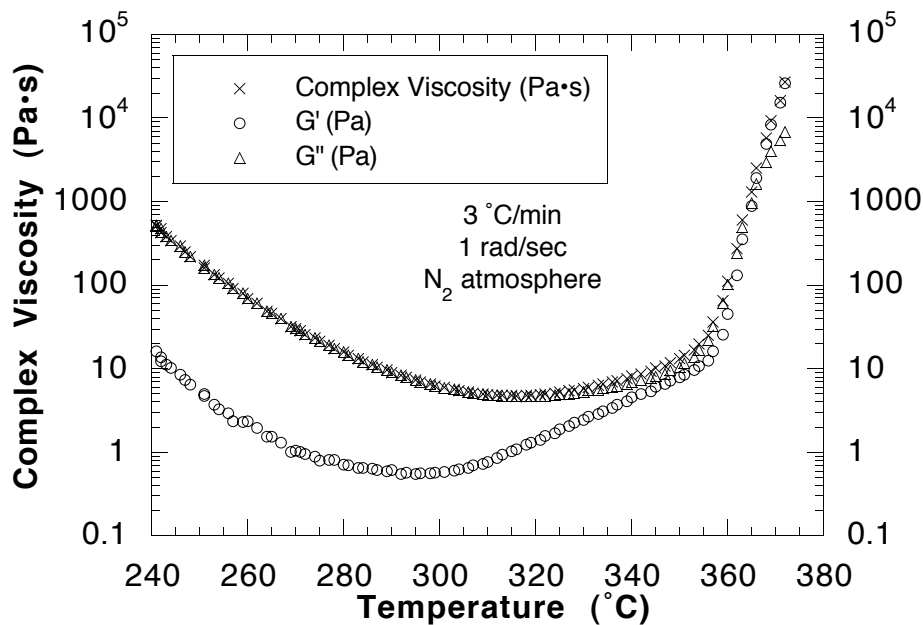


Figure 6.1.(b) Rheology Results for a 3 °C/min Ramp Using a 40 mm Diameter Sample

The development of a chemoviscosity model requires dynamic viscosity data from both isothermal holds and temperature ramps. This information may be obtained from parallel plate viscosity measurements; the details of the parallel plate arrangement will be addressed later. During these measurements, the motor driven plate is oscillated at a set frequency and shear strain. These measurements must be taken using shear strains within the linear viscoelastic limit, below which the viscosity is independent of shear strain. The linear viscoelastic limit may be determined for a specific temperature and frequency by performing a strain sweep. Beyond the linear viscoelastic limit, the viscosity begins to decrease with increasing shear strain. Dynamic measurements with small shear strains offer an advantage over large shear strains or steady shear measurements where the motor

driven plate is rotated at a constant rate; large strains or complete rotations may influence the cure rate by hindering network formation [2].

The use of dynamic parallel plate viscosity measurements for the modeling of steady flow of resin between fibers requires the Cox-Merz approximation to be satisfied; the steady shear and dynamic shear viscosities are equivalent at given shear rates [2]. This approximation becomes more inappropriate as the gel point is approached, but at lower degrees of cure, where the majority of fiber wet-out occurs, the Cox-Merz approximation appears to be reasonable [3,4]. In addition, composite consolidation models generally assume the resin to behave as a Newtonian fluid at the low shear rates seen during resin impregnation of the reinforcement [5-7]. These assumptions simplify the development of a chemoviscosity model for a polymeric composite matrix material.

The experimental rheology work will give the effects of time and temperature on the viscosity. It was seen previously that the degree of cure of the matrix material may be described as a function of time and temperature (Chapters 4 and 5). Union of the viscosity and combination kinetics reaction models produces a chemoviscosity model that gives viscosity as a function of degree of cure. Such a model allows for the determination of a processing window. Therefore, a process schedule that provides the best opportunity for complete fiber wet-out and resin cure may be developed.

Halley and Mackay [2] have tabulated several chemorheological models that have been developed: simple empirical models, probability based and molecular models, gelation models, Arrhenius models, and free volume models. Evaluation of experimental results is required before a modeling direction can be chosen. Thus, experimental rheological work was undertaken to provide for the development of a model predicting the time and temperature dependence of 2.5kPETU's viscosity.

6.2 Experimental

Dynamic rheological measurements were performed using circular aluminum parallel plates within a Rheometrics RMS-800. This test arrangement consists of one plate attached to a motor and the second plate attached to a transducer that measures the amount of torque transferred from the motor driven plate to the transducer plate through the test medium placed between the plates. The torque transferred to the transducer is directly proportional to the diameter of the parallel plates, thus the plate and sample diameter must be selected to provide sufficient torque to satisfy the minimum measurable levels of the transducer.

Temperature ramps were performed with 2.5kPETU to determine whether 25 mm diameter plates provided sufficient torque or if 40 mm diameter plates were necessary. Samples having 40 mm diameters would have been readily selected except for the difficulty in handling and loading 40 mm samples. Samples were prepared by pressing polymer powder, which had been degassed for 5 days under vacuum at 165 °C, into 1.1 mm thick disks. These disks of fused powder were formed by pressing the powder in dies under 200 kPa (29 psi) for 20 minutes at 196 °C. The fragility of these disks and the resultant difficulty of successfully loading them into the preheated parallel plate fixture made the use of 25 mm samples desirable as smaller samples were easier to handle and less likely to shatter.

These temperature ramp measurements were done at 3 °C/min from 240 °C to 380 °C in a nitrogen gas purged environment. The oscillation frequency was 1 rad/s with a variable shear strain. The shear strain was varied to maintain minimum torque levels, but was kept below the linear viscoelastic limit. The parallel plate fixture was preheated to 240 °C before the powder disks were inserted, and the fixture was allowed to recover to 240 °C following sample insertion before the temperature ramp was commenced. The results of these two preliminary runs are shown in Figure 6.1. A comparison of the complex viscosities measured using 25 mm and 40 mm samples is given in Figure 6.2. These results show that 25 mm samples are adequate for 2.5kPETU rheology measurements. Therefore, 25 mm samples were used for the rest of the rheology measurements.

Based on the results of the temperature ramps shown in Figure 6.1 and results from thermal analysis (Chapter 4), isothermal rheology measurements were run at the following temperatures: 315 °C, 320 °C, 325 °C, 330 °C, 340 °C, 350 °C, and 360 °C. The low end temperature of 315 °C was selected because the viscosity minimum was reached at 315 °C during the 3 °C/min ramp. The upper end temperature of 360 °C was selected due to the fast reaction occurring at this temperature; because the specimen cured too much in the time required to load the specimen and start the test, an accurate rheology measurement could not be completed. Thus, data was not recorded at 360 °C.

The specimens for these isothermal measurements were pressed from degassed powder in the same manner as those prepared for the temperature ramps. As with the temperature ramps, the fixture was preheated to the isothermal temperature prior to specimen insertion. Dynamic oscillation at 1 rad/s began as soon as the specimen was installed; reported data does not begin until the fixture temperature recovered to the testing temperature.

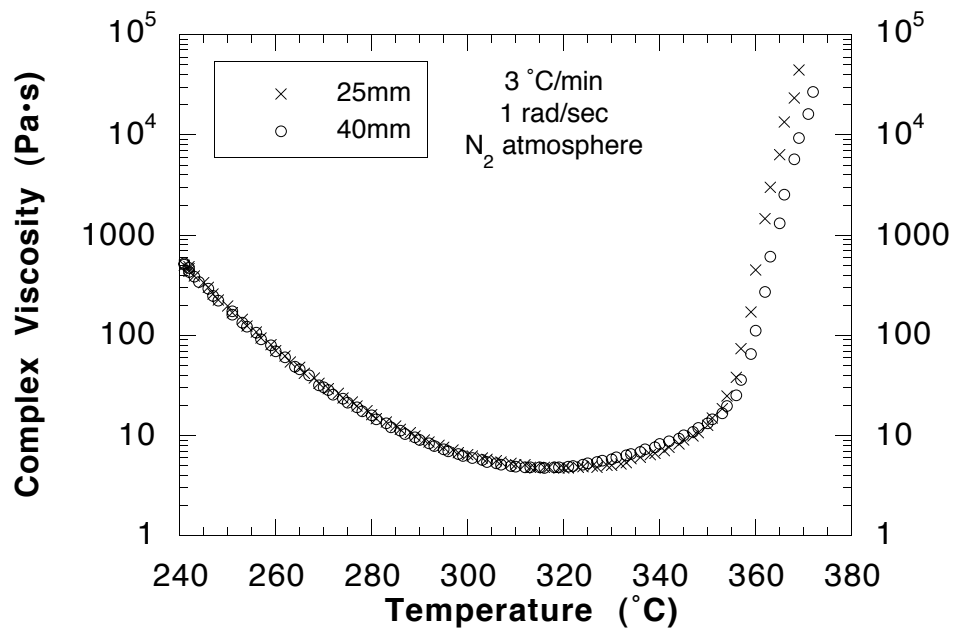


Figure 6.2. Comparison of 2.5kPETU Complex Viscosity: 25 mm Diameter Sample versus 40 mm Diameter Sample

6.3 Results

The results of the six isothermal measurements are summarized in Figure 6.3. The differences in reaction kinetics seen in DSC measurements (Chapter 4) below 325 °C is apparent in the isothermal viscosity results. A significant increase in initial reaction rate is apparent between 320 °C and 325 °C.

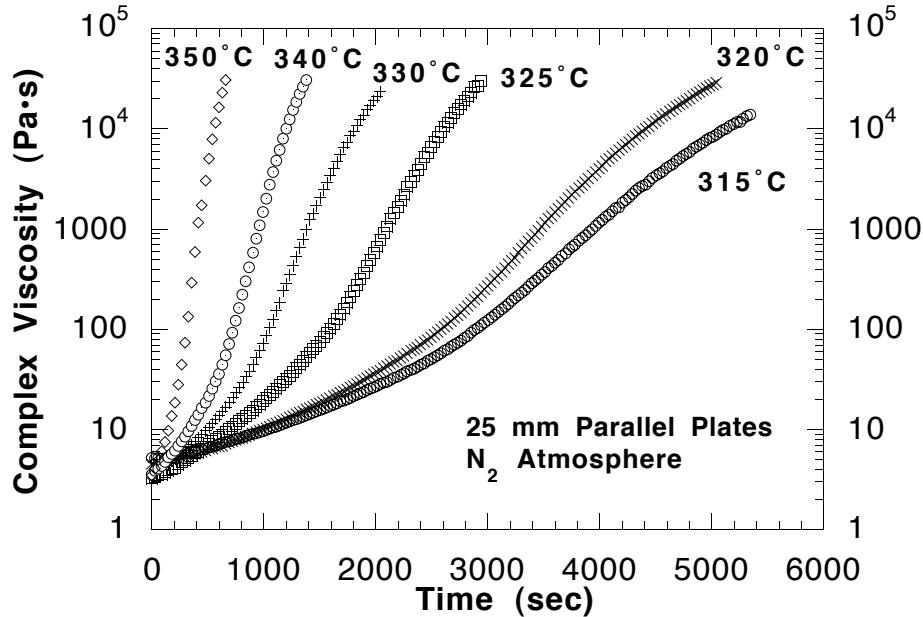


Figure 6.3. Results of Isothermal Rheology Measurements

6.4 Model Development

Thermal analysis by DSC demonstrated that three distinct regions existed, each displaying differing kinetics (Chapter 4). The center region of 325 °C to 360 °C was selected for cure kinetics modeling. This same range will be selected for rheology modeling, except the upper end will be reduced to 350 °C due to the inability to complete a measurement at 360 °C. A direct model of viscosity versus degree of cure was initially attempted using Equation 6.1:

$$\eta^* = \eta_\infty \exp\left[\frac{E_v}{RT} + k_\eta \alpha\right] \quad (6.1)$$

where:

η^* = complex viscosity (Pa•s);

η_∞ = pre-exponential factor for initial viscosity (Pa•s);

E_v = activation energy for viscous flow (J/mol);

R = gas constant;

T = absolute temperature (K);

k_η = constant, effect of chemical reaction on viscosity; and

α = degree of cure.

This model did not work well mainly because the results of the 350 °C isothermal run did not fit the trend of decreasing initial viscosity with increasing temperature as demonstrated by the other three isothermal temperatures in Figure 6.4. This figure is essentially a plot of $\ln \eta^*$ versus time, where degree of cure, α , has been calculated from time using the combination kinetics model developed in Chapter 4.

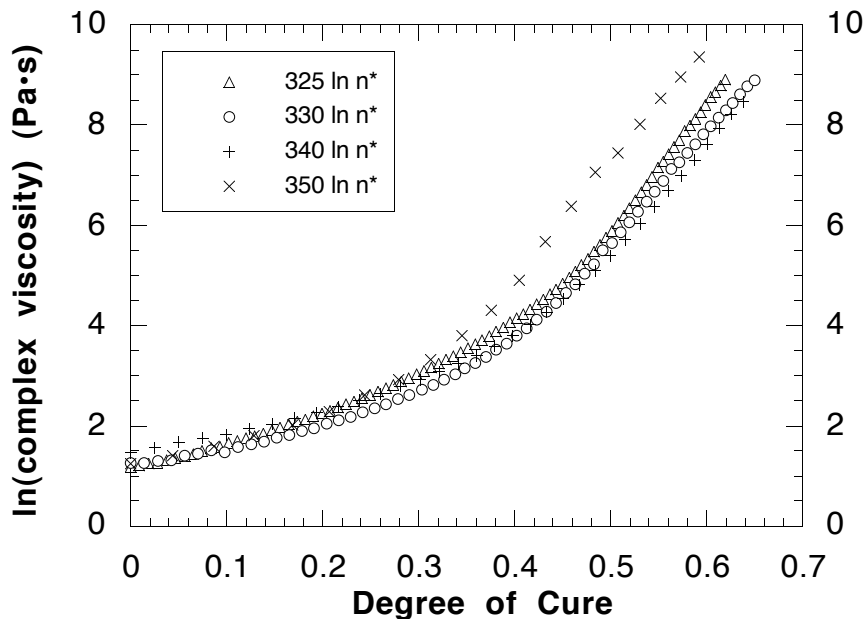


Figure 6.4. Isothermal Viscosities versus Degree of Cure

Rather than directly modeling η^* versus α , a dual-Arrhenius (DA) model was successfully applied to the isothermal results. Combining the DA model and the combination kinetics

models, a η^* versus α relation may be found. The basic equation for a DA model is:

$$\eta^* = \eta_0 \exp(kt) \Rightarrow \ln \eta^* = \ln \eta_0 + kt \quad (6.2)$$

where:

η_0 = initial (zero-time) viscosity (Pa•s);

k = rate constant of gelation (s^{-1}); and

t = time (s).

The DA model describes the first region of the schematic plot shown in Figure 6.5. The slope and intercept of the less steep portion of the schematic curve give k and $\ln \eta_0$, respectively. The actual data for the four temperatures are shown in Figure 6.6 from the beginning of each run up to the gel point. The gel point times, t_{gel} , are given in Table 6.1 for each temperature. Along with complex viscosity, the elastic and viscous moduli were measured. The time it took to reach the first measurement in which the elastic modulus was greater than the viscous modulus was defined as the gel time, or the time to reach the gel point. These are apparent gel points for the test frequency of 1 rad/s. The true gel point is defined by the frequency independent point at which elastic modulus overtakes viscous modulus.

As can be seen in Figure 6.6, there is not a linear relationship between $\ln \eta^*$ and time up to the gel point as is necessary for use of the DA model. But, for each temperature the data can be broken into two regions which are fairly linear with time. Thus, for each temperature, $\ln \eta^*$ versus time was broken into a DA1 and DA2 region, and the DA Model was applied separately to these two regions.

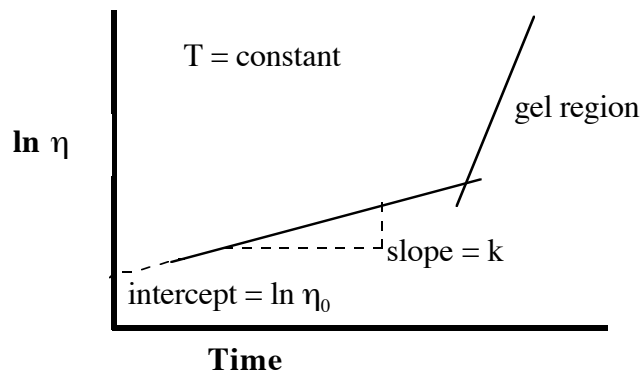


Figure 6.5. Schematic DA Representation of DA Isothermal Viscosity Behavior

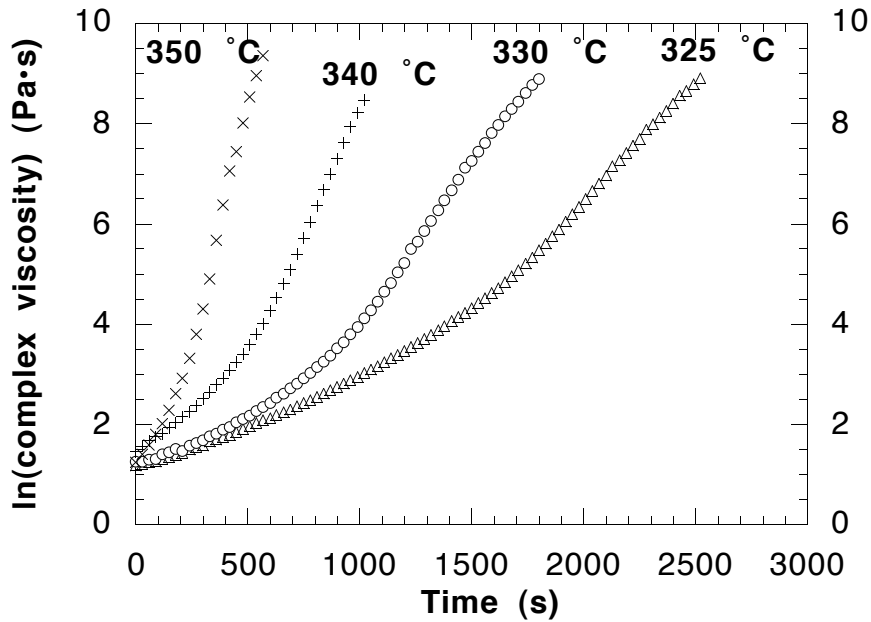


Figure 6.6. Isothermal Complex Viscosities versus Time to Gel Points

Table 6.1. Time to Gel Point

Temperature (°C)	Gel Time (s)
325	2354
330	1458
340	872
350	397

6.4.1 Model Development for DA1

Discussion of the development of the model will first focus on DA1 (the lower time range). The linear fits shown in Figure 6.7 were applied over specific time ranges for each temperature. The time ranges for each temperature are given in Figure 6.7. The linear fits provide the values for $\ln \eta_0$ (intercept) and k (slope) of Equation 6.2, and these values are summarized in Table 6.2.

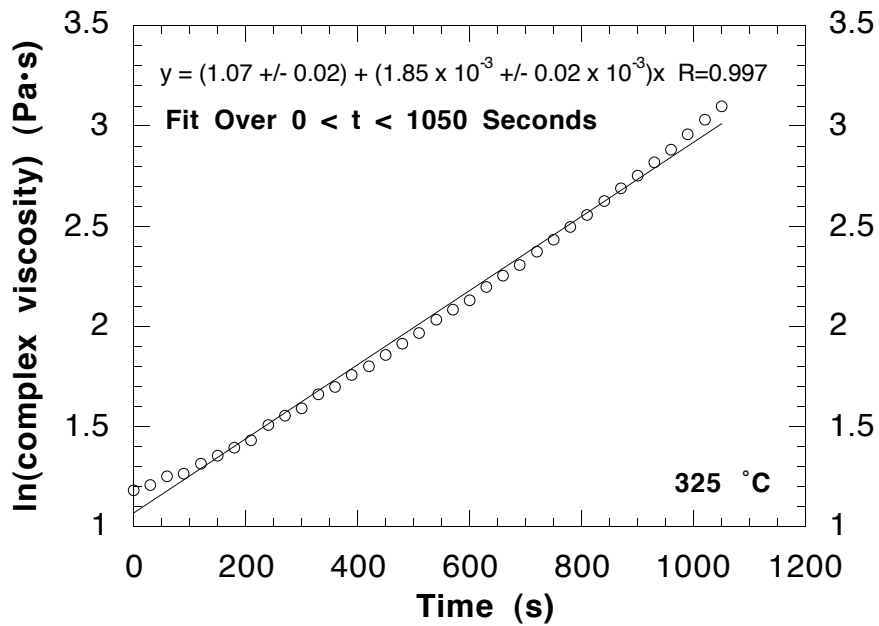


Figure 6.7.(a) Linear Fit of Lower Time Range of 325 °C Complex Viscosity

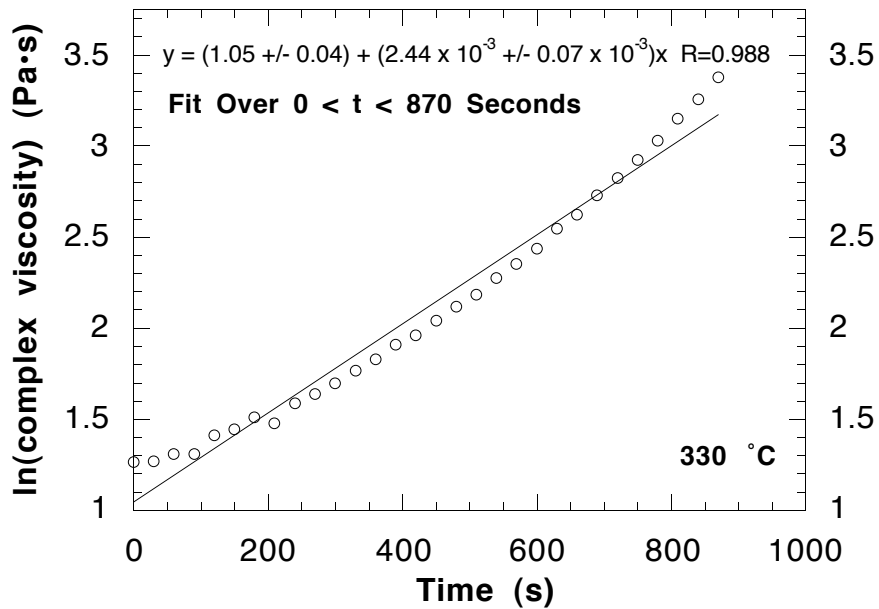


Figure 6.7.(b) Linear Fit of Lower Time Range of 330 °C Complex Viscosity

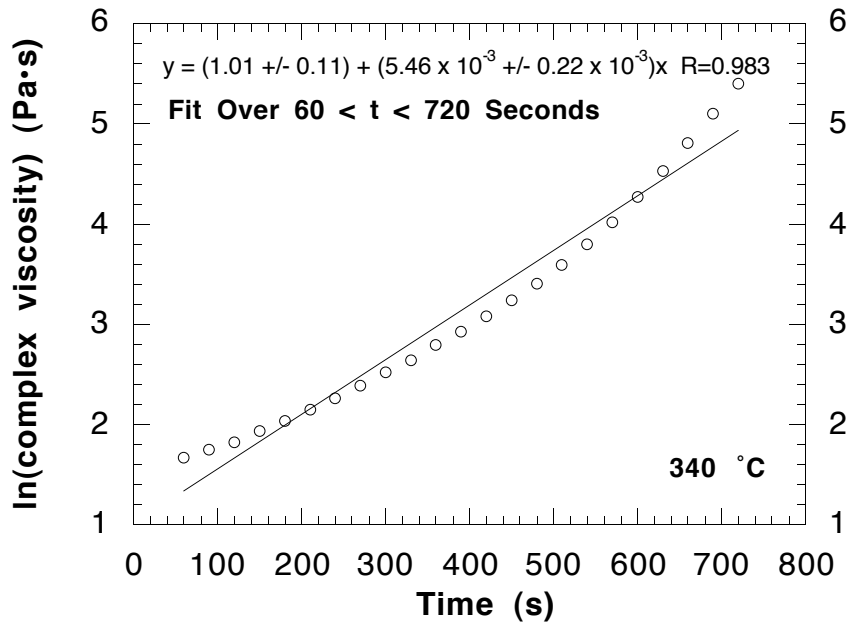


Figure 6.7.(c) Linear Fit of Lower Time Range of 340 °C Complex Viscosity

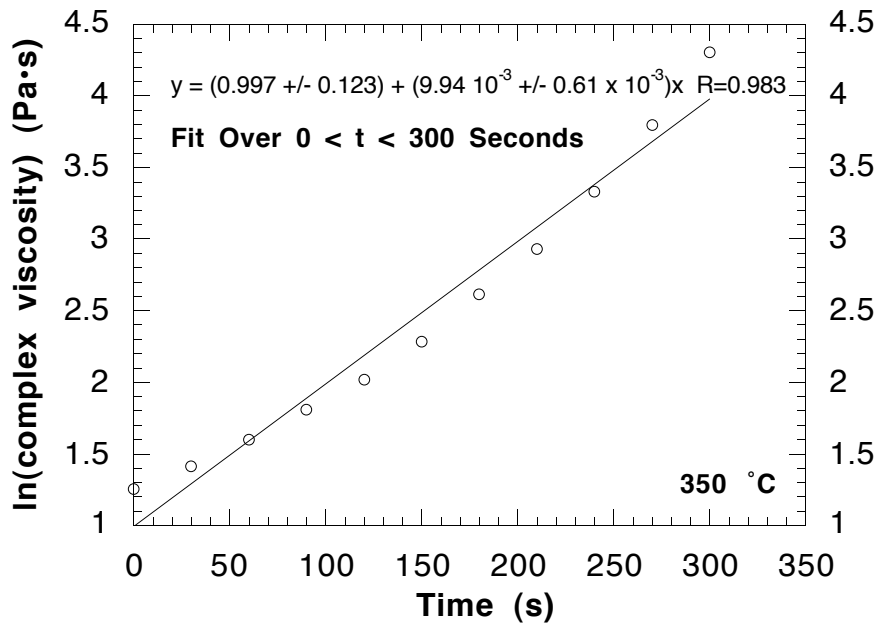


Figure 6.7.(d) Linear Fit of Lower Time Range of 350 °C Complex Viscosity

Table 6.2. DA1 Values for Initial Viscosity and Rate Constant of Gelation

Temperature (°C)	$\ln \eta_0$ (Pa•s)	k (s ⁻¹)	$\ln k$ (s ⁻¹)
325	1.07 ± 0.02	$1.85 \times 10^{-3} \pm 0.02 \times 10^{-3}$	-6.29
330	1.05 ± 0.04	$2.44 \times 10^{-3} \pm 0.07 \times 10^{-3}$	-6.02
340	1.01 ± 0.11	$5.46 \times 10^{-3} \pm 0.22 \times 10^{-3}$	-5.21
350	0.997 ± 0.123	$9.94 \times 10^{-3} \pm 0.61 \times 10^{-3}$	-4.61

The term “dual-Arrhenius” derives from the fact that both k and η_0 have an Arrhenius temperature dependence as shown in Equations 6.3 and 6.4. The natural logarithm may be taken of both relationships to provide a linear relationship between $\ln \eta_0$ and $1/T$ and $\ln k$ and $1/T$ (Equations 6.3 and 6.4). From plots of $\ln \eta_0$ versus $1/T$ and $\ln k$ versus $1/T$ (Figures 6.8 and 6.9), the pre-exponential factors and activation energies may be determined. Calculation of the pre-exponential factors and activation energies is commenced by applying linear fits to the data of Figures 6.8 and 6.9. The results of these fits and the calculated values of the pre-exponential factors and activation energies are given in Calculations 6.1 and 6.2.

$$\eta_0 = \eta_\infty \exp\left[\frac{\Delta E_\eta}{RT}\right] \Rightarrow \ln \eta_0 = \ln \eta_\infty + \left(\frac{\Delta E_\eta}{RT}\right) \quad (6.3)$$

$$k = k_\infty \exp\left[\frac{-\Delta E_k}{RT}\right] \Rightarrow \ln k = \ln k_\infty + \left(\frac{-\Delta E_k}{RT}\right) \quad (6.4)$$

where:

η_∞ = pre-exponential factor for initial viscosity (η_0 at $T = \infty$ (Pa•s));

ΔE_η = apparent activation energy for initial viscosity (J/mol);

k_∞ = pre-exponential factor for gelation rate constant (k at $T = \infty$) (s⁻¹); and

ΔE_k = apparent activation energy for gelation (J/mol).

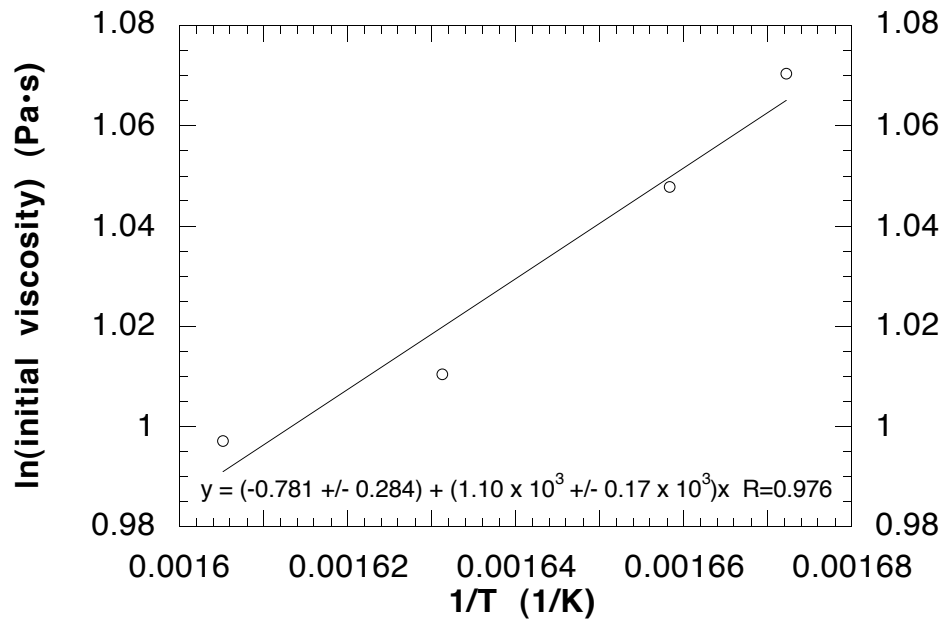


Figure 6.8. Arrhenius Fit of $\ln \eta_0$ versus $1/T$ for DA1

Calculation 6.1. Viscosity Terms for DA1

$$\text{slope} = \frac{\Delta E_\eta}{R} = 1.10 \times 10^3 \pm 0.17 \times 10^3 \text{ K} \Rightarrow \Delta E_\eta = 9.18 \times 10^3 \text{ J/mol}$$

$$\text{intercept} = \ln \eta_\infty = -0.781 \pm 0.284 \Rightarrow \eta_\infty = 0.458 \text{ Pa} \cdot \text{s}$$

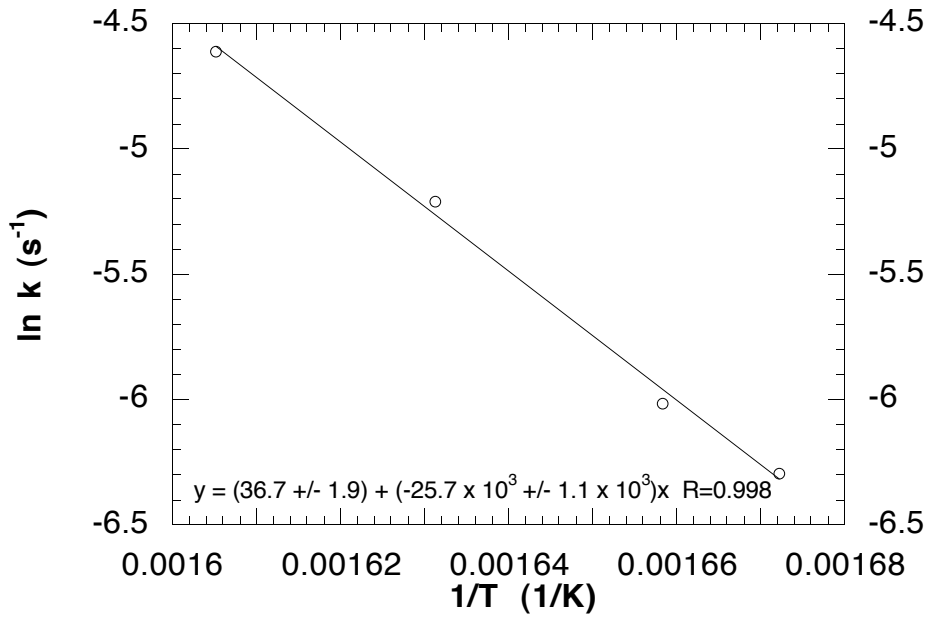


Figure 6.9. Arrhenius Fit of $\ln k$ versus $1/T$ for DA1

Calculation 6.2. Gelation Terms For DA1

$$\text{slope} = \frac{-\Delta E_k}{R} = -25.7 \times 10^3 \pm 1.1 \times 10^3 \text{ K} \Rightarrow \Delta E_k = 2.14 \times 10^5 \text{ J/mol}$$

$$\text{intercept} = \ln k_\infty = 36.7 \pm 1.9 \Rightarrow k_\infty = 8.85 \times 10^{15} \text{ s}^{-1}$$

These values for pre-exponential factors and activation energies can be used to assemble the complete DA1 model and specific complex viscosity versus time relationships for each experimental temperature as shown in Scheme 6.1 using Equations 6.2, 6.3, and 6.4. These relationships can then be used to model the first stage of $\ln \eta^*$ versus time (Figure 6.10).

Scheme 6.1. Development of DA1

$$\ln \eta^* = \ln \eta_0 + kt$$

$$\ln \eta^* = \ln \eta_\infty + \left(\frac{\Delta E_\eta}{RT} \right) + k_\infty t \exp\left(\frac{-\Delta E_k}{RT} \right)$$

$$\ln \eta^* = -0.781 + \left(\frac{1100K}{T} \right) + (8.85 \times 10^{15} s^{-1}) t \left[\exp\left(\frac{-25700K}{T} \right) \right] \quad \Leftarrow \text{DA1 Model}$$

$$T = 325 \text{ }^\circ\text{C} = 598 \text{ K}; \ln \eta^* = 1.07 + (0.00180 \text{ s}^{-1})t$$

$$T = 330 \text{ }^\circ\text{C} = 603 \text{ K}; \ln \eta^* = 1.05 + (0.00258 \text{ s}^{-1})t$$

$$T = 340 \text{ }^\circ\text{C} = 613 \text{ K}; \ln \eta^* = 1.02 + (0.00517 \text{ s}^{-1})t$$

$$T = 350 \text{ }^\circ\text{C} = 623 \text{ K}; \ln \eta^* = 0.991 + (0.0101 \text{ s}^{-1})t$$

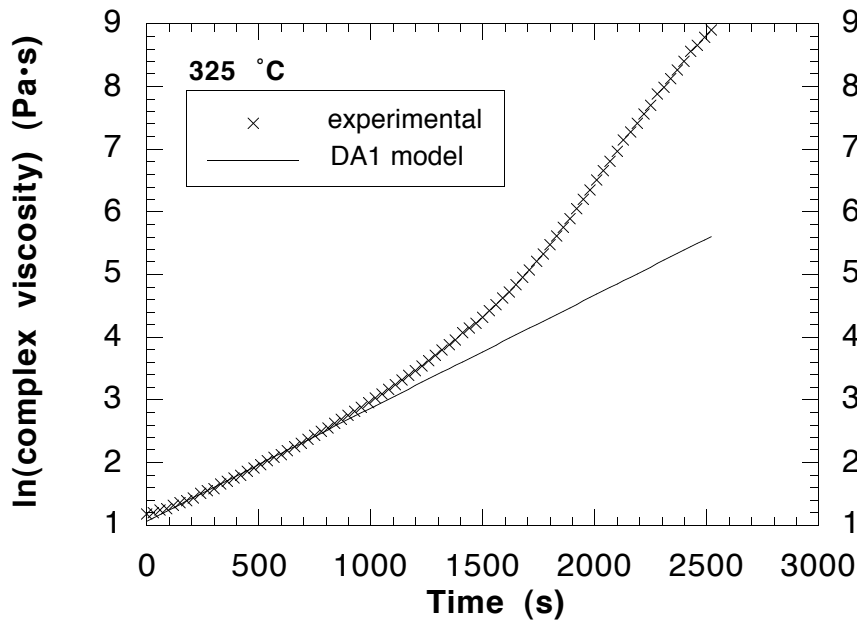


Figure 6.10.(a) DA1 Fit of $\ln \eta^*$ versus Time for 325 °C

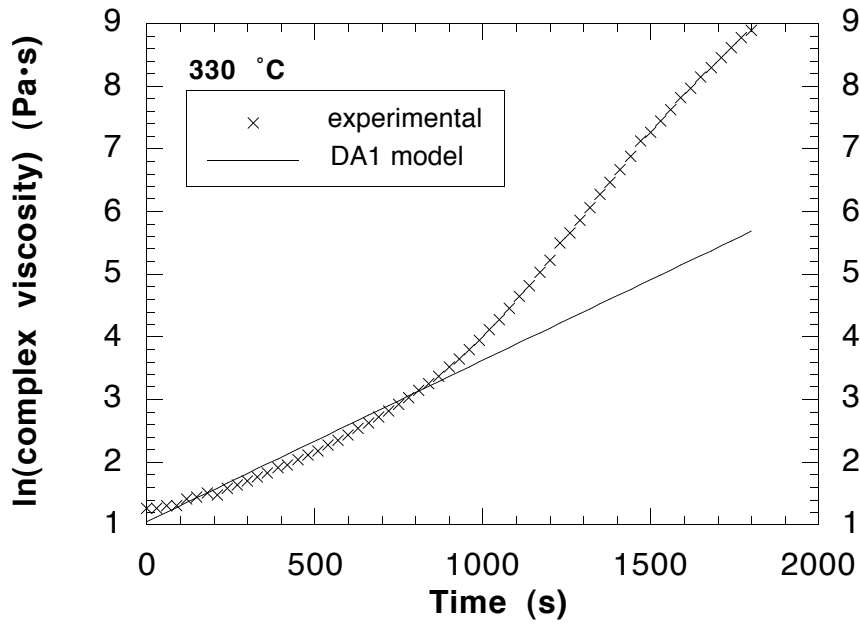


Figure 6.10.(b) DA1 Fit of $\ln \eta^*$ versus Time for 330 °C

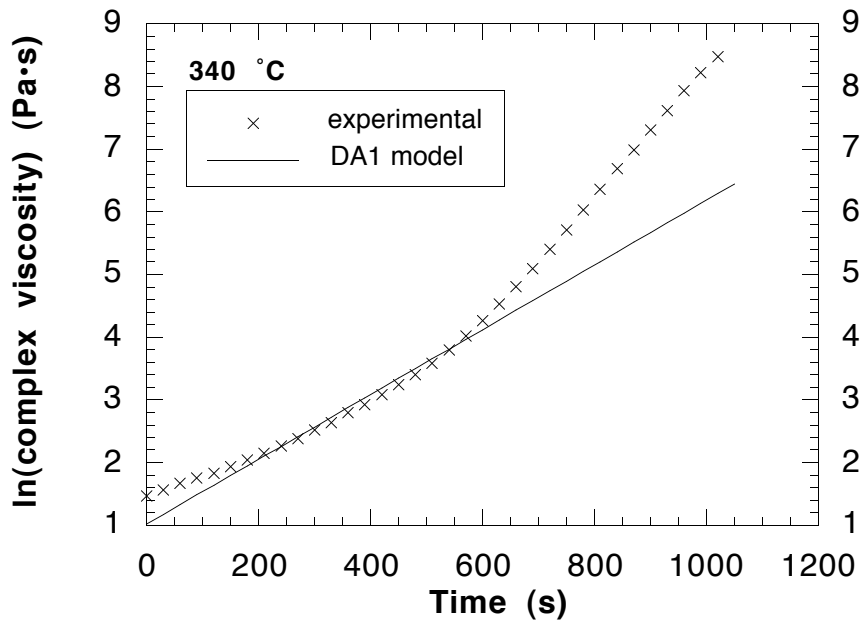


Figure 6.10.(c) DA1 Fit of $\ln \eta^*$ versus Time for 340 °C

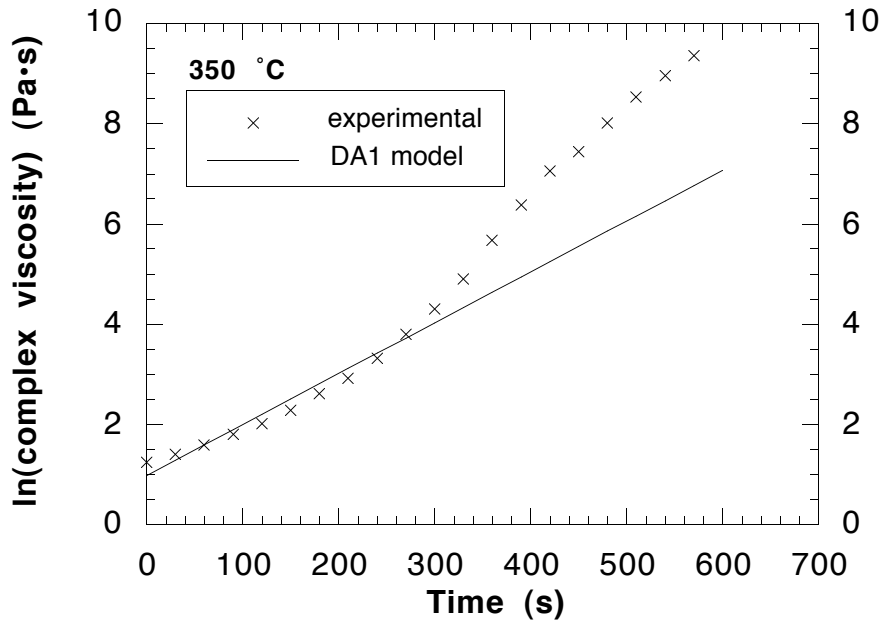


Figure 6.10.(d) DA1 Fit of $\ln \eta^*$ versus Time for 350 °C

6.4.2 Model Development for DA2

The second stage of the model development focuses on DA2 (the upper time range), and the procedure followed for model development over this time range is identical to the procedure used for DA1. First, linear fits (Figure 6.11) of $\ln \eta^*$ versus time were generated at each experimental temperature to determine the values of $\ln \eta_0$ (intercept) and k (slope) for Equation 6.2 (Table 6.3).

Table 6.3. DA2 Values for Initial Viscosity and Rate Constant of Gelation

Temperature (°C)	$\ln \eta_0$ (Pa·s)	k (s ⁻¹)	$\ln k$ (s ⁻¹)
325	-1.67 ± 0.14	$4.09 \times 10^{-3} \pm 0.08 \times 10^{-3}$	-5.50
330	-1.81 ± 0.14	$5.95 \times 10^{-3} \pm 0.11 \times 10^{-3}$	-5.12
340	-2.04 ± 0.06	$1.04 \times 10^{-2} \pm 0.01 \times 10^{-2}$	-4.57
350	-2.30 ± 0.24	$2.22 \times 10^{-2} \pm 0.07 \times 10^{-2}$	-3.81

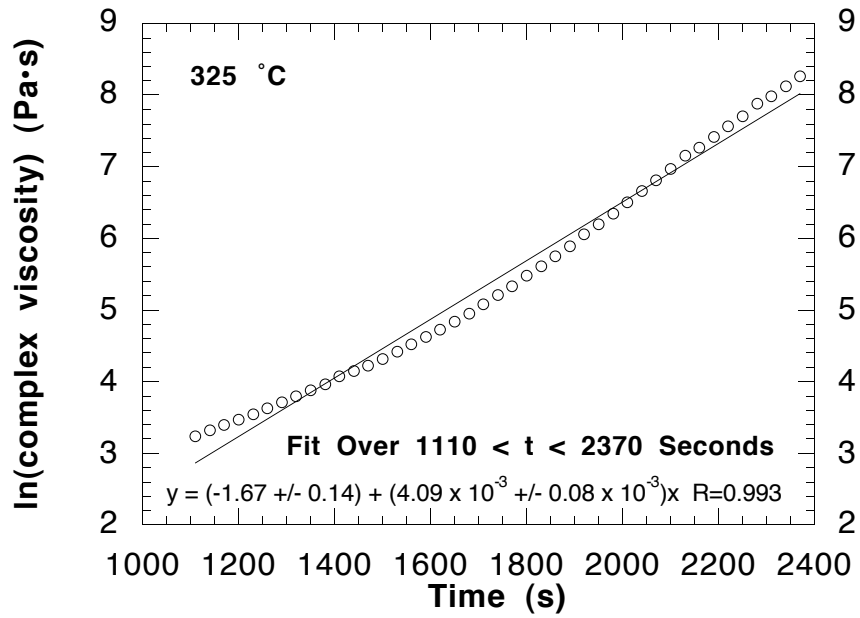


Figure 6.11.(a) Linear Fit of Upper Time Range of 325 °C Complex Viscosity

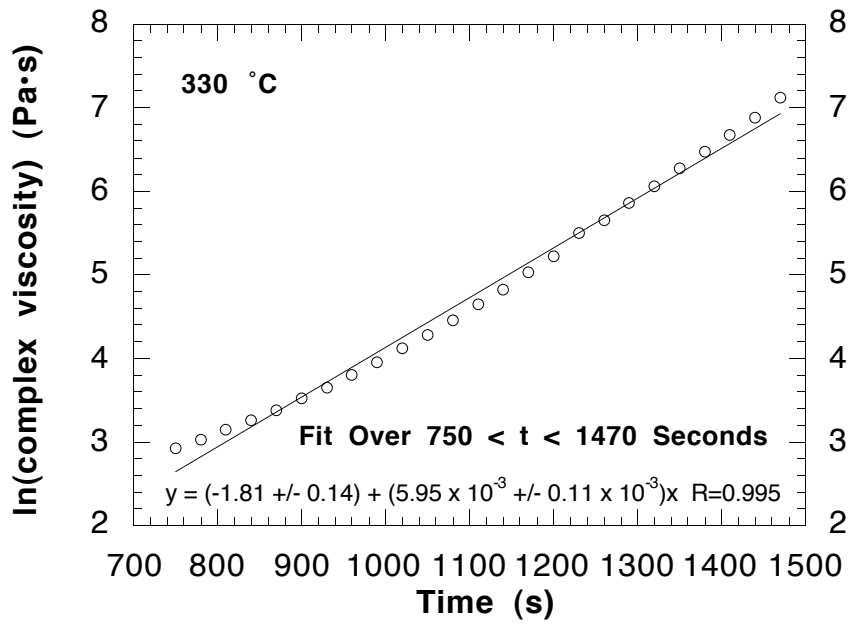


Figure 6.11.(b) Linear Fit of Upper Time Range of 330 °C Complex Viscosity

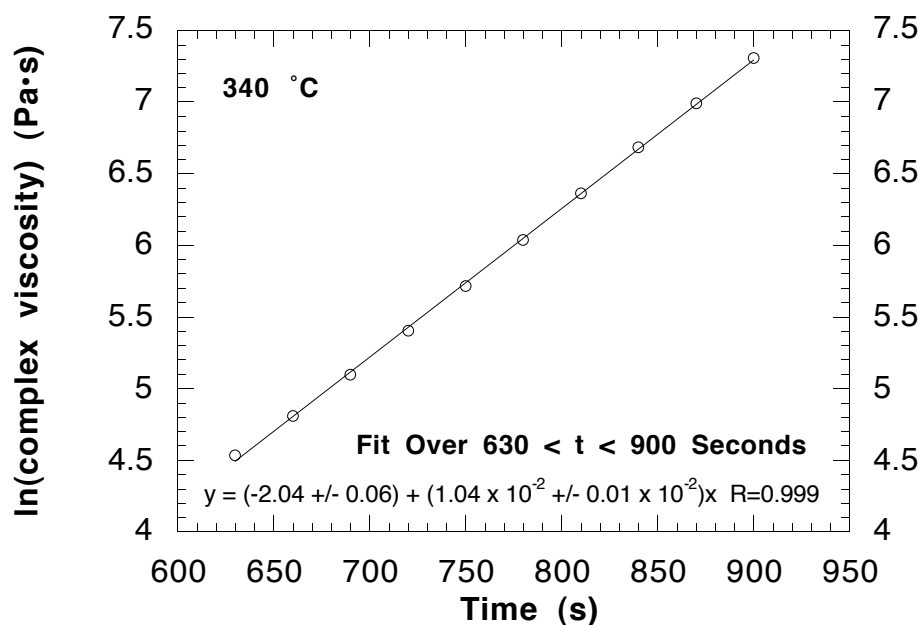


Figure 6.11.(c) Linear Fit of Upper Time Range of 340 °C Complex Viscosity

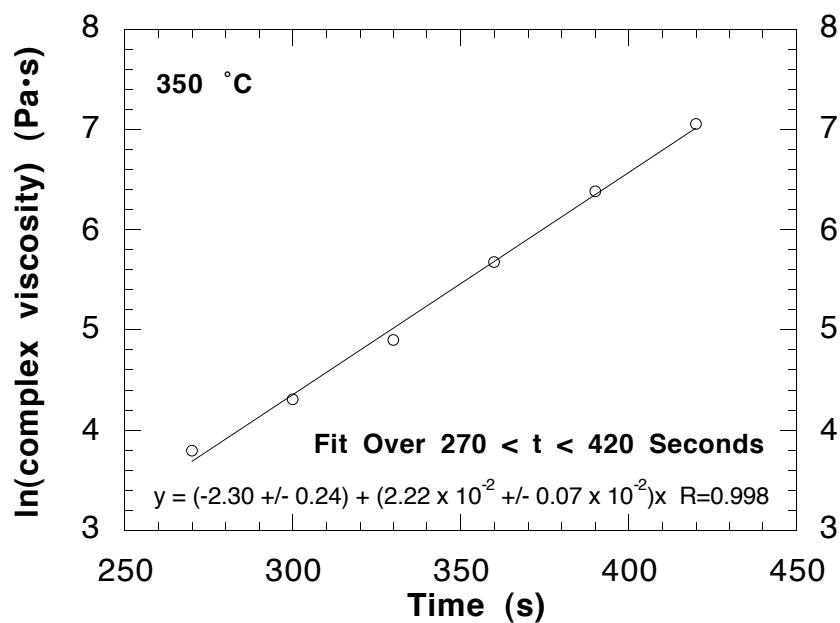


Figure 6.11.(d) Linear Fit of Upper Time Range of 350 °C Complex Viscosity

Figures 6.12 and 6.13 show the Arrhenius fits of $\ln \eta_0$ versus $1/T$ (Equation 6.3) and $\ln k$ versus $1/T$ (Equation 6.4), from which the pre-exponential factors and activation energies may be determined. The results of these Arrhenius fits and the calculations of the pre-exponential factors and activation energies are shown in Calculations 6.3 and 6.4.

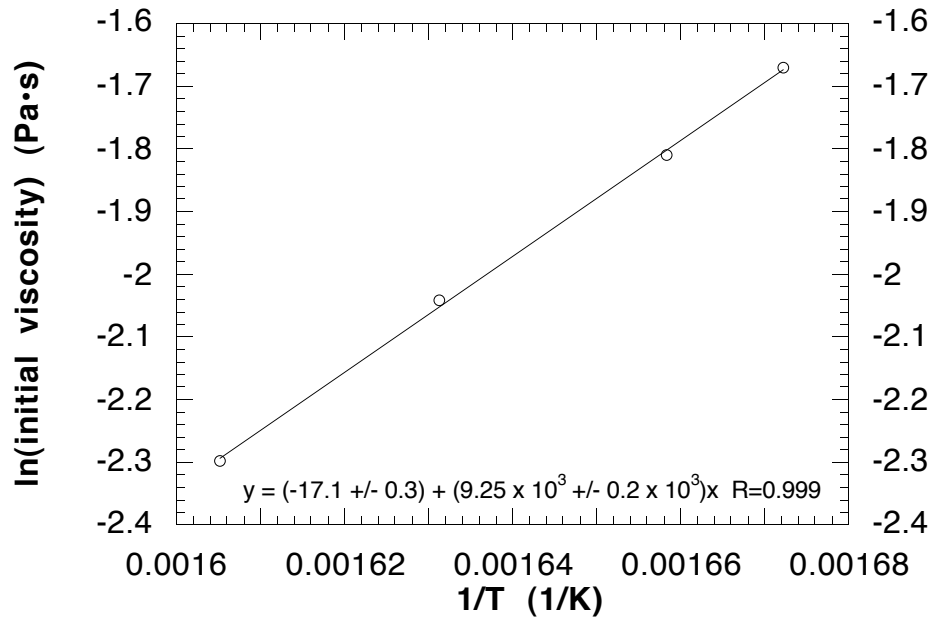


Figure 6.12. Arrhenius Fit of $\ln \eta_0$ versus $1/T$ for DA2

Calculation 6.3. Viscosity Terms for DA2

$$\text{slope} = \frac{\Delta E_{\eta}}{R} = 9.25 \times 10^3 \pm 0.2 \times 10^3 \text{ K} \Rightarrow \Delta E_{\eta} = 7.69 \times 10^4 \text{ J/mol}$$

$$\text{intercept} = \ln \eta_{\infty} = -17.1 \pm 0.3 \Rightarrow \eta_{\infty} = 3.60 \times 10^{-8} \text{ Pa} \cdot \text{s}$$

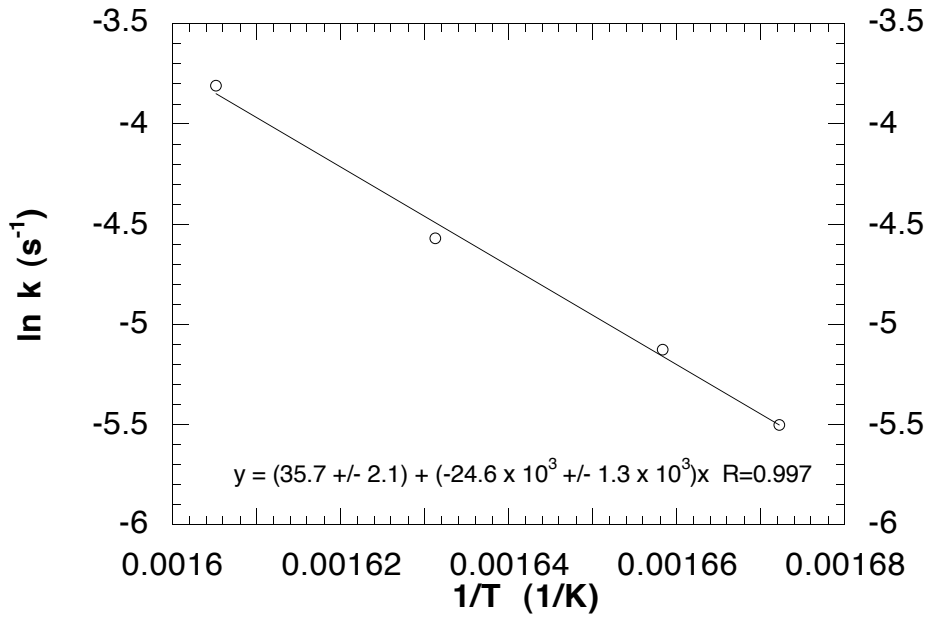


Figure 6.13. Arrhenius Fit of $\ln k$ versus $1/T$ for DA2

Calculation 6.4. Gelation Terms For DA2

$$\text{slope} = \frac{-\Delta E_k}{R} = -24.6 \times 10^3 \pm 1.3 \times 10^3 \text{ K} \Rightarrow \Delta E_k = 2.05 \times 10^5 \text{ J/mol}$$

$$\text{intercept} = \ln k_\infty = 35.7 \pm 2.1 \Rightarrow k_\infty = 3.24 \times 10^{15} \text{ s}^{-1}$$

As with DA1, these values for pre-exponential factors and activation energies can be used to assemble the complete DA2 model and specific complex viscosity versus time relationships for each experimental temperature as shown in Scheme 6.2 using Equations 6.2, 6.3, and 6.4. These relationships can then be used to model the second stage of $\ln \eta^*$ versus time (Figure 6.14); Figure 6.14 shows the models for both DA1 and DA2.

Scheme 6.2. Development of DA2

$$\ln \eta^* = \ln \eta_0 + kt$$

$$\ln \eta^* = \ln \eta_\infty + \left(\frac{\Delta E_\eta}{RT} \right) + k_\infty t \exp\left(\frac{-\Delta E_k}{RT} \right)$$

$$\ln \eta^* = -17.1 + \left(\frac{9250K}{T} \right) + (3.24 \times 10^{15} \text{ s}^{-1}) t \left[\exp\left(\frac{-24600K}{T} \right) \right] \Leftarrow \text{DA2 Model}$$

$$T = 325 \text{ }^\circ\text{C} = 598 \text{ K}; \ln \eta^* = -1.67 + (0.00408 \text{ s}^{-1})t$$

$$T = 330 \text{ }^\circ\text{C} = 603 \text{ K}; \ln \eta^* = -1.80 + (0.00575 \text{ s}^{-1})t$$

$$T = 340 \text{ }^\circ\text{C} = 613 \text{ K}; \ln \eta^* = -2.05 + (0.00112 \text{ s}^{-1})t$$

$$T = 350 \text{ }^\circ\text{C} = 623 \text{ K}; \ln \eta^* = -2.29 + (0.0214 \text{ s}^{-1})t$$

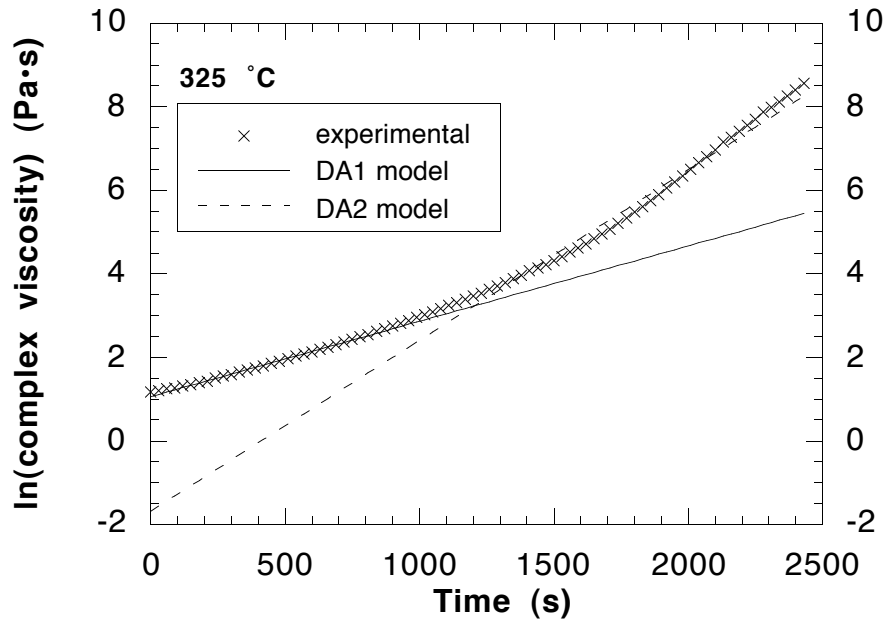


Figure 6.14.(a) DA1 and DA2 Fit of $\ln \eta^*$ versus Time for 325 °C

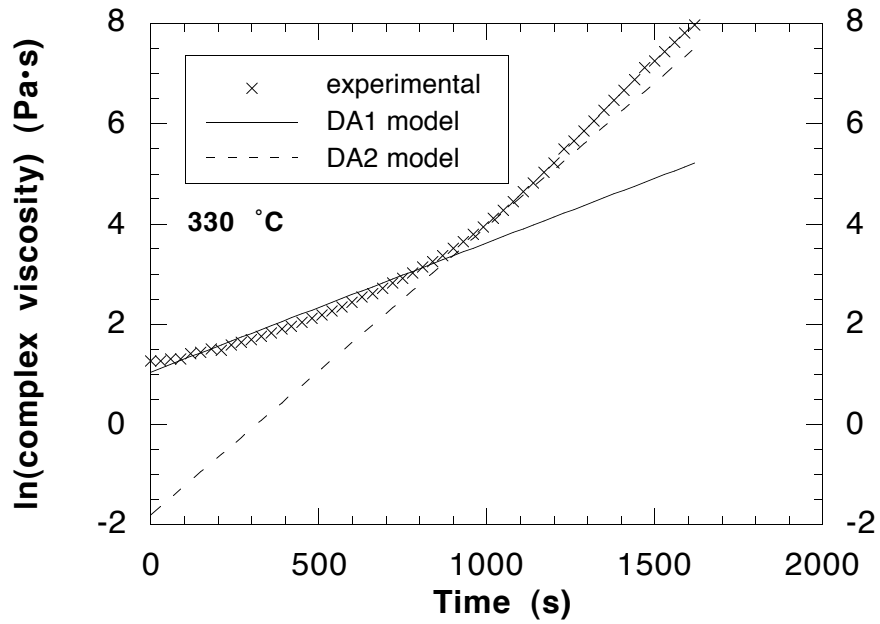


Figure 6.14.(b) DA1 and DA2 Fit of $\ln \eta^*$ versus Time for 330 °C

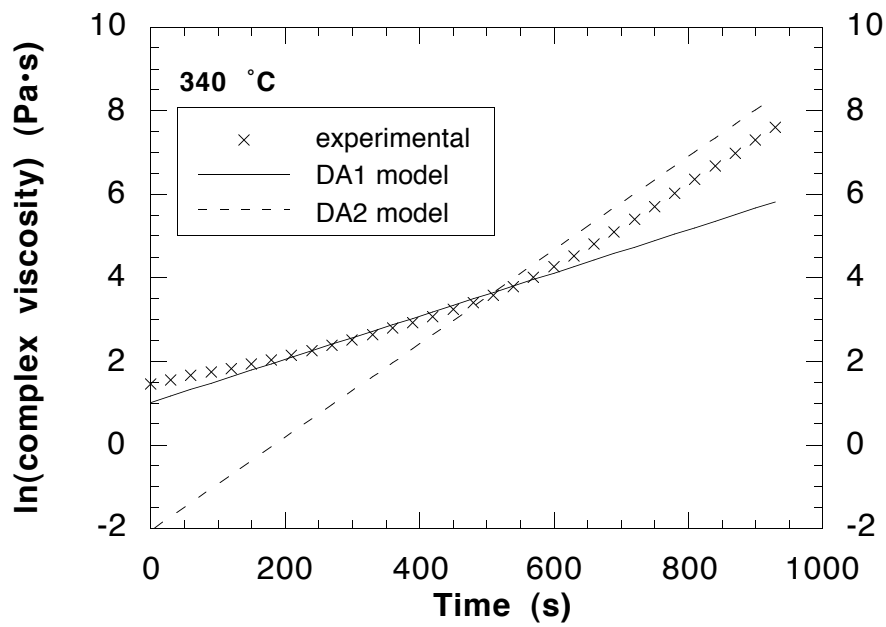


Figure 6.14.(c) DA1 and DA2 Fit of $\ln \eta^*$ versus Time for 340 °C

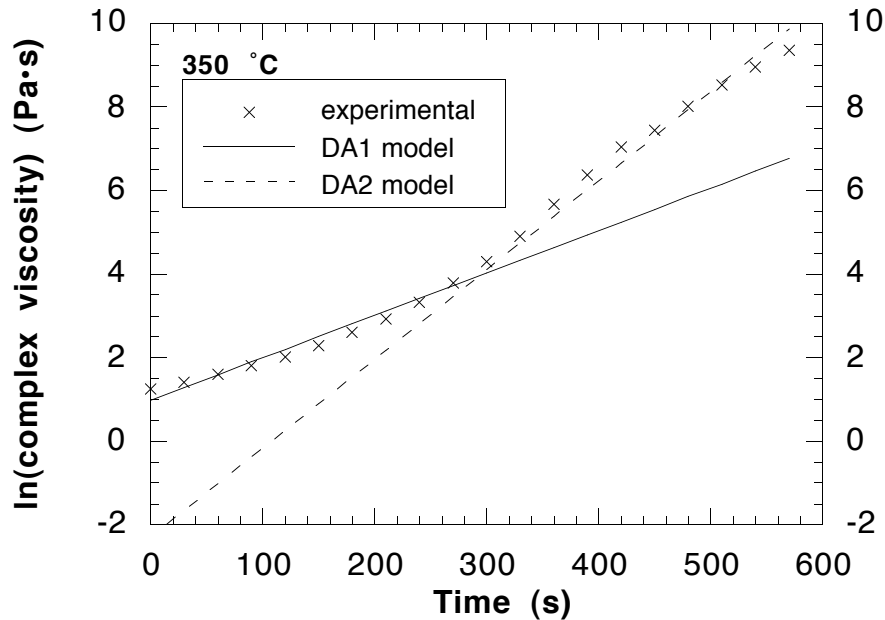


Figure 6.14.(d) DA1 and DA2 Fit of $\ln \eta^*$ versus Time for 350 °C

6.4.3 Completion of Model

It is apparent in Figure 6.14 that for each temperature there is a time at which DA1 and DA2 intersect. Knowing this intersection time is integral to predicting viscosity at a specific time or degree of cure since it must be known whether the time of interest lies within the realm of DA1 or DA2. Intersection times for the experimental temperatures may be found by setting the DA1 and DA2 models in Schemes 6.1 and 6.2 equal to each other and solving for time (Calculation 6.5). The degree of cure at the intersection times may be determined for each experimental temperature either by looking at the experimental degree of cure versus time data from the DSC analysis of Chapter 4 or using the combination kinetics model developed in Chapter 4 to calculate the degree of cure. These values are tabulated in Table 6.4. In general, it appears as though the transition from DA1 to DA2 occurs around a degree of cure of 0.37.

Calculation 6.5. Determination of Intersection Times

$$T = 325 \text{ °C} = 598 \text{ K: } 1.07 + (0.00180 \text{ s}^{-1})t = -1.67 + (0.00408 \text{ s}^{-1})t$$

$$T = 330 \text{ °C} = 603 \text{ K: } 1.05 + (0.00258 \text{ s}^{-1})t = -1.80 + (0.00575 \text{ s}^{-1})t$$

$$T = 340 \text{ °C} = 613 \text{ K: } 1.02 + (0.00517 \text{ s}^{-1})t = -2.05 + (0.0112 \text{ s}^{-1})t$$

$$T = 350 \text{ °C} = 623 \text{ K: } 0.991 + (0.0101 \text{ s}^{-1})t = -2.29 + (0.0214 \text{ s}^{-1})t$$

Table 6.4. Time and Degree of Cure at DA1 to DA2 Transition

Temperature (°C)	Intersection Time (s)	Calculated $\alpha^{(a)}$	Experimental α
325	1200	0.344	0.380
330	899	0.381	0.380
340	509	0.379	0.373
350	290	0.369	0.357
Average		0.368	0.373
Standard Deviation		0.0169	0.0109

a. Combination Kinetics Model of Chapter 4

Creation of an isothermal viscosity versus degree of cure model is begun by calculating the time to reach a specified degree of cure using the combination kinetics model in Chapter 4. Then, the intersection time for the isothermal temperature is determined using the Arrhenius plot of the natural logarithm of intersection time versus $1/T$ in Figure 6.15. Next, it is determined whether the time calculated to reach a specific degree of cure is greater than or less than the intersection time and the appropriate dual-Arrhenius model (DA1 or DA2) of complex viscosity from Scheme 6.1 or 6.2 is selected. Finally the complex viscosity is calculated for the chosen isothermal temperature and the time necessary to obtain a desired degree of cure.

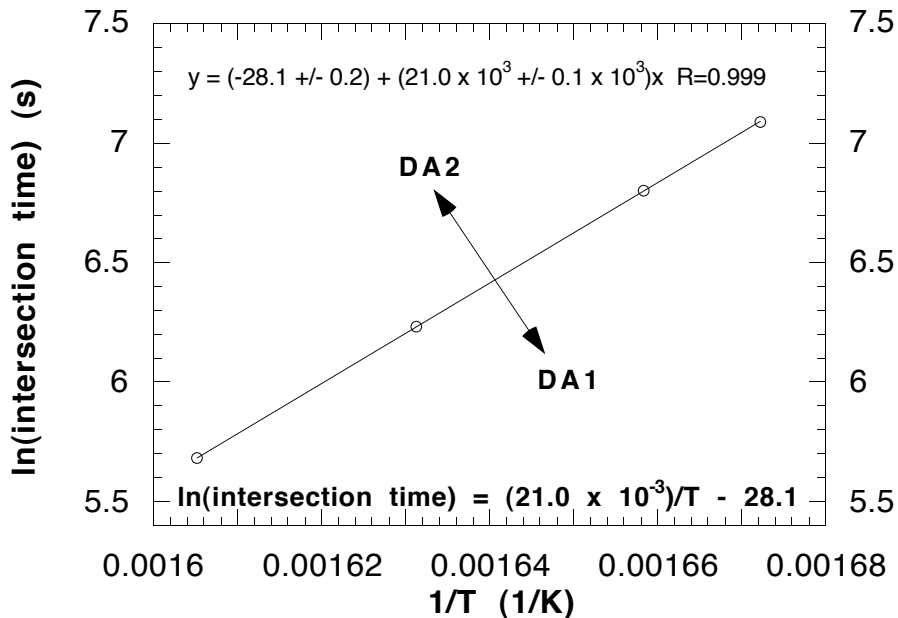


Figure 6.15. Arrhenius Plot of $\ln(\text{intersection time})$ versus $1/T$

6.4.4 Model Analysis

The values of ΔE_k and k_∞ were calculated to develop both the DA1 and DA2 models using a dual-Arrhenius approach. These values may also be determined via analysis of an Arrhenius plot of $\ln(t_{gel})$ versus $1/T$ (Figure 6.16). The data in this plot may be represented by Equation 6.5:

$$t_{gel} = t_{gel}^\infty \exp\left[\frac{\Delta E_g}{RT}\right] \Rightarrow \ln t_{gel} = \ln t_{gel}^\infty + \left(\frac{\Delta E_g}{RT}\right) \quad (6.5)$$

where:

t_{gel} = time to reach gel point (s);

t_{gel}^∞ = pre-exponential factor for gel time (t_{gel} at $T = \infty$) (s); and

ΔE_g = apparent activation energy for gelation (J/mol).

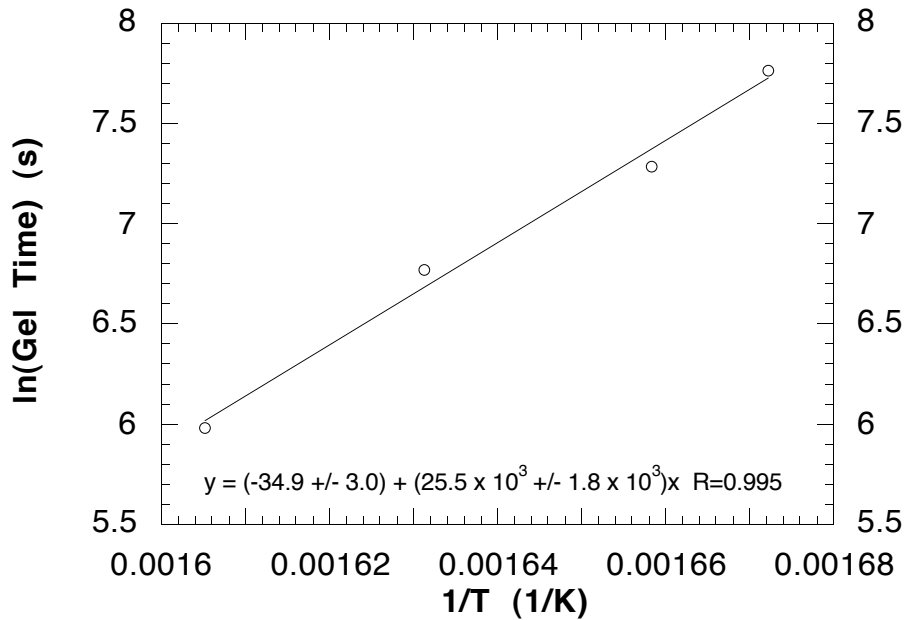


Figure 6.16. Arrhenius Fit of $\ln(t_{gel})$ versus $1/T$

The values for t_{gel}^∞ and ΔE_g are determined in Calculation 6.6 from the linear fit in Figure 6.16. These values may be used to predict the time to reach the gel point at any isothermal temperature within the experimental temperature range of 325 °C to 350 °C.

Calculation 6.6. Gel Time versus Temperature

$$\text{slope} = \frac{\Delta E_g}{R} = 25.5 \times 10^3 \pm 1.8 \times 10^3 \text{ K} \Rightarrow \Delta E_g = 2.12 \times 10^5 \text{ J/mol}$$

$$\text{intercept} = \ln t_{gel}^\infty = -34.9 \pm 3.0 \Rightarrow t_{gel}^\infty = 7.27 \times 10^{-16} \text{ s}$$

The value of ΔE_g compares well with the values calculated for ΔE_k for both DA1 and DA2 (Calculations 6.2 and 6.4). Furthermore, there is only about a ten percent difference between the activation energies calculated for reaction (gelation) using rheological data and those calculated using DSC data (1.90×10^5 J/mol - Figure 4.10 and 1.97×10^5 J/mol - Figure 4.11). The value of t_{gel}^∞ is defined as the time necessary to reach the gel point at infinite temperature. Thus, this value (Calculation 6.6) should be proportional to the inverse of k_∞ , the reaction rate at infinite temperature. The inverse values of k_∞ for DA1 and DA2 are 1.13×10^{-16} s and 3.09×10^{-16} s, respectively, and within the same order of magnitude as t_{gel}^∞ . These comparisons between activation energies and gelation rates determined via different techniques are useful for the purpose of validating the results obtained by each technique.

6.5 Summary

In summary, a two-stage, dual-Arrhenius model was successfully utilized to model the isothermal complex viscosity of 2.5kPETU over the experimental temperature range of 325 °C to 350 °C. The presence of a two-stage reaction process concurs with the general description of the reaction mechanism for PETU. The phenylethynyl termination sites at both ends of the PETU oligomers each provide the oligomer with the ability to form two single bonds with other oligomers, thus creating a structure in which three chains are emanating from a single carbon atom. It is thought that the PETU oligomers initially undergo chain growth by end-to-end connections at the phenylethynyl termination sites. In this first stage of the reaction, there are more available sites for reaction and the oligomers are shorter and more mobile, thus reactions may take place at a greater frequency during the first stage of reaction than during the second stage of reaction. Before the secondary reactions begin to take place, the polymer is in a thermoplastic form with increased molecular weight versus the original oligomers. During the thermoplastic chain growth stage, complex viscosity is gradually building with time due to increased occurrence of entanglements and other physical impediments to movement resulting from increased chain length. Then as the number of unreacted sites available for end-to-end connection decreases, an increasing number of secondary reactions begin to take place at once-reacted

ethynyl sites that have already undergone end-to-end reactions, thus beginning the crosslinking stage of the reaction. When secondary reactions begin to take place, an increase in steric hindrance combined with a decrease in chain mobility makes it more difficult for chains to get to the fewer sites available for reaction. This second stage of reaction, which appears to onset when the degree of cure is near 0.37, transforms the polymer from a thermoplastic structure to a thermoset structure. During the thermoset reaction stage, complex viscosity increases at a much greater rate due to the formation of chemical bonds between chains leading to a drastic reduction in their mobility. These two stages of reaction explain the transition seen in the relationship between complex viscosity and time during isothermal cures (Figure 6.4).

It is important to note that the influence of carbon fiber on reaction progress that was found during the T_g study (Chapter 5) was not considered in the development of the rheology model. A suggested future study of CFR PETU would allow estimation of the chemorheological response to the presence of carbon fiber. The neat PETU combination reaction kinetics model of Chapter 4 combined with the two-stage, dual-Arrhenius model described in this chapter allows for the development of a relationship between degree of cure and viscosity. Development of a combination reaction kinetics model for CFR PETU (towpreg) would provide a relationship between isothermal cure time and degree of cure for the fiber-influenced reaction. Knowing a relationship between viscosity and degree of cure based on the neat PETU studies would allow for the development of a relationship between viscosity and isothermal cure time for the CFR PETU via the CFR PETU combination reaction kinetics model.

6.6 References

1. A. Yousefi, P.G. Lafleur, and R. Gauvin, "Kinetic Studies of Thermoset Cure Reactions: A Review," *Polymer Composites*, **18**, (2), 157-168 (1997).
2. P.J. Halley and M.E. Mackay, "Chemorheology of Thermosets - An Overview," *Polymer Engineering and Science*, **36**, (5), 593-609 (1996).
3. M.R. Dusi, W.I. Lee, P.R. Ciriscioli, and G.S. Springer, "Cure Kinetics and Viscosity of Fiberite 976 Resin," *Journal of Composite Materials*, **21**, (3), 243-261 (1987).
4. W.I. Lee, A.C. Loos, and G.S. Springer, "Heat of Reaction, Degree of Cure, and Viscosity of Hercules 3501-6 Resin," *Journal of Composite Materials*, **16**, (6), 510-520 (1982).
5. A.C. Loos and G.S. Springer, "Curing of Epoxy Matrix Composites," *Journal of Composite Materials*, **17**, (2), 135-169 (1983).

6. L. Ye, V. Klinkmuller, and K. Friedrich, "Impregnation and Consolidation in Composites Made of GF/PP Powder Impregnated Bundles," *Journal of Thermoplastic Composite Materials*, **5**, 32-48 (1992).
7. M. Connor, S. Toll, J.-A. E. Manson, and A.G. Gibson, "A Model for the Consolidation of Aligned Thermoplastic Powder Impregnated Composites," *Journal of Thermoplastic Composite Materials*, **8**, 138-162 (1995).

Chapter 7 - Manufacture of 2.5kPETU Specimens for Moisture Exposure and Thermal-Oxidative Aging

7.1 Introduction

This chapter will briefly describe the manufacture of the composite panels and neat resin plaques for the moisture exposure (Chapter 8) and thermal-oxidative aging (Chapter 9) studies.

7.2 Composite Panel Manufacture

7.2.1 Dry Powder Prepregging

Approximately 4500 meters of towpreg were manufactured using the electrostatic, fluidized bed system described in Chapter 1. All towpreg was produced by depositing 2.5kPETU powder on unsized, 24k, 5 μm diameter, G40-800 carbon fiber tow. This fiber is manufactured by Toho Carbon Fibers, Inc. and has tensile strength and modulus of 5.86 GPa and 290 GPa, respectively. Powder coating runs generally ran at line speeds of 5 to 9 m/min with an overall average speed of about 6 m/min; these runs lasted between 20 to 90 minutes. Longer continuous runs were not available due to limited powder quantities, tow snags, and tow spreading problems. Due to the limited powder quantity, longer powder coating runs were terminated when not enough powder remained to charge the fluidizing bed. At this point, powder had to be recovered from the recycling chamber and returned to the powder feeder and the fluidized bed. Often, coating runs were aborted due to instances when the tow would not spread properly or the tow would snag somewhere along the powder coating line and result in tow breakage. Approximately 30 powder coating runs were completed before the supply of fluidizable powder was exhausted.

Several processing variables were important to producing consistent towpreg with the proper fiber-to-resin ratio (FRR). The electrostatic, fluidized bed operated with a fluidizing velocity ranging from $6.0 \times 10^{-2} \text{ m}^3/\text{min}$ to $9.5 \times 10^{-2} \text{ m}^3/\text{min}$; the velocity was adjusted as needed due to changes seen downline in the FRR. Also, the electrostatic voltage was fixed at 20 kV. After the tow passed through the cloud of powder fluidized by these conditions, it passed through the tube furnace where the powder-coated tow was exposed to 420 °C for approximately 10 seconds. This exposure time and temperature was adequate for softening the polymer enough to tack it onto the fiber and produce the towpreg that was wound on a take-up spool after exiting the tube furnace.

7.2.2 Ply Production

Assembly of square plies of towpreg followed the description given in the drum winding description of Chapter 2 (section 2.4.2). Towpreg was wound around the drum 47 to 53 times to generate each of the 38 sheets of towpreg having widths of approximately 160 mm. The plies for the 152.4 mm square panels were cut from these sheets. To produce the 80 mm wide sheets needed for 76.2 mm square panels, 24 to 27 turns of towpreg were needed.

7.2.3 Composite Panel Consolidation

For each 152.4 mm x 152.4 mm x ~3.2 mm composite panel, 26 plies were selected from the 38 different windings. For each panel, these 26 plies were stacked unidirectionally in the mold and trimmed as described in Chapter 2 (section 2.4.3). Due to variation in the FRR amongst the sheets of towpreg, a detailed ply lay-up scheme was developed to provide a consistent sequence of ply FRRs from top to bottom of each stack. This sequence was created to provide both uniformity between panels and to give the panels the best chance for good fiber wet-out with low void contents. Two 76.2 mm x 76.2 mm x ~1.9 mm composite panels were also manufactured to provide materials for dynamic mechanical thermal analysis specimens; these panels contained 15 plies cut from 80 mm wide sheets.

These stacks of towpreg plies were then consolidated and cured in the hot press as described in section 2.4.3 of Chapter 2. The details of the processing schedule for these panels follows. The mold was placed under a compaction pressure of 172 to 207 kPa (25 to 30 psi) at room temperature. This pressure was held as the mold temperature was ramped at 5 °C/min to 250 °C. The ramp rate was then changed such that the temperature was ramped from 250 °C to 350 °C at 3 °C/min. Compaction pressure was increased during this second temperature ramp. When the mold temperature reached ~270 °C, a gradual increase of pressure was commenced such that the compaction pressure reached ~690 kPa (~100 psi) as the mold temperature reached 325 °C. This compaction pressure setting was held for the remainder of the processing schedule. The mold temperature was held at 350 °C for 50 minutes before cooling back to room temperature at -4 °C/min. This 50 minute hold provided approximately 70 minutes above 325 °C; the importance of time above 325 °C is addressed in Chapter 5. These composite panels were manufactured prior to the T_g study of Chapter 5, thus the cure schedule was based on the results of the neat resin cure kinetics study of Chapter 4.

7.2.4 Post Consolidation

Each panel was imaged ultrasonically to assist in the layout of specimen locations within each panel. Specimen locations were positioned with the main consideration being that obvious panel flaws either be completely avoided or placed in non-load bearing portions of specimens. In addition, machining of specimens from the panels was considered in determining the specimen layout. Though the layouts varied a little from panel to panel, Figure 7.1 provides a general idea of where the specimens were cut from the panels for moisture exposure and thermal-oxidative aging. Moisture exposure specimens were cut prior to exposure, whereas thermal-oxidative aging specimens were cut after aging. The reasoning behind cutting specimens before or after aging will be presented in Chapter 9 for thermal-oxidative aging and has been discussed in Chapter 3 for moisture sorption.

Knowing the specific stacking sequence of each panel provides the information needed to calculate the mass of fiber in each panel. Assuming no fiber is lost during consolidation, the remaining matrix mass is the difference between the final mass of the panel and the original fiber mass. Thus, knowing the densities of the fiber [1] and matrix (given later in this chapter), the volumes of fiber and matrix in each panel may be calculated. Subsequently, the fiber volume fraction can be estimated for each panel assuming no voids. These values were compared with fiber volume fraction calculations based on calculating the volume of each panel from its external dimensions. The two methods of calculation produced fiber volume fractions that differed by less than one percent. The calculated fiber volume fractions of all the panels ranged from 0.61 to 0.63.

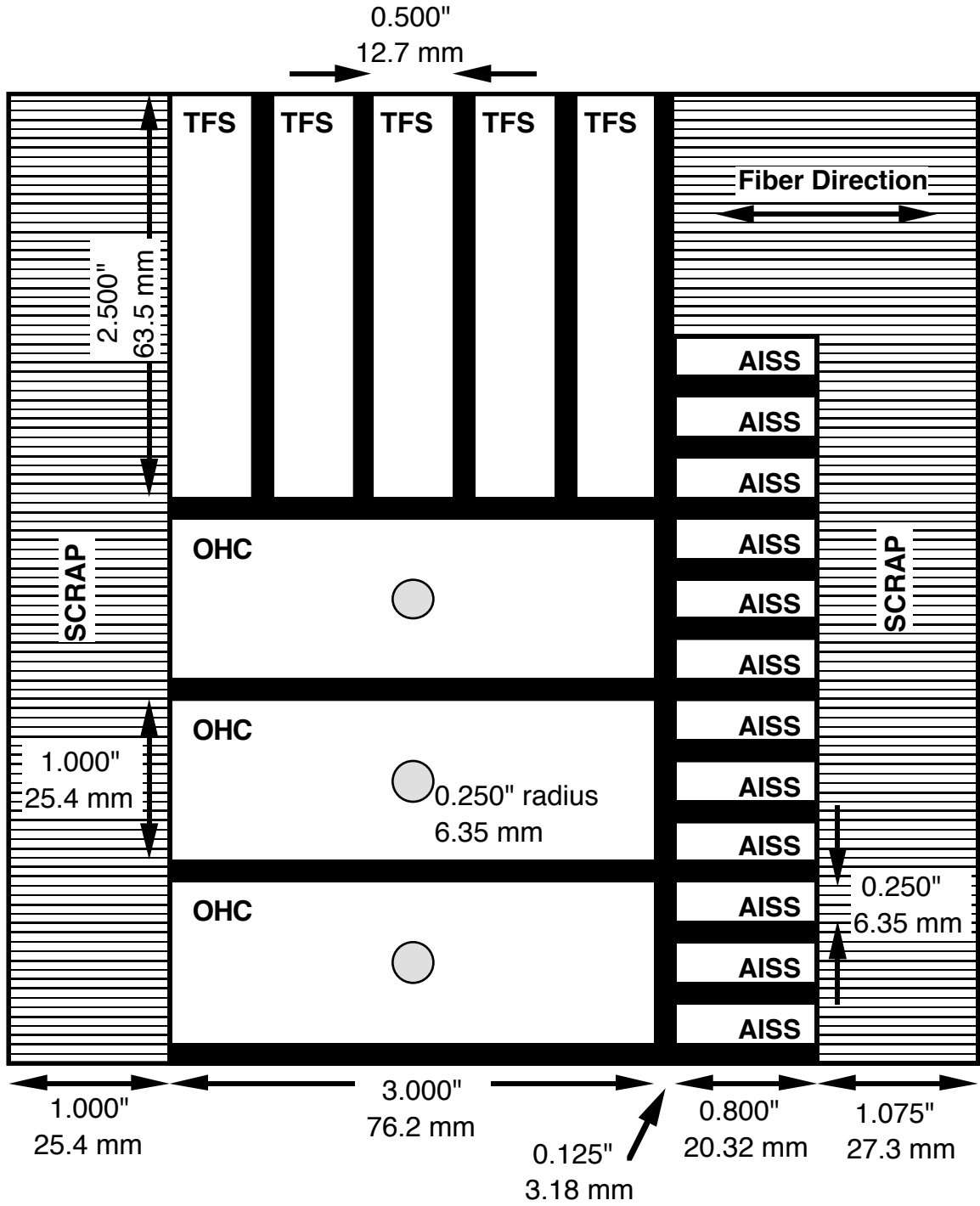


Figure 7.1. Specimen Layout

7.3 Neat Resin Plaques

Two 2.5kPETU neat resin plaques were manufactured for density measurements, as well as, to investigate moisture exposure and thermal-oxidative aging effects on the neat polymer. These plaques were manufactured from 50 g of polymer that was placed in the 76.2 mm x 76.2 mm steel mold. The mold was then placed in a vacuum oven at ambient pressure to preheat to 270 °C. At this temperature, the 2.5kPETU will be fluid enough to allow entrapped air to escape, but will not begin crosslinking. Once the thermocouple in the mold reached 270 °C, vacuum was pulled for 20 hours to remove entrapped air. Next, the vacuum was released and the oven temperature setting was reduced to 30 °C to allow the mold and resin to slowly cool. When the mold had cooled to approximately 50 °C, the mold and fused resin plaque were removed from the oven. The steel plunger was then inserted in the mold and the mold was placed between the platens of the hot press. The neat resin plaque was then cured following the same temperature schedule described above for the composite panels. However, the top platen was positioned about 1 mm above the steel plunger to provide heat transfer, but not compaction pressure. The weight of the steel plunger provided light compaction pressure. Following cure, the neat resin plaques were imaged ultrasonically to locate voids. Specimens for density measurements, moisture exposure, and thermal-oxidative aging were then cut from the plaques.

The density measurements followed the ASTM Standard Test Method for Density and Specific Gravity (Relative Density) of Plastics by Displacement (D 792-91) using distilled water as the immersion fluid. The density of neat 2.5kPETU was determined to be $1.28 \pm 0.01 \text{ g/cm}^3$.

7.4 References

1. Toho Carbon Fibers, Inc., *Material Brochure*, 444 High Street, Suite 200, Palo Alto, CA 94301.

Chapter 8 - Moisture Sorption Effects on CFR 2.5kPETU Composites

8.1 Introduction

This chapter investigates the effects of moisture sorption on the mechanical properties of 2.5kPETU/G40-800 carbon fiber composites. In addition to mechanical properties, moisture sorption rates, moisture content versus relative humidity, and moisture induced strain were studied. This investigation is rather similar to the one undertaken in Chapter 3, though it is meant to be more extensive in the amount of information garnered regarding moisture sorption effects on the composite material. Moisture exposure experiments will follow the guidelines of the ASTM Test Method for Moisture Absorption Properties and Equilibrium Conditioning of Polymer Matrix Composite Materials (D 5229-92).

An important issue that was examined in Chapter 3 was whether specimens intended for mechanical testing should be cut before (Pre-Cut) or after (Post-Cut) moisture exposure. The results in Chapter 3 demonstrated that cutting the specimens before or after exposure had no effect on mechanical property retention. In addition, no difference was seen in the effective moisture equilibrium content, M_m , values for Pre-Cut and Post-Cut specimens. However, the through-the-thickness diffusion coefficient, D_z , was higher for the transverse flexural strength (TFS) specimens than for the larger rectangular panels. The experiments in this chapter will use pre-cut specimens, despite the discrepancies in D_z values. In general, it is preferred that the value of D_z for a composite be as low as possible. By using the smaller TFS and open-hole compression strength (OHCS) specimens to measure D_z , a conservative value will be obtained. An additional advantage to pre-cutting specimens is that specimens may be taken from different panels versus just one, thus obtaining a better representation of material properties.

8.2 Mechanical Test Specimens - Experimental

8.2.1 Specimen Preparation

8.2.1.1 Specimen Distribution

Three of the 152.4 mm square panels manufactured in Chapter 7 were selected and TFS, OHCS, and apparent interlaminar shear strength (AISS) specimens were cut from these panels in a manner similar to that of Figure 7.1, with the dimensions given in Figure 7.1. The specimens from the three panels were distributed into three groups labeled: Controls, Wet, and Wet/Dry. Each panel was represented in each group by one OHCS, one or two TFS, and four AISS specimens. In other words, each group consisted of three OHCS

specimens (one from each panel), five TFS specimens (one from one panel and two from the other two panels), and twelve AISS specimens (four from each panel).

8.2.1.2 Aluminum Specimens

To act as controls for moisture sorption measurements, eight specimens were cut from an aluminum sheet having a thickness of 3.18 mm. Five of these eight specimens were cut with the same dimensions as the composite TFS dimensions. The remaining three specimens were cut with the same dimensions as the composite OHCS specimens. These eight aluminum specimens were sealed in the same manner as the composite specimens were; sealant applications is described later. In addition to the aluminum specimens, a 75 mm x 140 mm aluminum panel was cut from this sheet. The aluminum panel will allow for the measure of aluminum moisture content. Using the aluminum panel as a control, the sealed aluminum specimens will allow for the measure of sealant moisture content. Thus, the moisture content of the sealants on the composite specimens may be taken into account when calculating the composite moisture content.

8.2.1.3 As-Manufactured Dimensions and Masses

Prior to any environmental conditioning, the dimensions and masses of the OHCS and TFS specimens were measured and recorded. All measurements were made using an anvil-faced micrometer with a precision of 0.0025 mm. The widths and thicknesses of the TFS specimens and the widths of the OHCS specimens were measured at three points along the length of the specimens. The thicknesses of the OHCS specimens were measured at four locations: near both ends of the specimen and in the spaces between the center hole and two long edges.

Following measurement of dimensions and masses, the Control TFS, OHCS, and AISS specimens were mechanically tested. Thus, they were not dried and were tested as-manufactured.

8.2.1.4 Drying

Prior to sealing, the Wet, Wet/Dry, and aluminum specimens were placed in a vacuum oven at 90 °C under a vacuum of approximately 95 kPa to bring the specimens to an equilibrium baseline moisture content. After the composite specimens reached a stable mass (1053 hours), all specimens were removed from the vacuum oven and their equilibrium vacuum dried masses were recorded. The ten composite TFS specimens had

an average vacuum-dried mass of 4.06 ± 0.03 g. The six composite OHCS specimens had an average vacuum-dried mass of 9.54 ± 0.06 g. The five aluminum TFS specimens had an average vacuum-dried mass of 6.76 ± 0.01 g. The three aluminum OHCS specimens had an average mass of 15.95 ± 0.01 g. Therefore, the composite TFS specimens were the only ones smaller in mass than the 5.0 g minimum stated by ASTM D 5229-92.

8.2.1.5 Sealant Application

To achieve one-dimensional, through-the-thickness diffusion, a sealant was needed to block moisture diffusion into the edges of the Wet and Wet/Dry specimens. Based on the results of Chapter 3, the stainless steel tape was selected for sealing the edges of the OHCS and TFS specimens. The GC Electronics insulating varnish used in Chapter 3 was used to seal the interior exposed edges of the hole in the OHCS specimens. The edges of the AISS specimens were not sealed since the moisture content of these specimens was not monitored; it was assumed their M_m was equivalent to that of the OHCS and TFS specimens. Initially, only the varnish was added to the OHCS specimens and the specimens were returned to the vacuum oven to dry the varnish. Following 168 hours of drying, the varnish was no longer losing mass and was assumed to be dry. The OHCS specimens were weighed to determine the dry mass of sealant. Then, the stainless steel tape was added to the edges of the TFS and OHCS specimens. Following another 230 hours of vacuum drying, the tape mass stabilized and the specimens were ready for moisture absorption.

8.2.2 Moisture Absorption and Preparation for Mechanical Testing

To begin moisture absorption, the sealed specimens were placed into a temperature/humidity (T/H) chamber (Blue M Model FRS-13C) at 85% relative humidity (RH) and 90 °C (Chapter 3 explains the selection of these conditions). Moisture uptake was recorded by periodically removing the specimens from the T/H chamber; allowing them to cool for approximately 10 minutes in a sealed, humid environment; individually weighing each specimen; and then quickly returning the specimens to the T/H chamber. The specimens were kept at 90 °C and 85% RH until the composite specimens reached M_m , which was defined to be achieved when the percent moisture content changed less than 0.01% by mass in 168 hours.

The composite specimens reached M_m following 777 hours of exposure; the specimens remained in the 90 °C / 85% RH environment for an additional 66 hours before the Wet TFS specimens were removed for thickness measurements and mechanical testing. Upon

removal from the T/H chamber, the specimens were kept in a sealed environment until they were tested; mechanical testing was completed within 62 minutes of the specimens' removal from the T/H chamber. Immediately prior to mechanical testing, the stainless steel tape was peeled from the specimen edges; residual tape adhesive was left on the specimens. Upon completion of the testing of the Wet TFS specimens, the Wet AISS specimens were removed from the T/H chamber and immediately tested; the last specimen was tested 35 minutes after the specimens were removed from the chamber. After a total of 990 hours of exposure, the Wet OHCS specimens were removed for thickness measurements and mechanical testing. Upon removal from the T/H chamber, the specimens were kept in a sealed environment until they were tested; mechanical testing was completed within 2 hours of the specimens' removal from the T/H chamber. Immediately prior to mechanical testing, the stainless steel tape was peeled from the specimen edges; residual tape adhesive and varnish were left on the specimens. The remaining specimens (Wet/Dry and aluminum) stayed in the 85% RH T/H chamber for an additional 211 hours, a total of 1201 hours, before the relative humidity in the T/H chamber was reduced to 10%; the temperature was maintained at 90 °C.

8.2.3 Moisture Desorption and Preparation for Mechanical Testing

The composite and aluminum specimens were kept in the 90 °C / 10% RH environment until the specimens reached M_m , which again was defined by the point at which the percent moisture content changed less than 0.01% by mass in 168 hours. Moisture desorption was recorded by periodically removing the specimens from the T/H chamber; allowing them to cool for approximately 10 minutes in a sealed, dry environment; individually weighing each specimen; and then quickly returning the specimens to the T/H chamber. The lower limit of the T/H chamber's relative humidity capabilities is just below 10% RH, thus 10% RH was selected such that the T/H chamber could reliably maintain this condition for long-term exposures. The Blue M convection oven used in Chapter 3 was not used during this experiment since the T/H chamber provided better control of the relative humidity.

Following 1181.5 hours at 90 °C / 10% RH, the composite specimen masses had stabilized at an M_m . All of the Wet/Dry and aluminum specimens were removed from the T/H chamber, weighed, measured for thickness, and placed in sealed plastic bags with Drierite desiccant. Due to unforeseen circumstances, the specimens were kept in this desiccant environment for 1794 hours. After this time, the specimen masses had decreased some; presumably, the desiccant absorbed a small amount of moisture from the composite specimens. Therefore, the composite specimens were returned to the 90 °C / 10% RH

environment to restore them to their original 10% RH M_m ; this recovery was complete within 336 hours. After an additional 50 hours at 90 °C / 10% RH, the Wet/Dry TFS and AISS specimens were removed for testing. The TFS testing was completed within 15 minutes of specimen removal from the T/H chamber. Immediately prior to mechanical testing, the stainless steel tape was peeled from the specimen edges; residual tape adhesive was left on the specimens. The AISS testing was completed within 90 minutes of specimen removal from the T/H chamber; each specimen was kept in a sealed, dry environment until it was tested. Four-hundred and ten hours after the specimens were returned to the T/H chamber from the desiccant containing bags, the Wet/Dry OHCS specimens were removed from the T/H chamber for testing; two specimens were tested. These two specimens failed in the grips; thermal-oxidatively aged specimens being tested concurrently were also failing in the grips. Thus, further OHCS testing was postponed. The remaining Wet/Dry OHCS specimen was stored with Drierite desiccant for another 1632 hours before ultimately being tested. Immediately prior to mechanical testing, the stainless steel tape was peeled from the specimen edges; the tape adhesive and varnish was left on the specimens.

8.2.4 Mechanical Testing

8.2.4.1 Transverse Flexural Strength

The TFS tests were performed according to the ASTM Standard Test Method for Flexural Properties of Unreinforced and Reinforced Plastics and Electrical Insulating Materials (D 790-92) following the four-point bend method with the load span (16.9 mm) equal to one-third of the support span (50.7 mm) (Test Method II - Procedure A); the loading and support noses had diameters of 12.7 mm. A crosshead rate of 1.50 mm/min was used with a 5 kN load cell.

8.2.4.2 Open-Hole Compression Strength

The OHCS tests were performed following the Northrop Material Specification for Open-Hole Compression Test Method (NAI-1504C) using a test fixture from Wyoming Test Fixtures, Inc. Though, the fiber orientation was 100 percent unidirectional along the length of the specimens. A crosshead rate of 1.27 mm/min was used with a 150 kN load cell.

8.2.4.3 Apparent Interlaminar Shear Strength

The AISS tests were performed according to the ASTM Test Method for Apparent Interlaminar Shear Strength of Parallel Fiber Composites by Short-Beam Method (D 2344-

84) for flat laminates; the loading and support noses had diameters of 6.35 mm. The specimens were loaded in three-point bend with a support span of 12.7 mm to give a span-to-depth ratio of four-to-one. A 1.3 mm/min crosshead rate was used with a 5 kN load cell.

8.3 Dependence of Specimen Moisture Content and Dimensions on Relative Humidity - Experimental

8.3.1 Moisture Content versus Relative Humidity

Following testing of the five Control TFS specimens, the longer halves of the fractured specimens were procured for the measurement of the dependence of specimen moisture content on the relative humidity of the environment. The fractured ends of these specimens were trimmed leaving five specimens with masses ranging from 2.0 to 2.4 g. These five specimens were allowed to reach M_m in the T/H chamber during exposure to four different relative humidities: 25%, 40%, 55%, and 75%. The temperature of the chamber was at 90 °C for all moisture exposure. Three neat resin specimens, cut from the plaques manufactured in Chapter 7, joined the composite specimens during these four exposures. The neat resin specimens had masses ranging from 4.3 to 5.5 g. In addition to measurement of composite and neat resin M_m at these four relative humidities, four neat resin specimens traveled with the composite TFS, OHCS, and AISS specimens during their exposure to 85% RH and 10% RH. This group of four neat resin specimens included the three neat resin specimens that were later exposed to 25% RH, 40% RH, 55% RH, and 75% RH. Consequently, M_m values were also obtained at 85% RH and 10% RH for composite and neat resin specimens. The M_m for 85% RH was calculated by averaging the M_m calculated from masses recorded over the time range of 609 hours (24.7 hours^{1/2}) to 1201 hours (34.7 hours^{1/2}). The M_m for 10% RH was calculated by averaging the M_m calculated from masses recorded over the time range of 843 hours (29.0 hours^{1/2}) to 1176 hours (34.3 hours^{1/2}). The effective moisture equilibrium contents reported for the other relative humidities were calculated from the masses at the first measurement during which the masses changed by less than 0.01% over the past 168 hours.

8.3.2 Moisture Induced Strain

Following testing of the three Control OHCS specimens, pieces were cut from both ends of each specimen for density measurements. Five of these six end pieces were procured for measurement of dimension changes with changes in moisture content. These five specimens were approximately 15 mm wide in the fiber direction and 25.4 mm long

transverse to the fiber direction prior to humidity conditioning. Dimensions were measured using an anvil-faced micrometer with a precision of 0.0025 mm. Following initial measurement of width, length, and thickness, the specimens were vacuum dried at 90 °C to an equilibrium mass. Upon reaching this equilibrium mass, the dimensions were again measured. This procedure was repeated with exposures to 25% RH, 50% RH, and 75% RH. The mass measurements provided effective moisture equilibrium contents at each relative humidity. The dimension measurements provided the strain induced by the absorption of moisture at each relative humidity relative to the vacuum dried dimensions.

8.4 Results and Discussion - Moisture Sorption and Content

8.4.1 Through-the-Thickness Moisture Diffusion Coefficient

Moisture mass uptake versus the square root of time is shown in Figures 8.1.(a), 8.2.(a), and 8.3.(a) for exposure of the ten TFS and six OHCS specimens to 90 °C / 85% RH. Moisture mass loss versus the square root of time is shown in Figures 8.4.(a) and 8.5.(a) upon moving the five Wet/Dry TFS and three Wet/Dry OHCS specimens from a 90 °C / 85% RH environment to a 90 °C / 10% RH environment. The moisture absorption and desorption trends in Figures 8.1.(a) - 8.5.(a) demonstrate behavior consistent with Fickian diffusion. The values of D_z for both absorption and desorption were calculated using Equation 3.2. The slopes of the linear regions of the moisture sorption plots were necessary to calculate D_z as described in Chapter 3. The fits of these linear regions are shown in Figures 8.1.(b) - 8.5.(b). Calculation of D_z for both absorption and desorption utilized the value of M_m obtained following 85% RH exposure. The resultant values of D_z are listed in Table 8.1. These values may be compared with D_z and 85% RH M_m values of other fiber-reinforced polymeric composites in Table 3.2.

Table 8.1. Comparison of D_z values for TFS, OHCS, Absorption, and Desorption

Specimen Group	Absorption D_z ^(a) (mm ² /s)	Desorption D_z ^(a) (mm ² /s)
TFS	5.1×10^{-6} $\pm 0.5 \times 10^{-6}$	3.0×10^{-6} $\pm 0.3 \times 10^{-6}$
OHCS	3.6×10^{-6} $\pm 0.6 \times 10^{-6}$	2.3×10^{-6} $\pm 0.5 \times 10^{-6}$
TFS & OHCS Average	4.5×10^{-6} $\pm 0.9 \times 10^{-6}$	2.7×10^{-6} $\pm 0.5 \times 10^{-6}$

a. \pm Standard Deviation

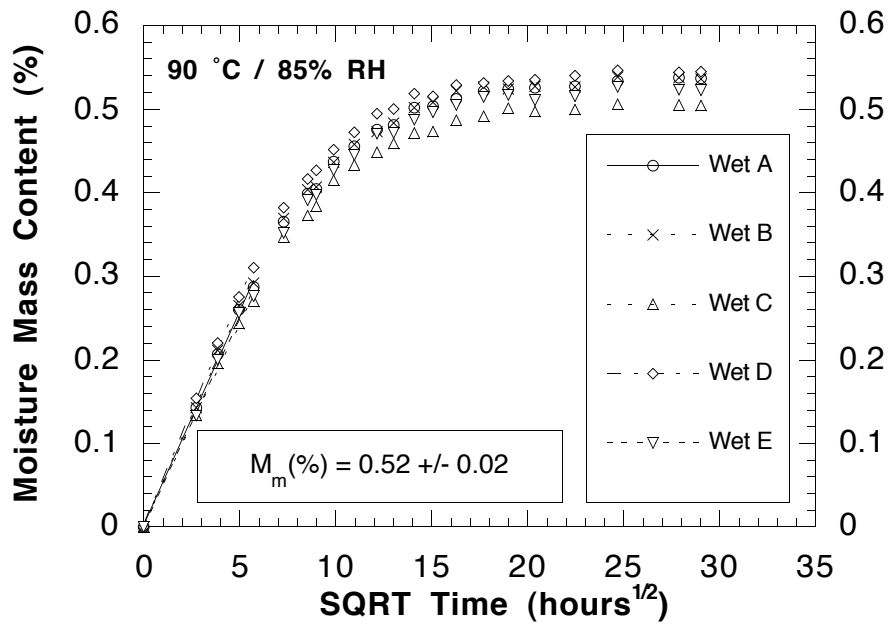


Figure 8.1.(a) Moisture Absorption by Wet TFS Specimens

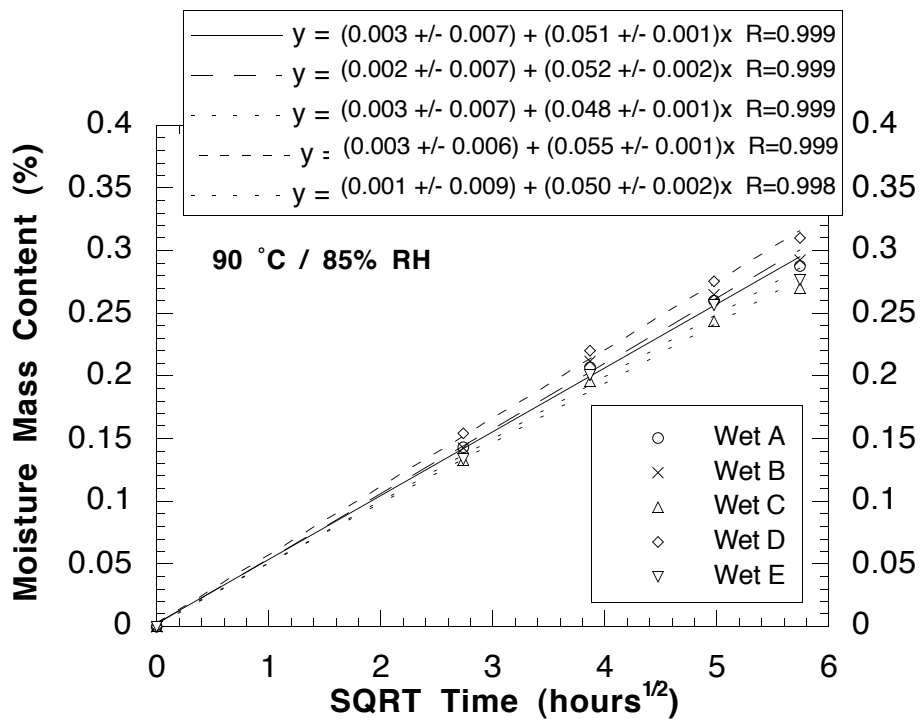


Figure 8.1.(b) Linear Fit of Wet TFS Specimen Moisture Absorption

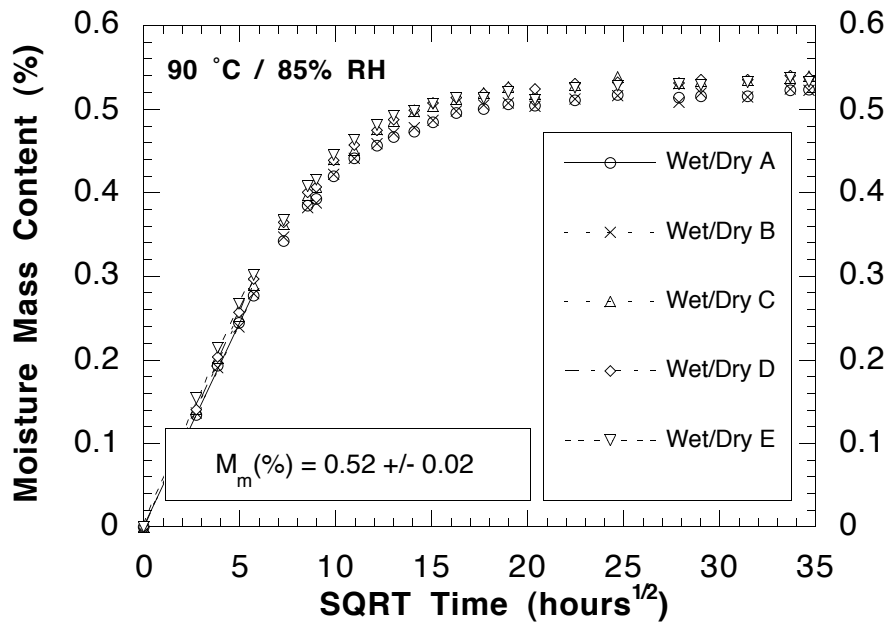


Figure 8.2.(a) Moisture Absorption by Wet/Dry TFS Specimens

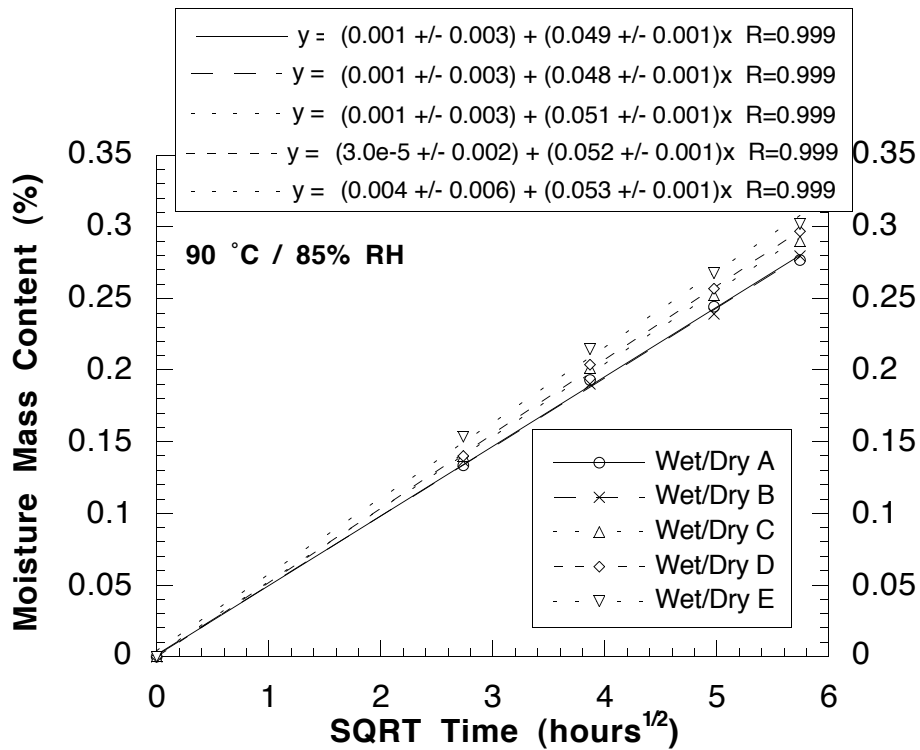


Figure 8.2.(b) Linear Fit of Wet/Dry TFS Specimen Moisture Absorption

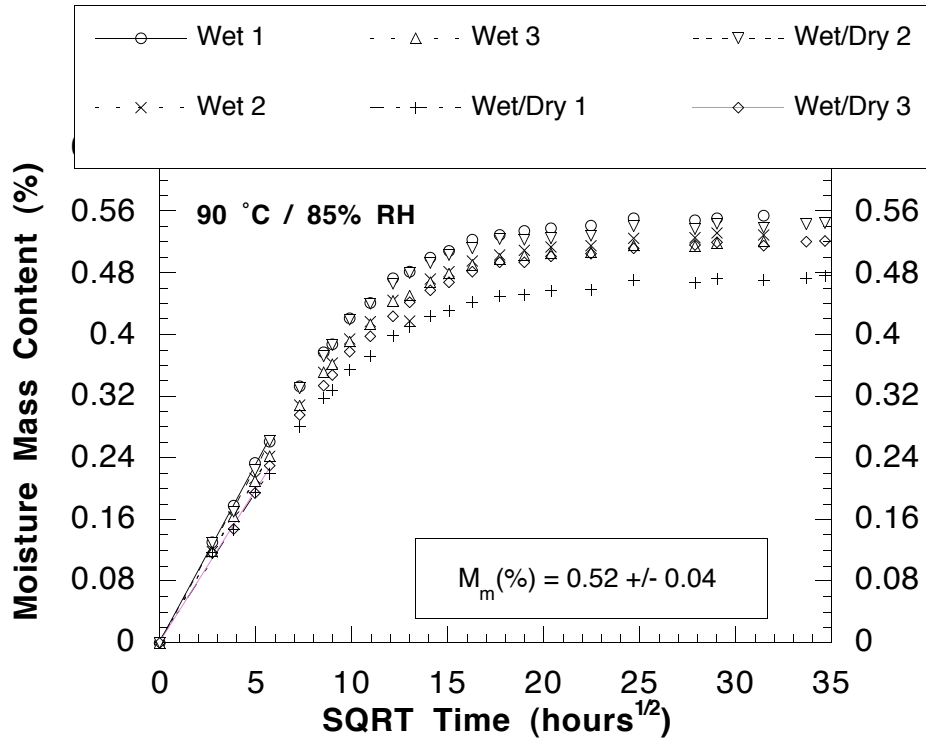


Figure 8.3.(a) Moisture Absorption by OHCS Specimens

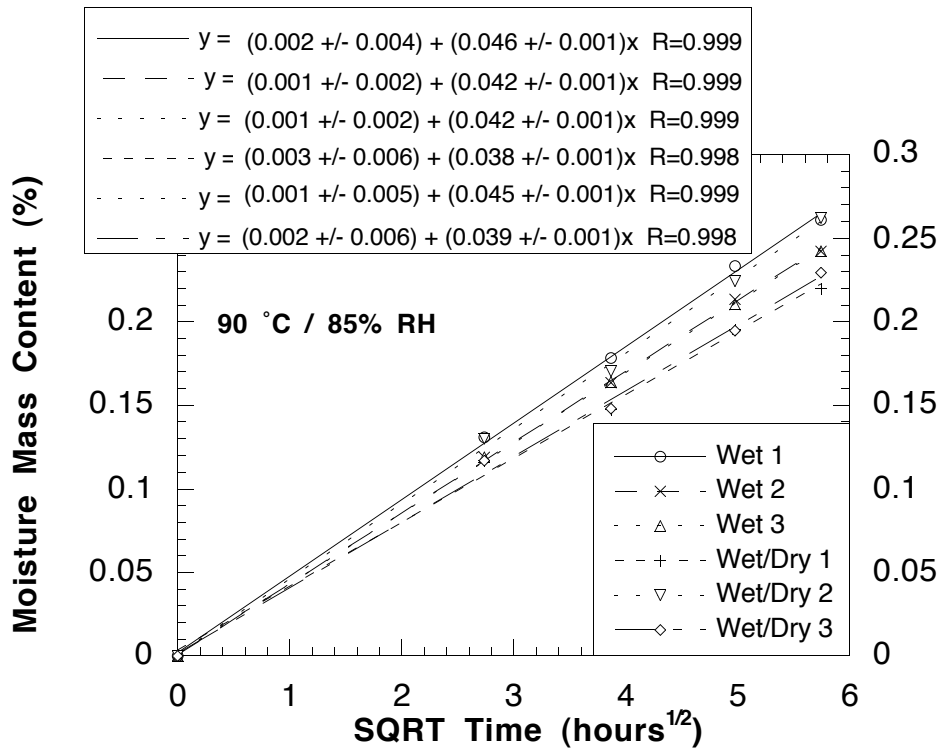


Figure 8.3.(b) Linear Fit of OHCS Specimen Moisture Absorption

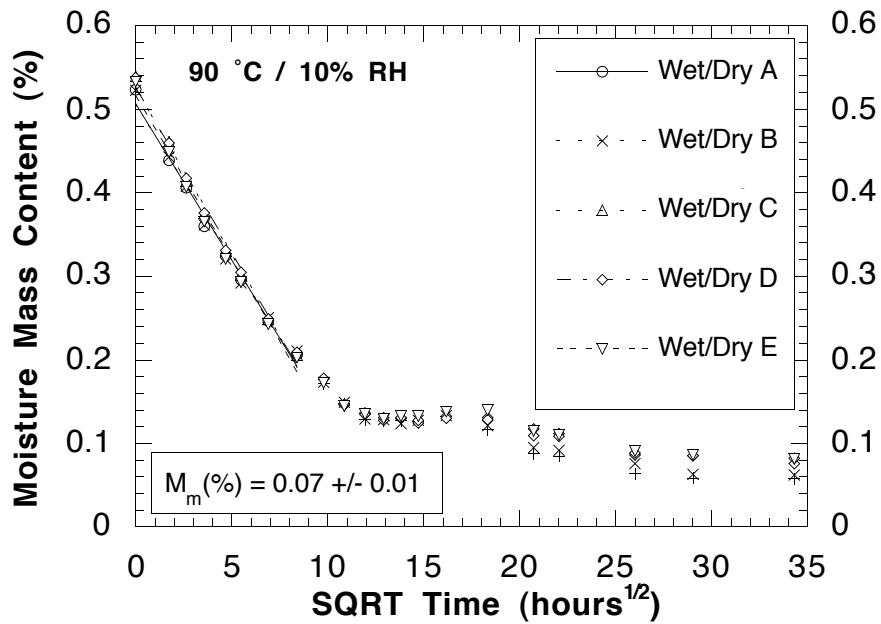


Figure 8.4.(a) Moisture Desorption by Wet/Dry TFS Specimens

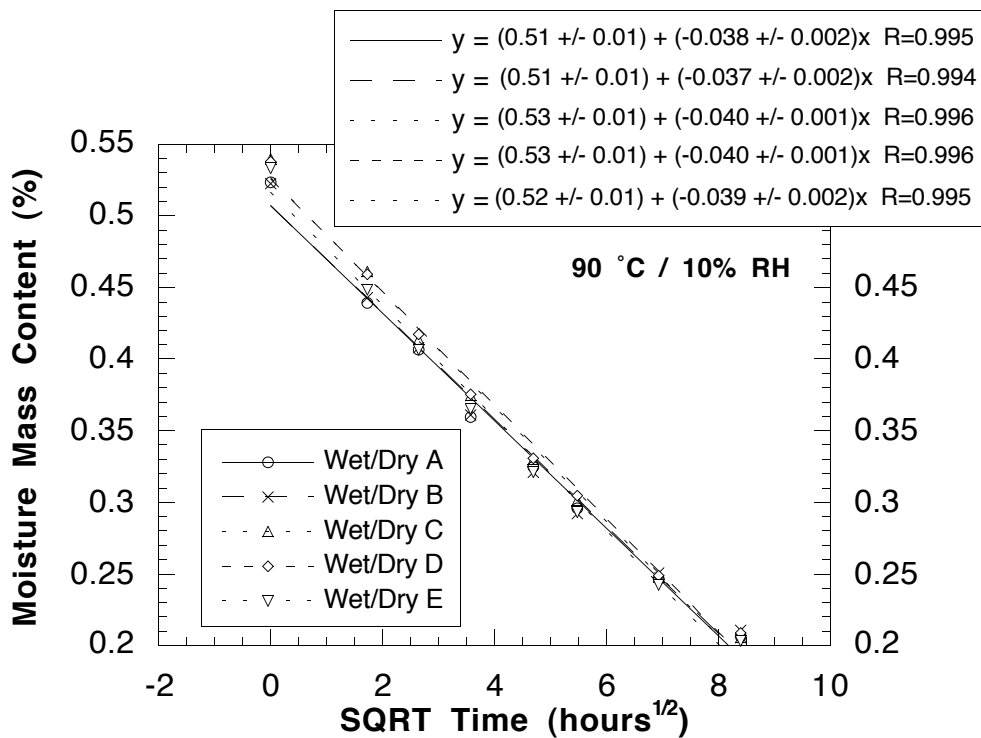


Figure 8.4.(b) Linear Fit of Wet/Dry TFS Specimen Moisture Desorption

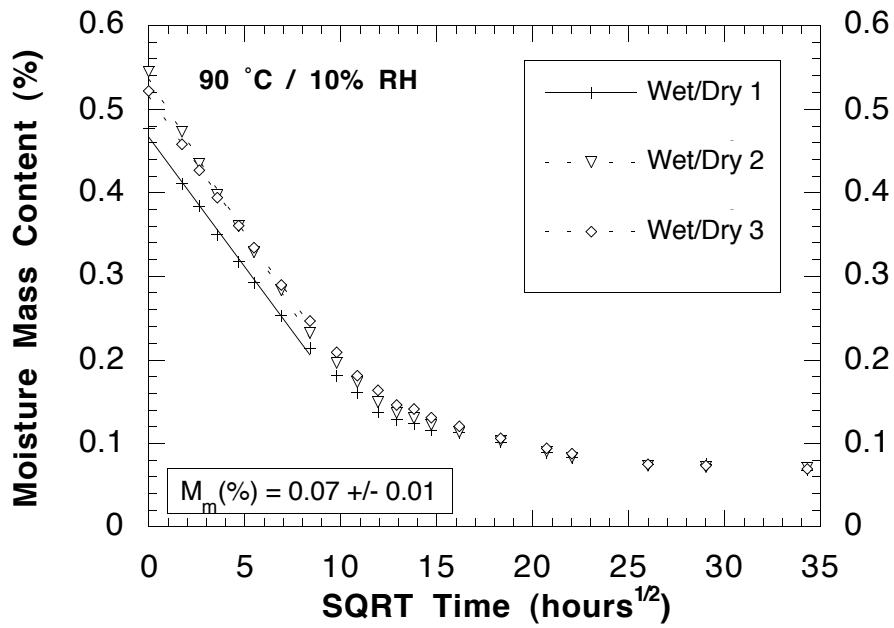


Figure 8.5.(a) Moisture Desorption by OHCS Specimens

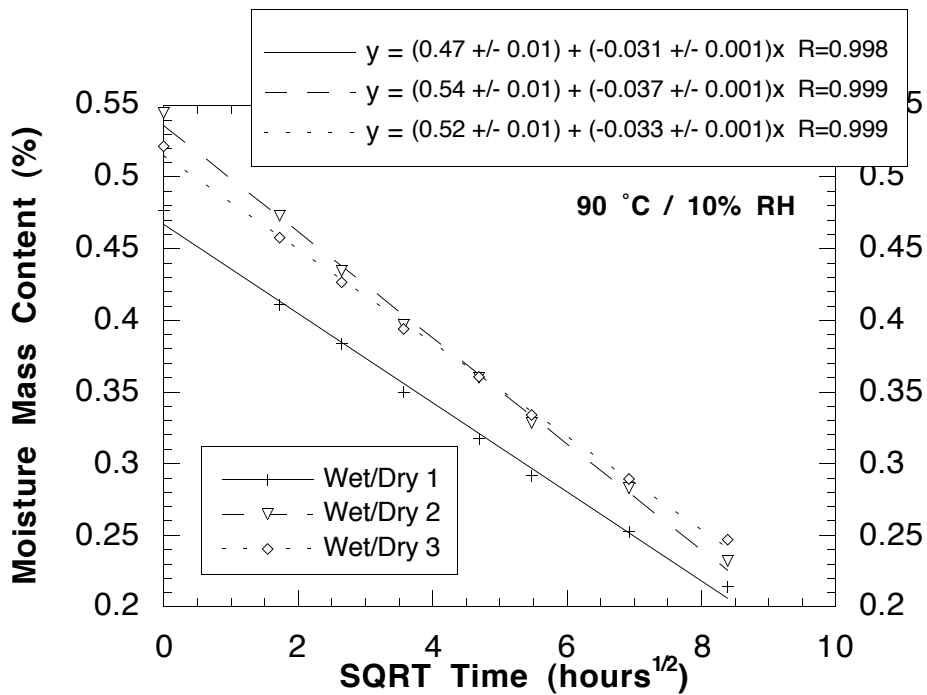


Figure 8.5.(b) Linear Fit of OHCS Specimen Moisture Desorption

Chapter 3 reported that desorption measurements on 76.2 mm x 12.7 mm TFS specimens resulted in significantly higher D_z values than desorption measurements on a 132 mm x 75.3 mm panel. The results shown in Table 8.1 again show that reducing the specimen size produces an increase in D_z . In Chapter 3, this increase in D_z with decreasing specimen size was attributed to error introduced by the aluminum sealant control specimens since the same error in adjustment for moisture mass content of sealants would be more significant in smaller specimens. In addition, decreasing the specimen size decreases the ratio of exposed surface area to sealed surface area. This reduction results in diffusion at sealed edges playing a larger role in the overall specimen moisture content. Though the TFS D_z values may be taken as conservative values, ASTM D 5229-92 would recognize the OHCS D_z values since these specimen masses were approximately twice that of the minimum required specimen mass of 5.0 g.

In addition to specimen size influencing the measured values of D_z , there is a difference in the values of D_z measured during moisture absorption versus those measured during moisture desorption. The higher diffusion coefficient for moisture absorption may be due to the vacuum drying prior to exposure to 85% RH at 90 °C. This vacuum drying eliminates moisture from not only the matrix, but also from microvoids throughout the composite. Empty microvoids near the surface of the composite may aid initial moisture uptake by providing additional space for incoming moisture to reside. As moisture moves into these microvoids, additional moisture may be absorbed by the matrix, thus increasing the overall rate of moisture uptake. Once the composite reaches M_m at 85% RH, and moisture desorption is begun at 10% RH, the microvoids would not contribute in the same manner to moisture loss. As moisture moves out of the microvoids, into the matrix, and towards the surface, additional moisture from interior matrix may move into the microvoids, thus the flux of moisture through the microvoids would be the same as through the matrix after the composite has reached M_m . Moisture desorption may also be slowed versus moisture absorption by PETU/moisture interactions. Evident in the reduction of TFS following moisture exposure, moisture absorption and desorption degrade the matrix. Some of this degradation may be hydrolytic in which moisture forms weak bonds with PETU. This interaction between the polymer and moisture molecules would likely slow the diffusion of moisture out of the matrix.

The possible influence of microvoids and moisture content on D_z suggests an experiment in which D_z is measured on vacuum-dried specimens during moisture absorption in a relatively low relative humidity. Upon reaching M_m at this relative humidity, any

microvoids would be assumed to be occupied by moisture, thus their influence on additional moisture uptake would be negligible. The relative humidity would then be increased for another measurement of D_z . After reaching the next M_m , the relative humidity would again be increased for another D_z measurement. Repetition of this procedure would provide insight into the influence of moisture content on D_z via interactions between moisture and the matrix.

8.4.2 Equilibrium Moisture Contents

The results of the measurements of M_m versus relative humidity are given in Table 8.2 and Figure 8.6. The typical method for fitting M_m versus relative humidity data is to use the power law shown in Equation 8.1:

$$M_m = a \cdot (\%RH)^b \quad (8.1)$$

where a and b are material constants [1]. For CFR 2.5kPETU the results are linear, so $b = 1$. The values of a for both the composite and neat resin are given in Figure 8.6 and may be compared to those of other fiber-reinforced polymer matrix composites in Table 8.3. Assuming only resin absorbs moisture, the ratio of the neat resin and composite values of a may be used to estimate the fiber volume fraction of the composite assuming no voids. The values of a in Figure 8.6 produce a fiber volume fraction of 0.61, which agrees well with the estimates in Chapter 7.

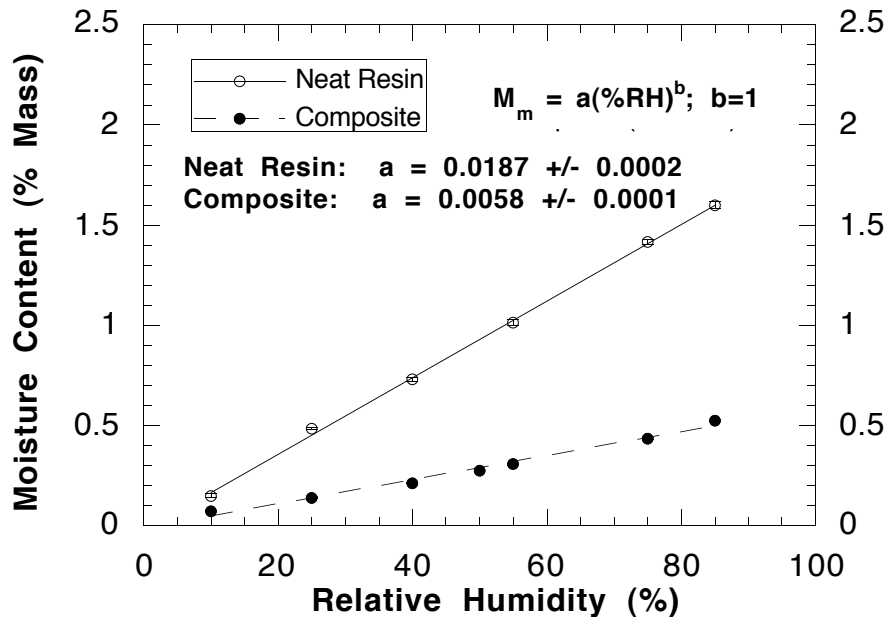


Figure 8.6. Moisture Equilibrium Content versus Relative Humidity

Table 8.2. Moisture Content versus Relative Humidity

Relative Humidity (%)	Composite Moisture Content (% Mass) ^(a)	Neat Resin Moisture Content (% Mass) ^(a)
10	0.07 ± 0.01	0.151 ± 0.003
25	0.139 ± 0.007	0.486 ± 0.003
40	0.214 ± 0.011	0.733 ± 0.003
50	0.275 ± 0.007	
55	0.309 ± 0.012	1.02 ± 0.01
75	0.436 ± 0.014	1.42 ± 0.01
85	0.52 ± 0.02	1.60 ± 0.01

a. ± Standard Deviation

Table 8.3. Coefficients *a* and *b* for Selected Composite Materials

Fiber / Matrix	<i>a</i>	<i>b</i>	Reference
T300 Graphite / 1034 Epoxy	0.017	1	1
T300 Graphite / 3501-5 Epoxy	0.015	1	1
AS Graphite / 5208 Epoxy	0.019	1	1
Carbon / PMR15	0.014	1	2
IM7 / Avimid K3B	0.0011	1.34	3

8.4.3 Moisture Induced Strain

The specimens were too thin (~3.2 mm) to accurately measure specimen expansion in the thickness direction transverse to the fibers due to moisture uptake. Furthermore, measurements in this direction would be skewed by the presence of resin rich layers on the molded surfaces. In addition, expansion in the fiber direction (specimen width) was too small to accurately measure. Significantly larger specimens are needed for accurate moisture expansion measurements in the fiber direction. However, the specimen lengths were long enough to obtain a measure of specimen expansion transverse to the fibers. In addition, this transverse direction extended from machined surface to machined surface so there were no molded surfaces to skew the measurements. The results of the transverse moisture induced strain, ϵ_M^t , measurements along the 25.4 mm length of the specimens are shown in Figure 8.7.

The average transverse moisture expansion coefficient calculated from the strains induced by moisture uptake at 25% RH, 50% RH, and 75% RH is $1.1 \times 10^{-3} \pm 0.7 \times 10^{-3}$. The transverse moisture expansion coefficient for G40-800 / 2.5kPETU is comparable to or

less than the transverse moisture expansion coefficients of other fiber-reinforced polymers listed in Table 3.5.

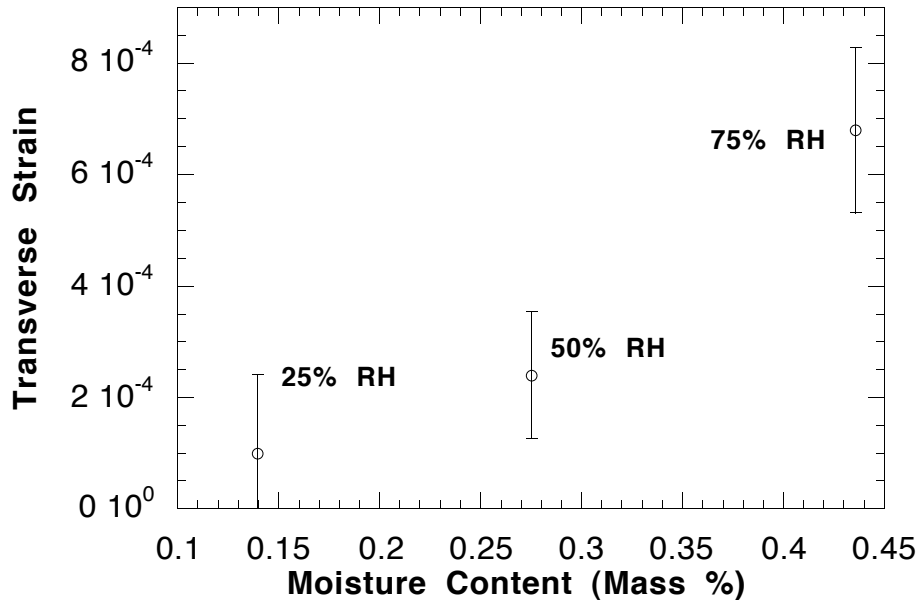


Figure 8.7. Moisture Induced Transverse Strain

8.5 Results - Mechanical Property Tests

The mechanical properties of TFS, OHCS, and AISS were tested following completion of moisture absorption and desorption. Results from AISS and OHCS testing gave no conclusive results. No conclusive results may be obtained from the AISS results due to the fact that the Control, Wet, and Wet/Dry specimens all failed in bearing mode.

Limited results were obtained from the OHCS specimens due to a tendency for specimens to fail at the edge of the grips rather than around the circumference of the center hole, which creates a stress concentration. All three Control OHCS specimens failed in the proper mode of compression shear in which the fracture ran from the edge of the hole to the outer edge of the specimen in a direction perpendicular to the fiber orientation. The OHCS of the Control specimens was: 506 ± 23 MPa. Two Wet OHCS specimens, having an average OHCS of 483 ± 48 MPa, failed in the proper mode described above. Only one Wet/Dry OHCS specimen failed in the proper mode; the OHCS for this one specimen was 528 MPa. Based on the measured strengths and limited quantity of specimens that failed in the proper

failure mode, no statistical conclusion regarding the effects of moisture sorption on OHCS is possible.

The lack of reliable results from OHCS and AISS tests limits conclusions regarding moisture sorption effects on mechanical properties to the TFS results. The TFS specimens exhibited 61 ± 1 percent retention (following absorption) and 84 ± 7 percent retention (following desorption) of the control value of 136 ± 10 MPa (Figure 8.8). These results suggest permanent damage of the composite may result from the one moisture sorption cycle at 90°C . Permanent damage is likely since the TFS did not recover to the control value after drying to the 10% RH M_m (Table 8.2), which was less than the as-manufactured (Control) M_m of $0.132 \pm 0.003\%$. It was seen in Chapter 3 that the 3kPETU/G40-800 composite recovered to its control TFS upon drying to the 2% RH M_m , which was equivalent to the vacuum-dried M_m (Figure 3.5). In addition, comparison of the WET TFS results for 2.5kPETU (Figure 8.8) and 3kPETU (Table 3.6) demonstrate a distinct difference in the abilities of the materials to endure moisture sorption. The Wet TFS of the 3kPETU composites does not statistically differ from the controls, whereas, the Wet TFS of the 2.5kPETU is only about 60 percent of the Control TFS. The full recovery of mechanical properties in Chapter 3 suggested no permanent damage was incurred during one moisture sorption cycle. This suggestion was verified by inspection of exposed composite surfaces showing no visible damage (Figure 3.4). Therefore, 2.5kPETU/G40-800 TFS specimens were inspected via optical microscopy for signs of permanent damage. These micrographs are shown in Figures 8.9 (Control), 8.10 (Wet), and 8.11 (Wet/Dry). As is evident by these micrographs, surfaces of all three types of specimens displayed damaged and undamaged regions. What is not represented by these micrographs is that the Control specimens displayed very little surface damage, whereas, the majority of the inspected surfaces of the Wet and Wet/Dry surfaces were damaged. Damage was generally apparent as a loss of matrix at the specimen surface leaving cavities and cracks in the surface and exposing bare fiber versus the smooth, resin-rich surfaces seen in undamaged regions. As shown by the arrows in Figure 8.10.(c), damage was also present as cracks that ran along, and jumped between, fiber/matrix interfaces. These cracks likely would lead to the eventual loss of matrix resulting in additional surface cavities and exposure of bare fiber.

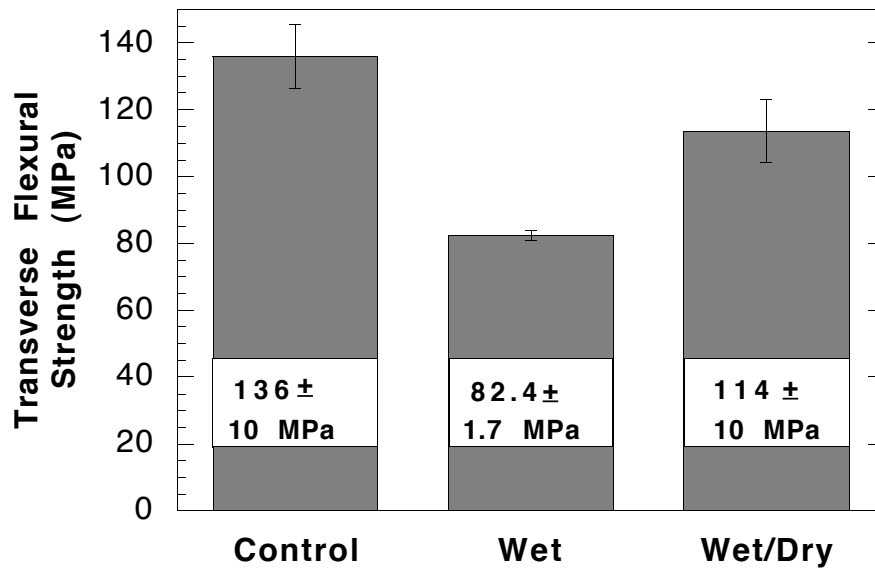


Figure 8.8. Effect of Moisture Exposure on Transverse Flexural Strength

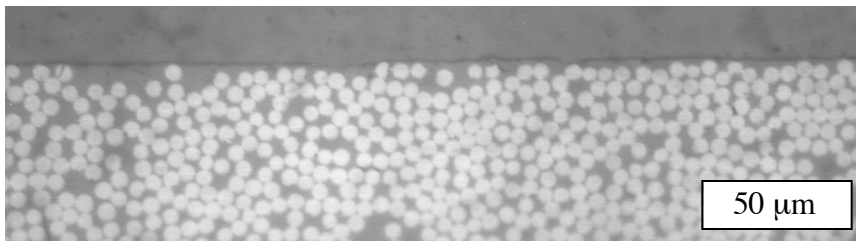


Figure 8.9.(a) Control TFS - Undamaged Exposed Surface

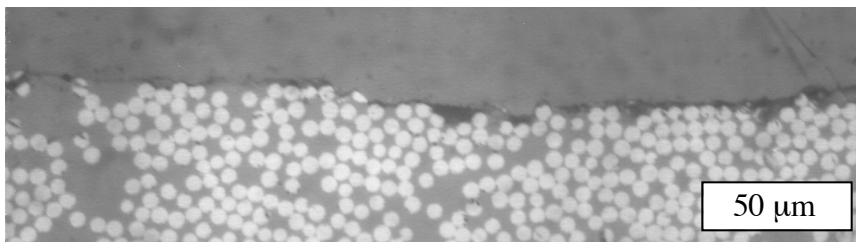


Figure 8.9.(b) Control TFS - Damaged Exposed Surface

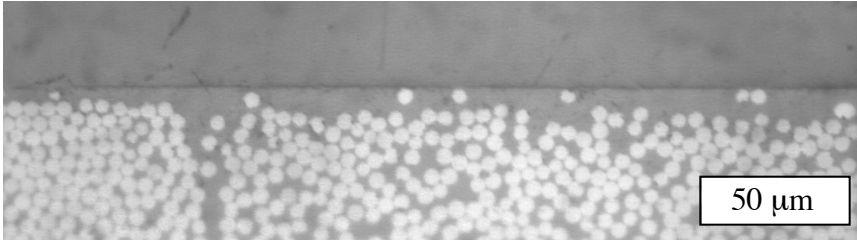


Figure 8.10.(a) Wet TFS - Undamaged Exposed Surface

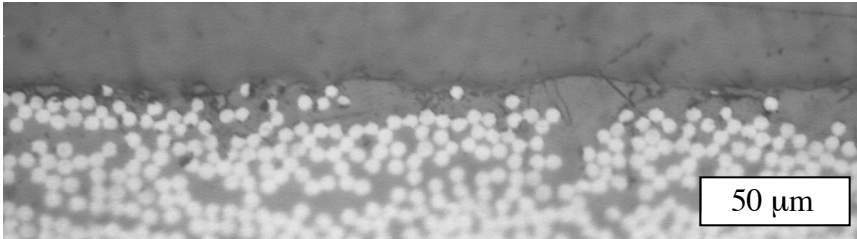


Figure 8.10.(b) Wet TFS - Damaged Exposed Surface: Crevices, Cracks, and Exposed Fibers

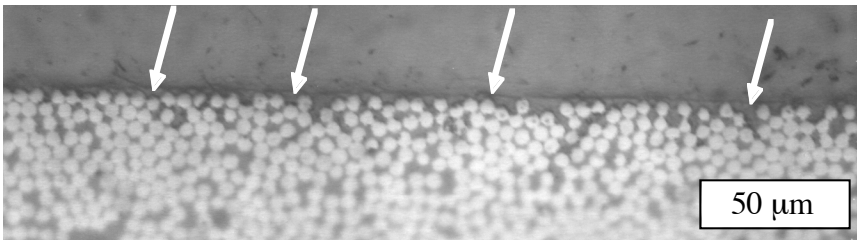


Figure 8.10.(c) Wet TFS - Fiber/Matrix Interface Cracks

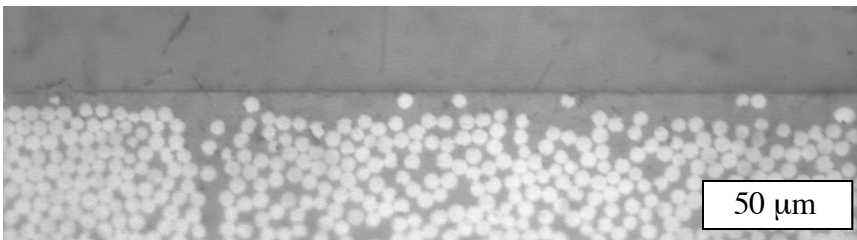


Figure 8.11.(a) Wet/Dry TFS - Undamaged Exposed Surface

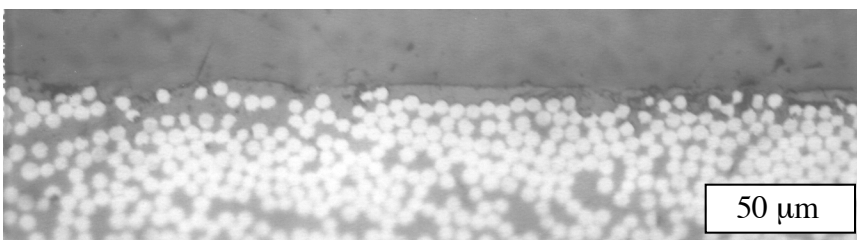


Figure 8.11.(b) Wet/Dry TFS - Damaged Exposed Surface: Crevices, Cracks, and Exposed Fibers

The difference in the processing schedules used to manufacture the 2.5kPETU and 3kPETU composites likely accounts for their different responses to enduring one moisture sorption cycle. The 3kPETU composites were consolidated under 1.4 kPa with a 90 minute, 350 °C hold. In contrast, the 2.5kPETU composites were consolidated under 0.7 kPa with a 50 minute 350 °C hold. Chapter 5 demonstrates that the difference between a 50 minute hold and a 90 minute hold at 350 °C results in a significant difference in the glass transition temperature, and thus the degree of cure, of 2.5kPETU composites (Figures 5.19 and 5.21).

There is also a difference in PETU molecular weight to be considered. However, the ability to withstand one moisture sorption cycle without damage versus incurring damage is not likely due to the initial oligomers having number average molecular weights of 2,500 g/mol versus 3,000 g/mol; the polydispersity indices are not known. First, the reaction kinetics are unlikely to differ significantly based on DSC studies of both materials by both the author and Tan [4]. Tan reported activation energies for 3kPETU and for a system containing 50 weight percent 3kPETU and 50 weight percent 2kPETU. The pure 3kPETU had an activation energy of 139 kJ/mol versus an activation energy of 143 kJ/mol for the combined system. Furthermore, the lower molecular weight of the 2.5kPETU oligomer versus the 3kPETU oligomer should result in a higher crosslink density for 2.5kPETU if the two PETUs were at the same degree of cure. This higher crosslink density should make the lower molecular weight PETU more resistant to invasion and subsequent damage by moisture. Considering that during 85% RH exposure 2.5kPETU neat resin reached a M_m of $1.60 \pm 0.01\%$ (Table 8.2) and 3kPETU neat resin reached a M_m of $1.44 \pm 0.02\%$ (section 3.3.3), the 3kPETU appears more resistant to moisture uptake. Thus, the damage incurred by the 2.5kPETU/G40-800 composites during one moisture sorption cycle is most likely due to the matrix being at a lower degree of cure than that of the 3kPETU/G40-800 composites.

8.6 Conclusion

In summary, moisture sorption in the 2.5kPETU/G40-800 composites followed Fickian behavior, and the composite displayed moisture sorption properties similar to other fiber-reinforced polymer matrix composites. However, the one moisture sorption cycle caused permanent damage to the composites, which is evident in the significant reduction of the Wet TFS versus the Control TFS, the inability of the TFS to recover to the Control value upon drying, and the crevices and cracks seen in the exposed surfaces of the composite specimens.

8.7 References

1. A.C. Loos and G.S. Springer, "Moisture Absorption of Graphite-Epoxy Composition Immersed in Liquids and Humid Air," in Environmental Effects on Composite Materials, G.S. Springer, ed., Technomic Publishing, Inc., Westport, CT, 1981, pp. 34-50.
2. P.M. Jacobs, M. Simpson, and F.R. Jones, "Generation of Thermal Strains in Carbon Fibre-Reinforced Bismaleimide (PMR-15) Composites," *Composites*, **22**, (2), 99-104 (1991).
3. M.R. VanLandingham, R.F. Eduljee, and J.W. Gillespie, Jr., "The Effects of Moisture on the Material Properties and Behavior of Thermoplastic Polyimide Composites," in High Temperature and Environmental Effects on Polymeric Composites, Vol. 2, ASTM STP 1302, T.S. Gates and A.H. Zureick, eds., American Society for Testing and Materials, Philadelphia, 1997, pp. 50-63.
4. B. Tan, "Synthesis and Characterization of Phenylethynyl Endcapped Polyetherimide Oligomers," Doctoral Dissertation, Virginia Polytechnic Institute and State University, Blacksburg, VA, 1997.

9.0 Thermal-Oxidative Aging Effects on Composite Properties

9.1 Thermal-Oxidative Aging Background

Design requirements for High Speed Civil Transport (HSCT) components that may be constructed from fiber-reinforced polymeric composites (FRPCs) specify a minimum lifetime of 60,000 service hours. This service includes 20,000 three hour flights in which the aircraft will endure temperatures ranging from -40 °C to +177 °C while experiencing air pressures ranging from 101 kPa (1 atm) at sea level to a reduced pressure of 13.8 kPa (0.136 atm) at cruise altitude [1,2]. The moisture content of the atmosphere will also fluctuate, but its effects are outside the scope of this chapter and were considered in Chapter 8.

The stability of polymer matrixes as they are exposed to elevated temperatures and oxidizing conditions in the HSCT's environment is an area of major concern. Research into epoxy, thermoplastic-toughened cyanate ester, semicrystalline thermoplastic, and reactive imide matrix materials indicates that oxidation, not thermal effects, is the more critical degradation mechanism in the polymer matrixes at elevated temperatures: 121 °C, 150 °C, 177 °C, 232 °C, 288 °C, and 316 °C [3-11].

Kerr and Haskins [3] concluded that matrix degradation by oxidation was the primary cause of mechanical property losses during thermal aging of epoxy / graphite fiber composites. Tensile specimens were aged at 121 °C and 177 °C in a 101 kPa environment and at 177 °C in a 13.8 kPa environment for up to 50,000 hours. Following 25,000 hours at 121 °C and 101 kPa, tensile testing caused the epoxy matrix at the surface to break and crumble off the specimen. Specimens aged to 50,000 hours lost not only the epoxy at the surface, but also much of the matrix throughout the thickness. Increasing the aging temperature to 177 °C resulted in embrittlement of the epoxy matrix in less than 5,000 hours. Tensile testing of the 5,000 and 10,000 hour specimens resulted in large portions of matrix crumbling away, leaving bare, yarn-like bundles of fiber tow. By reducing the atmospheric pressure to 13.8 kPa, the first sign of embrittlement during 177 °C aging did not occur until 25,000 hours. In addition, tensile testing of 50,000 hour specimens resulted in resin loss comparable to only 5,000 hours exposure to 177 °C pressure at 101 kPa.

Tsotsis [4] observed results similar to Kerr and Haskins [3]. Tsotsis noted edge cracking and severe property degradation after exposing epoxy / carbon fiber composites for 5,000

hours at 177 °C and 101 kPa. By reducing the pressure to 13.8 kPa, these signs of degradation were not observed until the specimens were exposed for over 25,000 hours. Tsotsis [4] also investigated degradation of epoxy resins via thermogravimetric analysis (TGA). He found that activation energies in air were approximately one-half those in nitrogen. Tsotsis [4] suggests, with reference to other investigators, that a correlation between increasing polymer degradation and increasing air (or oxygen) pressure exists. Evidence of this correlation is given by Tsotsis in results of isothermal TGA experiments done on two neat epoxy (R922-1 and R6376; Ciba Composites, Anaheim, CA) resin powders in nitrogen, air, and oxygen environments. The results are given in Table 9.1 and demonstrate the importance of oxygen concentration to the degradation of epoxies. An increase in the percent weight loss per hour is seen with increasing oxygen content. Ciutacu, et al. [10], attempted to accelerate degradation of glass-reinforced epoxy by using oxygen atmospheres at pressures of 304 kPa and 507 kPa. Changes in flexural strength demonstrated the significance of oxygen pressure as an accelerating factor in thermal-oxidative degradation.

Table 9.1. Isothermal TGA Results of Epoxy Powders in Various Gases at 100 ml/min

Epoxy	Temperature (°C)	Percent Weight Loss Per Hour		
		N ₂	Air	O ₂
R922-1	177	0.020	0.149	0.262
	204	0.111	0.412	0.566
R6367	177	0.010	0.023	0.135
	204	0.038	0.247	0.380

From Reference 4: Tsotsis

Crossland, et al. [11], used TGA to measure the weight loss of three different polyimides in atmospheres of air and nitrogen. The three polyimides investigated were Thermid 600 (Gulf Oil Chemicals), NR150 (DuPont), and Polyimide 2080 (Upjohn). The activation energy of the Thermid 600 to reach a weight loss of 5% - 10% was 140 kJ/mol in air and 176 kJ/mol in nitrogen. The activation energy of the Polyimide 2080 to reach 5% - 10% weight loss was 114 kJ/mol in air and 218 kJ/mol in nitrogen. Finally, the activation energy of the NR150 to reach a weight loss of 10% - 15% was 181 kJ/mol in air and 233 kJ/mol in nitrogen. The TGA results reported by Tsotsis [4] and Crossland, et al. [11], indicate that significantly less energy is required for oxidation than thermal degradation.

Parvatareddy, et al.[5], investigated carbon fiber composites with either a thermoplastic-toughened cyanate ester matrix (Fiberite 954-2) or a semi-crystalline thermoplastic matrix (Fiberite ITX). Specimens from these materials were aged at 150 °C in three different environments: ambient air, 13.8 kPa air, and nitrogen. After six months of aging, the three-point bending strength of the 954-2 composite decreased by 42% in ambient air, 31% in 13.8 kPa air, and 14% in nitrogen. Furthermore, the rate of strength reduction was fairly continuous for the air and reduced pressure atmospheres, whereas, the strength reduction rate in the nitrogen environment leveled off after two months .

The ITX specimens showed similar results. After six months at 150 °C in air, specimens lost 29% of the unaged strength. The reduced pressure specimens lost 21% and the nitrogen specimens lost only 4%. The strength reduction rate in the air and 13.8 kPa environments increased beyond two months. However, the reduction in the strength of the nitrogen specimens occurred during the first two months of aging; essentially no decrease was seen after two months.

Kerr and Haskins [3] also investigated pressure and elevated temperature aging effects on polyimide / graphite fiber composites. Polyimide / graphite fiber composites have significant potential for applications where the service temperature exceeds epoxy / graphite fiber capability. Tensile specimens were aged at 288 °C in 101 kPa and 13.8 kPa air environments. Specimens aged for 25,000 hours in 101 kPa air had significant weight loss and a large decrease in tensile strength to about 20% of the unaged specimen tensile strength. Specimens aged in reduced pressure had small weight losses and tensile strengths about 85% of the unaged specimen tensile strength. During tensile testing, the 101 kPa specimens' matrix broke and crumbled off showing the yarn-like graphite tows. The reduced pressure specimens were discolored, but displayed limited resin loss and bare fiber after testing.

After 50,000 hours of testing in the 101 kPa environments, too little matrix remained in the specimens to allow for testing. The specimens aged in the reduced pressure environment had minimal weight loss and little exposed surface fibers. The tensile strengths were almost 60% that of unaged specimens with the tested specimens showing the beginnings of matrix embrittlement, with the exposure of many graphite fibers by the loss of matrix material.

Bowles, et al. [6-8], have investigated the oxidation and thermal aging effects on PMR-15 (an addition cured polyimide) [12]. To determine the relative importance of oxidation and thermal effects, neat PMR-15 resin samples were aged in air at 316 °C [6]. Inspection of a specimen aged for 362 hours displayed a surface degradation layer with a thickness of 0.1 - 0.2 mm. Beyond this surface layer, no effects of aging were visually noticeable.

A similar surface layer was analyzed by x-ray diffraction (XD) and x-ray photoelectron spectroscopy (XPS) [6]. This sample was also analyzed by XD and XPS after the degraded surface layer was removed with 40 grit emery paper. The XD results were compared with a XD analysis of an unaged specimen. The XD scan of the unaged specimen showed a small peak at a scattering angle of about 16°, indicating that there is some crystallinity or order present in the unaged material. This peak was barely evident in the XD scan of the aged surface. After removal of the aged surface layer, the original peak was seen in a subsequent scan. The existence of the peak below the degraded layer indicates that the core material may not have been affected by the degradation process.

Analysis of specimen surfaces by XPS further contributed to understanding the degradation mechanism [6]. The oxygen to carbon ratio of the surface of an aged specimen was 0.283. When this specimen was analyzed after sanding to remove the aged surface layer, the oxygen to carbon ratio dropped to 0.205. This value is closer to that obtained from the analysis of an unaged specimen that was sanded to remove any surface layer: 0.172. These results indicate that oxygen is important to the degradation of the material surface. The aging process appears to oxidize the polymer near the surface creating a layer structurally different than the initial cured polymer material. However, the interior of the material appears to be unaffected by the thermal exposure. Bowles, et al. [6], concluded that the XD and XPS results indicate that the interiors of PMR-15 neat resin specimens are not observably affected by aging at elevated temperatures. These results suggest that the majority, or all, of the observed dimensional and gravimetric changes take place near the surface of the specimens. Such a conclusion is in agreement with the observed dependence of neat PMR-15 resin weight loss on specimen surface area [6].

The above references display the sensitivity of polymer matrix degradation to changes in surrounding oxygen concentration. Therefore, it is important to consider that at cruise altitude, the HSCT will experience a reduced pressure of about 13.8 kPa. This reduced pressure decreases the oxygen content at the surface of aircraft components, relative to conditions near sea level, thus delaying the oxidation process compared to that at

atmospheric pressure (101 kPa) and the same temperature. The elevated temperatures of the HSCT service environment may assist in the polymer degradation process by providing energy for oxygen diffusion and activation of the oxidation reaction; however, actual chain scission due to thermal energy alone may be non-existent or negligible depending on the specific polymer matrix.

9.2 Anisotropic Degradation and Specimen Surface Area Effects

The significance of specimen surface area was investigated by Bowles and Meyers [8] via comparisons of the flexural strength of graphite fiber-reinforced PMR-15 composite specimens cut from larger panels before and after aging. The orientation of the tests was not specified, but the measured strengths indicate they were longitudinal. The precut specimens were exposed to air on all six surfaces. The specimens cut from panels following aging were exposed only on their two molded surfaces. Assuming degradation first takes place at the surface and migrates toward the interior of the specimen, any loss in mechanical properties of the postcut specimens should be due to degradation of the two molded surfaces. The cross-sections of the specimens were inspected following testing to determine the undegraded, or effective, cross-sectional area within the bulk of the specimens. If the effective cross-sectional area is used to calculate the flexural strengths of both the precut and postcut specimens, the precut specimens would be expected to have a flexural strength of 85% that of the postcut specimen. In actuality, the precut flexural strength was 82% that of the postcut flexural strength. This 3% difference between predicted and actual flexural strength gives additional evidence that the degradation of PMR-15 / graphite fiber composites occurs at exposed specimen surfaces with little or no degradation of the specimen interior.

Nelson [9] investigated the effects of thermal aging on three different polyimide / graphite fiber composite materials including PMR-15. Nelson presumes thermal oxidation to be the dominant degradation mechanism in his study and recognizes that this type of degradation is sensitive to specimen surface area and geometry. Nelson chose to compare the strength retention of apparent interlaminar shear strength(AISS) specimens cut from panels prior to aging and specimens cut from different regions of panels following aging of the panels. The AISS specimens were cut with dimensions of 16 x 6.3 x 3 mm. The panels were cut from larger unidirectional panels and had dimensions of 153 x 153 x 3 mm. The specimens cut following panel aging were taken from the interior of the panel and from three of the edges (Figure 9.1). From one edge, specimens were cut such that their lengths were parallel to the fiber direction and perpendicular to the panel edge. From the other two

edges, specimens were cut such that their lengths were parallel to both the fiber direction and the panel edge. Therefore, four different types of AISS specimens were available for testing: 1) those that were exposed to the aging environment on all surfaces (precut specimens); 2) those that had both top and bottom (16 x 6.3 mm) surfaces exposed along with one end (6.3 x 3 mm) (end specimens); 3) those that had both top and bottom surface exposed along with one edge (16 x 3 mm) (edge specimens); and 4) those that had only the top and bottom surfaces exposed (interior specimens) [9].

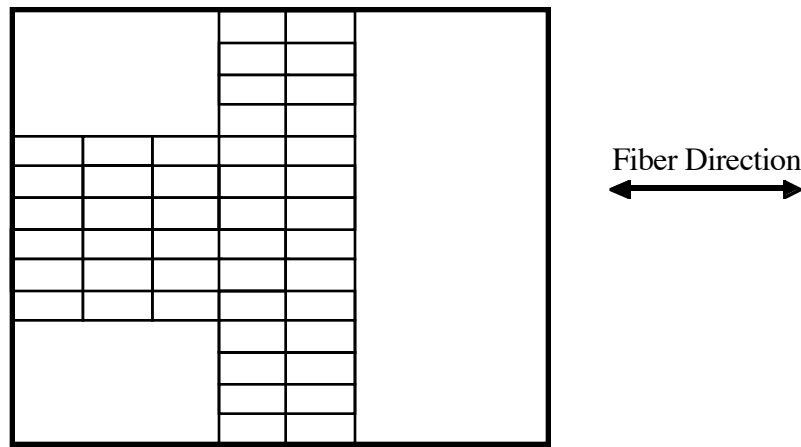


Figure 9.1. Description of Nelson's [9] AISS Specimen Selection

The top and bottom surfaces were molded surfaces and parallel to the fiber direction. The end surfaces were cut perpendicular to the fiber direction. The edge surfaces were cut parallel to the fiber direction. The strength retention comparisons followed 15,000 hours at 232 °C and are representative of other results given by Nelson [9]. The precut specimens retained 63% of the original AISS. The interior specimens increased in AISS by about 5%. Some of the edge specimens decreased a few percent in strength while others increased a few percent. The end specimens only retained 63% of the original AISS. Nelson implies that all specimens failed in the desired shear mode [9].

These results indicate that the surface area of aging specimens and possibly fiber orientation play a role in thermal-oxidative degradation. Surface area is shown to be important since individually aged AISS specimens experienced significant reductions in AISS, whereas, those specimens taken from the interior of a panel experience an increase in strength most likely due to postcure [9]. The fact that surface area is important reinforces the assumption that oxidation, a diffusion controlled process, is the dominant degradation process [9].

However, the role of surface area must be qualified by the importance of fiber orientation. The area of the panel surrounding interior specimens does not restrict degradation of the interior via diffusion of oxygen through the thickness of the panel. However, the surrounding material does restrict oxygen diffusion in the plane of the panel to the interior of the panel. This observation would lead one to think that oxidative degradation occurs by diffusion in the plane of the panel. Edge specimens from the panel saw little or no strength reduction despite having a greater exposed surface area than end specimens that saw a 37% reduction in strength. Furthermore, AISS tests measure strength at the specimen midplane. The interior specimens protect the midplane, but the edge specimens expose more of the midplane than the end specimens. These results may indicate the preference for oxidation progression along the fiber direction.

These AISS results can not give a definite answer to oxidation being preferred in the fiber direction because AISS specimens are designed to initiate failure at the specimen ends [13]. Therefore, a certain degree of degradation to the edge of a specimen may not weaken the specimen as much as the same degree of degradation at the end of the specimen. Reduced strength in end specimens may be more a result of specimen design rather than a result of anisotropic degradation.

Bowles [7] also saw no decrease in AISS with aging for specimens whose ends were not exposed during aging. However, Bowles and Meyers [8] concluded that “the AISS of an aged, precut specimen can not be measured with an [sic] degree of confidence.” This conclusion was due to two observations during their tests. All indications pointed to bearing failure at the center load point, not shear failure. Also, they noted that precut, aged specimens have a large number of cracks at the ends and that if shear failure were to occur, it could begin at one of the crack tips. Thus, the test would become a crack sensitivity test rather than a shear strength test.

Heretofore, studies that used mechanical properties to investigate specimen anisotropy effects were inconclusive. Techniques utilizing weight loss measurements on different specimen geometries have been more definite. Bowles and Meyers [8], Nelson [9], and Nam and Seferis [14] determined the effects of different specimen geometries and surface areas on degradation rates and weight loss in composite materials. Bowles and Meyers [8] studied the weight loss rate of PMR-15 / graphite fiber composites using specimens of three different geometries: 25 mm x 76 mm coupons, 5.1 mm x 76 mm longitudinal flexure specimens, and 5.1 mm x 15.2 mm AISS specimens. All specimens had a

thickness of about 2.5 mm. The specimens were aged in air convection ovens for 1600 hours at 316 °C. Optical microscopy revealed that greater degradation appeared to have occurred along the surface cut perpendicular to the fibers than either the molded surfaces or the surfaces cut parallel to the fibers. Weight loss measurements indicated the weight loss rate per unit area of surface cut perpendicular to the fibers was 35 times greater than that of the surface cut parallel to the fibers. In addition, the molded surface had a weight loss rate per unit area four times greater than that of the surface cut parallel to the fibers. The difference between these two surfaces is thought to be due to the resin rich surface on the molded surface. Once the degradation moves beyond the resin rich surface, it is expected that the degradation rate is the same as that for the surface cut parallel to the fibers. The results of the weight loss measurements for the different specimen surfaces indicate oxidative degradation is dependent on the anisotropy of a polymeric composite.

Nelson [9] measured weight loss of PMR-15 / graphite fiber specimens with three different geometries: 153 mm square panels with 3 mm thickness, 16 mm x 6.3 mm AISS specimens with 3 mm thickness, and 64 mm x 13 mm flexure specimens with 1.5 mm thickness. The specimens were precut and aged in flowing air at 232 °C. The AISS specimens had the greatest weight percentage loss, and the square panels the least. The flexure specimens had the greatest surface area-to-volume ratio, but not the greatest weight percentage loss. However, when only the surface areas perpendicular to the fiber direction were considered, the AISS specimens had the highest surface area-to-volume ratio and the square panels the lowest. Thus, a preference for oxidation at the fiber ends of the specimens was suggested.

Nam and Seferis [14] used isothermal aging experiments on a bismaleimide / carbon fiber composite at 290 °C to investigate anisotropic thermal-oxidative degradation. Six different sample geometries were aged. These samples were cut to expose different proportions of different types of surface areas: molded surfaces parallel to the fibers, cut surfaces parallel to the fibers, cut surfaces perpendicular to the fibers, and surfaces cut at acute angles to the fibers. The four samples having only surfaces cut parallel or perpendicular to the fibers were analyzed first to determine the average weight loss per unit surface area (W/A) for each type of surface. Nam and Seferis [14] found that after 50 hours of aging, the resin rich molded surfaces had the highest W/A. By the time 75 hours of aging had passed, the W/A rate for the molded surface had leveled off some, and the W/A rate for the surface cut perpendicular to the fibers had increased above that of the molded surface. After 100 hours of aging, all three surfaces appeared to reach constant rates of W/A, and the surface cut

perpendicular to the fibers was dominant in W/A. After 262 hours of aging, the surface cut perpendicular reached $\sim 0.045 \text{ g/cm}^2$, and the molded surface had a W/A of $\sim 0.015 \text{ g/cm}^2$. The surface cut parallel to the fibers had the lowest W/A; the W/A was between 0.005 g/cm^2 and 0.01 g/cm^2 after 262 hours.

Inspection of the exposed surfaces by optical microscopy revealed that the thermal-oxidative degradation starts at the surface and moves into the composite [14]. In addition, it was shown that the rate at which the degraded zone moves into the composite is strongly dependent on fiber orientation to the surface. Surfaces in which the fibers were oriented parallel, 15° , 40° , 75° , and perpendicular to the surface plane were inspected [14]. The depth of degradation after 164 hours of aging at 290°C steadily increased from very little for fibers oriented parallel to the surface to approximately a millimeter for fibers oriented perpendicular to the surface.

The work discussed above illustrates that the three different types of specimen surfaces in a unidirectional composite do exhibit different values of weight loss per unit area. A key point that should be taken from this work is that because surface area and fiber orientation play important roles in thermal-oxidative degradation rates, the aging specimens should be of a size more representative of actual components (e.g., a 153 mm square panel is more representative of a large structural panel than is a 16 mm x 6.3 mm AISS specimen).

9.3 Specimen Aging and Testing

The oxidation portion of this study attempts to accomplish several goals. Oxidative aging of CFR 2.5kPETU was studied with the primary objective being the assessment of the influence of oxygen concentration on mechanical property degradation. CFR 2.5kPETU composite panels were aged at 204°C in environments of four different oxygen partial pressures, $p(\text{O}_2)$: $p(\text{O}_2) = 0 \text{ kPa}$ (100 mol% N_2 gas), $p(\text{O}_2) = 2.84 \text{ kPa}$ (air at -87.5 kPa partial vacuum), $p(\text{O}_2) = 20.2 \text{ kPa}$ (20 mol% O_2 / 80 mol% N_2 gas mixture), and $p(\text{O}_2) = 40.4 \text{ kPa}$ (40 mol% O_2 / 60 mol% N_2 gas mixture). Aging times were 1750, 3500, and 5000 hours. Some lower temperature and shorter time aging was also done and is detailed in the experimental section. The 2.84 kPa $p(\text{O}_2)$ was selected as representative of cruise conditions for the HSCT [1]. The 0 kPa $p(\text{O}_2)$ environment was selected to provide an oxygen-free environment since during aging below T_g , oxidation, not thermal effects, is generally the most critical degradation mechanism for polymer matrices. The 0 kPa $p(\text{O}_2)$ environment was intended to provide a measure of only thermal degradation (e.g., physical aging) and act as a control for the oxygen-containing environments. The 20.2 kPa and

40.4 kPa $p(\text{O}_2)$ environments were selected to provide accelerated thermal-oxidative aging (TOA) relative to cruise conditions, since increased oxygen partial pressures would result in increased concentrations of diffused oxygen within the matrix material. In addition, the 20.2 kPa $p(\text{O}_2)$ simulates sea level oxygen partial pressure. Following the various aging times, the composite panels were removed from the aging environments and test specimens were cut (see Figure 7.1) to measure property retention. Mechanical properties tested include: transverse flexural strength (TFS), AISS, and open-hole compression strength (OHCS).

The TFS of a composite material is a measure of matrix strength and is very sensitive to the interfacial bonding between the fiber and matrix. The TFS should reveal any slight matrix weakening by oxidation. The design of the TFS test places the highest strain on the outer surfaces of the specimens. The outer surface is precisely the region that is expected to oxidize first. Therefore, decreases in TFS may be seen to taper off at a certain level.

Apparent interlaminar shear strength test results are not to be used for design purposes, but the test requires small specimens and provides a simple technique for monitoring interlaminar strength. One of the major deficiencies of high-performance laminated composite structures is their susceptibility to delamination [15]. The term delamination is often chosen to describe the propagation of an interlaminar crack, which can undermine the flexural stiffness of a composite laminate. Furthermore, delamination is the dominant failure mode of composite structures and is therefore an essential consideration in the study of composite durability and damage tolerance. The interlaminar plane usually has the lowest resistance to crack propagation since the fiber reinforcement of individual plies provides high strength and stiffness within the plane of the ply. Without a second or third dimension of interply reinforcement, a composite's resistance to delamination is significantly dependent on the strength of the matrix material in the interlaminar plane [13,16]. The effect of aging conditions on the interlaminar matrix material may be monitored by measuring changes in the AISS.

Another matrix dominated property is compression strength. The OHCS test measures compressive properties while including a stress concentration site. The hole in the specimen is representative of the real-life presence of fasteners through composite panels. Compressive loading attempts to buckle fibers; the surrounding matrix is called upon to support the fibers and keep them aligned against the load. Weakening of the matrix by aging conditions would reduce the composite's ability to resist movement of fibers under

compressive loading. The OHCS is more a measure of the bulk, or through-the-thickness, properties of a composite; it is not sensitive to degradation in a particular region. Therefore, a steady digression of OHCS is expected with a steady progression of degradation from the surface into the interior of the composite.

These three tests were chosen because their properties are all matrix dominated. However, failure initiation sites tend to differ. The TFS test is sensitive to flaws near the outer surfaces in the center span region of the specimen. The AISS is sensitive to weak points near the midplane at the specimen ends, while OHCS specimens generally fail near the stress concentrating hole. The OHCS is more a measure of overall bulk properties rather than near the surface or midplane.

Because oxidation is a diffusion controlled process, composite panels are more representative of HSCT surface components than the smaller test specimens. The depth of degradation in high-performance polyimide composite materials has previously been measured via optical microscopy due to discoloration of the matrix by degradation [7,14,17]. This same work showed oxidation rates to be anisotropic. Specimens of 2.5kPETU neat resin and composites did not display the expected discoloration, therefore, measurements of degradation depth and anisotropic oxidation were limited or not available. Thus the desired calculations of oxygen diffusivity constants in 2.5kPETU composites were not possible.

In the development of materials for long service lives, relatively quick tests that accelerate the relevant degradation mechanisms need to be performed to allow for correct lifetime predictions. Because the dominant degradation mechanism is expected to be oxidation, a diffusion controlled process, aging in an oxygen rich environment is expected to accelerate the degradation of mechanical properties. Measurement of mechanical property retention following aging in the environments of different oxygen concentration is expected to allow for predictions of property retention as a function of exposure time and oxygen concentration.

9.4 Experimental

9.4.1 Specimen Aging

9.4.1.1 Specimen Distribution

Aging was performed in two separate ovens; a Blue M Inert Gas Furnace convection oven (model IGF-6680G-MP) and a Precision Scientific (Model 524) vacuum oven. The vacuum oven was used for the 2.84 kPa $p(\text{O}_2)$ aging and the three other aging conditions were done in separate aluminum chambers (18.4 cm x 18.4 cm x 9.53 cm) placed within the convection oven. These aluminum chambers each had a volume of 3.23 L. The flow rates for the 100 mol% N_2 gas, 20 mol% O_2 / 80 mol% N_2 gas mixture, and 40 mol% O_2 / 60 mol% N_2 gas mixture varied between 25 to 50 ml/min over the aging period. The 2.84 kPa $p(\text{O}_2)$ was maintained by balancing vacuum and purge at a gauge pressure of 13.8 kPa. A desiccant tube attached at the purge entrance ensured a dry aging environment. Four aluminum screen shelves were placed in the vacuum oven and each aging chamber. This aluminum screen was fabricated from aluminum wire having a diameter of approximately 2 mm. The open holes in the screen were 6.35 mm x 6.35 mm. The screen was folded in a corrugated fashion such that the shelves had limited contact with the composite panels resting on them. Composite panels from Chapter 7 were placed on the top three shelves - one panel per shelf. A composite specimen for dynamic mechanical thermal analysis (DMTA) and a neat resin specimen were placed on the bottom shelf of each chamber and the vacuum oven. Each composite DMTA specimen was cut from the ~1.9 mm thick panels manufactured in Chapter 7. These composite specimens were cut with a width of 25.4 mm and length (in the fiber direction) of 76.2 mm. The neat resin specimens were cut from the plaques manufactured in Chapter 7. Due to a limited quantity of material, only enough DMTA and neat resin specimens were available for the longest aging times (5000 hours).

9.4.1.2 Details of Actual Aging History

Initially, TOA was to be done at 177 °C. Aging had commenced in the 2.84 kPa $p(\text{O}_2)$ environment while waiting on the expected delivery of the specialty gas mixtures necessary to commence aging in the convection oven. During the delay of the delivery of the gas mixtures, results were found in the literature that suggested a higher aging temperature may be needed to see degradation in the short aging times used in this study. Based on this literature, it was decided to increase the aging temperature to 204 °C. These literature results are discussed in the next section. The materials aging at 177 °C and 2.84 kPa $p(\text{O}_2)$ were allowed to continue until they reached a total aging time of 30 days (720 hours). At

this time, all materials were removed from both the vacuum oven and the 0.0 kPa p(O₂) aging chamber. One composite panel was taken for mechanical testing to evaluate the effects of [720 hr / 2.84 kPa p(O₂) / 177 °C] on mechanical properties. Since it was thought that 2.84 kPa p(O₂) aging would be more degradative than 0.0 kPa p(O₂) aging, the remaining two panels were placed in the 0.0 kPa p(O₂) chamber for 3500 and 5000 hours of aging at 204 °C. One remaining panel from those manufactured in Chapter 7 was placed in the 0.0 kPa p(O₂) chamber for 720 hour aging. The [720 hr / 2.84 kPa p(O₂) / 177 °C] neat resin specimen was cut in half. One half was saved for analysis, and the second half was placed in the 0.0 kPa p(O₂) chamber along with an unaged neat resin specimen. The [720 hr / 2.84 kPa p(O₂) / 177 °C] composite DMTA specimen was placed in the 0.0 kPa p(O₂) chamber. Those materials that had been awaiting the beginning of 0.0 kPa p(O₂) aging, but had been removed when the [720 hr / 2.84 kPa p(O₂) / 177 °C] materials were removed, were all placed in the vacuum oven. Thus completely unaged specimens were placed in the vacuum oven for 2.84 kPa p(O₂) / 204 °C aging. In summary, all of the materials that underwent 204 °C aging in any one of the three oxygen-containing environments were completely unaged prior to 204 °C. However, some of the materials that underwent 0.0 kPa p(O₂) / 204 °C aging had endured [720 hr / 2.84 kPa p(O₂) / 177 °C] aging prior to the 0.0 kPa p(O₂) / 204 °C aging. This “pre-aging” is summarized in Table 9.2.

Table 9.2. Pre-aging of 0.0 kPa p(O₂) / 204 °C Specimens

Final Specimen Aging Distinction	Pre-aging History
[5000 hr / 0.0 kPa p(O ₂) / 204 °C] Composite Panel	[720 hr / 2.84 kPa p(O ₂) / 177 °C]
[3500 hr / 0.0 kPa p(O ₂) / 204 °C] Composite Panel	[720 hr / 2.84 kPa p(O ₂) / 177 °C]
[720 hr / 0.0 kPa p(O ₂) / 204 °C] Composite Panel	None
[5000 hr / 0.0 kPa p(O ₂) / 204 °C] Composite DMTA Specimen	[720 hr / 2.84 kPa p(O ₂) / 177 °C]
[5000 hr / 0.0 kPa p(O ₂) / 204 °C] Neat Resin Specimen	[720 hr / 2.84 kPa p(O ₂) / 177 °C]
[5000 hr / 0.0 kPa p(O ₂) / 204 °C] Neat Resin Specimen	None

9.4.1.3 Discussion of 177 °C Aging versus 204 °C Aging

Consideration of raising the aging temperature to 204 °C was due to a concern that no significant degradation would occur under the planned aging environments at 177 °C.

Ideally, a material that does not degrade is desired, but realistically, one wants to find the conditions that do cause property degradation and study the specific relationship between the environment and the resulting degradation. Morgan's [18] statement: "Long-term 8000-hour isothermal tests of polyimide-carbon fiber composites at temperatures up to 200 °C do not produce any detectable mechanical, physical, or chemical performance related changes (R. Rothschilds, Boeing Commercial Aircraft, Seattle, WA, unpublished, 1993)" initially raised a concern that aging at 177 °C may not cause significant property degradation in 2.5kPETU. It is believed that the polyimide referenced by Morgan is either a BASF bismaleimide (thermoset) or more likely DuPont Avimid K (thermoplastic) [19]. Avimid K is similar in structure to Ultem™ and has a T_g of 280 °C [19]. Pederson, et al. [19], aged IM6 CFR Avimid K composites in air at 177 °C for up to 2232 hours with samples removed from aging at 744 hours, 1488 hours, and 2232 hours. The following bulleted statements point out the critical results reported by Pederson, et al., following aging of the Avimid K composites.

- Regarding composite weight loss: "Avimid K / IM6 yielded a loss of 0.05 weight percent after 2232 hours. These results show that the thermoplastic polyimide exhibits a higher resistance to oxidative degradation than the bismaleimide system."
- Regarding T_g : "Avimid K / IM6 shows a slight increase in T_g from 280 °C to 285 °C during aging at 177 °C."
- Regarding visual inspection for degradation: "The polyimide system showed little evidence of degradation during these aging times...The thermoplastic polyimide did not exhibit any noticeable surface degradation during aging."
- Regarding fracture toughness: "The thermoplastic polyimide shows significantly different results than the bismaleimide system. The results of the measurements show that although the BMI showed significant decreases in fracture toughness with aging, the thermoplastic polyimide shows little statistical evidence of decreasing trends with aging."

Another DuPont thermoplastic polyimide, K3B ($T_g = 242$ °C), was studied by Sacks and Johnson [20]. These authors reported results of aging studies on neat K3B resin at 177 °C in air for 5,000 and 10,000 hours and referenced results from an aging study on IM7 CFR

K3B [21]. The neat “K3B aged for 5,000 hours and K3B aged for 10,000 hours showed a decrease in fracture toughness compared to unaged material...[20]”. However, Arendt, et al. [21], reported: “Aging data for IM7 / K3B showed no weight change after 5,000 hours and very little after 30,000 hours....Aging at 177 °C does not result in significant chemical changes in IM7 / K3B.”

In making the final decision to raise the aging temperature to 204 °C, the 28/50 Rule was taken into account. This rule suggests aging at temperatures no greater than 28 °C (50 °F) below the T_g . The K3B and Avimid K were aged at approximately (2.3 x 28 °C) and (3.7 x 28 °C), respectively, below their glass transition temperatures and little or no degradation was incurred. PMR-15 ($T_g = 345$ °C) composites were aged at (1 x 28 °C) [6-8, 17] and (2 x 28 °C) [6-8, 17] below T_g and displayed significant degradation of properties, while aging at (3 x 28 °C) [17] below T_g caused minor degradation and aging at (4 x 28 °C) [9] below T_g resulted in no degradation of interior AISS specimens. A bismaleimide [14] aged at (1 x 28 °C) below T_g demonstrated significant degradation in less than 200 hours. Consideration of these results, along with those discussed in previous paragraphs, led to the decision to age 2.5kPETU at a temperature equal to, or greater than, 56 °C below its T_g (~258 °C - 260 °C); a temperature of 204 °C satisfied this criteria. This temperature was expected to be high enough to at least initiate degradation, but at the same time it was thought to be low enough to allow for long term aging without resulting in completely destructive degradation. Completely destructive degradation, where the material retains none of its original properties, eliminates the ability to correlate property changes with aging time and environment.

9.4.2 Monitoring Mass Change

Prior to placing the composite panels in the aging chambers, two weight loss specimens were cut from each panel. These specimens were created by cutting a strip from each panel in the scrap region on the left side of the panel (Figure 7.1) having a width of approximately 20 mm. Each strip was cut in half to produce two specimens having lengths of approximately 75 mm and masses between 8 to 9 g. These specimens were weighed prior to the beginning of aging and again when their parent panel was removed from aging for mechanical testing. Unfortunately, the 1750 hour weight loss specimens were not weighed before they were cut into smaller specimens for microscopy. Thus, similarly sized specimens were cut from unaged scrap remaining from the three panels that were cut into AISS, TFS, and OHCS specimens for moisture exposure in Chapter 8. These replacement specimens were aged in their respective TOA environments for 1000 hours.

The neat resin specimens in each environment were also weighed prior to aging and after 5000 hours of aging; these specimens weighed between 2.5 to 3 g.

9.4.3 Mechanical Testing

9.4.3.1 Open-Hole Compression Strength

The OHCS tests were performed following the Northrop Material Specification for Open Hole Compression Test Method (NAI-1504C) using a test fixture from Wyoming Test Fixtures, Inc. The specimens were end-loaded with a crosshead rate of 1.27 mm/min. A 150 kN load cell was used.

9.4.3.2 Apparent Interlaminar Shear Strength

The AISS tests were performed according to ASTM D 2344-84 for flat laminates; the loading and support noses had diameters of 6.35 mm. The specimens were loaded in 3-point bend with a support span of 12.7 mm to give a span-to-depth ratio of 4-to-1. A crosshead rate of 1.30 mm/min was used with a 5 kN load cell.

9.4.3.3 Transverse Flexural Strength

The TFS tests were performed according to the ASTM Standard Test Method for Flexural Properties of Unreinforced and Reinforced Plastics and Electrical Insulating Materials (D 790-92) following the four-point bend method with the load span (16.9 mm) equal to one-third of the support span (50.7 mm) (Test Method II - Procedure A); the loading and support noses had diameters of 12.70 mm. A crosshead rate of 1.50 mm/min was used with a 5 kN load cell.

9.4.4 Thermomechanical Analysis

Thermomechanical analysis (TMA) measurements of the 2.5kPETU / G40-800 softening temperature following each different TOA condition were performed using a DuPont Instruments 943 Thermomechanical Analyzer. TMA specimens were cut from the ends of the 6.35 mm wide, previously-tested AISS specimens. The end pieces cut for TMA were approximately 6.35 mm long. The specimens were placed under the 2.54 mm diameter quartz probe such that the probe was resting on a molded surface. Thus, dimensional changes were being measured through the thickness of the composite and the resin rich molded faces would have an influence on the results. Including the molded faces in the measurement was desired since this measurement was focusing on changes in the matrix and only looking for a transition temperature, not absolute dimension changes.

Dimensional changes were measured during a 5 °C/min temperature ramp from 150 °C to 300 °C with only the 2.43 g weight pan resting on top of the probe. The onset temperature of softening was determined to be at the intersection point of two lines tangent to the displacement versus temperature curve immediately prior to and immediately after the transition.

9.4.5 Dynamic Mechanical Thermal Analysis

Using a Polymer Laboratories DMTA, the specimens were tested in single cantilever mode at a frequency of 1 Hz, while the temperature was ramped at 2 °C/min from 220 °C to approximately 10 °C beyond the $\tan \delta$ peak. Prior to each test, the temperature was ramped from room temperature to 220 °C at 10 °C/min and allowed to soak for 10 minutes. Two specimens having lengths of 25 mm and widths of 11 mm were cut from each 76.2 mm x 25.4 mm DMTA aging panel. The specimens were clamped at either end such that there was a free length of 19 mm between the fixed clamp and the drive clamp. The T_g of each specimen was recorded as the $\tan \delta$ peak temperature.

9.4.6 Microindentation of Neat Resin

Vickers Hardness measurements were performed on neat resin specimens using a Tukon Microhardness instrument. Six neat resin specimens were selected for measurement. These six specimens included an unaged specimen, specimens that aged for 5000 hours in the four different oxygen partial pressures, and one specimen that aged for 720 hours in 2.84 kPa $p(O_2)$ followed by 5000 hours in 0.0 kPa $p(O_2)$. Each specimen was cut in half to reveal an unexposed cross section. Each specimen was then potted in epoxy potting compound and metallographically polished such that diamond-shaped microindentations spanning approximately 50 μm from point-to-point could clearly be resolved under a 20x microscope. These microindentations were made with a 200 g load. For each specimen, a hardness profile across the specimen thickness from one exposed surface to the other was generated by microindenting the polymer approximately every 175 μm , and then calculating the Vickers Hardness based on the dimensions of each indentation. Each indentation was measured three times to give an average hardness value.

9.5 Results and Discussion

9.5.1 Monitoring Mass Change

Thermal-oxidative aging had little effect on the masses of neat and CFR PETU specimens. During the 5000 hours of aging, the masses of the composite specimens changed by no

more than 0.05% from their original masses. After 5000 hours of aging, no neat resin specimen lost more than 0.2% of its original mass. Due to small sample sizes and small measured mass changes, the differences in mass changes from specimen to specimen were indiscernible from experimental error. Thus, no specific trends regarding the influence of aging time or oxygen partial pressure on mass change could be ascertained. Percent mass losses for aging of other carbon fiber-reinforced polymer composites in air are listed in Table 9.3 for comparison.

Table 9.3. Percent Mass Losses For TOA^(a) Carbon Fiber-Reinforced Composites

Matrix Material	28/50 Rule ^(b)	Mass Loss (%)	Time (hours)	Reference
Benzocyclobutene	5.3	0.05	4007	22
Bismaleimide	1	3.5	262	14
Bismaleimide	2.5	1.3	2232	19
K3B	2.3	none	5000	20, 21
Avimid K	3.7	0.05	2232	19
Cyanate Ester	3	1.05	180	5
PMR-15	0	18.0	300	23
PMR-15	1	~1.3	1639	8
PMR-15	2	~1.9	5000	17
PMR-15	3	~1.0	5000	17
PMR-15	4	0.7	5000	9
PMR-15	4	~2.5	15,000	9
PMR-15	5	~0.2	5000	17

a. All aging in air, except 2.5kPETU aged in 20% oxygen / 80% nitrogen mixture

b. Matrix T_g (°C) - (28/50 Rule Value • 28 °C) = Aging Temperature (°C)

9.5.2 TOA Effect on Softening Temperature Measured via TMA

The TMA results shown in Figure 9.2 demonstrate the material responses to the different aging conditions. The first 1750 hours of TOA increased the softening temperature, T_s , about 10 to 15 °C; the T_s of the specimen exposed to 0.0 kPa $p(O_2)$ increased by about 12 °C after 720 hours. Aging from 1750 to 3500 hours decreased the T_s values for the specimens aging in the three oxygen-containing environments. Further aging to 5000 hours produced no significant change in T_s for the specimens aging in the oxygen-containing environments. The explanation for this trend may be explained by the fact that the transition temperature measured by TMA is dominated by the transition in the molded surfaces. During the first 1750 hours of aging, the thin layers (<10 μm) of resin at the molded surfaces may be undergoing some combination of three processes that would all contribute to a rise in T_s : desorption of plasticizing moisture, physical aging, and additional

cure. As reported in Chapter 8, the as-manufactured composites contained 0.13 percent moisture by mass. Based on the results of Chapter 5, these panels were not fully cured when they were placed in the aging environments. The temperature of 204 °C is well below the reaction onset temperature (325 °C), but the energy and resultant increase in chain mobility provided by this elevated temperature may allow partially reacted chains to form bonds with other partially reacted sites, thus increasing crosslink density. This additional cure would be expected to take place only during the early stages of aging since the temperature would not be high enough to initiate new reactions and molecular mobility would be decreasing due to moisture desorption, physical aging, and the formation of new crosslinks throughout the matrix. During the second 1750 hours of aging, the T_s -increasing processes are completed or slowing down and oxidative degradation begins to dominate as the oxygen concentration in the matrix increases. Near 3500 hours of aging, the polymer at the composite surface may reach a point that most of the surface degradation that is going to occur in the respective TOA conditions has taken place; further specimen degradation is taking place at greater depths and is not detectable by TMA. Thus, T_s does not change from 3500 to 5000 hours.

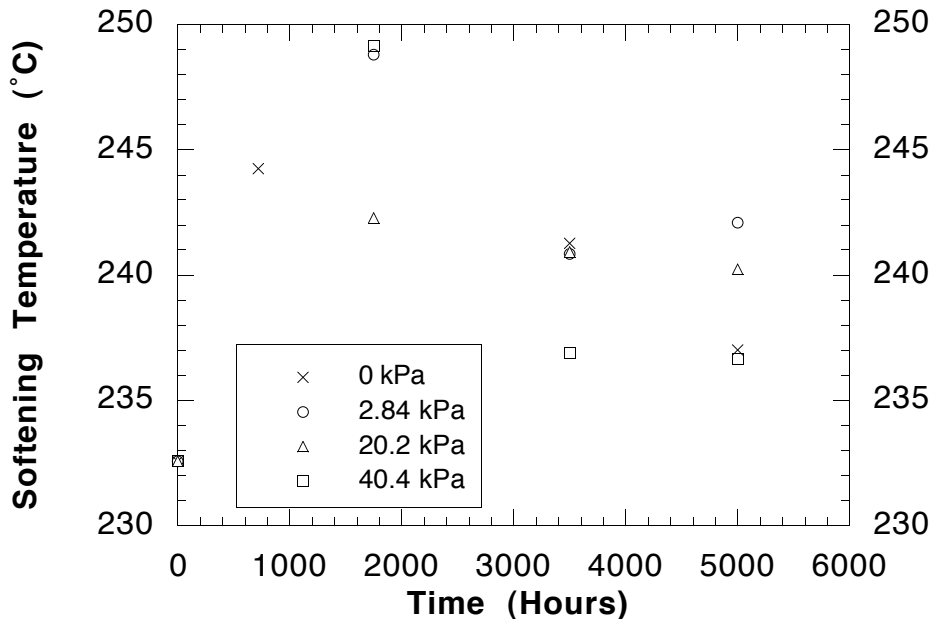


Figure 9.2. Softening Temperature Measured by TMA
(0.0 kPa $p(O_2)$ Specimens Aged for 3500 and 5000 Hours were Pre-aged)

Following the initial increase in T_g after 720 hours of aging in the 0.0 kPa $p(O_2)$ environment, additional aging would be expected to result in slight increases or no change in T_g as the moisture desorption, physical aging, and additional cure processes run their courses. Surprisingly, the T_g was seen to decrease from the 720 hour value after 3500 and 5000 hours of aging. The decreases seen in T_g following these two stages of aging may be attributable to the fact that the specimens aged for 3500 and 5000 hours were pre-aged; the 720 hour specimen was not pre-aged.

9.5.3 TOA Effect on Glass Transition Temperature Measured via DMTA

The results of DMTA T_g measurements (each data point in Figure 9.3 is an average of measurements on two separate specimens) following 5000 hours of aging agree with the T_g measurements. The glass transition temperatures resulting from all aging conditions are higher than that of the unaged specimen ($T_g = 255\text{ }^\circ\text{C}$) again indicating that material properties may be changing due to some combination of moisture desorption, physical aging, and additional cure. Though aging for 5000 hours resulted in an increase in T_g above the unaged value for all environments, the size of the increase decreased with increasing oxygen partial pressure indicating that increased oxygen partial pressure resulted in increased chemical degradation. Parvatareddy, et al. [5], observed T_g increases for aging of a semicrystalline thermoplastic in ambient air, 13.8 kPa air, and 100% nitrogen. The specimens aged in nitrogen had the highest glass transition temperatures, and the specimens aged in ambient air had the lowest glass transition temperatures. The authors [5] attributed these results to "...a combination of chemical degradation, physical aging, and other processes taking place in the polymer." Pederson, et al. [19], observed T_g increases during aging of a thermoplastic polyimide and a thermosetting bismaleimide. The increase of the thermoplastic's T_g may be due to either physical aging and/or chain extension, whereas, the increase of the thermoset's T_g was likely due to additional cure.

9.5.4 Open-Hole Compression Strength

As with the moisture exposure tests, limited results were obtained from the OHCS specimens due to a tendency for specimens to fail at the edge of the grips, rather than around the circumference of the center hole, which creates a stress concentration. For three of the aging conditions, all three specimens failed at the grips. At least one specimen failed at the grips for each of the remaining aging conditions. No discernible trends were observed for the limited results listed in Table 9.4. Two conclusions may be reached from these results. First, the TOA conditions of this study do not result in a drastic reduction in the OHCS of unidirectional composite specimens. However, due to the number of

specimens that failed at the grips it appears that unidirectional OHCS is not a good technique for evaluating TOA effects on CFR 2.5kPETU composite mechanical properties. This grip failure often included longitudinal cracks that ran from the center hole up to the transverse cracks at the edge of the grips. Brooming of specimen ends was also seen in some cases. Brooming and longitudinal splitting were reported as the failure modes for unidirectional OHCS specimens cut from graphite/epoxy composite panels that were tested using the same Northrop fixture that was used in this study [24].

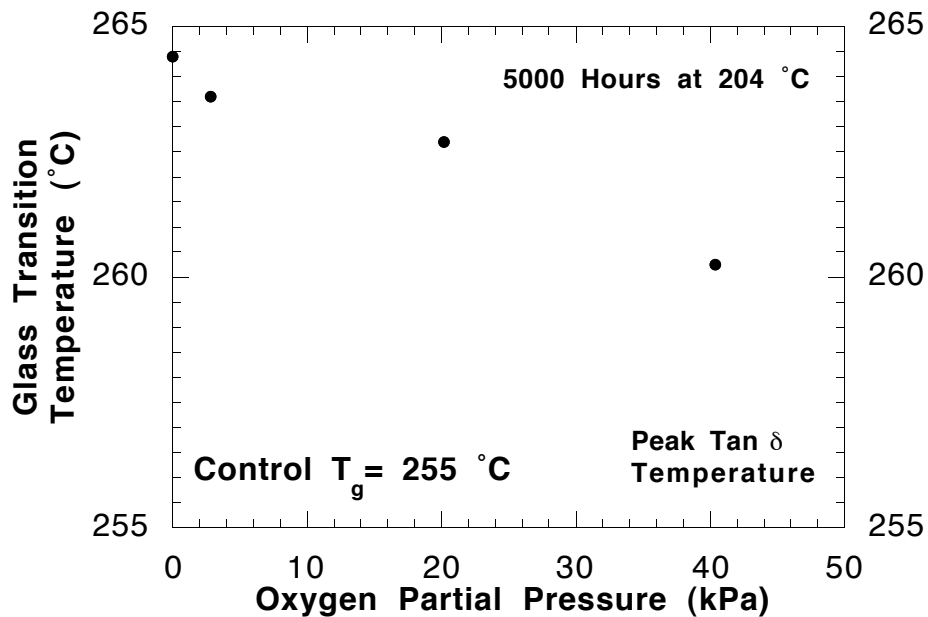


Figure 9.3. Influence of Oxygen Partial Pressure on T_g after 5000 Hours (0.0 kPa $p(\text{O}_2)$ Specimen was Pre-aged)

The use of angle-ply laminates is advisable in future OHCS studies. Hou, et al. [25], measured OHCS of IM7 reinforced PETI-5, a polymer similar to PETU (see section 4.2 of Chapter 4), using the “specimen size and test procedures of Northrop Corp.” They did not report any improper failure modes in reporting an OHCS of 429.3 MPa for specimens cut from panels having a lay up of $[\pm 45/90/0/0/\pm 45/0/0/\pm 45/0]_s$. Unidirectional OHCS CFR 2.5kPETU specimens were used to allow OHCS, AISS, and TFS specimens to be cut from the same panel as shown in Figure 7.1. The limited quantity of fluidizable 2.5kPETU powder caused the dry powder prepregging process to be difficult and excessively time consuming (see Chapter 7). Despite these hindrances, all of the fluidizable powder was consumed by the manufacture of the composite panels in Chapter 7. Use of angle-ply

laminates for OHCS would have required acquisition of additional fluidizable powder and a 50% increase in time devoted to dry powder prepregging. Thus, unidirectional OHCS specimens were selected. The successful testing of the three control specimens prior to beginning the TOA of the unidirectional composite panels gave no forewarning of the problems that arose during testing of the aging specimens.

Table 9.4. Open-Hole Compression Strength Results

Aging Condition	OHCS ^(a) (MPa)	Number of Specimens ^(b)
Control	506 ± 23	3
[720 hr / 0.0 kPa p(O ₂) / 204 °C]	467	1
[720 hr / 2.84 kPa p(O ₂) / 177 °C]	480 ± 10	2
[1750 hr / 2.84 kPa p(O ₂) / 204 °C]	528	1
[1750 hr / 20.2 kPa p(O ₂) / 204 °C]	492 ± 31	2
[1750 hr / 40.4 kPa p(O ₂) / 204 °C]	475	1
[3500 hr / 0.0 kPa p(O ₂) / 204 °C]	NA	0
[3500 hr / 2.84 kPa p(O ₂) / 204 °C]	542 ± 31	2
[3500 hr / 20.2 kPa p(O ₂) / 204 °C]	NA	0
[3500 hr / 40.4 kPa p(O ₂) / 204 °C]	606 ± 4	2
[5000 hr / 0.0 kPa p(O ₂) / 204 °C]	556 ± 29	2
[5000 hr / 2.84 kPa p(O ₂) / 204 °C]	546 ± 43	2
[5000 hr / 20.2 kPa p(O ₂) / 204 °C]	545	1
[5000 hr / 40.4 kPa p(O ₂) / 204 °C]	NA	0

a. Average of those specimens that failed in the proper mode

b. Out of the three tested specimens, the number that failed in the proper mode

9.5.5 Apparent Interlaminar Shear Strength

No conclusive results concerning TOA effects on CFR 2.5kPETU composite mechanical properties may be obtained from the AISS results since all specimens failed in bearing mode under the center loading nose.

9.5.6 Transverse Flexural Strength

The results of the TFS tests are given in Figure 9.4; the control TFS was 136 ± 10 MPa. Not included in Figure 9.4 is the TFS of the [720 hr / 2.84 kPa p(O₂) / 177 °C] panel, which was measured to be 141 ± 5 MPa. The results of Figure 9.4 demonstrate the dependence of TFS on time and oxygen partial pressure. However, specimens exposed to 0.0 kPa p(O₂) for 3500 hours and 5000 hours displayed an unexpected decrease in TFS

that did not follow the trend of the oxygen-containing environments. The TFS results for the oxygen-containing environments will be commented on first and then the discussion will return to the 0.0 kPa p(O₂) results.

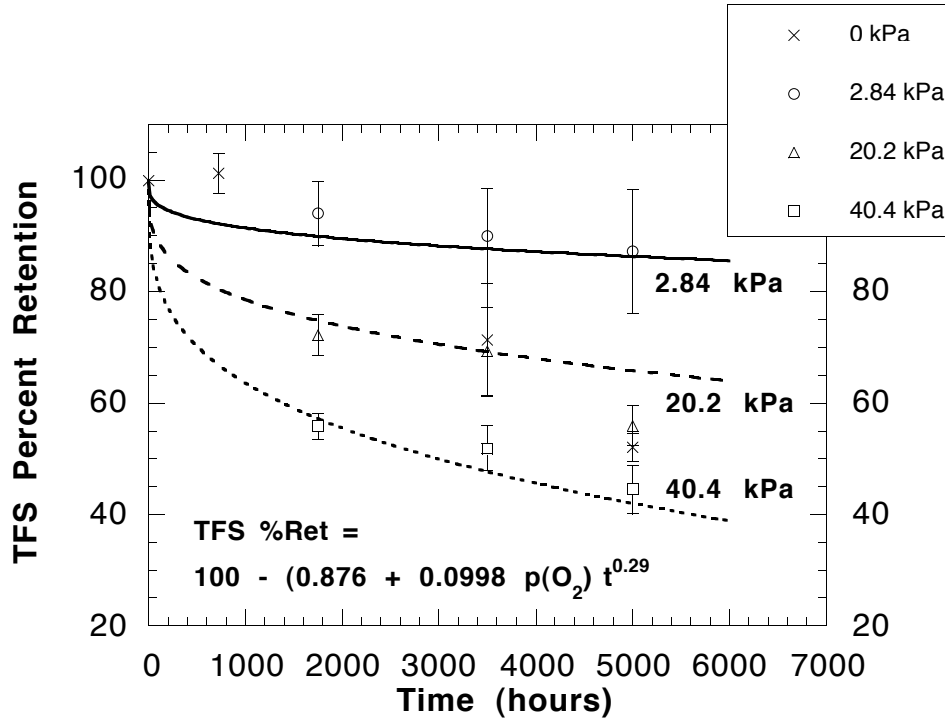


Figure 9.4. TFS Percent Retention Versus Time at 204 °C
(0.0 kPa p(O₂) Specimens Aged for 3500 and 5000 Hours were Pre-aged)

As expected, TFS decreased with increasing oxygen partial pressure and exposure time. Bowles [7] demonstrated that with increased TOA, the degraded surface layer in graphite fiber-reinforced PMR-15 increased and that the TFS of this composite was dependent on the depth of the degraded layer at the surface. The degraded layer was visible under a microscope and allowed for the measurement of an undegraded thickness and an undegraded width. Using these undegraded dimensions, rather than the actual specimen dimensions, the calculated TFS was within three percent of the control value indicating that the undegraded cross sectional area was responsible for the composite TFS. This finding allows for the estimation of degradation depth based on TFS percent retention of PMR-15 matrix composites. Assuming that the oxidative degradation reaction is controlled by the diffusion rate of oxygen through the aging material, one may initially conclude that the TFS percent retention measurements for CFR 2.5kPETU following exposure to different oxygen partial pressures for a variety of times would allow for the estimation of the oxygen diffusion coefficient through the thickness of CFR 2.5kPETU composite panels. To

estimate this oxygen diffusion coefficient, one would have to assume Fickian diffusion and use the case of a semi-infinite solid, where the depth of oxygen diffusion, and thus oxidative degradation, would be proportional to the square root of time. Using the assumption that TFS percent retention is a direct measure of degradation depth (i.e., diffusion depth) based on Bowles [7] results, oxygen diffusion through the thickness of CFR 2.5kPETU is not Fickian. This last statement is based on the power law fit developed by the method of least squares that shows TFS percent retention proportional to (time)^{0.29} (Figure 9.4 and Equation 9.1). Equation 9.1 is a result of a single least squares analysis of the nine data points for 2.84 kPa p(O₂), 20.2 kPa p(O₂), and 40.4 kPa p(O₂) at 1750, 3500, and 5000 hours versus individually fitting the three data points for each oxygen partial pressure.

$$\text{TFS (\%Retention)} = 100 - \{[0.876 + 0.0998(p(\text{O}_2))] t^{0.29}\} \quad (9.1)$$

This lack of Fickian behavior during long term aging of polymers is expected. Large scale motions of oxidation reaction products are generally limited, thus as oxidation reactions occur, the polymer matrix becomes heterogeneous [26]. A gradient of degradation develops between the exposed surface and the undegraded interior core. For further degradation to occur, oxygen has to diffuse through the outer degraded region into the undegraded core. With every oxidation reaction that takes place, the material through which the oxygen is diffusing changes. This constantly changing, heterogeneous polymer eliminates Fickian behavior and the subsequent square root of time dependence for diffusion depth. Other investigators have seen similar behavior during TOA of high-temperature polymers [6, 14]. Nam and Seferis [14] monitored the weight loss for the through-the-thickness, molded surface direction of graphite fiber-reinforced bismaleimide for 262 hours at 28 °C below its T_g. They found the weight loss, and diffusion depth, to be proportional to (time)^{0.47}. Bowles, et al. [6], measured the depth of degradation on neat PMR-15 for 1050 hours at 56 °C below its T_g. They found the depth of degradation to be proportional to (time)^{0.35}. Though these results, along with the ones presented here, are for different materials under different aging conditions, a general trend is seen: increasing aging time decreases the power dependency on time away from Fickian diffusion. After only 262 hours, the degraded surface region would be rather small, thus the time exponent was only reduced from 0.50 to 0.47 [14]. Aging for 1050 hours would provide more time for growth of the degraded region, thus the time exponent was reduced by a larger amount to 0.35 [6]. And finally, after aging CFR 2.5kPETU for 5000 hours at 56 °C below its T_g, the time exponent was reduced to 0.29. Again, it is emphasized that a general trend, not a

direct correlation, is being implied here since these results are for different materials under different aging conditions.

The decreases in TFS after 3500 and 5000 hours of aging in the 0.0 kPa $p(\text{O}_2)$ environment (Figure 9.4) were unexpected due to the review of literature investigating elevated temperature aging found at the beginning of this chapter. This review concludes that aging in pure nitrogen is less detrimental to material properties than aging in oxygen containing environments. Because 720 hours of 0.0 kPa $p(\text{O}_2)$ / 204 °C aging of a previously unaged specimen showed no effect on TFS, it is thought that the 720 hours of 2.84 kPa $p(\text{O}_2)$ / 177 °C pre-aging (Table 9.2) is the source of the TFS reduction resulting from 3500 and 5000 hours of 0.0 kPa $p(\text{O}_2)$ / 204 °C aging following the pre-aging despite the TFS following 720 hours of 2.84 kPa $p(\text{O}_2)$ / 177 °C aging being equivalent to the control TFS.

In summary, the TFS specimens exposed to oxygen-containing environments behaved as expected; longer exposure times and exposure to higher oxygen partial pressures resulted in greater reduction of TFS with the TFS reduction displaying a power law dependence on time. Pre-aging of specimens in a 2.84 kPa $p(\text{O}_2)$ / 177 °C environment for 720 hours possibly results in TFS reduction during subsequent aging in a 0.0 kPa $p(\text{O}_2)$ / 204 °C environment.

9.5.7 Optical Microscopy

Measurement of the depth of degradation in TOA polymers and fiber-reinforced polymer composites via optical microscopy is common [6,7,14,17]. Degraded polymers are generally reported to be discolored and/or cracked by oxidative degradation. In an attempt to measure the depth of degradation in 2.5kPETU, several composite and neat resin specimens were inspected by optical microscopy following different stages of aging. No samples displayed any visual indication of aging; no discoloration or cracking of the surfaces was evident. A typical composite specimen is shown in Figure 9.5. This micrograph was taken from the composite panel aged for 5000 hours in the 40.4 kPa $p(\text{O}_2)$ environment. Some cracking was observed in the edges of TFS specimens (Figure 9.6), but since this cracking was not observed in sections of the composite panels that were not mechanically tested, it is safe to assume that these cracks were mechanically induced. In addition, these cracks ran parallel to the surface rather than penetrating inwards from the surfaces as seen by other investigators [6,14]. Therefore, the degradation-induced reduction in TFS (Figure 9.4) during aging is likely due to weakening of the bulk matrix and fiber/matrix interface rather than stress concentrations resulting from the development

of surface cracks. Inspection of Figure 9.6 reveals that the cracks in the TFS specimens mainly ran along fiber/matrix interfaces rather than through the bulk matrix. Thus it appears that the critical mechanism for TFS reduction during TOA is weakening of the fiber/matrix interface. This finding is interesting because good fiber/matrix adhesion was observed during the mechanical testing of the feasibility study (Chapter 2).

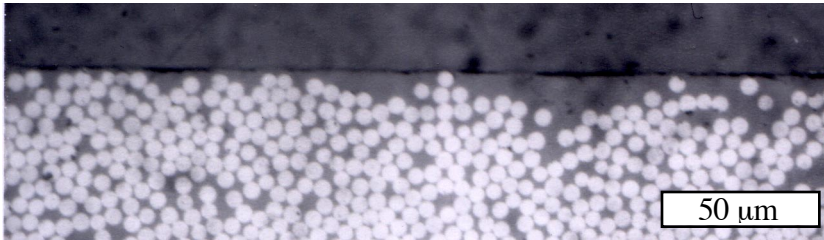


Figure 9.5. [5000 hr / 40.4 kPa $p(O_2)$ / 204 °C] Aged Composite Surface

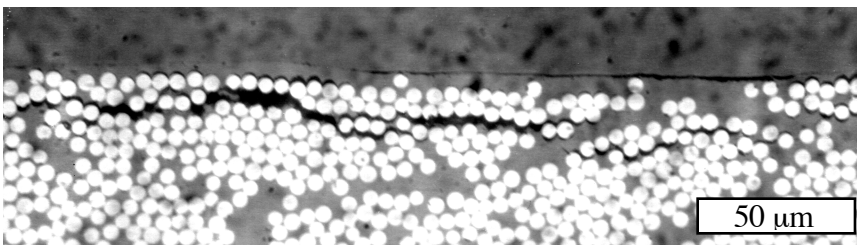


Figure 9.6. [5000 hr / 40.4 kPa $p(O_2)$ / 204 °C] Aged Composite TFS Specimen

The lack of visual evidence of degradation eliminated the ability to use optical microscopy to measure the depth of degradation in all of the composite specimens. Initially, the depths of degradation measured for different oxygen partial pressures and different aging times were going to be used to estimate the oxygen diffusion coefficient through the thickness of the CFR 2.5kPETU composite panels. As discussed previously, as the matrix oxidizes, it becomes a constantly changing, heterogeneous material that does not behave in a Fickian manner. Therefore, calculation of a through-the-thickness diffusion coefficient for oxygen based on degradation depth measurements was not pursued. However, degradation depth measurements were still desired for the purpose of obtaining a qualitative feel for the influence of aging conditions on degradation depth.

9.5.8 Vickers Hardness of Aged Neat Resin via Microindentation

Microindentation has been used by other investigators [5,27-29] to measure the mechanical properties of polymers across their cross sections in order to obtain a profile of the

influence of TOA on mechanical properties from exposed specimen surfaces to the interior of the specimens. In this study, microindentation measurements were used to measure the Vickers Hardness (VH) across the thickness of neat resin specimens. Profiles of VH for an unaged specimen and specimens exposed to five different aging conditions are shown in Figures 9.7 - 9.12.

The VH profiles help to clarify the TFS results. Figure 9.8 shows an overall increase in VH across the thickness of the [5000 hr / 2.84 kPa p(O₂) / 204 °C] specimen, but there is no sign of surface degradation, which would be indicated by a gradient in VH between the specimen interior and surface as seen in the profiles of the other specimens. This small overall hardness increase agrees well with the relatively small reduction in TFS following [5000 hr / 2.84 kPa p(O₂) / 204 °C] aging compared to changes seen following the other aging conditions.

Figure 9.9 displays that a step transition in VH located about 0.4 mm below the specimen surface resulted from the [5000 hr / 0.0 kPa p(O₂) / 204 °C] aging. The outer 0.4 mm layer of polymer has a hardness about 5 VH greater than that of the interior polymer. The results of the VH measurements on this nitrogen aged specimen that was not pre-aged indicates that pre-aging is not the only reason that degradation is being seen during aging in pure nitrogen environments; an additional experimental or phenomenological contribution exists. Figure 9.10 shows the results of VH measurements following [5000 hr / 0.0 kPa p(O₂) / 204 °C] aging on a pre-aged specimen. The key differences between the pre-aged specimen and the regular specimen is that the pre-aging appeared to result in a much higher VH increase within the 0.2 mm thickness just below the specimen surface, and the pre-aging appears to have increased the hardness to a uniform level within the interior of the specimen. This same increase to a uniform level of hardness was seen in Figure 9.8 also. Thus, 2.84 kPa p(O₂) aging, whether at 177 °C or 204 °C, in a vacuum oven appears to increase the hardness of the neat resin to a uniform level through the thickness.

Figures 9.11 and 9.12 give the VH results for 20.2 kPa p(O₂) and 40.4 kPa p(O₂) aging, respectively. Both specimens display a hardness gradient of 5 VH/mm. This gradient exists over the outer 1 mm for the 20.2 kPa p(O₂) specimen and over the whole 3 mm from the center to the surface for the 40.4 kPa p(O₂) specimen. The deeper degradation in the 40.4 kPa p(O₂) specimen would be expected based on Henry's Law in which the concentration of oxygen absorbing into the surface of the polymer would be proportional to the oxygen partial pressure in the surrounding environment. Increasing the oxygen

concentration at the polymer surface increases the flux of oxygen into the interior of the polymer allowing for oxidation to take place at a more rapid pace. These concepts were considered in the design of the TOA experiments, but it is helpful to revisit them with the visual aid of Figures 9.11 and 9.12. Another consequence of the increased oxygen concentration is the more severe surface degradation seen in the 40.4 kPa $p(\text{O}_2)$ specimen versus the 20.2 kPa $p(\text{O}_2)$ specimen; the hardness just below the surface of the 40.4 kPa $p(\text{O}_2)$ specimen is 10 to 15 VH greater than the unaged hardness in contrast to the increase of only about 5 VH for the 20.2 kPa $p(\text{O}_2)$ specimen. The qualities of deeper and more severe degradation with increased oxygen partial pressure were expected and validate the TFS results shown in Figure 9.4.

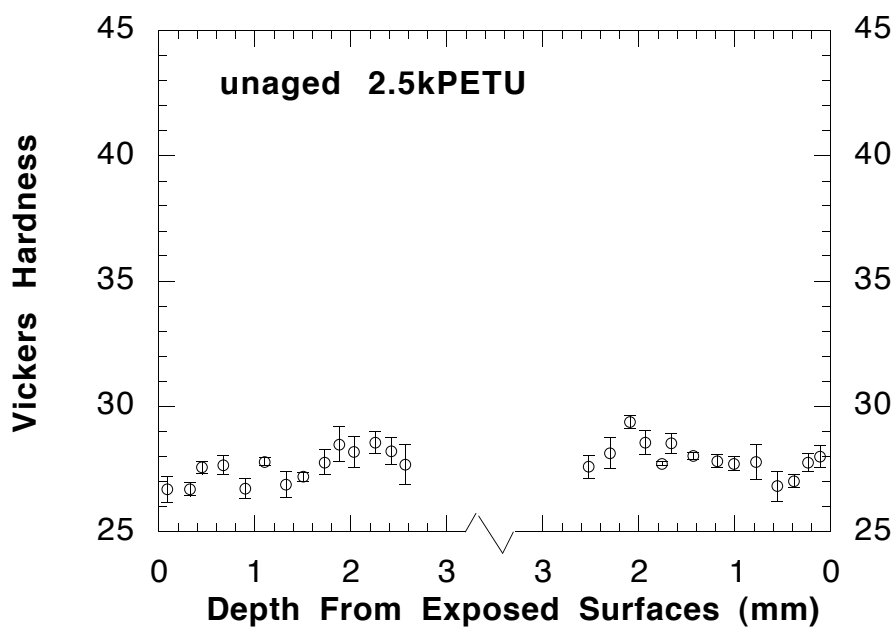


Figure 9.7. Vickers Hardness Profile of Unaged Neat Resin

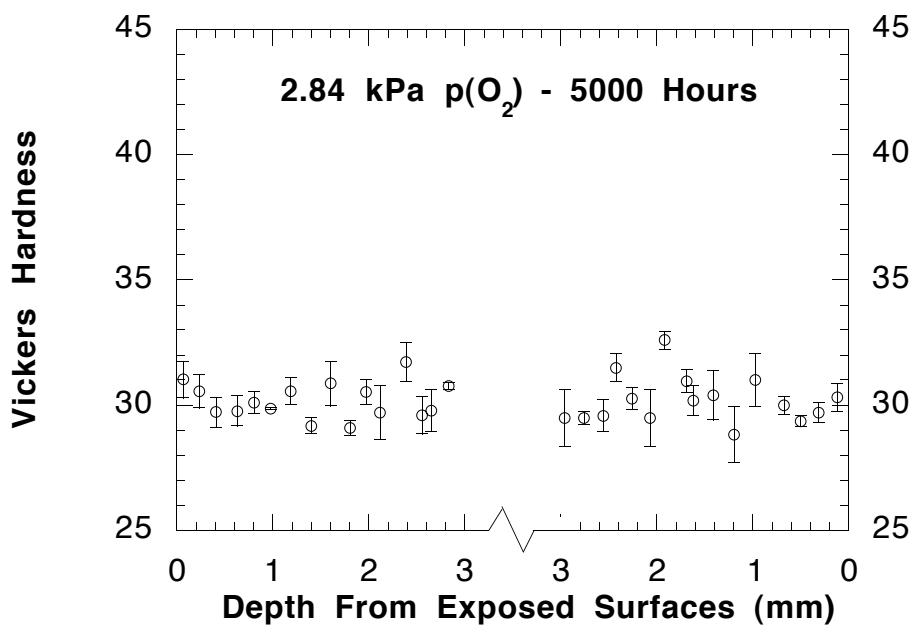


Figure 9.8. Vickers Hardness Profile of Neat Resin
[5000 hr / 2.84 kPa p(O₂) / 204 °C]

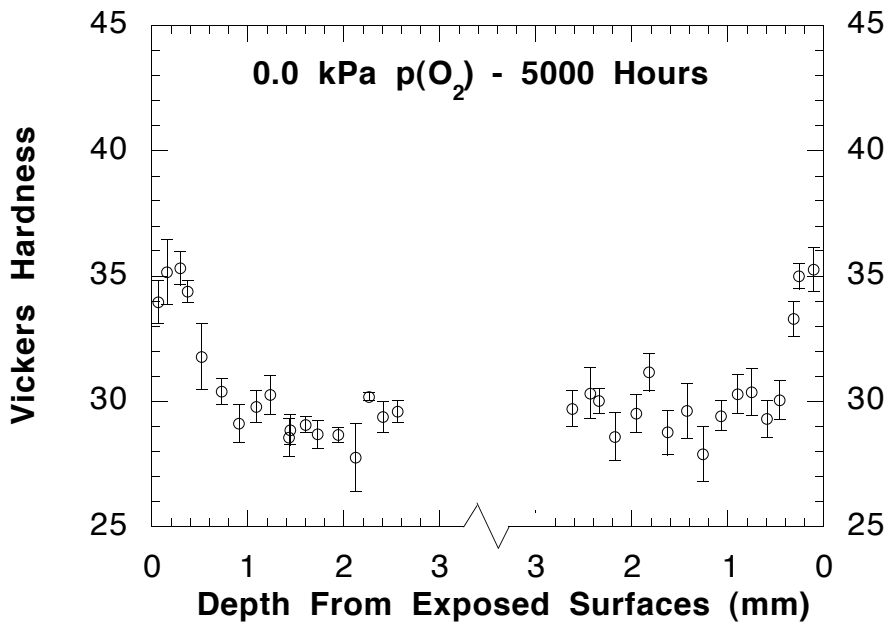


Figure 9.9. Vickers Hardness Profile of Neat Resin
[5000 hr / 0.0 kPa p(O₂) / 204 °C]

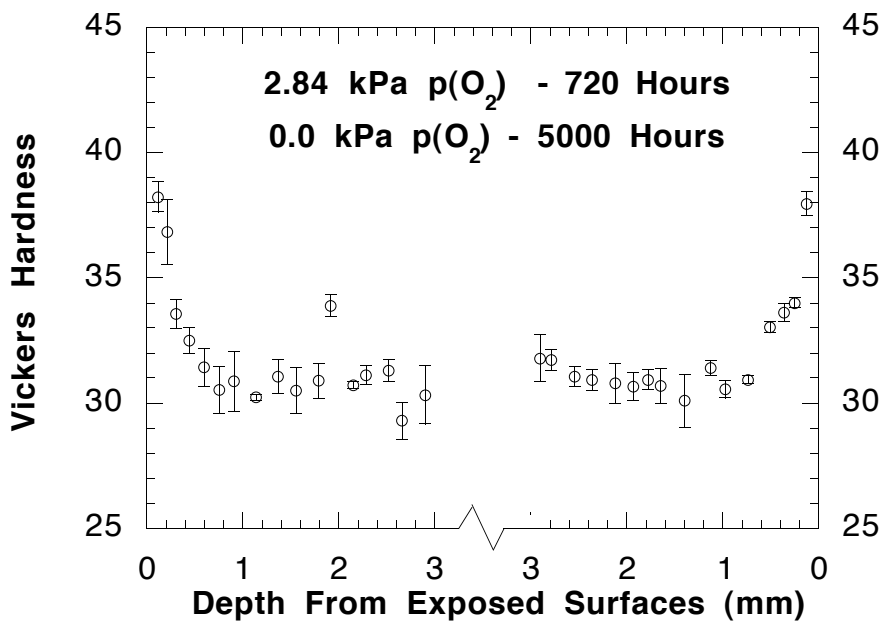


Figure 9.10. Vickers Hardness Profile of Neat Resin
[720 hr / 2.84 kPa p(O₂) / 177 °C // 5000 hr / 0.0 kPa p(O₂) / 204 °C]

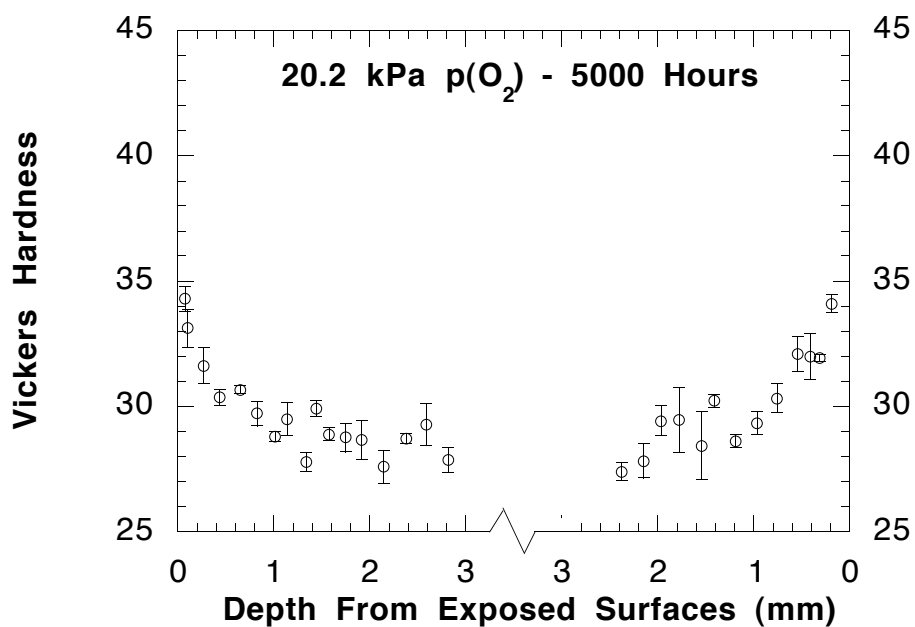


Figure 9.11. Vickers Hardness Profile of Neat Resin
[5000 hr / 20.2 kPa p(O₂) / 204 °C]

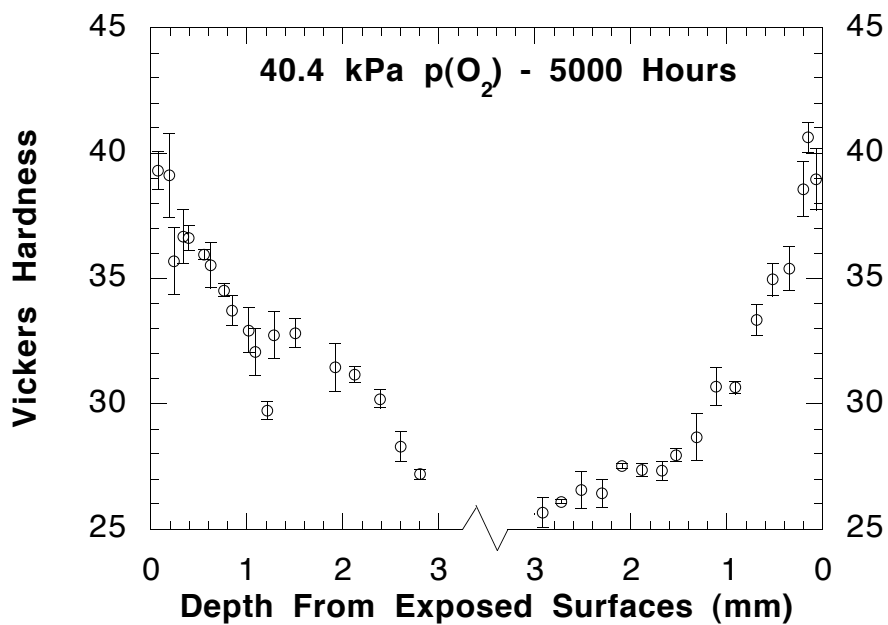


Figure 9.12. Vickers Hardness Profile of Neat Resin
[5000 hr / 40.4 kPa p(O₂) / 204 °C]

9.6 Summary Comments

The main purpose of the thermal-oxidative aging experiments was to assess the potential of using CFR 2.5kPETU in high-performance aerospace applications. The minimal mass loss from both composite and neat resin specimens following aging at 204 °C for up to 5000 hours in environments having oxygen partial pressures up to twice that of ambient air is encouraging. Complementing the minimal mass loss was the absence of any visual evidence of degradation (cracking, resin discoloration, etc.) following thermal-oxidative aging. Aging did produce a reduction in TFS. However, the aerospace applications for which this material is being considered rarely reach temperatures near 204 °C and rarely see oxygen partial pressures as great as 20.2 kPa. In addition, TFS is very sensitive to property changes near the surface of a material due to the test geometry. Thus, this thermal-oxidative aging study may have determined some limitations on the application of PETU, but it does not rule out long-term use at lower temperatures.

Based on the results of this study, it would be interesting to look at TOA in one specific environment (e.g., 20.2 kPa $p(\text{O}_2)$) at a range of temperatures above and below 204 °C to evaluate the temperature dependence of degradation. In addition, aging in pure nitrogen, without any pre-aging, should be studied further at different temperatures to better isolate the source(s) of property degradation during nitrogen aging. For both of these recommended studies, it is suggested that composite panels be consolidated using a cure schedule that provides optimal cure rather than the cure schedule of Chapter 7. This improved cure schedule would eliminate lack of full cure as a variable when evaluating sources of degradation.

The results shown in Figure 9.3 demonstrate that aging for 5000 hours at 204 °C results in a T_g increase, which was attributed to three possible mechanisms: densification by physical aging, desorption of plasticizing moisture, and additional cure. It may be possible to determine the contributions of these actions via different specimen preparation and conditioning. If specimens were cured in the same manner as those tested in this study, such that the control T_g was 255 °C, measurement of T_g following vacuum-drying would give a measurement of the influence of plasticizing moisture on the T_g . Aging of vacuum-dried specimens would provide a measure of the T_g increase due to both additional cure and physical aging. Annealing of aged specimens above the T_g would reverse physical aging and allow the contributions of additional cure and physical aging to be differentiated.

One additional recommended study is not specific to PETU. Diffusion depth was seen to have a power law dependence on time. However, the exponential term displayed a possible tendency to decrease with increasing aging time. To further investigate this possible tendency, a polymer in which diffusion depth is easily measured should be selected. Samples of this polymer should be aged for at least 5000 hours with samples removed from the aging environment at frequent intervals. A large number of data points would allow a power law fit to be applied up to different aging times. Consequently, dependence of the exponential term on time could be evaluated.

9.7 References

1. P.M. Hergenrother, "Development of Composites, Adhesives and Sealants for High-Speed Commercial Airplanes," *SAMPE Journal*, **36**, (1), 30-41 (2000).
2. M.D. Brunner and T. Cebeci, "Development of the California State University, Long Beach Composite Durability Laboratory," *Proceedings of the 39th International SAMPE Symposium and Exhibition*, 1554-1563 (1994).
3. J.R. Kerr and J.F. Haskins, "Effects of 50,000 h of Thermal Aging on Graphite/Epoxy and Graphite/Polyimide Composites," *AIAA Journal*, **22**, (1), 96-102 (1984).
4. T.K. Tsotsis, "Thermo-Oxidative Aging of Composite Materials," *Journal of Composite Materials*, **29**, (3), 410-422 (1995).
5. H. Parvatareddy, J.Z. Wang, D.A. Dillard, T.C. Ward, and M.E. Rogalski, "Environmental Aging of High-Performance Polymeric Composites: Effects on Durability," *Composites Science and Technology*, **53**, 99-409 (1995).
6. K.J. Bowles, D. Jayne, T.A. Leonhardt, "Isothermal Aging Effects on PMR-15 Resin," *SAMPE Quarterly*, **24**, (2), 2-9 (1993).
7. K.J. Bowles, "Transverse Flexural Tests as a Tool for Assessing Damage to PMR-15 Composites from Isothermal Aging in Air at Elevated Temperatures," *SAMPE Quarterly*, **24**, (2), 49-53 (1993).
8. K.J. Bowles and A. Meyers, "Specimen Geometry Effects on Graphite/PMR-15 Composites During Thermo-Oxidative Aging", *Proceedings of the 31st International SAMPE Symposium and Exhibition*, 1285-1299 (1986).
9. J.B. Nelson, "Thermal Aging of Graphite/Polyimide Composites", in Long-Term Behavior of Composites, ASTM STP 813, T.K. O'Brien, ed., American Society for Testing and Materials, Philadelphia, 1983, pp. 206-221.
10. S. Ciutacu, P. Budrugaec, and I. Niculae, "Accelerated Thermal Aging of Glass-Reinforced Epoxy Resin Under Oxygen Pressure," *Polymer Degradation and Stability*, **31**, (3), 365-372 (1991).

11. B. Crossland, G.J. Knight, and W.W. Wright, "Thermal Degradation of Some Polyimides," *British Polymer Journal*, **19**, 291-301 (1987).
12. M.A. Meador, "High-Temperature Polymer Matrix Composites," Flight Vehicle Materials, Structures, and Dynamics - Assessment and Future Directions, vol. 2, 406-415 (1994).
13. J.M. Whitney, "Experimental Characterization of Delamination Fracture," in Interlaminar Response of Composite Materials, N.J. Pagano, ed., Elsevier Science Publishers 1989, pp. 162-163.
14. J.D. Nam and J.C. Seferis, "Anisotropic Thermo-Oxidative Stability of Carbon Fiber Reinforced Polymeric Composites," *SAMPE Quarterly*, **24**, (1), 10-18 (1992).
15. ASTM Standard D 5528-94a, "Standard Test Method for Mode I Interlaminar Fracture Toughness of Unidirectional Fiber-Reinforced Polymer Matrix Composites".
16. S. Hashemi, A.J. Kinloch, and J.G. Williams, "The Analysis of Interlaminar Fracture in Uniaxial Fibre-Polymer Composites," *Proceedings of the Royal Society of London*, **A427**, 173-199 (1990).
17. K.J. Bowles, L. McCorkle, and L. Ingrahm, "Comparison of Graphite Fabric Reinforced PMR-15 and Avimid N Composites After Long-Term Isothermal Aging at Various Temperatures," *Journal of Advanced Materials*, **30**, (1), 27-35, 1998.
18. R.J. Morgan, "Thermal Characterization of Composites," in Thermal Characterization of Polymeric Materials, 2nd Edn., E.A. Turi, ed., Academic Press, New York, 1997, pp. 2237-2238.
19. C.L. Pederson, J.W. Gillespie, Jr., R.L. McCullough, R.J. Rothschilds, and S.L. Stanek, "The Effect of Isothermal Aging on Transverse Crack Development in Carbon Fiber Reinforced Cross-Ply Laminates," *Polymer Composites*, **16**, (2), 154-160 (1995).
20. S. Sacks and W.S. Johnson, "Effects of Thermal Aging on the Mechanical Behavior of K3B Matrix Material," *Journal of Thermoplastic Composite Materials*, **11**, 429-442 (1998).
21. C. Arendt, M. Finefield, M. Grayson, D. Harmon, and S. Wanthal, "Durability of Composite Materials McDonnell Douglas Aerospace," Semi-Annual Review of HSR Materials Durability Research - Composites, internal document (Feb, 1996).
22. W.M. Lee, S.A. Laman, S. Yalvac, and R.L. McGee, "Thermal Oxidative Stability of Diketone-Bis-Benzocyclobutene (DK-BIS-BCB) / Graphite Fabric Composite," *Proceedings of the 37th International SAMPE Symposium and Exhibition*, 679-689 (1992).
23. R.D. Vanucci, "PMR Polyimide Compositions For Improved Performance at 371 °C," *SAMPE Quarterly*, **19**, (1), 31-36 (1987).
24. J.A. Daniels and R.S. Sandhu, "Evaluation of Compression Specimens and Fixtures for Testing Unidirectional Composite Laminates," in Composite Materials: Testing and Design, Vol. 11, ASTM STP 1206, E.T. Camponeschi, Jr., ed., American Society for Testing and Materials, Philadelphia, 1993, pp. 103-123.

25. T.H. Hou, B.J. Jensen, and P.M. Hergenrother, "Processing and Properties of IM7/PETI Composites," *Journal of Composite Materials*, **30**, (1), 109-122 (1996).
26. L. Audouin, V. Langlois, J. Verdu, and J.C.M. de Bruijn, "Review Role of Oxygen Diffusion in Polymer Ageing: Kinetic and Mechanical Aspects," *Journal of Materials Science*, **29**, (3), 569-583 (1994).
27. R.L. Clough and K.T. Gillen, "Degradation Mechanisms and Accelerated Aging Test Design," *Proceedings of the ACS Division of Polymeric Materials: Science and Engineering*, **52**, 592-597 (1985).
28. K.T. Gillen, R.L. Clough, and C.A. Quintana, "Modulus Profiling of Polymers," *Polymer Degradation and Stability*, **17**, 31-47 (1987).
29. R.L. Clough and K.T. Gillen, "Oxygen Diffusion Effects in Thermally Aged Elastomers," *Polymer Degradation and Stability*, **38**, 47-56 (1992).

Chapter 10 - Conclusions and Recommendations for Future Work

This research endeavor was built around three questions:

- Can well-consolidated, fiber-reinforced composites be manufactured with a PETU matrix?
- If so, how do the mechanical properties compare to other fiber-reinforced polymer matrix composites?
- What is the effect of environmental exposure on these mechanical properties?

10.1 Conclusions

The preliminary, or feasibility, study of 3kPETU focused mainly on how to manufacture carbon fiber-reinforced (CFR) 3kPETU composites and their mechanical properties. Dry powder prepregging was selected for production of towpreg from which the composites were manufactured via compression molding. This technique produced well-consolidated composites with low void content. The mechanical properties of these composites compared well with other high-performance fiber-reinforced polymeric composites.

The preliminary study of 3kPETU continued by investigating the effects of moisture absorption and desorption on the mechanical properties of CFR 3kPETU. Composites reached an effective moisture equilibrium content, M_m , of 0.48% by mass during exposure to 90 °C / 85% relative humidity. This moisture uptake resulted in a slight reduction in mechanical properties. This reduction was concluded to be due to matrix plasticization since the original mechanical properties were recovered following exposure to 90 °C / 10% relative humidity. This moisture exposure study also concluded that cutting mechanical specimens from larger composite panels prior to, or after, moisture exposure had no bearing on resultant M_m or mechanical property retention. However, the through-the-thickness diffusion coefficient, D_z , was higher for the transverse flexural strength (TFS) specimens than for the larger rectangular panels. This discrepancy is thought to be due to specimen edges that were not perfectly sealed or error in estimation of moisture content of the sealants. The stainless steel foil tape was preferred to the insulating varnish since the moisture content of the foil tape was much less sensitive to relative humidity than the

insulating varnish. In addition, the tape was easier to apply and remove than the varnish. The success of the preliminary studies led to a full scale study of 2.5kPETU.

A first-order reaction kinetics model was developed for 2.5kPETU based on DSC thermal analysis that displayed cure onset around 325 °C, an exothermic peak around 370 °C, and a total heat of reaction of 112.5 J/g. This model is good for quick estimates of degree of cure versus time within the experimental temperature range of 330 °C to 360 °C. A combination reaction kinetics model more accurately modeled degree of cure versus time for isothermal conditions and better represented the character of the reaction. The onset of diffusion control results in poor correlation between the combination reaction kinetics model and experimental results beyond a degree of cure of 0.90. Thus, a different technique was sought to provide a better measure of the influence of cure time and temperature on the degree of cure, or reaction progress.

Other investigators reported that PET imides appear to continue to cure despite additional cure being undetected by DSC and FTIR; the additional cure was detected by increases in glass transition temperature, T_g . Therefore, the T_g of 2.5kPETU was chosen as a gauge for monitoring reaction progress. A modified central composite design experimental method was used to determine the optimal ranges of cure time and temperature for neat and CFR 2.5kPETU to reach the maximum T_g of approximately 260 °C. The neat resin reaches this maximum T_g with a hold temperature around 355 °C and 50 minutes above 325 °C. The time to ramp from 325 °C to the hold temperature and back down to 325 °C was taken into account since cure onset was around 325 °C. These cure conditions agree fairly well with the predictions of the combination reaction kinetics model. Carbon fiber-reinforced 2.5kPETU reaches the maximum T_g with a hold temperature around 380 °C and 90 minutes above 325 °C. Obviously, inclusion of fiber in the matrix retards reaction progress resulting in a need for higher cure temperatures and longer cure times. It is thought that oxidation of the carbon fiber resulted in interactions between the fiber and PETU that slowed reaction and possibly contributed to the good fiber/matrix adhesion seen throughout this study. An important point to take from these results is that the processing schedule for a CFR polymer should not be based solely on the cure kinetics of the neat resin, but that influences of the fiber on the cure kinetics should be considered.

A two-stage, dual-Arrhenius model was successfully utilized to model the isothermal complex viscosity of 2.5kPETU over the processing range of 325 °C to 350 °C. The transition between the first and second stages of the model occurs when the degree of cure

approaches 0.37. This transition is thought to take place as a result of the crosslinking stage of the reaction overtaking the chain growth stage of the reaction. As an additional note, the activation energies for gelation, or reaction, calculated via rheological measurements agree well with those calculated from DSC thermal analysis.

As indicated by the three questions presented at the beginning of this chapter, in conjunction with the thermal and rheological characterization of 2.5kPETU, investigations of environmental effects on the properties of neat and CFR 2.5kPETU were conducted. In contrast to the results seen for 3kPETU, there was a significant reduction of TFS with moisture uptake to a M_m of 0.53% by mass at 85% relative humidity. In addition, following moisture desorption in a 10% relative humidity environment, which reduced the composite moisture content to less than that of the as-manufactured composite, the TFS did not recover to the as-manufactured level. This inability to fully recover to the as-manufactured strength indicates the composite incurred permanent damage, which was apparent in the form of cracks and cavities along composite surfaces in contrast to the smooth, resin-rich surfaces seen in undamaged areas. Damage was also present in the form of cracks that ran around the circumference of fiber/matrix interfaces and traversed the bulk matrix to neighboring fiber/matrix interfaces.

The difference in the processing schedules used to manufacture the CFR 2.5kPETU and CFR 3kPETU composites likely accounts for their different responses to enduring one moisture sorption cycle. The CFR 3kPETU composites were consolidated under 1.4 kPa compaction pressure for 90 minutes at 350 °C. In contrast, the CFR 2.5kPETU composites were consolidated under 0.7 kPa compaction pressure for 50 minutes at 350 °C. Chapter 5 demonstrates that the difference between a 50 minute hold and a 90 minute hold at 350 °C results in a significant difference in the T_g , or the degree of cure, of CFR 2.5kPETU composites (Figures 5.19 and 5.21).

The measured D_z was higher in the TFS specimens than in the open-hole compression strength specimens (OHCS). As with the measurements on CFR 3kPETU, the smaller specimens produced a larger value for the diffusion coefficient, which varied between approximately 2.5×10^{-6} mm²/sec to 6.5×10^{-6} mm²/sec for the composite specimens. Thus, it is recommended that larger specimens be used to obtain the most accurate measurements of D_z , even if sealants are used. However, using smaller specimens should provide a worst case value for moisture desorption, since a low diffusion coefficient is generally desired.

The main purpose of the thermal-oxidative aging experiments was to assess the potential of using CFR 2.5kPETU in high-performance aerospace applications. The minimal mass loss from both composite and neat resin specimens following aging at 204 °C for up to 5000 hours in environments having oxygen partial pressures up to twice that of ambient air is encouraging. Complementing the minimal mass loss was the absence of any visual evidence of degradation (cracking, resin discoloration, etc.) following thermal-oxidative aging. However, thermal-oxidative aging did reduce TFS with the magnitude of the reduction increasing with increasing oxygen partial pressure. In addition, this reduction was proportional to (time)^{0.29}. Unfortunately, no significant results could be obtained from the OHCS tests nor the apparent interlaminar shear strength tests. Many of the OHCS specimens failed at the grips, and all of the apparent interlaminar shear strength specimens failed in bearing mode.

Due to the lack of visual evidence of damage, Vickers Hardness was profiled through the depth of neat resin specimens using a microindentation technique. These measurements did reveal the progression of degradation from the surface inwards to the specimen interiors. The depth of degradation was three times greater in the specimen aged in the 40.4 kPa p(O₂) environment than in the specimen aged in the 20.2 kPa p(O₂) environment. However, the gradient of hardness between the specimen surfaces and the undegraded interior regions was the same for both environments. Neat resin specimens aged in the 100% nitrogen environment displayed hardness changes also; these results support the reduction seen in TFS during aging in the 100% nitrogen environment.

In response to the three questions posed at the beginning of this chapter, well-consolidated CFR PETU composites can be manufactured utilizing dry powder prepregging and the mechanical properties of these composites compare well with other high-performance fiber-reinforced polymer matrix composites. The results of moisture exposure on the properties of CFR 3kPETU and CFR 2.5kPETU are promising, since the damage to the CFR 2.5kPETU composites can most likely be attributed to incomplete cure. Thermal-oxidative aging resulted in degradation of neat and CFR PETU properties. However, the aerospace applications for which this material is being considered rarely reach temperatures near 204 °C and generally operate in environments having oxygen partial pressures less than 20.2 kPa. In addition, TFS is very sensitive to property changes near the surface of a material due to the test geometry. Thus, this thermal-oxidative aging study may have determined some limitations on the application of PETU, but it does not rule out long-term use at lower temperatures.

10.2 Recommendations for Future Work

Relationships between reaction progress and cure time and temperature were developed for neat 2.5kPETU using DSC measurements of both heat of reaction and T_g . In addition, a relationship between reaction progress and cure time and temperature was developed for CFR 2.5kPETU using measurements of T_g . Considering the differences in these relationships regarding suggested processing schedules to reach full cure, DSC measurements of heat of reaction for CFR 2.5kPETU should be performed to develop a cure kinetics model of degree of cure versus cure time and temperature for CFR 2.5kPETU. The predictions of this model could then be compared with those of the three existing relationships.

Thermal analysis via DSC heat of reaction measurements would allow for the determination of the activation energy for reaction and total heat of reaction for CFR 2.5kPETU. Comparison of these values with their neat resin counterparts would allow for further evaluation of the influence of carbon fiber on reaction progress. Furthermore, the predictions of a reaction kinetics model for CFR 2.5kPETU would provide clarification of the predictions of the T_g versus cure time and temperature relationship developed via the central composite design experimental method. Overall, adding this fourth relationship between reaction progress and reaction parameters would further clarify the differences in reaction characteristics of neat and CFR 2.5kPETU.

Because there was a significant difference in the response of CFR 3kPETU and CFR 2.5kPETU composites to moisture exposure, another set of 2.5kPETU composite panels should be manufactured for moisture exposure. The processing schedule for these panels should be based on the cure kinetics model that would be developed for CFR 2.5kPETU and the already existing relationship between T_g and reaction parameters. The results of moisture exposure on these fully cured CFR 2.5kPETU composite panels should clarify the results seen in the two moisture exposure studies presented in this dissertation. Though the poor performance of the CFR 2.5kPETU composite panels was attributed to lack of full cure, basic differences between 2.5kPETU and 3kPETU could have been responsible. The difference in their molecular weights was discussed in Chapter 8 as an unlikely source for their different responses to moisture exposure. Another difference in the two batches of PETU is that 3kPETU was synthesized in lab scale (maybe 50 g at a time), whereas, 2.5kPETU was manufactured at a small scale production level (about 23 kg). It is believed that moisture exposure, and subsequent mechanical testing, of fully cured CFR 2.5kPETU

composite specimens would verify the important role that degree of cure plays in the ability of the properties of CFR 2.5kPETU to endure moisture absorption and desorption.

Additional future work involving the study of moisture exposure on PETU was discussed in Chapter 8. This moisture exposure experiment would study the influence of M_m on D_z by initially exposing vacuum-dried composite specimens to a low relative humidity environment until M_m for that relative humidity is reached. This first exposure should fill any microvoids in the composite with moisture. The relative humidity would then be increased for a measurement of D_z unaffected by the influence of microvoids. After reaching the next M_m , the relative humidity would again be increased for another D_z measurement. Repetition of this incremental procedure would provide insight into the influence of moisture content on D_z via interactions between moisture and the matrix.

After the issues concerning the influence of degree of cure on survivability and the effect of moisture content on the diffusion coefficient are addressed, the effect of multiple moisture cycles on mechanical property retention should be investigated. Up to this point, the harshest moisture conditioning prior to mechanical testing was one cycle of moisture absorption at a high relative humidity followed by moisture desorption at a low relative humidity. Mechanical property retention and diffusion coefficients should be measured following multiple (e.g., 5, 10, 20) moisture sorption cycles. Depending on the material's response to these relatively low number of cycles, exposure to higher numbers of moisture sorption cycles should follow until the reduction of mechanical properties is unacceptable or the material proves to be able to survive a number of cycles equivalent to a predetermined service lifetime.

Based on the results of the thermal-oxidative aging study, it would be interesting to look at thermal-oxidative aging in one specific environment (e.g., 20.2 kPa $p(O_2)$) at a range of temperatures above and below 204 °C to evaluate the temperature dependence of degradation. In addition, aging in pure nitrogen, without any pre-aging, should be studied further at different temperatures to better isolate the source(s) of property degradation during nitrogen aging. For both of these recommended studies, it is suggested that composite panels be consolidated using a cure schedule that provides optimal cure rather than the cure schedule of Chapter 7. This improved cure schedule would eliminate lack of full cure as a variable when evaluating sources of degradation.

Composites aged for 5000 hours at 204 °C experienced an increase in T_g , which was attributed to three possible actions: densification by physical aging, desorption of plasticizing moisture, and additional cure. It may be possible to determine the contributions of these actions via different specimen preparation and conditioning. If specimens were cured in the same manner as those tested in this study, such that the control T_g was 255 °C, measurement of T_g following vacuum-drying would give a measurement of the influence of plasticizing moisture on the T_g . Aging of vacuum-dried specimens would provide a measure of the T_g increase due to both additional cure and physical aging. Annealing of aged specimens above the T_g would reverse physical aging and allow the contributions of additional cure and physical aging to be differentiated.

More general and broader research topics that may be addressed with PETU include the study of the durability of CFR PETU; basic mechanical properties were measured in this project, but the actual application of CFR PETU will require a knowledge of its response to fatigue. Another issue to address with PETU is the modification of its chemistry in a manner that mechanical properties are not sacrificed while slightly reducing the viscosity at processing temperatures such that more cost-effective melt impregnation composite manufacturing techniques may be utilized.

One additional recommended study is not specific to PETU. Diffusion depth was seen to have a power law dependence on time. However, the exponential term displayed a possible tendency to decrease away from the Fickian exponent of 0.50 with increasing aging time. To further investigate this possible tendency, a polymer in which diffusion depth is easily measured should be selected. Samples of this polymer should be aged for at least 5000 hours with samples removed from the aging environment at frequent intervals. A large number of data points would allow a power law fit to be applied up to different aging times. Consequently, dependence of the exponential term on time could be evaluated.

The goals of this research project were accomplished in that it was shown that it is feasible to manufacture well-consolidated CFR PETU composites with good mechanical properties, and basic knowledge of the material's response to moisture exposure and thermal-oxidative aging was obtained. However, a large quantity of future research is needed to fully characterize the processing of PETU, its responses to environmental exposure, and the effect of dynamic loading on material properties. The information presented in this dissertation should act as a foundation for this future research.

Vita

TODD AARON BULLIONS

EDUCATION

Virginia Polytechnic Institute and State University

Ph.D., Materials Engineering Science Program,
August 1995 - September 2000

RESEARCH: Fiber-Reinforced Polymeric Composites: Investigation of a novel high-performance polymer: cure and rheological characterization, composite manufacture, and environmental effects on composite physical and mechanical properties

ADVISOR: Dr. Alfred C. Loos

GPA: 3.7677

HONORS: Perkin Elmer Scholarship Award, 1999 - 2000; Presented by the Composites Division of the Society of Plastics Engineers
Virginia Space Grant Consortium Fellowship, 1998 - 2000
Student Recipient: GENCORP Signature University Award, 1998
National Defense Science & Engineering Graduate Fellowship, 1995 - 1998

ACTIVITIES: Center For Composite Materials and Structures:
Student Representative for Administrative Board, 1996 - 1998
Blacksburg Striders, 1995 - Present; Newsletter Editor, 1997 - 1998

North Carolina State University

B.S., Materials Science and Engineering, May 1994

GPA: 4.0, *summa cum laude*

HONORS: Valedictorian
Honor Society of Phi Kappa Phi, 1993
Alpha Sigma Mu International Materials Science Honor Society, 1992

SCHOLARSHIPS: College of Engineering Faculty Senior Scholarship, 1993 - 1994
United Technologies Scholarship, 1992 - 1993
Engineering Alumni Fund Scholarship, 1990 - 1994

ACTIVITIES: Materials Technical Society, 1991 - 1994
Crew Team, 1993

EXPERIENCE

VIRGINIA POLYTECHNIC INSTITUTE & STATE UNIVERSITY, Blacksburg, VA

Mentor Summers: 1998 & 1999
National Science Foundation Summer Undergraduate Research Program

Undergraduate Research Assistant Summers: 1992 & 1993
National Science Foundation Summer Undergraduate Research Program

LORD CORPORATION, Cary, NC

Research Assistant, Advanced Technology Group May 1994 - August 1995

UNDERGRADUATE STUDIES TUTORIAL CENTER, NCSU, Raleigh, NC

Individual Tutor and Group Supplemental Instruction Leader 1991 - 1994
First and Second Semester Physics